Proceedings of The CEReS International Symposium on Radiation Budget and Atmospheric Parameters Studied by Satellite and Ground Observation Data—Toward the Understanding of Long Term Trend in Asia

February 17 - 18, 2005
Chiba University, Japan

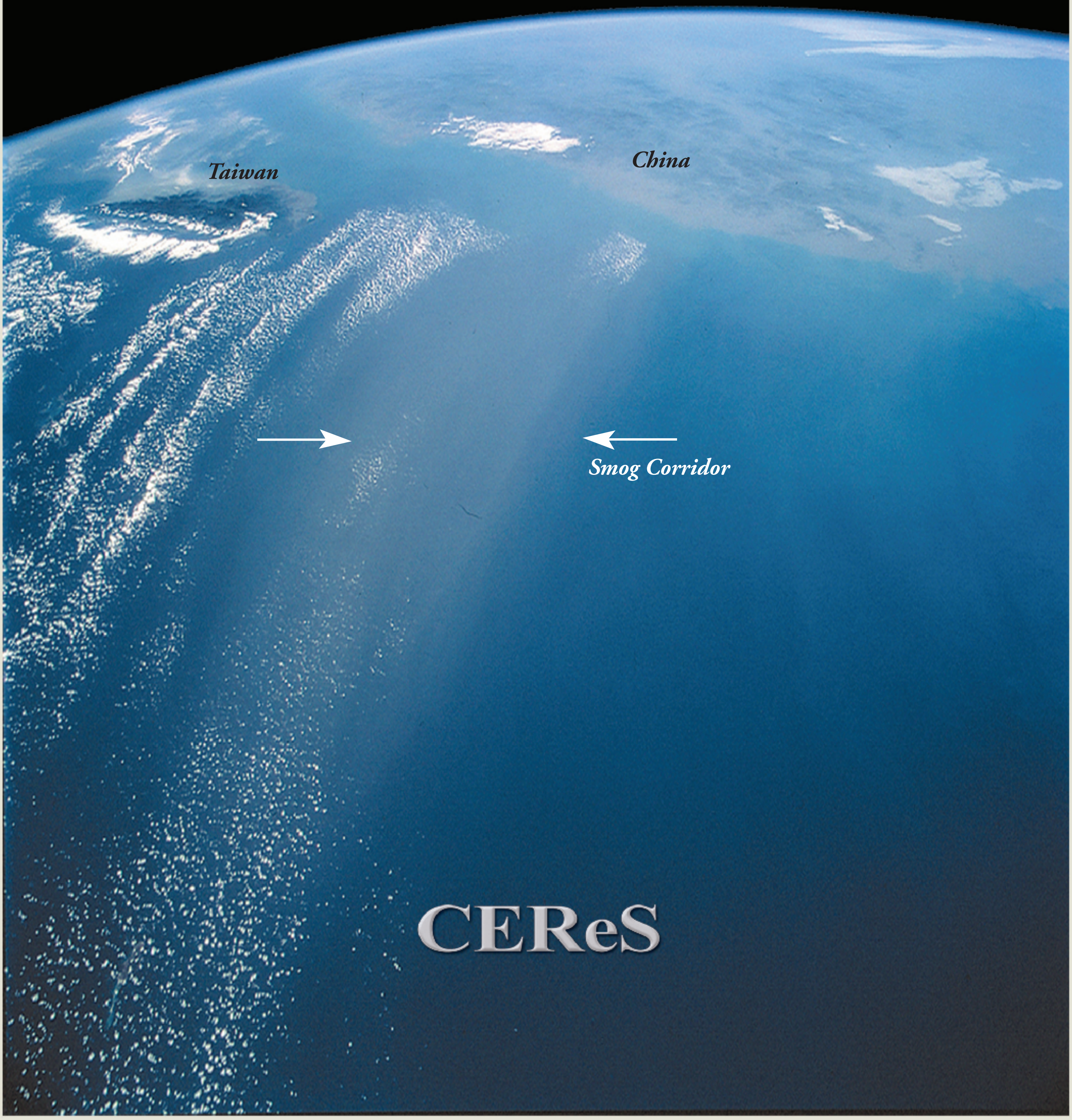

CEReS

Published by Center for Environmental Remote Sensing,
Chiba University,
1-33 Yayoi-cho, Inage, Chiba, 263-8522 Japan

Cover layout by T. Ishiyama
and cover image was provided by NASA-JSC

当シンポジウムの開催資金の一部は
「財団法人ちば国際コンベンションビューロー」
の援助によりました

INDEX (Click the Article No. to jump to the manuscript)

Keynote Talk

Session 1

Session 2

Session 3

Session 4

Session 5

Poster Session

CEReS International Symposium 2005

CEReS International Symposium on
Radiation Budget and Atmospheric Parameters
Studied by Satellite and Ground Observation Data
— Toward the Understanding of Long Term Trend in Asia

February 17 (Thur.) & 18 (Fri.), 2005

Keyaki-Hall, Chiba University, Chiba, Japan

Editors
N.Takeuchi, T.Takamura and H. Kuze

Hosted by
CEReS, Chiba University
http://www.cr.chiba-u.jp/

Center for Environmental Remote Sensing
Chiba University, Japan

PREFACE

Center for Environmental Remote Sensing (CEReS), Chiba University was established in 1995 for the purpose of developing remote sensing technology and its application to environmental science. Since then, CEReS has hosted an international symposium every year in a variety of fields in remote sensing(2003); vegetation (1995, 1998), oceanography (1999), atmosphere (1998, 2001), hydrology (1997), arid land (1997) and cryosphere (2003). In the field of atmosphere, a symposium entitled “Atmospheric correction of satellite data and its application to global environment” was held in 1998, and another one “Remote sensing of the atmosphere and validation of satellite data” in 2001. For the title of the coming symposium in 2005, we have selected the topic of radiation budget and related validation activities. Radiation budget is of vital importance in the consideration of global warming and climate. Remote sensing (RS) provides the capability of global-scale monitoring; in particular, the atmospheric RS has a considerable potential for future development. At the present stage, we still need intensive validation activities in order to establish the relationship between the satellite monitoring and true atmospheric/ground conditions. Furthermore, long-term satellite and ground observations will provide us with the precious data concerning the environmental trend. This symposium is organized to present and discuss these state-of-the-art issues in this fast developing field of the atmospheric RS.

This symposium consists of a keynote talk, 5 oral sessions, 1 poster session and 1 session for introducing the center projects. This covers a wide field including aerosol and cloud and their validation on the ground.

If this symposium will become useful in promoting the relating study, then it is the greatest pleasure as an organizer.

Nobuo Takeuchi
Symposium Chair
Prof. of Chiba University
Director of CEReS

CEReS Symposium Program

CEReS International Symposium on
Radiation Budget and Atmospheric Parameters Studied by Satellite and Ground Observation Data
— Toward the Understanding of Long Term Trend in Asia
February 17 (Thu) and 18 (Fri), 2005,
Keyaki-Hall, Chiba University, Japan

February 17
9:30-9:40
Opening Remark Nobuo Takeuchi

9:40-10:10
Keynote Talk
Invited (30) Teruyuki Nakajima
On the recent progress of atmospheric satellite remote sensing and radiation budget studies

Session 1
Long-term trend in the radiation budget and atmospheric parameters from satellite observations

10:10-10:40
1-1. *Invited* (30) Yuanchong Zhang, William B. Rossow and Paul W. Stackhouse Jr.
ISCCP-FD's surface radiation flux datasets: characteristics and comparison with GEWEX SRB

10:40-11:00
1-2. (20) Yuichiro Oku, Hirohiko Ishikawa and Zhongbo Su
Estimation of land surface energy fluxes over the Tibetan Plateau using GMS data

11:00-11:20 BREAK

11:20-11:40
1-3. (20) Jules R. Dim, Tamio Takamura, Itaru Okada, Hideaki Takenaka
Comparative Study of cloud parameters derived from Terra-MODIS and GMS-VISSR

11:40-12:00
1-4. (20) Kun Yang, Toshio Koike
Development and validation of a general model for estimating global solar radiation from hourly, daily and monthly surface meteorological data

12:00-12:20
1-5. (20) Takashi Y. Nakajima, Teruyuki Nakajima, Shuichiro Katagiri
The characteristics of the cloud properties retrieved from Global Imager aboard the ADEOS-II (Midori-II) Earth observation satellite

12:20-13:30 LUNCH BREAK

Session 2
Interpretation of satellite data for atmospheric analysis and meteorological applications

13:30-14:00
2-1. *Invited* (30) Ehrhard Raschke, Makoto Wada and Takashi Yamanouchi
Measurement of clouds, and radiation from space for climate studies

14:00-14:20
2-2. (20) Y. Kawata , T. Umeki and K. Takemata
Reflectance band ratios in Japan using satellite and sky observation data

14:20-14:40
2-3. (20) Katsutoshi Kozai, Anna Sasaki
SeaWiFS and MODIS-derived product verification using normalized water-leaving radiance model in the western equatorial Pacific Ocean

14:40-15:00
2-4. (20) Hideaki Takenaka, Tamio Takamura
Uncertainty in cloud optical thickness estimation from GMS-5 VISSR algorithm, explained by quantization noise and, it's Influence on the estimated radiative budget

15:00-15:20
2-5. (20) Mitsuo Minomura, Yoshiyasu Todate, Hiroaki Kuze, Nobuo Takeuchi
Retrieval of aerosol optical properties over Chiba land area from Landsat/TM imagery
— Part I: Determination of spatial distribution of aerosol optical thickness

BREAK 15:20-15:30

CEReS Projects

15:30-15:45
Project-1 (15) Ryutaro Tateishi
Monitoring and analysis of global surface environmental changes by satellite data

15:45-16:00
Project-2 (15) Yoshiaki Honda and Koji Kajiwara
Study on earth surface, vegetation and land cover change with changing of surface 3D structure on Eurasian continent and satellite data analysis, processing method, development of data verification methods

16:00-16:15
Project-3 (15) Hiroaki Kuze
Evaluation of radiation budget on the basis of satellite data and ground observation network, and study of long-term changes in atmospheric parameters

16:15-16:30
Project-4 (15) Akihiko Kondoh
Application of remote sensing methods to local communities — enlightenment activities by means of the synergy effect of various spatial data

BREAK 16:30-16:40

16:40-17:40
Poster Session

P-1. Hiroshi Okayama
Laboratory test of atmospheric turbulence and its implication in the satellite observations

P-2. Hu Bo, Wang Yuesi, Liu Guangren, Ma Zhiqiang
Comprehensive study on photosynthetically active radiation in Beijing

P-3. Shunsuke Fukagawa, Ikue Kouga, Hiroaki Kuze, Nobuo Takeuchi, Makoto Sasaki, Yoichi Asaoka, , Satoru Ogawa
Environmental application of the all-sky survey high-resolution air-shower(ASHRA) telescope — aerosol distribution measurement using a bistatic, imaging lidar

P-4. Gerry Bagtasa, Nofel Lagrosas, Hiroaki Kuze, Nobuo Takeuchi, Shunsuke Fukagawa, Yotsumi Yoshii, Suekazu Naito, Masanori Yabuki
Mie-scattering simulation and measurement of mass extinction efficiency from portable automated lidar and suspended particulate matter measurements

P-5. J. Batbayar, S.Tuya, N. Tugjsuren
Net radiation estimation using MODIS-TERRA data for clear sky days over homogeneous areas in Mongolia

P-6. Toru Kimura, Toyofumi Umekawa, Si Fuqi, Hiroaki Kuze, Nobuo Takeuchi
Measurement of NO_2, SO_2, O_3, H_2O and aerosol in the troposphere using differential optical absorption spectroscopy (DOAS)

P-7. Dodi Sudiana, Mitsuo Minomura, Hiroaki Kuze, Nobuo Takeuchi
Analysis of the Asian dust aerosol optical properties over the ocean

P-8. Koji Asakuma, Mitsuo Minomura, Hiroaki Kuze, Nobuo Takeuchi
Retrieval of aerosol optical properties over land in Chiba area from Landsat/TM imagery — Part II: Determination of aerosol size distribution

P-9. Jin-jia Guo, Zhi-shen Liu, Zhao-ai Yan
Micro Pulse Lidar Observation of Low Relative Humidity Layer

P-10 Nobuhiro Kikuchi, Hiroshi Kumagai, Hiroshi Kuroiwa, Teruyuki Nakajima, Akihide Kamei, Ryosuke Nakamura
Cloud optical thickness and effective particle radius derived from transmitted solar radiation measurements: Comparison with cloud radar observations

BANQUET 17:45-19:15

February 18

Session 3
Observation of aerosols and their impact on atmospheric radiation

9:00-9:30
3-1. *Invited* (30) Zhi-shen Liu, Zhao-ai Yan Bing-yi Liu Zhao-bin Sun
Characters of marine atmospheric boundary layer structure and aerosol profile observed by HSRL

9:30-9:50
3-2. (20) Toshiyuki Murayama, Miho Sekiguchi, Detlef Mueller, Katsuya Wada, and Yasuharu Saito
Characterization of Asian tropospheric aerosols with multi-wavelength Mie-Raman lidar and skyradiometer

9:50-10:20
3-3. *Invited* (30) Qiu Jinhuan
A study of optical properties of urban aerosols in China

10:20-10:40
3-4. (20) M. Shiobara, M. Yabuki, H. Kobayashi, and K. Hara
Optical, physical and chemical properties of aerosols around Japan based on the R/V Shirase shipboard measurements

BREAK 10:40-10:50

10:50-11:10
3-5. (20) Pradeep Khatri, Yutaka Ishizaka, and Tamio Takamura
Observation on radiative properties of aerosol particles over the urban area of Nagoya

11:10-11:30
3-6. (20) Jugder Dulam and Erdenetsetseg Baasandai
Dust storm observations in Mongolia in spring 2004

Session 4
Network observation of the atmosphere

11:30-12:00
4-1. *Invited* (30) Yuesi Wang
The radiation monitoring network of Chinese ecosystem research: (CERN)
LUNCH BREAK 12:00-13:00

13:00-13:30
4-2. *Invited* (30) Ulla Wandinger
EARLINET: the first continental-scale lidar network for vertical aerosol profiling

13:30-13:50
4-3. (20) Pinhua Xie, Yihuai Lu, Yujun Zhang, Ang Li, Jianguo Liu and Wenqing Liu
Ultraviolet radiation measurement in the south of Sinkiang using a compact zenith-sky spectrometer

Session 5
Improved determination of radiation and atmospheric parameters from satellite and ground observations

13:50-14:20
5-1. *Invited* (30) Rachel Pinker
Progress and outstanding challenges in estimating surface radiation budgets by methods of remote sensing

14:20-14:50
5-2. *Invited* (30) Tadahiro Hayasaka, Kazuaki Kawamoto, Jianqing Xu and Guangyu Shi
Seasonal and long-term variations of shortwave radiation in China

14:50-15:10
5-3. (20) Kisei Kinoshita, Hiroyuki Kikukawa, Naoko Iino, Wang Ning, Zhang Gang, Jugder Dulam, Tsatsaral Batmunkh, and Satoshi Hamada
Properties of long-time digital camera records in Changchun and Ulaanbaatar

BREAK 15:10-15:20

15:20-15:40
5-4. (20) D. Rajan and GR. Iyengar
Analysis and impact study of global positioning system radio occultation precipitable water vapor obtained from Chiba University over East Asia region

15:40-16:00
5-5. (20) Shoji Asano, Masaya Kojima, Tamio Takamura
Optical and microphysical properties of the 2003 Yamase clouds estimated from satellite remote sensing and shipboard observation

16:00-16:20
5-6. (20) Nick Schutgens, Hiroshi Kumagai
Improving along-beam spatial resolution of radar measurements

16:20-16:40
5-7. (20) Itaru Sano, Sonoyo Mukai
Aerosol properties over Asia with ADEOS-1 & -2/POLDER

16:40-17:00
5-8. (20) Toshiaki Takano, Ken-ichi Akita, Hiroshi Kubo, Youhei Kawamura, Hiroshi Kumagai, Tamio Takamura, Yuji Nakanishi and Teruyuki Nakajima
Observations of cloud properties using the developed millimeter-wave FM-CW radar at 95 GHz

17:00-17:20
5-9. (20) Makoko Kuji, Nobuyuki Kikuchi and Akihiro Uchiyama
Retrieval of precipitable water using ADEOS-II / GLI near infrared data

CLOSING REMARK Tamio Takaumura

CEReS Symposium Contents

CEReS International Symposium on Radiation Budget and Atmospheric Parameters Studied by Satellite and Ground Observation Data — Toward the Understanding of Long Term Trend in Asia

Keynote Talk

Session 1

Long-term trend in the radiation budget and atmospheric parameters from satellite observations

Session 2

Interpretation of satellite data for atmospheric analysis and meteorological applications

Session 3
Observation of aerosols and their impact on atmospheric radiation

Session 4
Network observation of the atmosphere

Session 5
Improved determination of radiation and atmospheric parameters from satellite and ground observations

Poster Session

On the Recent Progress of Atmospheric Satellite Remote Sensing and Radiation Budget Studies

Teruyuki Nakajima (teruyuki@ccsr.u-tokyo.ac.jp)
Center for Climate System Research, The University of Tokyo

1. Introduction

In the last two decades the atmospheric satellite remote sensing and radiation budget studies have made a great progress partly because of the strong demand of accurate evaluation of the radiative forcing of anthropogenic climate change factors such as direct and indirect climate effects of man-made aerosols. IPCC (e.g., IPCC, 2001) has devoted a considerable effort on accessing these various radiative forcings. Another important key to the progress is that the modeling of atmospheric radiative transfer processes has become more comprehensive and accurate to describe the processes in the real earth's atmosphere. Optical properties of aerosols and clouds have been extensively measured and modeled in several large-scale field experiments of aerosols and radiation as in INDOEX (Ramanathan et al., 2001), IGAC/ACE-Asia (Hubert et al., 2003), Japan Science and Technology Corporation/APEX (Nakajima et al., 2003), etc. Surface networks, such as NASA AERONET (Holben et al., 2001), WCRP/BSRN, and JAXA SKYNET, also have started providing quantitative data useful for validating the satellite remote sensing and model simulation.

In this paper I like to discuss the recent progress in satellite remote sensing of atmosphere and radiation budget studies, especially those related with radaiative forcing evaluation issue.

2. Studies on satellite remote sensing of atmosphere and radiation budget

A variety of satellite remote sensing techniques of atmospheric aerosols and clouds have been proposed in the last two decades. ADEOS-II/GLI, EOS/MODIS, ENVISAT/MERIS are new satellite-borne sensors to explore the utilities of information included in multi-wavelength spectral radiances. Radiances at wavelengths from UV to near infrared spectral regions have provided good information to retrieve the aerosol optical thickness, size index or Ångström exponent, and aerosol types. Further use of bidirectional angular information and polarization are also found to be useful to stabilize the inversion process such as aerosols over land area. Figure 1 shows an example of aerosol type classification using the four channel algorithm of Higurashi and Nakajima (2002) with MODIS radiances from UV to near infrared spectral region. Comparing with surface-measured values of optical thickness contributions from sulfate, carbonaceous, mineral dust, and sea salt aerosols, it is found that the technique can provide useful information about the dominant aerosol type that determines satellite-received radiances. Our study found that the most popular aerosol type in the East Asian region is of carbonaceous that absorb strongly the solar radiation in blue spectral region. The single scattering albedo (SSA) of aerosols from AERONET also shows a typical value about 0.9 in most areas where anthropogenic aerosols are dominant.

It is interesting to study what is the globally averaged clear sky radiative forcing of anthropogenic aerosols with such low SSA. Kaufman et al. (2003) derived the clear sky direct radiative forcing of anthropogenic aerosols as -0.46 W/m^2 from MODIS global measurements of aerosols as summarized in Fig. 2. On the other hand, -0.70 W/m^2 is our value of the clear sky direct radiative forcing of anthropogenic aerosols estimated by CCSR/NIES AGCM combined with SPRINTARS aerosol chemical transport model (Takemura et al., 2005). These values show that the anthropogenic aerosols have very small forcing even in the clear sky condition due to their strong absorption of solar radiation. It is also important to find that the direct forcing of anthropgenic aerosols in the whole sky condition is as small as -0.02 W/m^2. This large reduction of the magnitude of forcing is a result of large positive forcing due to strong absorption by aerosols in cloudy regions. Since the MODIS clear sky forcing is smaller in magnitude than that from GCM, the real value of the radiative forcing in the whole sky condition may be near zero or positive. This discussion suggests that measurements of solar radiation absorption by aerosols in cloud regions will be needed for better estimation of the aerosol direct forcing.

On the other hand, the recent evaluation of indirect forcing is still in confusion. Even with the same SPRINTARS model with CCSR/NIES AGCM, there have been several estimates ranging from -0.94W/m^2 to -2.4 W/m^2 as summarized in Fig. 2, depending on what parameterization is adopted for conversion of aerosol particle number to cloud particle number (Takemura et al., 2005) and for autoconversion of cloud water to precipitation (Suzuki et al., 2003). A lower value of of -0.94 W/m^2 is obtained when they take into a updraft velocity effect and a large background aerosol number (Takemura et al., 2005). A key parameter for the magnitude of the indirect forcing is the increase rate of number of anthropogenic aerosols after industrial revolution, i.e., $\nu = N_{\mathrm{a,present}}/N_{\mathrm{a,pre\text{-}industrial}} - 1$. The ν-value takes 1.3 in Takemura et al. (2003) and 0.3 in Takemura et al. (2005) suggesting a large uncertainty in the estimation of aerosol number increase after the industrial revolution. This suggests that a study of natural source aerosols is important for better estimation of anthropogenic aerosol forcings.

Satellite remote sensing techniques can also be used to estimate the aerosol indirect forcing. Nakajima et al. (2001) used AVHRR-retrieved aerosol and cloud optical thickness and effective radius (or Ångström exponent) to derive column numbers of aerosols and clouds. They found a decrease in the effective particle radius and an increase in the aerosol optical thickness with increasing column aerosol number. By assuming $\nu = 0.30$, they found the indirect forcing over ocean as -1.3 W/m^2. Sekiguchi et al. (2003) re-examined this analysis more carefully and found that for the forcing is similar as -1.4 W/m^2. They also newly found that there is a cloud fraction increase with increasing aerosol number. A contradiction, however, is that the forcing becomes very small as -0.18 W/m^2 over ocean and -0.14 W/m^2 over land when they use POLDER-retrieved parameters. It is suggested that we need a more careful study of remote sensing data for evaluation of the indirect radiative forcing.

3. Conclusions

As discussed in the previous section, the direct forcing of anthropogenic aerosols is close to zero due to a large absorption of solar radiation by aerosol particles. This conclusion consequently raises a question: how large is the surface forcing by aerosol particles. Large absorption causes a large reduction in the solar radiative flux reaching the earth's surface, but at the same time the evaluation of forcing becomes difficult. So far, our GCM simulation produces surface radiative forcing values of -1 W/m^2 and -2.3 W/m^2 over ocean and land, respectively, so that there is a large diabatic forcing between ocean and land areas to drive secondary general circulation. More studies should be devoted for simultaneous measurements of surface radiative flux and aerosol absorption. Key parameters to be studied for better understanding of the radiative budget in cloudy regions are the single scattering albedo of aerosols and also the CCN ability of aerosols. Especially water activity of carbonaceous aerosols and size distribution should be studied more intensively. Considerable efforts are now being planned in a new project of UNEP/Atmospheric Brown Cloud (ABC) for comprehensive understanding the aerosol effects to climate, agriculture, and public health (Ramanathan et al., 2003).

References

Higurashi, A., and T. Nakajima, 2002: Detection of aerosol types over the East China Sea near Japan from four-channel satellite data. *Geophys. Res. Lett.*, **29**(17), 1836, doi:10.1029/2002GL015357.

Holben, B.N., D. Tanré, A. Smirnov, T.F. Eck, I. Slutsker, N. Abuhassan, W.W. Newcomb, J.S.Schafer, B. Chatenet, F. Lavenu, Y.J. Kaufman, J.V. Castle, A. Setzer, B. Markham, D. Clark, R. Frouin, R. Halthore, A. Karneli, N.T. O'Neill, C. Pietras, R.T. Pinker, K. Voss, and G. Zibordi , 2001: An emerging ground-based aerosol climatology: Aerosol optical depth from AERONET. *J. Geophys. Res.*, **106**, 12067-12097.

Huebert, B.T., T. Bates, P.B. Russell, G.Y. Shi, Y.J. Kim, K. Kawamura, G. Carmichael, and T. Nakajima, 2003: An overview of ACE-Asia: Strategies for quantifying the relationships between Asian aerosols and their climatic impacts. *J. Geophys. Res.*, **108**, No. D23, 8633, doi:10.1029/2003JD003550.

Kaufman, Y.J., A., 2003: The global aerosol system and its direct forcing of climate results from MODIS, AERONET and GOCART. *IUGG General Assembly, Sapporo*, June 30-July 4.

IPCC, 2001: Climate Change 2001-The Scientific Basis J. T. Houghton, Ed., Cambridge Univ. Press.

Nakajima, T., A. Higurashi, K. Kawamoto, and J. E. Penner, 2001: A possible correlation between satellite-derived cloud and aerosol microphysical parameters. *Geophys. Res. Lett.*, **28**, 1171-1174.

Nakajima, T., M. Sekiguchi, T. Takemura, I. Uno, A. Higurashi, D.H. Kim, B.J. Sohn, S.N. Oh, T.Y. Nakajima, S. Ohta, I. Okada, T. Takamura, and K. Kawamoto, 2003: Significance of direct and indirect radiative forcings of aerosols in the East China Sea region. *J. Geophys. Res.* , **108**(D23), 8658, doi: 10.1029/2002JD003261.

Nozawa, T., S. Emori, A. Numaguti, Y. Tsushima, T. Takemura, T. Nakajima, A. Abe-Ouchi, and M., Kimoto, 2001: Projections of future climate change in the 21st century simulated by the CCSR/NIES CGCM under the IPCC SRES scenarios, In 'Present and Future of Modeling Global Environmental Change-Toward Integrated Modeling', Matsuno, T. and H. Kida eds., *Terra Scientific Publishing Company*, Tokyo, pp.15-28.

Ramanathan, V., P.J. Crutzen, J. Lelieveld, A.P. Mitra, D. Althausen, J. Andersen, M.O. Andreae, W. Cantrell, G.R. Cass, C.E. Chung, A.D. Clarke, J.A. Coalkey, W.D. Collins, W.C. Conant, F. Dulac, J. Heinzenberg, A.J. Heymsfield, B. Holben, S. Howell, J. Hudson, A. Jayaraman, J.T. Kiehl, T.N. Krishnamurti, D. Lubin, G. McFarquhar, T. Novakov, J.A. Ogren, I.A. Podgorny, K. Prather, K. Priestley, J.M. Prospero, P.K. Quinn, K. Rajeev, P. Rasch, S. Rupert, R. Sadourny, S.K. Satheesh, G.E. Shaw, P. Sheridan, and F.P.J. Valero, 2001: Indian Ocean Experiment: An integrated analysis of the climate forcing and effects of the great Indo-Asian haze, *J. Geophys. Res.*, **106**, 28371-28398.

Ramanathan, V., and P.J. Crutzen, 2003: New directions: Atmospheric Brown Clouds, *Atmos. Environ.*, **37**, 4033-4035.

Sekiguchi, M., T. Nakajima, K. Suzuki, K. Kawamoto, A. Higurashi, D. Rosenfeld, I. Sano, and S. Mukai, 2003: A study of the direct and indirect effects of aerosols using global satellite datasets of aerosol and cloud parameters. *J. Geophys. Res.*, in press.

Suzuki, K., T. Nakajima, A. Numaguti, T. Takemura, K. Kawamoto, and A. Higurashi, 2003: A study of the aerosol effect on a cloud field with simultaneous use of GCM modeling and satellite observation. *J. Atmos. Sci.*, in press.

Takemura, T., T. Nakajima, O. Dubovik, B. N. Holben, and S. Kinne, 2002: Single scattering albedo and radiative forcing of various aerosol species with a global three-dimensional model. *J. Climate*, **15**, 333-352.

Takemura, T., 2003: Private communication regarding SPRINTARS simulations with different aerosol-cloud interaction parameterizations.

Takemura, T., T. Nozawa, S. Emori, T.Y. Nakajima, and T. Nakajima, 2005: Simulation of climate response to aerosol direct and indirect effects with aerosol transport-radiation model. *J. Geophys. Res.*, doi:10.1029/2004JD005029.

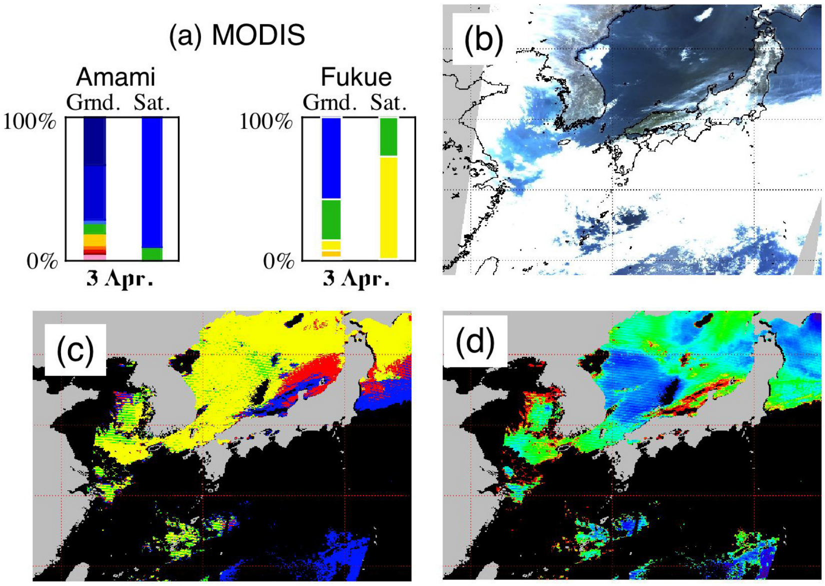

Fig. 1. Satellite classification of aerosol chemical properties by the four channel algorithm of Higurashi and Nakajima (2002) applied to a East Asian region. The panel (a) shows a comparison of aerosol optical thickness contributions of sulfate (green), carbonaceous (yellow), mineral dust (red), and sea-salt (blue)

compositions as estimated by the satellite remote sensing (Sat.) and surface chemical measurements (Grnd.) at Fukue-jima Island and Amami-Oshima Island on 3 April 2003. RGB composite (b), aerosol types (c), and optical thickness (d) are also shown.

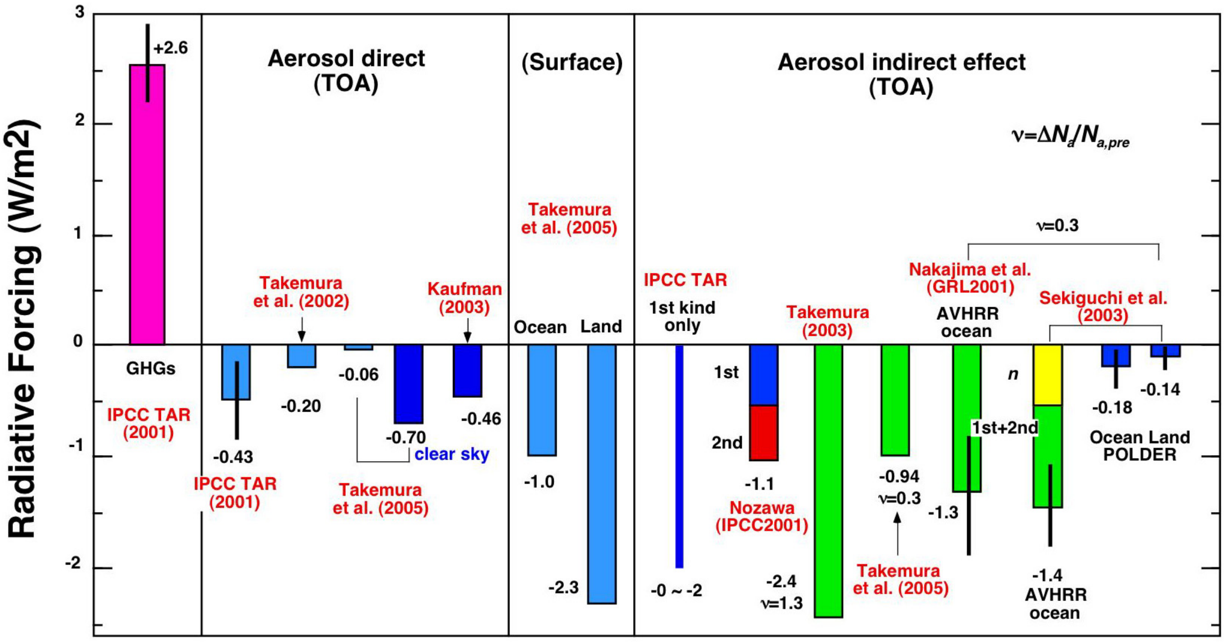

Fig. 2. Radiative forcing of anthropogenic greenhouse gases and aerosols since 1850 as estimated by IPCC (2001), Takemura et al. (2002; 2003; 2005); Kaufman et al. (2003); Nozawa et al. (2001); Nakajima et al. (2001); Sekiguchi et al. (2003). ν□□the inrease rate of aerosol number since 1850.

♣ISCCP-FD's Surface Radiation Flux Dataset: Characteristics and Comparison with GEWEX SRB

Yuanchong Zhang[1], William B. Rossow[2] and Paul W. Stackhouse Jr.[3]

[1]*Department of Applied Physics and Applied Mathematics, Columbia University, New York, NY, USA*
[2]*NASA Goddard Institute for Space Studies, New York, NY, USA*
[3]*Atmospheric Science Division, NASA Langley Research Center, Hampton, VA,,USA*

Abstract. Two decades-long global surface radiative flux products, ISCCP-FD and GEWEX/SRB, have been characterized and their 85-89 annual means are compared. Although their global-mean values agree quite well, their regional differences are larger, reflecting differences in their input datasets and radiative transfer treatments, mainly for surface albedo, aerosols and clouds for SW and temperature/humidity profiles and surface skin temperature for LW, respectively. Studying and resolving these differences are necessary to further improve surface radiation budget estimates so that the long-term climate trend may be derived in the future.

Key Words: Surface radiation budget (SRB), ISCCP-FD, GEWEX/SRB, radiative transfer model.

1. INTRODUCTION

Radiation is the primary forcing that drives the weather and climate within the Earth-atmosphere system. Since *Simpson* (1929), estimating Earth's radiation budget has long been pursued. But it is only the advent of satellites that has made it feasible to produce global radiation budget at top of the atmosphere (TOA) and various datasets measuring the physical properties of the atmosphere, clouds and surface that can be put into a radiative transfer model to calculate the radiation budget at the surface (SRF), TOA, and in the atmosphere (ATM). Such calculations are also essential for numerical modeling of the weather and climate. In the past two decades or so, numerous authors have produced satellite-based radiative flux datasets at TOA/SRF; but only recently have there appeared global, decades-long radiative flux datasets produced using more sophisticated radiative transfer models and improved input datasets. Among them are the two flux products from ISCCP-FD (International Satellite Cloud Climatology Project Flux product using the ISCCP D-series data) and GEWEX/SRB (Global Energy and Water Cycle Experiment Surface Radiation Budget project).

2. ISCCP-FD PRODUCT

ISCCP-FD is a self-consistent and integrated radiative flux profile (PRF) product. It contains radiative flux profiles defined by fluxes at five levels: SRF, 680 mb, 440 mb, 100 mb and TOA, and the input atmospheric and surface physical quantities used to calculate them. All of this information is collected into four datasets: FD-TOA, FD-SRF, FD-PRF and FD-INP, where FD-INP is a complete input dataset with virtually all the parameters used in the flux calculation. There is also an additional fifth monthly-mean FD-PRF dataset. Table 1 shows the definition of the five datasets of the ISCCP-FD product.

The FD product has complete global coverage with a spatial resolution of 280 km and time interval of 3-hour and monthly. At the time of writing, it covers a time period from July 1983 to June 2001 but will soon be extended to 2004.

The version of the radiative transfer model used in the flux calculation is 2001 NASA Goddard Institute for Space Studies (GISS) model. The most important characteristics of the

---

♣ Extended abstract presented at CEReS International Symposium on Radiation Budget and Atmospheric Parameters Studied by Satellite and Ground Observation Data Toward the Understanding of Long Term Trend in Asia, February 17 (Thur.) & 18 (Fri.), 2005, Chiba, Japan.

Table 1. Five Datasets of the ISCCP-FD Product

	Dataset Name	Definition
A	FD-TOA	All the radiative flux components at TOA[a]
B	FD-SRF	All the radiative flux components at SRF[a]
C	FD-PRF	All the radiative flux components for PRF (TOA and SRF, inclusive)[a]
D	FD-INP	Complete input variables used in flux calculation
E	FD-MPF	Radiatively linearly averaged monthly-mean FD-PRF

[a]Including summary of the most important input variables for it.

new GISS model are: (1) higher spectral resolution employing 15 non-contiguous correlated k-intervals to model overlapping cloud-aerosol and gaseous absorption for the shortwave (SW) (nominally 0.2-5.0 :m) with UVA and UVB treatment incorporated; (2) 33 non-contiguous correlated k-intervals for the longwave (LW) (nominally 5.0-200.0 :m, including one for a "window" wavelength: 11.1-11.3 :m) to match line-by-line fluxes to within 1 Wm$^{!2}$ and provide a significant improvement for upper stratospheric cooling rates due to water vapor over the old 1983 GISS model [*Oinas et al*., 2001]; (3) improved surface visible albedo (0.2-0.7 :m) values and a more precise 5-band near-infrared (NIR: 0.7-5.0 :m) albedo representation for 11 "vegetation" type; (4) more comprehensive set of atmospheric gaseous absorbers and aerosols with realistic spatio-temporal variations; (5) explicit treatments of non-spherical ice cloud microphysics and cloud macro-inhomogeneity; (6) realistic non-unit spectral emissivities for surface and cloud LW emission.

With the model, the 5-level downwelling and upwelling SW and LW radiative flux profiles are calculated using the following datasets to specify the properties of the Earth's atmosphere and surface: ISCCP-D1 (*Rossow and Schiffer,* 1999) cloud dataset with a statistical cloud vertical structure (CVS) model, the TIROS Operational Vertical Sounder (TOVS) temperature/humidity profile products, the Total Ozone Mapping Spectrometer (TOMS) ozone products, a climatology of near-surface air temperature (and surface skin temperature) diurnal cycle constructed from NOAA National Weather Service National Meteorological Center (NMC) surface weather reports and the first NCEP reanalysis, a climatology of cloud particle sizes from *Han et al.* (1994), and a climatology of stratospheric and upper tropospheric water vapor and stratospheric aerosols from Stratospheric Aerosol and Gas Experiment II (SAGE-II), a climatology of tropospheric aerosols used in the current NASA GISS climate model.

The complete description of the model, input data, and the sensitivity-study/validation results for FD product may be referred to *Zhang et al.* (2004). The information to obtain the datasets can be found at the ISCCP website (http://isccp.giss.nasa.gov/projects/flux.html),

3. ISCCP FD-SRF DATASET

As the bottom boundary part of the integrated FD flux profiles, the FD-SRF dataset has all the characteristics described above. In *Zhang et al.* (2004), we have repeated virtually all the validation studies for FD-SRF that were done for FD's precursor FC (C for ISCCP C-series data, the precursor of D-series) (*Zhang et al.,* 1995). Overall, FD decreases uncertainties about 5 Wm$^{!2}$ over FC. In addition, we have validated FD using new and more accurate ground 'truth' from the Baseline Surface Radiation Network (BSRN). The BSRN started operations in 1992 with 9 stations and has 35 sites currently. The original target accuracies for BSRN were ±10 Wm$^{!2}$ for downwelling SRF SW (S9$_S$) and ±20 Wm$^{!2}$ for downwelling SRF LW (L9$_S$). But significant improvements in procedures, instrument calibration and knowledge have led to estimated accuracies of ±5 Wm$^{!2}$ for S9$_S$ and ±10 Wm$^{!2}$ for L9$_S$ (*Ohmura et al.,* 1998). The comparisons of monthly, regional mean values from

FD with BSRN values suggests that we have been able to reduce the overall uncertainties to 10-15 W/m^2 at SRF from 20-25 W/m^2 for FC (*Zhang et al.,* 2004).

Table 2a summarizes the statistics of the comparison of all the available and matched, monthly mean FD and BSRN values, totaling 1970 and 1831 data points for $S9_s$ and $L9_s$, respectively. For $S9_s$, the mean (rms) difference (FD ! BSRN) is 2.0 (18.5) Wm$^{!2}$ and the correlation coefficient between the two sets is 0.98. For $L9_s$, these statistics are 2.2 (19.0) Wm$^{!2}$ and 0.97, respectively. Tables 2b and 2c show the same comparison statistics but for seven separate latitudinal zones. For the SW, most zones exhibit differences # 10 Wm$^{!2}$; the largest mean differences appear in the tropical zone (21.3 Wm$^{!2}$), where biomass burning aerosol effects have not been (completely) accounted for in our calculations, and at southern high latitudes (-20.0 Wm$^{!2}$), where the sample size at the surface is very small (23). The largest rms differences appear in the southern and northern polar regions (20.6 and 21.8 Wm$^{!2}$, respectively) with the rest of the zones exhibiting values # 16 Wm$^{!2}$. The correlation coefficients in all zones are above 0.97 except in the tropical zone (0.89). For the LW, all the zones have mean differences # 10 Wm$^{!2}$, except at southern high latitudes (18.8 Wm$^{!2}$) where the sample size is very small. Generally, the LW flux rms differences are slightly larger than for the SW and the correlation coefficients are lower, but still ∃ 0.81, except again at southern high latitudes.

Table 2a. SRF Downwelling SW and LW Fluxes for all FD-SRF and BSRN data[♦]

Quantity	FD	BRSN	mean difference	Stdv	corr coefficient	Slope	intercept	Norm dev	sample #
$S9_s$	168.20	166.19	2.017	18.491	0.9825	0.96	3.90	13.07	1970
$L9_s$	302.23	300.01	2.219	19.042	0.9706	1.05	-17.40	12.89	1831

Table 2b. SRF Downwelling SW from FD-SRF and BSRN Separated into Latitudinal Zones[♦]

Lat. Zone	FD	BRSN	mean difference	Stdv	corr coefficient	Slope	intercept	Norm dev	sample #
90E S 6 65E S	114.23	122.36	-8.133	20.599	0.9907	1.05	2.31	13.38	302
65E S 6 35E S	145.18	165.15	-19.972	15.370	0.9822	1.03	15.08	10.53	23
35E S 6 15E S	217.11	219.53	-2.412	11.728	0.9847	1.00	2.32	8.29	144
15E S 6 15E N	247.72	226.40	21.318	13.963	0.8928	0.95	-9.03	10.07	218
15E N 6 35E N	210.87	200.61	10.262	16.092	0.9742	0.97	-4.65	11.45	243
35E N 6 65E N	168.34	168.23	0.116	14.180	0.9847	0.95	7.96	9.88	819
65E N 6 90E N	86.64	86.63	0.005	21.798	0.9724	0.97	3.01	15.51	221

Table 2c. SRF Downwelling LW between Latitudinal-zonal FD-SRF and BSRN[♦]

Lat. Zone	FD	BRSN	mean difference	Stdv	corr coefficient	Slope	intercept	Norm dev	sample #
90E S 6 65E S	194.11	184.12	9.994	19.127	0.9478	1.14	-36.49	11.90	276
65E S 6 35E S	316.67	297.85	18.820	17.132	0.2916	0.60	107.75	14.40	23
35E S 6 15E S	357.99	360.82	-2.828	22.663	0.8122	1.09	-30.75	15.18	141
15E S 6 15E N	414.65	415.33	-0.680	8.797	0.8094	0.80	84.20	6.49	136
15E N 6 35E N	360.45	356.36	4.096	19.956	0.8634	1.00	-4.25	14.11	237
35E N 6 65E N	305.72	307.05	-1.327	17.688	0.9209	0.98	7.50	12.62	814
65E N 6 90E N	251.83	244.61	7.217	20.080	0.9293	1.33	-91.49	10.18	204

[♦] Regression statistics are from a linear least squares fit to the scatter of points, X/Y for FD-SRF/BSRN. All values are in Wm$^{!2}$, except the correlation coefficients and slopes, which are unitless. "Norm Dev" is the rms distance of all the points from the regression line.

4. GEWEX SRB DATASET

GEWEX-SRB (Release 2) dataset is also a global, long-term set with a higher spatial resolution of 1^o X 1^o at 3-hour temporal interval. It covers a time period of 12 years (July 1983 - October 1995) (*Stackhouse et al.,* 2001, 2004) but will soon be extended to 2004. Its radiative transfer algorithms are from *Pinker and Laszlo* (1992) and *Fu et al.* (1997) for broadband SW (0.2-4.0 :m) and LW (4.5-∞ :m), respectively. Among the input datasets, cloud information is from ISCCP-DX (*Rossow et al.,* 1996), the atmospheric temperature/humidity profiles are from the Goddard Earth Observing System (version1, GEOS-1) reanalysis, surface skin temperature is from GEOS-1 (originally from *Reynolds,* 1988) over oceans and land with more than 50% cloud cover and from ISCCP for land with less than 50% cloud cover and snow/ice covered surfaces. Ozone data is from TOMS integrated with TOVS when needed. The surface albedo is obtained from Pinker/Laszlo algorithm (*Pinker and Laszlo,* 1992) and the emissivity map is adapted from the CERES-SARB surface emissivity map (*Wilbur et al.,* 1999). A background aerosol is assumed based upon surface type in the Pinker/Laszlo model adapted from the *WCP-55* (1983) aerosol types. The effective optical depths are scaled in the algorithm to account for differences between composite clear-sky and observed clear radiances. The monthly averaged mean (RMS) difference of GEWEX SRB compared against all BSRN site measurements from 1992 – 1995 is -3.4 (23) Wm^{-2} for SW fluxes and –5.2 (15.5) Wm^{-2} for LW fluxes, respectively. That exclusion of polar sites reduces SW monthly mean (rms) difference to –0.2 (18.5) Wm^{-2} indicates a need for further study in the polar regions (*Stackhouse, et al.,* 2004).

5. SURFACE FLUX COMPARISON BETWEEN FD-SRF AND SRB

Table 3 shows statistical results from the comparison between FD-SRF and SRB for global averages of all the primary and derived surface flux components based on 5-year (85-89) annual means (with SRB map regridded to ISCCP's standard 280-km equal-area map).

Table 3. Comparison of Global Mean for 85-89 Annual Mean between FD-SRF and SRB [†]

Quantity	FD	SRB	mean diff.	STDV.	Cor.Coef.	SLOPE	Intercept	norm dev	Cell #
$S\downarrow_s$	189.2	186.9	2.34	10.50	0.9832	1.007	-3.69	7.39	6596
$S\uparrow_s$	24.0	21.8	2.21	7.01	0.9542	0.812	2.30	4.38	6596
ALB$_s$	15.0	13.9	1.13	3.47	0.9846	0.876	0.74	2.04	6596
CLR-$S\downarrow_s$	248.3	244.3	3.98	11.76	0.9766	0.990	-1.39	8.35	6596
CLR-$S\uparrow_s$	29.8	28.6	1.22	7.96	0.9571	0.826	3.96	5.04	6596
CLR-ALB$_s$	14.3	14.1	0.25	3.15	0.9843	0.907	1.07	2.03	6596
NS$_s$	165.2	165.1	0.13	9.91	0.9876	0.976	3.86	7.01	6596
CLR-NS$_s$	218.5	215.7	2.76	13.12	0.9821	0.964	5.17	9.27	6596
$L\downarrow_s$	344.7	343.2	1.49	10.16	0.9894	1.035	-13.69	6.88	6596
$L\uparrow_s$	395.6	393.7	1.90	11.15	0.9889	0.980	6.19	7.89	6596
CLR-$L\downarrow_s$	313.6	306.2	7.43	11.30	0.9888	1.002	-8.16	7.98	6596
CLR-$L\uparrow_s$	394.1	393.2	0.96	11.26	0.9888	0.973	9.81	7.94	6596
NL$_s$	-50.9	-50.5	-0.40	13.04	0.7878	0.733	-13.17	9.53	6596
CLR-NL$_s$	-80.5	-87.0	6.48	13.38	0.7230	0.823	-20.73	10.08	6596
N$_s$	114.3	114.6	-0.28	16.48	0.9612	1.041	-4.42	11.31	6596
CLR-N$_s$	137.9	128.7	9.24	19.93	0.9623	0.987	-7.42	14.17	6596
CFC-NS$_s$	-53.3	-50.6	-2.63	6.55	0.9544	0.942	-0.45	4.68	6596
CFC-NL$_s$	29.6	36.5	-6.88	3.95	0.9515	0.929	8.98	2.82	6596
CFC-N$_s$	-23.7	-14.2	-9.51	7.56	0.9356	0.902	7.19	5.39	6596

[†] In addition to the symbols/acronyms similar to those in Table 2 (X/Y for FD/SRB now), CLR=clear-sky, CFC=cloud flux change ("cloud forcing"), ALB=albedo, N=net, and ↑ is for those upwelling fluxes.

Generally speaking, the two's agree reasonably well: for all the primary flux components (i.e., $S\downarrow_s$, $S\uparrow_s$, $L\downarrow_s$ and $L\uparrow_s$ and their clear-sky counterparts, see footnotes in Table 3 for symbol definitions), their mean differences are < 4 Wm^{-2} (except CLR-$L\downarrow_s$) with rms < 12 Wm^{-2}, and their spatial correlation coefficients are > 0.95.

However, regional differences are evident and there seem to be some systematic patterns associated with specific meteorological, cloud and aerosol conditions in some regions. Figure 1 shows global difference maps of $S\downarrow_s$, $S\uparrow_s$, CLR-$S\downarrow_s$ and CLR-$S\uparrow_s$, respectively. The three big yellow circular patterns in CLR-$S\uparrow_s$ map are obviously related to view angle of individual geostationary satellites, primarily from the surface albedo retrieval method of SRB. Comparing CLR-S$\downarrow_s$ and CLR-S$\uparrow_s$ maps shows FD has lower surface albedo than SRB in most of the northern part of South America and the southern part of Africa. In the polar regions, FD has generally higher surface albedo than SRB. There is an area in

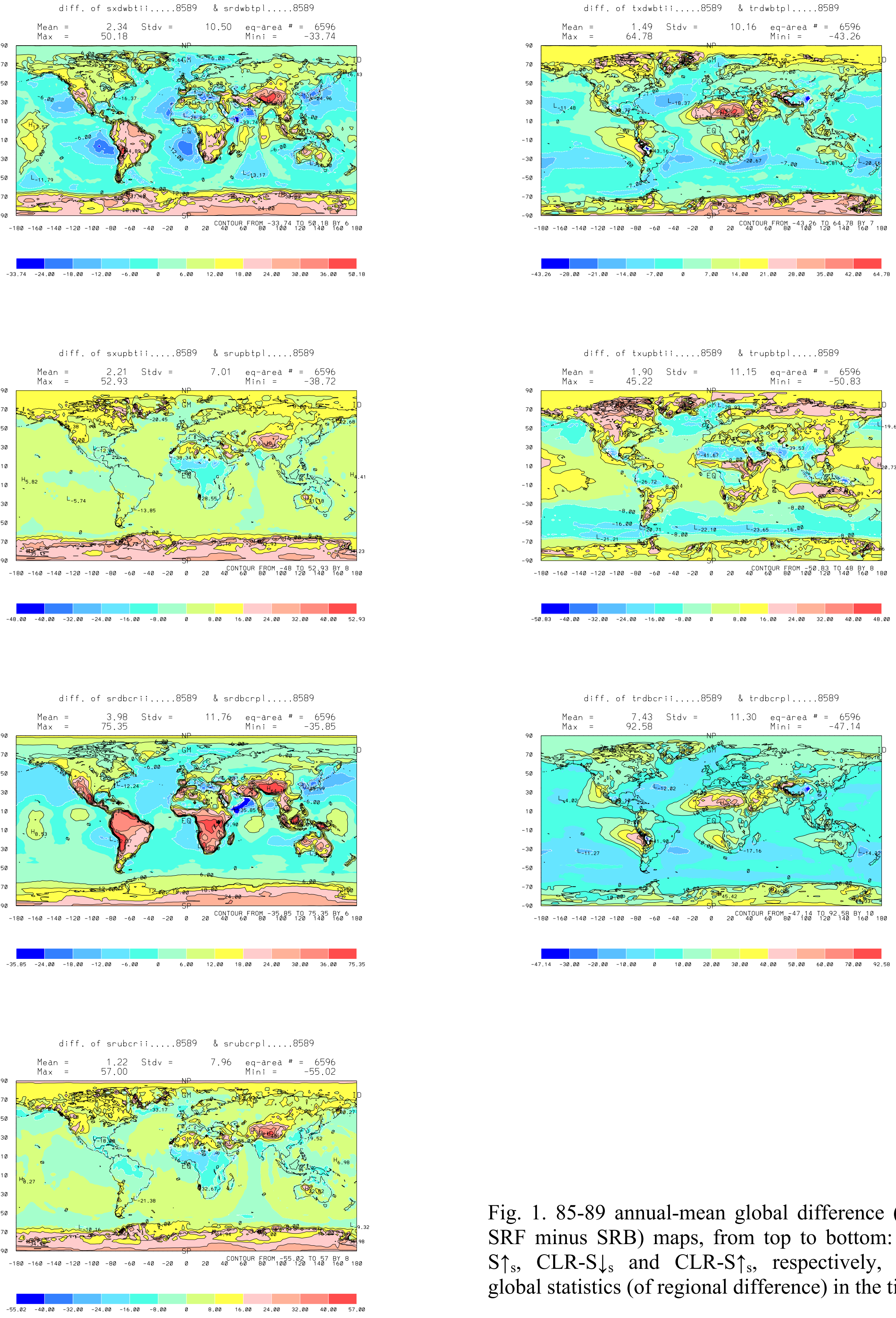

Fig. 1. 85-89 annual-mean global difference (FD-SRF minus SRB) maps, from top to bottom: S$\downarrow_s$, S$\uparrow_s$, CLR-S$\downarrow_s$ and CLR-S$\uparrow_s$, respectively, with global statistics (of regional difference) in the titles.

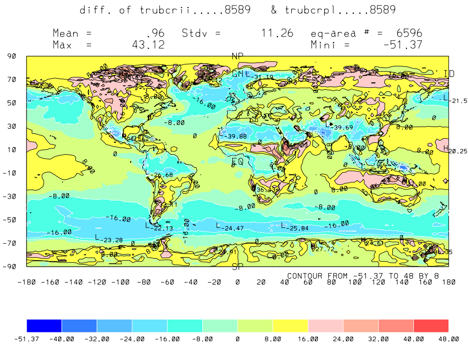

Fig. 2. 85-89 annual-mean global difference (FD-SRF minus SRB) maps, from top to bottom: $L\downarrow_s$, $L\uparrow_s$, CLR-$L\downarrow_s$ and CLR-$L\uparrow_s$, respectively, with global statistics (of regional difference) in the titles.

central China where FD has up to > 40 Wm^{-2} higher SW than SRB (for both CLR-$S\downarrow_s$ and CLR-$S\uparrow_s$). This is because FD's aerosols are much less than SRB in that area, where FD's absorbed atmospheric SW is up to 30 Wm^{-2} less than SRB (not shown). In the top panel ($S\downarrow_s$) of Fig. 1, there are several oceanic areas (two in the eastern Pacific, two in the eastern Atlantic, and one in the northwestern Pacific) where FD is as much as 18 Wm^{-2} less than SRB, likely caused by two different treatments of clouds: although both data products draw their cloud-related information from ISCCP, the FD product uses all of the cloud properties reported by ISCCP whereas SRB uses only cloud cover and visible reflectance. Figure 2 shows the LW counterparts of Fig. 1. The first and third panels ($L\downarrow_s$ and CLR-$L\downarrow_s$) suggest that there are some fundamental differences (with a global mean difference > 7 Wm^{-2} for CLR-$L\downarrow_s$) in the input temperature/humidity profiles from TOVS and GEOS-1 that the most of the larger differences of FD's values in west coast areas in eastern Pacific and Atlantic oceans and the belt from northern Africa to mid-east areas but a reverse difference in central-western China. Such large systematic differences need further study. The upwelling LW (panels 2 and 4 in Fig. 2) differences are primarily caused by different input surface skin temperature data sets: for ocean area and land areas with > 50% cloud cover, it reflects the differences between ISCCP and Reynolds, and for the rest land areas, it reflects FD's diurnal adjustment (*Zhang et al.,* 2004) that makes its surface skin temperature different from the original ISCCP's.

6. CONCLUSIONS

Two decades-long global surface radaitive flux data products are introduced and their 85-89 annual means are compared. Although their global mean values agree reasonably well, there are regional differences that require further investigation. The main comparable causes are likely the two's different input datasets and treatments for surface albedo, aerosols and clouds for SW, and temperature/humidity profiles and surface skin temperature for LW. Nevertheless, the overall agreement of these two products, to within 10-20 Wm^{-2}, indicates that they both can be usefully applied to study the factors controlling the weather-scale variations of surface fluxes. Resolution of some of the differences will allow these data products to be used to study interannual variations as well.

7. REFERENCES

Fu. Q., K.-N. Liou and A. Grossman, 1997, Multiple scattering parameterization in thermal infrared radiative transfer, *J. Atmos. Sci., 54,* 2799-2812.

Han, Q., W.B. Rossow, and A.A. Lacis (1994), Near-global survey of effective droplet radii in liquid water clouds using ISCCP data, *J. Climate, 7,* No. 4, 465-497.

Ohmura, A., E.G. Dutton, B. Forgan, C. Fröhlich, H. Gilgen, H. Hegner, A. Heimo, G. König-Langlo, B. McArthur, G. Müller, R. Philipona, R. Pinker, C.H. Whitlock, K. Dehne, and M. Wild (1998), Baseline surface radiation network (BSRN/WCRP): new precision radiometry for climate research, *Bull. Amer. Meteor. Soc., 79,* No. 10, 2115-2136.

Oinas, V., A.A. Lacis, D. Rind, D.T. Shindell and J.E. Hansen (2001), Radiative cooling by stratospheric water vapor: Big differences in GCM results, *Geophys. Res. Lett., 28*, 2791-2794.

Pinker, R.T. and I. Laszlo (1992), Modeling surface solar irradiance for satellite applications on global scale, *J. Appl. Meteor., 31,* 194-211.

Reynolds, C.D. (1988), A real time global sea surface temperature analisys, *J. Climate, 1,* 75-86.

Rossow, W.B., A.W. Walker, D.E. Beuschel and M.D. Roiter (1996), *International Satellite Cloud Climatology Project (ISCCP) documentation of new cloud datasets,* WMO/TD-No. 737, World Climate Research Programme (ICSU and WMO), 115 pp.

Rossow, W.B. and R.A. Schiffer (1999), Advances in understanding clouds from ISCCP, *Bull. Amer.Meteor. Soc., 80,* 2261-2287.

Simpson, G.C. (1929): The distribution of terrestrial radiation. *Mem. Roy. Meteor. Soc., 3,* 53-78.

Stackhouse Jr., P.W., Stephen J. Cox, Shashi K. Gupta, Marc Chiacchio, and J. Colleen, Mikovitz (2001), The WCRP/GEWEX surface radiation budget project release 2: An assessment of surface fluxes at 1 degree resolution. International Radiation Sysposium, St.-Petersburg, Russia, July 24-29, 2000. *IRS 2000: Current Problems in Atmospheric Radiation,* W.L. Smith and Y. Timofeyev (eds.), A. Deepak Publishing, 147.

Stackhouse Jr., P.W., S.K. Gupta, S.J. Cox, J.C. Mikovitz, T. Zhang, and M. Chiacchio, and (2004), 12-Year Surface Radiation Budget Data Set, *GEWEX News,* November,10-12.

WCP-55 (1983). *World Climate Research Report of the experts meeting on aerosols and their climatic effects,* Williamsburg, Virginia, 28-30 March 1983, Eds: A. Deepak and H. E. Gerber, 107 pp.

Wilber, A. C., D. P. Kratz, S. K. Gupta, 1999: *Surface emissivity maps for use in satellite retrievals of Longwave Radiation*, NASA Technical Publication, 1999-209362*,* 35 pp.

Zhang, Y.-C., W.B. Rossow and A. A. Lacis (1995), Calculationof surface and top of atmosphere radiative fluxes from physical quantities based on ISCCP data sets, 1. Method and sensitivity to input data uncertainties, *J. Geophys. Res., 100,* 1149-1165.

Zhang, Y-C., W.B. Rossow, A.A. Lacis, V. Oinas and M.I. Mishchenko (2004), Calculation of radiative fluxes from the surface to top-of-atmosphere based on ISCCP and other global datasets: Refinements of the radiative transfer model and the input data, *J. Geophys. Res., 109,* D19105, doi:10.1029/2003JD004457.

Estimation of Land Surface Energy Fluxes over the Tibetan Plateau using GMS data

Yuichiro Oku[1], Hirohiko Ishikawa[1], Zhongbo Su[2]

[1] *Disaster Prevention Research Institute, Kyoto University, Japan*

[2] *International Institute for Geo-Information Science and Earth Observation, the Netherlands*

A Surface Energy Balance System (SEBS) originally developed for NOAA/AVHRR is applied to GMS-5/VISSR data in combination with meteorological information. Land surface temperature obtained from GMS data are input to SEBS to estimate hourly regional distribution of land surface heat fluxes over the Tibetan Plateau. In SEBS, latent heat flux is obtained as the residual of the energy budget. Estimated fluxes are validated by corresponding field observations measured by sonic anemometer-thermometer with using the eddy correlation methodology at Amdo. Diurnal cycle of estimated fluxes is in good agreement with the field measurement. For example, diurnal range of estimated sensible heat flux decreases from June to August, which reflects the change of surface characteristics from dry to wet due to frequent precipitation in the summer monsoon. Over the Tibetan Plateau, the diurnal range of land surface temperature is as large as the annual range, so that the resultant sensible heat flux has large diurnal variation. Hence, the hourly estimation with GMS data may contribute better understanding of land surface-atmosphere interaction of this important area.

Key Words: land surface energy flux, surface energy balance, Tibetan Plateau, GMS.

1. Introduction

The Tibetan Plateau has been thought to play an important role in the progress of the Asian summer monsoon through thermal effects on the surrounding mid-troposphere. In order to understand the role of the Tibetan Plateau as an elevated heat source in this region, intensive meteorological observations were conducted in the Global Energy and Water Cycle Experiment (GEWEX) Asian Monsoon Experiment (GAME) Tibet project. During GAME/Tibet, surface sensible and latent heat fluxes were measured at a set of sites together with monitoring of relevant surface parameters. Using the data obtained in these experiments, the land surface interaction was observed experimentally at these sites, it only represents flux over a patch scale around the measurement sites. Patch-scale knowledge needs to be integrated with a regional-scale understanding of the plateau. Remote sensing from satellites offers the possibility to derive regional distributions of land surface energy fluxes in combination with sparsely distributed set of field experiment stations. Ma (2003) estimated the distributions of land surface variables over the GAME/Tibet enhanced observation area by combining NOAA/AVHRR data with field observations. According to Tanaka et al. (2001), however, strong diurnal variations are one of the outstanding features of the plateau surface, which cannot be detected in the data of polar-orbiting satellites. In this study, a method for the land surface energy fluxes from geostationary satellite data is presented. The retrieval algorithm SEBS (Surface Energy Balance System) used for NOAA/AVHRR data (Su, 2002) is applied to GMS/VISSR data.

2. Surface Energy Balance System (SEBS)

The net radiation flux R_{n} is estimated as

$$R_{\mathrm{n}} = (1 - \quad) R_{\mathrm{S}}^{\downarrow} + {}_{air} R_{\mathrm{L}}^{\downarrow} - {}_{\mathrm{sfc}} \quad T_{\mathrm{sfc}}^{4} \tag{1}$$

where $R_{\mathrm{S}}^{\downarrow}$ is the downward shortwave radiation which is a function of the solar constant, atmospheric transmittance at the location and time. is surface albedo, $_{\mathrm{air}}$ and $_{\mathrm{sfc}}$ are the emissivity of the air and the surface, respectively. $R_{\mathrm{L}}^{\downarrow}$ is downward longwave radiation parameterized by atmospheric temperature, is Stephan-Boltzmann constant and T_{sfc} is land surface temperature. The soil heat flux G_0 is estimated by net radiation as

$$G_0 = R_{\mathrm{n}} \left[\Gamma_{\mathrm{c}} + (1 - f_{\mathrm{c}})(\Gamma_{\mathrm{s}} - \Gamma_{\mathrm{c}}) \right] \tag{2}$$

where Γ_{s} and Γ_{c} are the ratios between G_0 and R_{n} for bare soil and fully covered vegetation surface, respectively. The fractional vegetation cover f_{c} is determined by NDVI. In order to derive the sensible heat flux H, use is made of the similarity theory. Over a complex landscape there is a height, the blending height, where the distinct impacts of the underlying surfaces diminish. At the blending height z, wind speed u and air temperature T_{air} satisfy the general conditions given by Monin-Obukhov's similarity theory. They are described as

$$u = \frac{u^*}{k} \left[\ln\left(\frac{z - d_0}{z_{0\mathrm{m}}} \right) - \Psi_{\mathrm{m}} \left(\frac{z - d_0}{L} \right) - \Psi_{\mathrm{m}} \left(\frac{z_{0\mathrm{m}}}{L} \right) \right] \tag{3}$$

$$T_{\mathrm{sfc}} - T_{\mathrm{air}} = \frac{H}{k u^* \; C_{\mathrm{p}}} \left[\ln\left(\frac{z - d_0}{z_{0\mathrm{h}}} \right) - \Psi_{\mathrm{h}} \left(\frac{z - d_0}{L} \right) - \Psi_{\mathrm{h}} \left(\frac{z_{0\mathrm{h}}}{L} \right) \right] \tag{4}$$

where $k = 0.4$ is von Karman's constant, is air density, C_{p} is specific heat constant, u^* is the friction velocity, d_0 is the zero plane displacement height, $z_{0\mathrm{m}}$ and $z_{0\mathrm{h}}$ are the roughness heights for momentum and heat transfer, Ψ_{m} and Ψ_{h} are the stability correction functions for momentum and sensible heat transfer, respectively. L Is the Monin-Obukhov stability length defined as

$$L = \frac{C_{\mathrm{p}} T_{\mathrm{air}} u^{*}}{kgH} \tag{5}$$

where g is the acceleration due to gravity. Derivation of the sensible heat flux H using Eqns. (3–5) requires only the wind speed u and temperature T_{air} at the blending height z as well as the surface temperature T_{air}. The latent heat flux E is derived as the residual of the energy budget theorem for the land surface, i.e.

$$R_{\mathrm{n}} = G_0 + H + \ E\,. \tag{6}$$

3. Data

Land surface temperature T_{sfc} is one of the most important parameter in diurnal flux retrieval. According to Oku and Ishikawa (2004), hourly T_{sfc} is estimated by using infrared split-window technique from GMS-5/VISSR data. Other surface parameters, such as albedo and emissivity $_{\mathrm{sfc}}$, do not vary in inter-diurnal scale severely, but change seasonal scale. These are estimated from visible reflectance measured in NOAA-14/AVHRR channels 1 and 2, as 1 month mean. All available GMS and NOAA images from May 1998 to April 1999 are prepared to estimate flux distribution over the Tibetan Plateau.

However, neither GMS nor NOAA data could derive wind speed u and air temperature T_{air} at the blending height z, ECMWF 40 years re-analysis data (ERA40) is used. To assess the reality of ERA40 data, u and T_{air} are compared with independent data sets of sonde observations at Amdo (32.24N, 91.63E, 4,700mASL). At the 500hPa level, it corresponds to nearly 1,000mAGL at Amdo, root mean square error (RMSE) between ERA40 and sonde data of T_{air} and u are 1.29K and 3.44m/s, respectively. These RMSEs have a possibility to induce several-ten W/m^2 error in daytime and several W/m^2 in nighttime in sensible heat flux retrieval. Study area is defined as the area higher than 4,000m ASL. The data in grid format over longitude and latitude having a resolution of 0.1 degree are interpolated from original image data that are archived in line-pixel format.

Surface energy fluxes measured at Amdo during GAME/Tibet intensive observation period are used as ground truth for verification fluxes estimated by presented algorithm. The net radiation flux is obtained using data from the 4-component radiation system. The soil heat flux is computed from a thermal conductivity equation with using soil temperature and moisture profiles (Tanaka et al., 2003). The sensible heat flux is calculated form turbulence

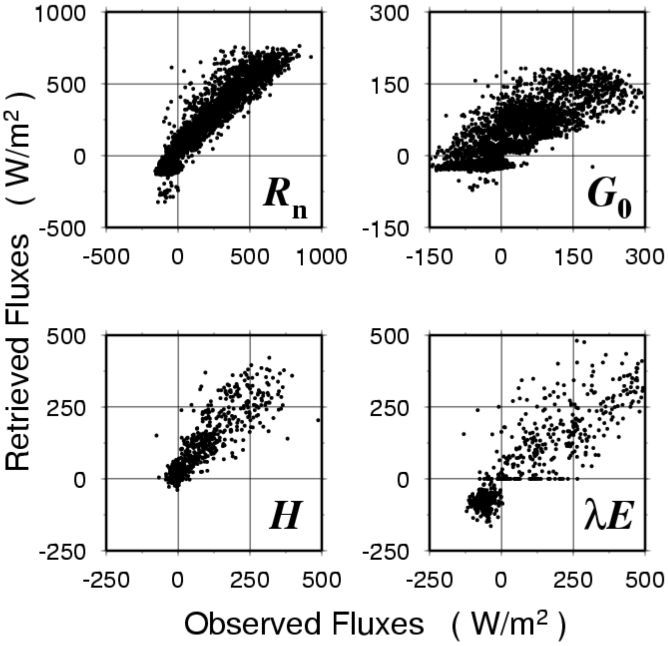

Fig. 1: A scatter diagram of surface energy fluxes observed at Amdo (horizontal axis) and fluxes estimated by SEBS (vertical axis). Upper left panel is net radiation $\boldsymbol{R}_{\mathbf{n}}$, upper right is soil heat flux $\boldsymbol{G}_{\mathbf{0}}$, lower left is sensible heat flux $\boldsymbol{H}$ and lower right is latent heat flux ***lE***.

data measured by sonic anemo-thermometer with using eddy correlation method. A problem is identified in the latent heat flux data calculated by eddy correlation method, attributed to the performance of the infrared hygrometer, the latent heat flux is derived as the residual of the energy budget theorem for the land surface as described in Eq. (6)

4. Validation and Remarks

Surface energy fluxes retrieved by presented algorithm are compared with corresponding ground truth at Amdo, as is shown in Fig. 1 and Table 1. High correlation coefficient implies diurnal cycles of retrieved flux are a good match to observed values. Overestimation in net radiation seems to be attributed to the difference in the spatial resolution between GMS images and ground based observations. The pixel size of GMS images is about 50km^2 at Amdo, since GMS views the plateau from geostationary orbit at 140E. Surface measurements are not always representative of the typical value over a GMS pixel, particularly in that subpixel-scaled cloud formations affect the surface measurement would be missed by GMS. Estimated soil heat fluxes exhibit considerable RMSE with respect to observed value. This can be partially explained that Eq. (2) does not take account for soil moisture conditions. Wet condition in ground soil makes thermal conductance large. This process might be needed to include soil heat flux retrieval.

Table. 1: Statistics of measured versus retrieved surface energy fluxes at Amdo. $\boldsymbol{R}$ is correlation coefficient, RMSE is root mean square error in W/m^2 and $\boldsymbol{N}$ is number of data used. $\boldsymbol{R}_\mathrm{n}$ is net radiation, $\boldsymbol{G}_0$ is soil heat flux, $\boldsymbol{H}$ is sensible heat flux, and $\boldsymbol{lE}$ is latent heat flux.

	$\boldsymbol{R}_\mathrm{n}$	$\boldsymbol{G}_0$	$\boldsymbol{H}$	$\boldsymbol{lE}$
$\boldsymbol{R}$	0.9645	0.8228	0.8866	0.8999
RMSE	67.45	46.63	52.78	88.43
$\boldsymbol{N}$	6477	5588	945	743

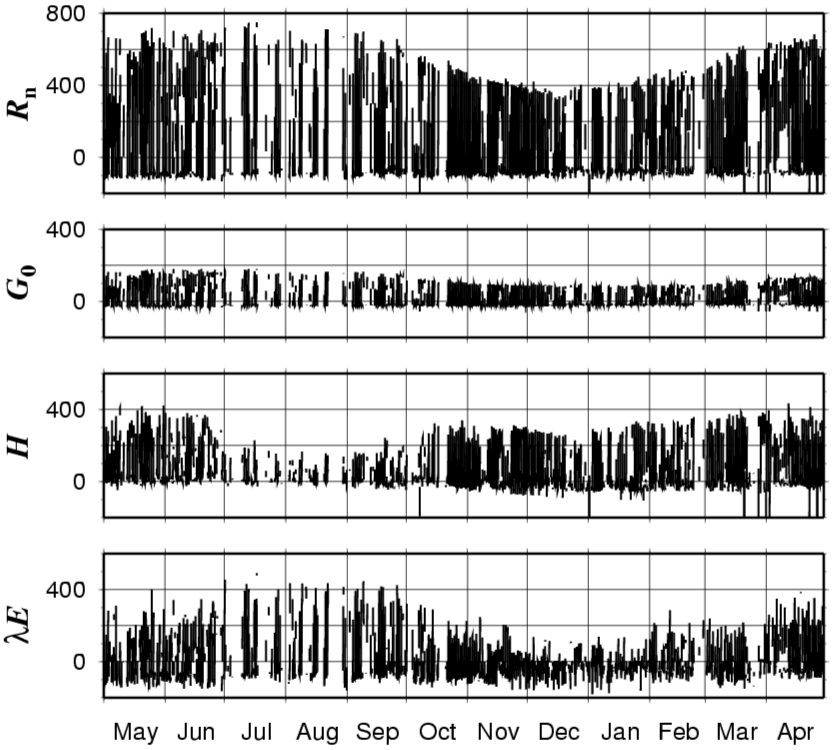

Fig. 2: Time series of surface energy fluxes estimated by SEBS (net radiation $\boldsymbol{R}_{\mathbf{n}}$, soil heat flux $\boldsymbol{G}_{\mathbf{0}}$, sensible heat flux $\boldsymbol{H}$ and latent heat flux $\boldsymbol{lE}$ from upper to lower) at Amdo from May 1998 to April 1999. Unit is W/m^2.

Fig. 2 displays seasonal variation of retrieved fluxes. The sensible heat flux decreases and the latent heat flux increases from June to July. This remarkable change can be seen in observed fluxes, because the plateau surface becomes wet due to daily precipitation as the monsoon progress. Fig.3 shows spatial distributions of retrieved fluxes. The greatest advantage of GMS is that observations of the earth are made from a stationary position which meteorological phenomena can be monitored continuously, making the analysis intra-diurnal variations over large scale possible.

Acknowledgements

This research was partially supported by the Ministry of Education, Science, Sports and Culture, Grant-in-Aid for the Japan Society for the Promotion of Science Fellows and Joint Research on Center for Environmental Remote Sensing, Chiba University. The surface energy fluxes data at Amdo was provided by Dr. Kenji Tanaka of Kumamoto University.

References

Ma, Y., 2003: Remote sensing parameterization of regional net radiation over heterogeneous land

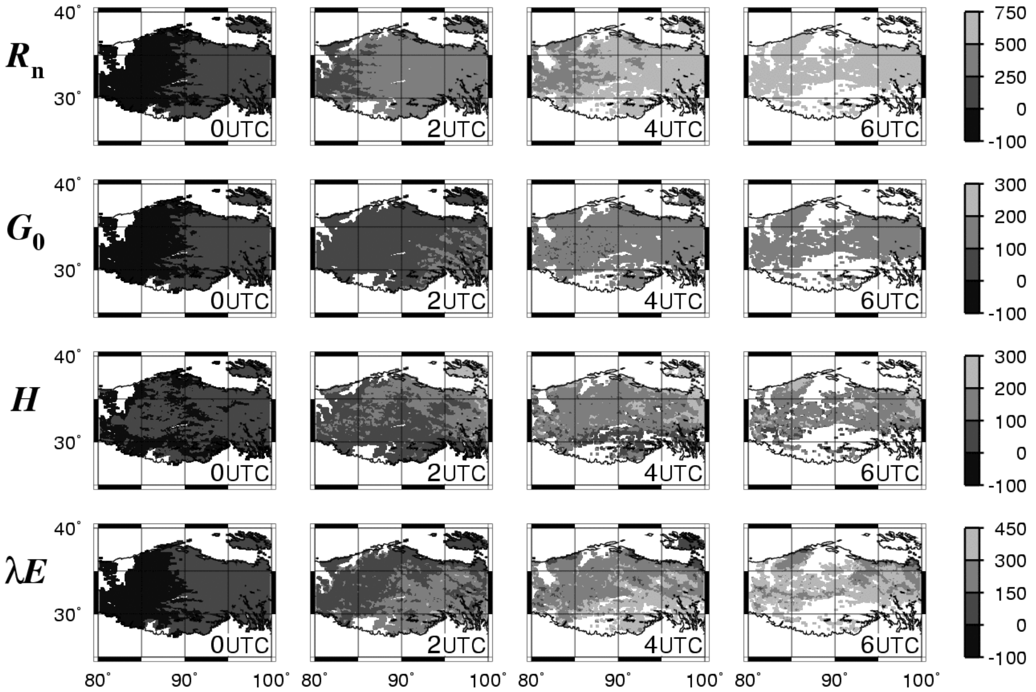

Fig. 3: Horizontal distribution of available retrieved surface energy fluxes (net radiation **R_n**, soil heat flux **G_0**, sensible heat flux ***H*** and latent heat flux ***lE*** from upper to lower) from 0000UTC (0600LST at 90E) to 0600UTC 25 Apr. 1998. Blank white region over the Tibetan Plateau is cloudy area. Unit is W/m^2.

surface of Tibetan Plateau and arid area. *Int. J. Remote Sens.*, **24**(15), 3137-3148.

Oku, Y. and Ishikawa, H., 2004: Estimation of land surface temperature over the Tibetan Plateau using GMS data. *J. Appl. Meteorol.*, **43**(4), 548-561.

Su, Z. 2002: The surface energy balance system (SEBS) for estimation of turbulent heat fluxes. *Hydrol. Earth Syst. Sci.*, **6**(1), 85-99.

Tanaka, K, Ishikawa, H., Hayashi, T., Tamagawa, I., and Ma, Y., 2001: Surface energy budget at Amdo in the Tibetan Plateau using GAME/Tibet IOP98 data. *J. Meteorol. Soc. Jpn.*, **79**, 505–517.

Tanaka, K., Tamagawa, I., Ishikawa, H., Ma, Y. and Hu, Z., 2003: Surface energy budget and closure of the eastern Tibetan Plateau during GAME-Tibet IOP 1998. *J. Hydrol,* **283**, 169-183.

Comparative Study of Cloud Parameters Derived From Terra-MODIS and GMS-VISSR

Jules R. Dim, Tamio Takamura, Itaru Okada, Hideaki Takenaka
Center for Environmental Remote Sensing, Chiba University
1-33 Yayoi-cho, Inage-ku
CHIBA 263-8522, JAPAN
(E-mail: dim@ceres.cr.chiba-u.ac.jp, takamura@ceres.cr.chiba-u.ac.jp, iokada@ceres.cr.chiba-u.ac.jp, takenaka_ceres@graduate.chiba-u.jp)

Abstract

Top cloud reflected solar radiance measurements directly recorded by satellites at various spectral bands and observation conditions are used to understand clouds' optical and physical characteristics. The magnitude of these radiance measurements modulates the energy balance of the Earth through absorption and scattering. The accuracy of the data obtained highly depends on the sensitivity of the recording sensors. The Visible and thermal infrared channels are mainly employed to extract, through various inversion techniques, cloud microphysical parameters such as the brightness temperature, optical depth, effective radius, top cloud temperature etc. This study examines reflectance and optical depth retrievals derived from cloud radiative measurement data collected by the SVISSR (Stretched Visible Infrared Spin-Scan Radiometer) and the MODIS (MODerate resolution Imaging Spectroradiometer) sensors onboard the geostationary satellite (GMS-5) and the polar-orbiting satellite (Terra) respectively. MODIS cloud optical depth as well as reflectance appears systematically higher than the SVISSR corresponding data. And, the largest differences are mostly seen in thick cloud areas. To understand these discrepancies, a cloud classification based on the split-window method, has been conducted and, the influence of various parameters on the measurements and retrievals among which, dimensional radiative effects (asymmetry of the clouds) and the sun-earth-satellite viewing geometry are examined.

Key Words: MODIS, SVISSR, cloud optical depth, reflectance

1. INTRODUCTION

Retrieval of cloud properties from passive remote sensing has extensively relied on satellite data. The cloud characteristics therefore retrieved from radiance measurements are mainly the clear or cloudy scenes distribution, the cloud fraction, reflectance and emissivity, liquid water content, phase (water or ice clouds), optical depth, effective radius, top cloud temperature etc. Various factors such as the solar altitude, the view angle geometry and the cloud inhomogeneity influence the accuracy of the cloud properties measurements. The degree to which satellite measurements are influenced by cloud inhomogeneities depends on the spatial resolution of the instrument, the sun-earth-satellite viewing geometry, and whether the observations are analyzed at the local pixel scale or over larger regions by averaging pixel-level values (Loeb and Coakley, 1998).

Various cloud detection methods have been adopted among which the maximum temperature (retaining of the highest temperature of a given area), the infrared variability, the two-wavelength infrared (split-window method), the two-wavelength visible-infrared (using reflected sunlight to detect clouds).

The GMS-5 satellite, launched in 1995 into a geostationary orbit above 0^o N, 140^oE, carries a Stretched Visible and Infrared Spin-Scan Radiometer (SVISSR) with four channels, one in the visible part of the spectrum (0.5 – 0.75 μm) and two in the infrared (10.5 - 11.5 μm and 11.5 –

12.5 µm) then one water vapor channel (6.5 – 7.0 µm). The ground resolution at the subsatellite point is 1.25 km in the visible channel and 5 Km in the infrared. It is not possible to derive cloud particle size with the SVISSR sensor due to the non-existence of the 3.9 µm channel (therefore, for optical parameters' retrievals, a fixed value of 10 µm was used as effective radius). The satellite however has a good time resolution with scanning intervals at least every hour. The SVISSR instrument noise is around 0.5 K (MSC, 1997).

MODIS (MODerate resolution Imaging Spectroradiometer) sensor onboard The Terra polar orbiting satellite is a 36-band spectrometer (ranging from 0.41 to 14.38 µm) providing a global data set every 1-2 days with a 16-day repeat cycle. The spatial resolution of MODIS (pixel size at nadir) is 250m for channels 1 and 2 (0.6 µm - 0.9 µm), 500m for channels 3 to 7 (0.4 µm - 2.1 µm) and 1000 m for channels 8 to 36 (0.4 µm - 14.4 µm), respectively. The sensitivity at the 11µm channel permits the detection of temperature differences as small as 0.01 K and the noise equivalent temperature difference is about 0.05 K. Because of this thermal detection capacity, adjacent pixels from MODIS data show higher variability than those from SVISSR data.

In the present study, we would like to examine cloud mocrophysical parameters retrievals derived from cloud radiative measurements collected by the SVISSR and the MODIS sensors. Then investigations will be conducted on the effects that the random geometry of the clouds would have on the accuracy of the cloud reflected radiation. Beyond the comparison of satellite data, this study was motivated by the search of reasonable explanations and corrections of some important differences noticed in the optical and radiative properties retrievals and, measurements from SVISSR and MODIS sensors. The area of study chosen to conduct this work is mainly centered on the southern part of the Sea of Japan and limited by the following geographical coordinates 25N - 35N latitude and 125E - 135E longitude. The SVISSR and MODIS matching images on this area, have time differences of 3 to 28 minutes. A grid resolution of 0.05^o or 5 Km pixel's length is used for data processing.

2. METHODOLOGY AND OBSERVATIONS

Data from the MODIS sensor almost temporally coincident with the SVISSR images are analyzed. Visible and infrared channels are used to retrieve cloud microphysical properties such as the brightness temperature, optical depth, top cloud temperature, particle effective radius etc. Using the split-window technique (Brightness temperature difference at 11µm and 12 µm) on the SVISSR IR data, clouds were classified as cumulus, cumulo-nimbus and dense cirrus and, cirrus. This classification was attempted in order to understand the sensors' sensitivity to the morphological structure of the clouds encountered in the region. Large discrepancies in the microphysical properties (reflectance, optical depth mainly) of the clouds, generally in areas of thick clouds were observed. The MODIS data appear systematically higher than the SVISSR data in such areas. The best correlation between MODIS and SVISSR data is found with the relatively thin mid- and low-level clouds i.e. at cloud optical depth (COD)<20. Figure 1 is the illustration of the frequency distribution of the differences in cloud optical properties between MODIS and SVISSR. The split-window classification following these observations is made to identify the types of clouds associated with the strongest differences in cloud properties between both sensors. The last part of this study is devoted to investigations on possible causes of the discrepancies noticed. Among the reasons generally accounted for as influential in the accuracy of cloud microphysical properties: size, geometry and differentiation of cloud phases (water and ice clouds), differences in the resolution and spectral channels' separation, accuracy of the characterization of the cloud scenes, threshold for cloud detection, calibration errors of the sensors, misalignment of images (geolocation problem) and time differential in the scanning of the sensors, solar zenith and satellite view angles, scattering patterns and cloud geometries.

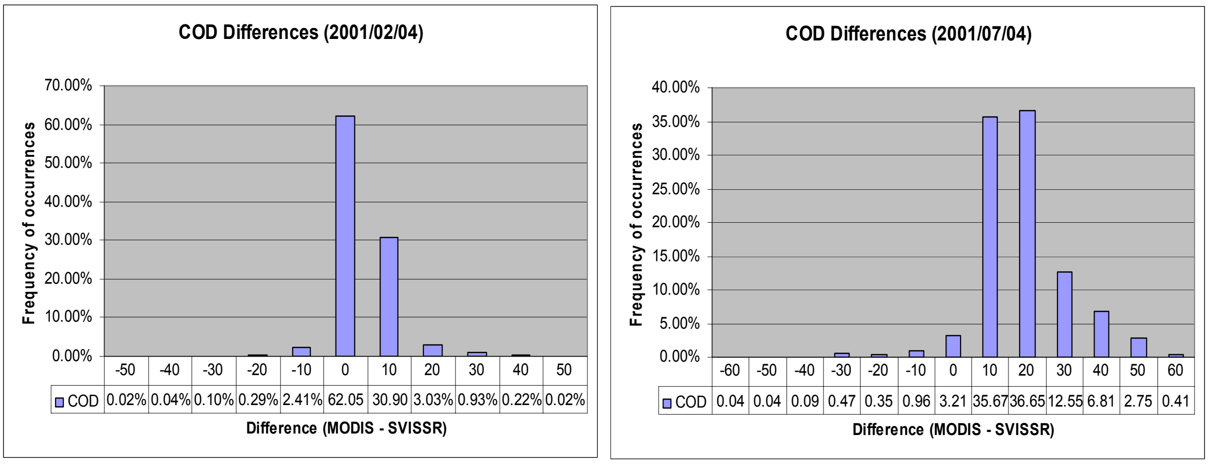

Fig. 1. Frequency histograms of the differences between the cloud optical properties obtained from SVISSR and MODIS

3. DATA ANALYSIS

As stated earlier, cloud optical properties data retrieved from MODIS appear systematically higher than those of SVISSR (See Figure 1). In order to understand these discrepancies, the first step of our work consisted in adopting a classification method permitting the differentiation of clouds based on their morphological structure. The method used in this study takes advantage of the existence of the 11µm and 12µm channels on the GMS-5/SVISSR. This method is based on split-window data (11µm-12µm) as suggested by Inoue et al. (1987). The cloud types identified are: Cirrus, dense cirrus, cumulo-nimbus and cumulus.

It was observed that the largest discrepancies in the cloud properties between both sensors mostly occur in the vertically well-developed cumulo-nimbus/dense cirrus type of clouds.
Most of the differences noticed in the optical properties between MODIS and SVISSR mainly occur in the vertically developing cloud structures represented by the cumulo-nimbus and dense cirrus clouds. The smallest differences are found in the cumulus type. It appears therefore that the morphology of the clouds may play an important role in the accurate determination of radiation measurements by both sensors. The second step of this work consisted in reviewing and evaluating the other possible causes of the optical properties differences. Particular emphasis will be placed among others on the relation between the cloud surfaces and the sun radiation geometry.

4. RESULTS AND DISCUSSION

For the visible channels, the radiance measurements made by the SVISSR are converted into reflectance products; the MODIS data available for this study are calibrated geolocated radiance products (at 0.86μm wavelength). These MODIS radiances can be translated into reflectance by using the following formula:

$$R(\mu,\mu_0,\phi)=\frac{\pi I(\pi,\mu_0,\phi)}{\mu_0 F}$$

With $I =$ radiance $\left(W\,m^{-2}sr^{-1}\mu\,m^{-1}\right)$

$F =$ Solar irradiance $\left(W\,m^{-2}\mu\,m^{-1}\right)$

$\mu =$ Cosine of the observer's zenith angle

$\mu_0 =$ Cosine of solar zenith angle

$\phi =$ Azimuth angle relative to the solar plane

In this section, observed reflectance data are discussed together with retrieved optical depths in order to evaluate factors likely to influence measurements and retrievals of satellite data. Among these factors:

1) Differences in resolution and spectral channels:
MODIS has a higher resolution (1 km at subsatellite) than SVISSR (1.25 km for visible and 5 km for IR). Lower accuracies expected for the SVISSR data could be most likely due the poorer spatial (5 km pixel against 25 pixel averages for the MODIS data) and lower digitization (8-bit against 10-bit for the MODIS). The higher resolution MODIS data should allow for better discrimination between clear and cloudy pixels than SVISSR but, as cloud thermal infrared brightness comparisons show relatively good matches, the resolution alone can not explain the differences in reflectance and optical depth noticed between both sets of data.

2) Improper thresholds for cloud detection and, accuracy in the characterization of the clear scenes (algorithm problem):
Equivalent assumptions were made in the algorithms used for the retrievals of both sets of data, this, minimizing possible retrieval errors. Furthermore, MODIS Cloud reflectance data appear too, generally higher than the SVISSR derived reflectance and show a trend consistent with that of COD retrievals from both satellite measurements.

3) Errors in calibrations:
Though, the calibration tables for IR channels 1 and 2 have errors of ±0.2 K due to quantization (Tanahashi et al. 2000), a consistent error trend is not visible in either IR data or reflectance data from both sensors.

4) Geolocation problem and Time differential in the scanning of both sensors:
A simple comparison of the SVISSR IR channel 1 images at 02 UTC and 03 UTC shows that in some areas, large temperature differences (therefore cloud movements) can occur in just an hour

time interval separating both measurements. This suggests that some of the wide temperature differences between MODIS and SVISSR IR data may be much more due to the time differential (3 to 28 minute-difference) than to possible geolocation problems. Figure 2 shows the images of the SVISSR (at 02 UTC and 03 UTC) and MODIS (around 45 mn after and 15 mn before the SVISSR 02 UTC and 03 UTC respectively) cloud movements and the corresponding IR temperature cross-section at 30N, on April 2, 2001.

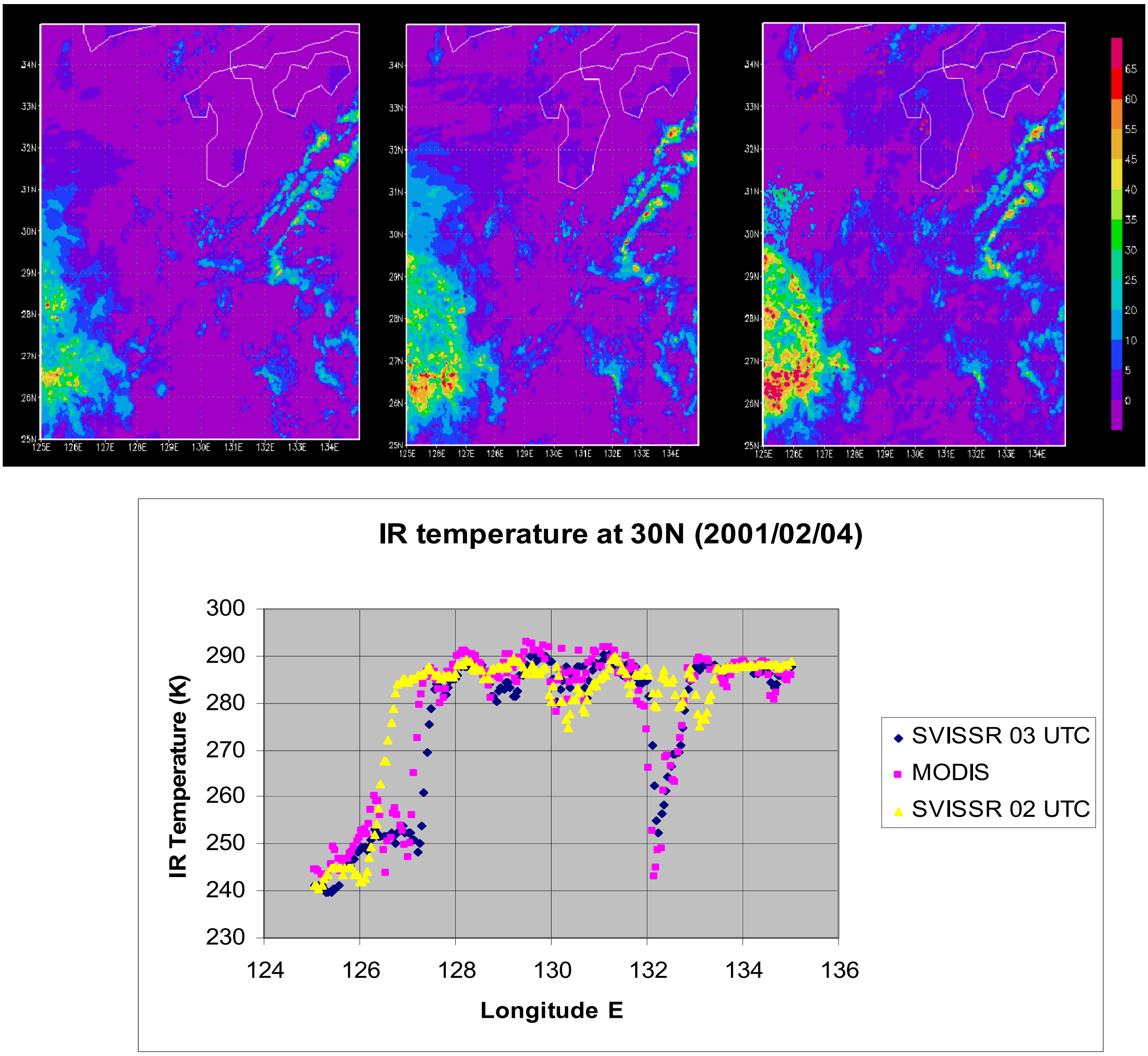

Fig. 2. Cloud movements as illustrated by the optical depth images (upper) and equivalent IR brightness temperature at 30° N latitude (lower diagram).

5) Size, geometry and cloud phase (water and ice clouds):
Due to the lack of channel 3.9 µm, cloud effective radius (r_{eff}) is not available from SVISSR; a constant cloud effective radius of 10 µm was used in the SVISSR retrieval of cloud microphysical data. The r_{eff} from MODIS retrievals vary widely from around 2 to 40 µm. This variation follows a unimodal distribution whose peak is generally around 10 µm. Regarding the cloud phases, it was noticed that the large cloud properties differences occur as much in the water as in the ice phase.

6) Influence of the solar zenith angle:
The solar zenith angles from the satellite images used are generally below 35^o. Analyses made so far, didn't allow us to give enough evidence of the existence of cloud properties' dependence on this parameter.

7) Dimensional radiative effects (cloud asymmetry) and relation with satellite viewing geometry:
The effects of finite cloud geometry have been analyzed with satellite observations mainly at infrared wavelengths. To understand the cloud asymmetry effect on the measurements of cloud properties, we'll use a technique of detection of these radiative effects over a chosen area, as proposed by Varnai and Marshak (2002). The method's basic idea is to estimate, for each basic pixel in the area, whether 3D effects are likely to have increased or decreased relatively to 1D theory, the pixel's brightness at the visible channel. The technique assumes that the question of whether 3D effects enhance or reduce the brightness of a pixel depends mainly on whether the pixel is on a slope tilted toward (illuminated slopes) or away from the sun (shadowy slopes). An area of (50 Km)^2 size is chosen with the goal that the area contains many pixels for statistical calculations but that they do not contain clouds from different cloud fields too often. Significant 3D effects can be revealed from the average brightness difference between the brightened (illuminated) pixels and darkened (shadowy) pixels. The implementation of the technique follows the steps below:

Step1: use the geolocation data to determine from which direction the sun illuminates the area of a pixel, and thus, which neighboring pixels are closest to the solar azimuth in front of it and behind it. Only cloudy pixels are examined. In our study area, the solar azimuth angle varies between 150 and 180^o, the sun incident direction adopted will be therefore from South to North.

Step2: determine whether the pixel is on an illuminated slope or shadowy slope. To detect this, the local gradient of brightness temperature (g) is calculated from the pixels in front and behind:

$$g = \left(T_{front} - T_{behind}\right)/d$$

Where d is the distance separating the pixels in front and behind (10 km)
-If $g > 0$, the pixel is on an illuminated slope
-If $g < 0$, the pixel is a shadowy slope

Step 3: After all cloudy pixels in a (50 km)^2 area are designated as either illuminated or shadowy the mean brightness (reflectance) of the illuminated (R_i) and shadowy (R_s) pixels is calculated. If the 2 mean values are close to each other, this indicates that 3D effects do not make much a difference in the (50 km)^2 area. If however, R_i is much larger than R_s, 3D effects (asymmetry) are expected to be strong.

Application of this technique to the data of this study shows that for the SVISSR Cloud optical depth and reflectance, the illuminated pixels are much more brighter than shadow pixels. This effect is less strong for MODIS data. This supposes that 3D effects due to the asymmetry of the cloud faces relative to the exposition to solar radiation influence both the cloud properties measurements and retrievals. High differences in cloud properties between both sensors are generally found when the SVISSR thermal gradient is negative i.e. the cloud face is on the shadow side relative to the solar radiation. This implies that the SVISSR data measurements and retrievals would be strongly affected and therefore lowered at the shadowy faces.

5. CONCLUSION AND FUTURE WORK

Comparison of MODIS and SVISSR derived cloud properties made in this study shows large discrepancies between the data retrievals and measurements from both sensors. Possible reasons of these discrepancies were discussed. It appears that time difference (in the scanning of both sensors) and the asymmetry effects of the clouds are the factors mostly accounted for as being at the origin of the differences noticed. Many more uncertainties related to the accuracy of the data acquired remain to be clarified. Future work would therefore consist of identifying these uncertainties (view angle differences and other aspects of the specific geometry of the clouds) and their quantification.

Acknowledgments
The MODIS data used in this study were kindly provided by Dr. T. Nakajima of JAXA-EORC, Japan, whom we'd like to thank here.

References

Inoue, T., 1987. A cloud type classification with NOAA 7 split-window measurements. *J. Geophys. Res*., **92**, 3991-4000.

Loeb N. G., and J. A., Jr. Coakley, 1998. Inference of marine stratus cloud optical depths from satellite measurements: does 1D theory apply? *J. Climate*, **11**, 215-232.

MSC, 1997. The GMS user's guide. *Meteorological satellite Center of Japan*, 190 pp.

Tanahashi S., Kawamura H., Matsuura T., Tomoyuki T., and H. Yusa, 2000. Improved estimates of wide-ranging sea surface temperature from GMS S-VISSR data. *J. Oceanogr*., **56**, 345-358.

Varnai T., and A. Marshak, 2002. Observations of three-dimensional radiative effects that influence MODIS cloud optical thickness retrievals. *J. Atmos. Sci*., **59**, 1607-1618.

Development and validation of a general model for estimating global solar radiation from hourly, daily and monthly surface meteorological data

Kun Yang and Toshio Koike

River Lab., Dept. of Civil Engineering, University of Tokyo, Bunkyo-ku, Tokyo 113-8656, Japan

Abstract: Long-term recorded data at world-widely distributed meteorological stations provides an opportunity to construct historical solar radiation for studies on crop productivity, hydrology, climate change, and solar power-relevant designs The Ångström–Prescott model has been widely used to estimate global solar radiation from measured sunshine duration. However, this model has site-dependent coefficients, which have to be calibrated for different climate zones and elevations, because this model does not explicitly take into account radiative extinction processes in the atmosphere. In this study, we developed a general radiation model available with global data sets for turbidity and ozone from remote sensing. Its development followed the four principles below: (1) it keeps the simple form of Angstrom model while can explicitly and accurately deal with radiative extinction processes in the atmosphere; (2) model inputs are surface meteorological data (sunshine duration, air temperature, and relative humidity) so that the model can be applied easily; (3) under clear skies, the estimated solar radiation is equal to the value calculated by sophisticated spectral models; (4) at the top of atmosphere, the estimated solar radiation is exactly equal to the theoretical value of solar radiation. The model is calibrated with data in Japan, while it is successfully applied to China, Saudi Arab, and America, where have distinct climate zones and elevations. We expect the radiation output of this model could be used for cross-validation with satellite products.

Key words: surface solar radiation, Ångström–Prescott model, general radiation model, turbidity data set, ozone data set.

1. Introduction

Solar radiation reaching the Earth drives most of physical and biological cycle in the Earth system. The surface solar radiation is an indispensable input for many studies on agriculture, hydrology, and climate change. Also, it is a crucial index in designing solar devices. However, direct measurements of solar radiation are still too sparse to support scientific and technological research. The situation is particularly true in remote areas and mountainous areas, where snowmelting and glacier retreat become hot topics in hydrological and climate change studies, due to global warming and water resources crisis. A feasible approach to provide solar radiation for these studies is to estimate it from other surface meteorological data, such as temperature, humidity, precipitation, sunshine duration, and so on. They often have a long record at meteorological and hydrological stations and thus provide a possibility to construct historical solar radiation for relevant studies.

There exist two major methods to estimate global solar radiation from the surface meteorological data. The first one is the so-called Ångström–Prescott model, which estimate surface solar radiation from measured bright sunshine duration. This model has been widely applied to agricultural meteorology and hydrology for nearly one century. However, it does not consider radiative extinction processes in the atmosphere, so model parameters are site-dependent, and have to be calibrated locally. Although a number of studies have focused on how to tune the parameters, but their success is still limited. The second one is so-called Bristow-Campbell model, which uses daily temperature (minimum and maximum) and precipitation records for the estimation. In general, the first method can provide better radiation estimation than the second one. Also, the second cannot be applied to estimate hourly solar radiation.

In this study, we made efforts to develop a more general model for solar radiation estimation from surface meteorological variables and available global data set for turbidity and ozone thickness. This model follows the simple form of Ångström–Prescott approach while it can account for the radiative extinction processes. The input data are sunshine duration, air temperature, and relative humidity. The output are hourly, daily and monthly global solar radiation, depending on the temporal resolution of the input.

The paper is organized as follows: First, we develop a sub-model to calculate solar radiation from surface air temperature and relative humidity under clear skies. Second, several globally covered data sets are introduced into the solar radiation model to calculate Ångström turbidity coefficient and ozone. Third, the global solar radiation under cloudy conditions is scaled by the surface solar radiation under clear skies, rather scaled by than radiation at the extraterrestrial level. Fourth, model parameters are tuned for estimation of hourly, daily, or monthly-mean daily radiation respectively, using data at 53 stations of Japan in 1995. The Ångström–Prescott model is calibrated by the same data sets. Finally, we apply the new model and Ångström–Prescott model to world-widely distributed stations. These stations have distinct climate from humid to dry zones and surface elevation varying from the sea-level to as high as near 4000 m.

2. Global solar radiation model under clear sky conditions

The global solar radiation is affected by a number of extinction processes in the atmosphere. They are Rayleigh scattering, aerosol extinction, ozone absorption, water vapor absorption and permanent gas absorption. A spectral model can be used for calculating global solar radiation under clear skies:

$$R_{b0} \equiv \sin h \int_{\lambda_{\min}}^{\lambda_{\max}} I_{0i}(\lambda)\tau_{oz}(\lambda)\tau_w(\lambda)\tau_g(\lambda)\tau_r(\lambda)\tau_a(\lambda)d\lambda\,, \tag{2.1}$$

$$R_{d0} \equiv 0.5\sin h \int_{\lambda_{\min}}^{\lambda_{\max}} I_{0i}(\lambda)\tau_{oz}(\lambda)\tau_w(\lambda)\tau_g(\lambda)[1-\tau_r(\lambda)\tau_a(\lambda)]d\lambda\,. \tag{2.2}$$

where R_{b0} (W m^{-2}) is solar beam and R_{d0} (W m^{-2}) is solar diffuse radiation at ground level under clear skies.

We then simplify the spectral model as follows

$$R_{b0} = I_0 \overline{\tau_{b0}} \cos Z\,, \tag{2.2a}$$

$$R_{d0} = 0.5 I_0 \overline{\tau_{d0}} \cos Z\,, \tag{2.2b}$$

where

$$\overline{\tau_{b0}} \approx \overline{\tau}_{oz}\overline{\tau}_w\overline{\tau}_g\overline{\tau}_r\overline{\tau}_a - 0.013\,, \tag{2.3a}$$

$$\overline{\tau_{d0}} \approx \overline{\tau}_{oz}\overline{\tau}_g\overline{\tau}_w(1-\overline{\tau}_a\overline{\tau}_r) + 0.013 \tag{2.3b}$$

$$\overline{\tau}_{oz} = \exp[-0.0365(ml)^{0.7136}]\,, \tag{2.3c}$$

$$\overline{\tau}_w = \min[1.0, 0.909 - 0.036\ln(mw)]\,, \tag{2.3d}$$

$$\overline{\tau}_g = \exp(-0.0117 m'^{0.3139})\,, \tag{2.3e}$$

$$\overline{\tau}_r = \exp(-0.008735 m' \overline{\lambda}_r^{-4.08})\,, \tag{2.3f}$$

$$\overline{\tau}_a = \exp(-\beta m \overline{\lambda}_a^{-1.3})\,, \tag{2.3g}$$

$$\overline{\lambda}_r = 0.547 + 0.014m' - 0.00038m'^2 + 4.6\times10^{-6} m'^3\,, \tag{2.3h}$$

$$\overline{\lambda}_a = 0.6777 + 0.1464(m\beta_t) - 0.00626(m\beta_t)^2\,, \tag{2.3i}$$

$$m = 1/[\sin h + 0.15(57.296h + 3.885)^{-1.253}] \tag{2.3j}$$

$$m' = m\, p / p_0 \tag{2.3k}$$

According to the preceding equations, R_{b0} and R_{d0} can be calculated given surface pressure p, Ångström turbidity β, precipitable water w, and ozone thickness l.

This model was evaluated as one of the best models in calculating surface solar radiation under clear skies (Gueymard, 2003a, 2003b).

For practical application, the precipitable water is calculated from relative humidity (rh, %) and air temperature (T_a, K):

$$w = 0.493\, rh\, T_a^{-1} \exp[26.23 - 5416 T_a^{-1}]\,.$$

3. Global distribution of Angstrom turbidity coefficient and ozone

The aerosol scattering is one of the most important radiation-damping processes. The Ångström turbidity coefficient, a key parameter for the scattering, generally decreases with respect to elevation and also decreases toward to high latitude. Ångström gives a formula to estimates it, but the formula can be questionable in some areas such as India and China because of its high variability in both space and time.

In the new model, we introduce two data sets to calculate the turbidity. First, we follow Hess et al. (1998) and calculate optical depth at wavelength $0.5\,\mu$m. The optical length is then converted to Ångström turbidity β. This method can provide a global cover, but its spatial resolution ($5^0 \times 5^0$) and temporal resolution (summer and winter) are low, so we use it as a background of turbidity; that is, it is used if no other data sources are available. The second data set is a monthly mean data provided by AVHRR. It has a higher spatial resolution ($1^0 \times 1^0$) and temporal resolution (monthly), but no data is available beyond 70 degrees latitude in both hemispheres.

The thickness of ozone is provided by a NASA global dataset with a $1^0 \times 1^0$ spatial resolution and monthly temporal resolution.

4. Framework to develop a new general model

The traditional Ångström–Prescott model assumes that globe solar radiation can be scaled by the solar radiation at the top of the atmosphere. That is

$$R = (a + b\,S + c\,S^2)R_0 \tag{4.1}$$

However, the new model assumes that the globe solar radiation can be scaled by its value under clear skies.

$$R = (a + b\,S + (1 - a - b)\,S^2)(R_b + R_d) \tag{4.2}$$

The new model has four features: (1) it has a simple form as Ångström–Prescott model; (2) model inputs are surface meteorological data (sunshine duration, air temperature, and relative humidity) so that the model can be applied easily; (2) under clear skies, the estimated solar radiation is equal to the value calculated by sophisticated spectral models. (3) At the top of atmosphere, the estimated solar radiation is exactly equal to the theoretical value of solar radiation. Hereafter, it is called hybrid model.

5. Model calibration

We calibrated the two models using the data at 53 stations in Japan. The maximum surface elevation is less than 300 m, and the humidity is relative high. The models are calibrated for hourly, daily and monthly solar radiation estimation

6. Model validation

We compare the two models at a number of stations by three indices: mean bias error (MBE), root mean square errors (RMSE), and correlation coefficient (R^2). The following only shows the major index RMSE in USA and Saudi Arabia.

(1) In USA.

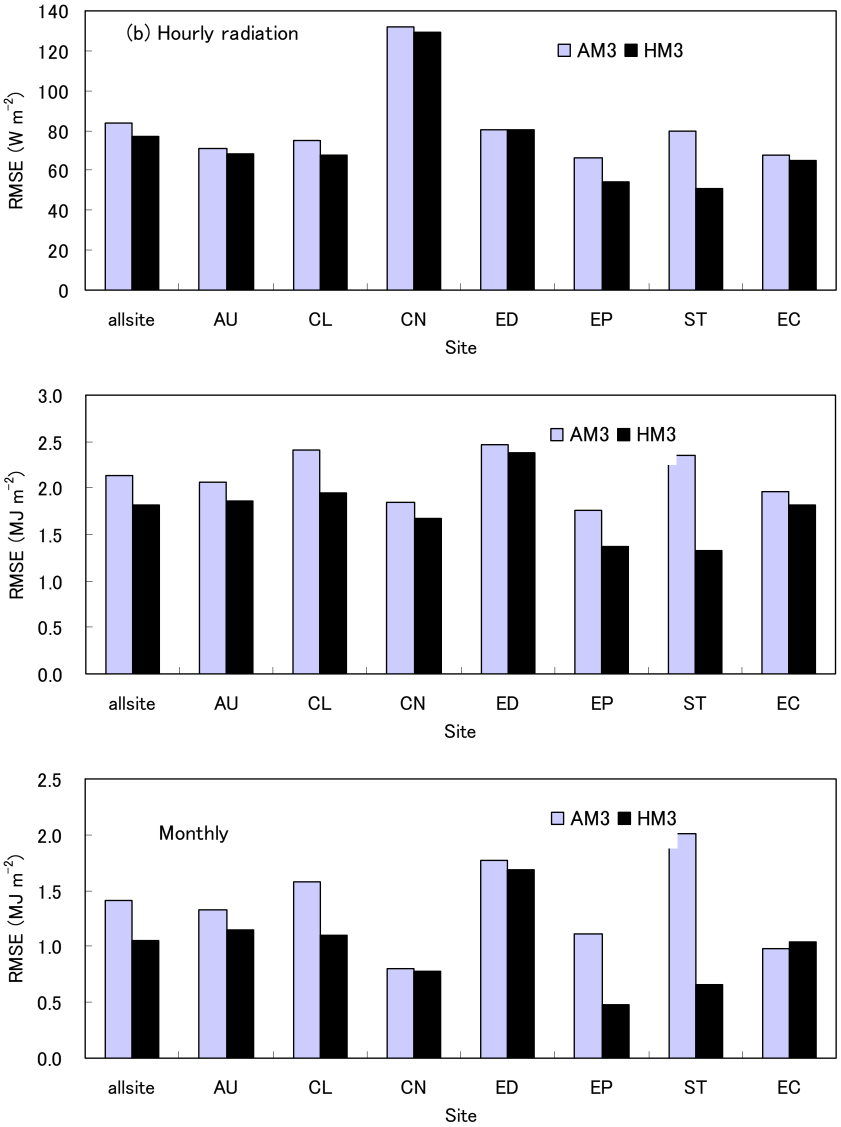

Figure 1 Validation in USA. AM: Ångström–Prescott model; HM: Hybrid model. Upper panel, hourly data; Middle panel: daily data; Lower panel: monthly-mean daily data

(2) In Saudi Arabia.

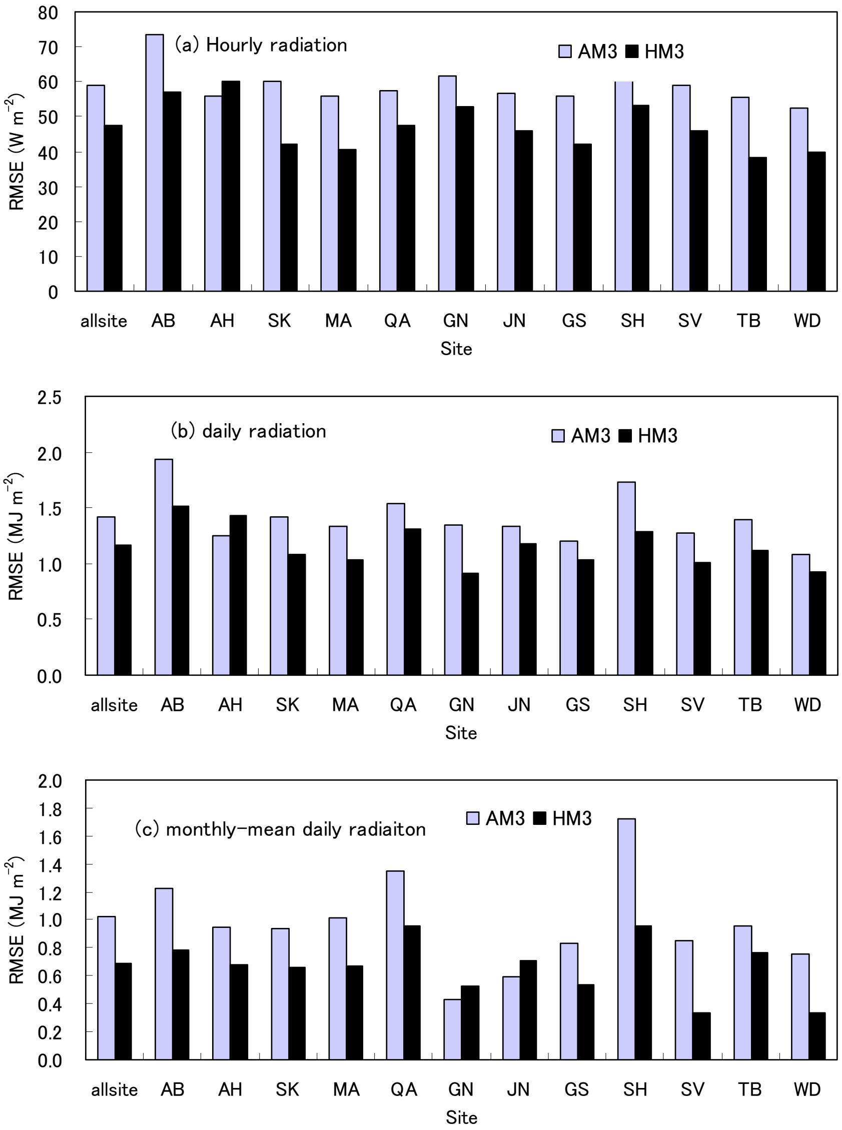

Figure 2 Validation in Saudi Arabia. AM: Ångström–Prescott model; HM: Hybrid model. Upper panel, hourly data; Middle panel: daily data; Lower panel: monthly-mean daily data

7. Conclusion

We develop a new model. The new model much improved the estimation for solar radiation from surface meteorological data compared to the traditional Ångström–Prescott model.

1-5

The Characteristics of the Cloud Properties Retrieved from Global Imager Aboard the ADEOS-II (Midori-II) Earth Observation Satellite

Takashi Y. Nakajima[1], Teruyuki Nakajima[2]
Shuichiro Katagiri[3]
[1] JAXA and CEReS/Chiba University, [2]CCSR/University of Tokyo, [3]RIHN

Abstract : The characteristics of the cloud optical and microphysical properties obtained from GLI aboard the ADEOS-II satellite were shown in the presentation. The GLI-derived results were compared with the MODIS-derived results and got a different feature in the effective radius between GLI and MODIS. The investigation of the difference has just started.

INTRODUCTION

It is pointed out by the Intergovernmental panel on Climate Change (IPCC) 2001, that the aerosol-cloud interaction process is one of the largest uncertainties in the climate change studies (IPCC 2001). It emerged that aerosol in the atmosphere can influence the Earth radiation budget through changes in the cloud optical and microphysical properties by the two kinds of indirect effect of aerosol (e.g., *Twomey et al*. 1984; *Coakley et al*. 1987; *Radke et al*. 1989). The first kind effect is a change in the cloud radiative properties due to cloud particle radius reduction by aerosols, and the second kind effect is a change in the cloud lifetime and precipitation efficiency. The observations and the progress in cloud and aerosol microphysical modeling in the climate model will contribute to improving the accuracy of future climate predictions.

DATA ANALYSIS

The optical and microphysical properties of the warm water and cold ice clouds were retrieved from the ADEOS-II (Midori-II) GLI data by use of the GLI data analysis system

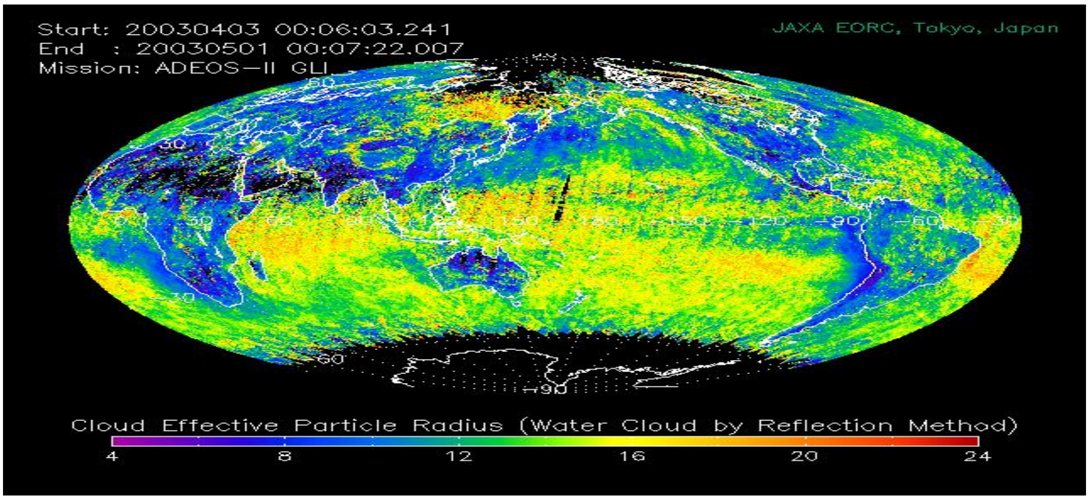

Fig. 1 Cloud effective particle radii (water cloud) in April 2003, obtained from GLI data analysis.

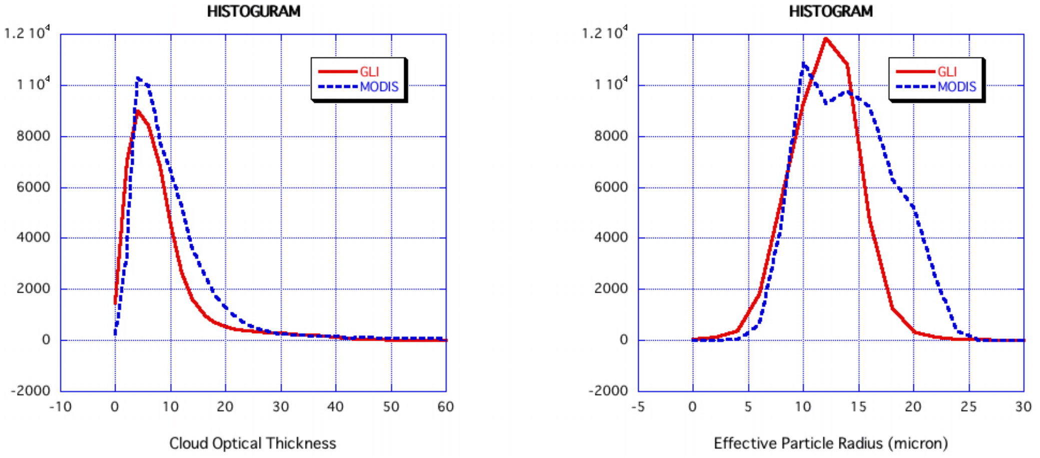

Fig.2 Histogram of the global analysis obtained from GLI (red curve) and MODIS (blue curve). Cloud optical thickness (Left), and cloud effective particle radius (Right) .

based on Nakajima and Nakajima (1995) algorithm with an enhancement of the water vapor correction for the global scale analysis by Kawamoto et al (2001). The GLI data were analyzed every four days and merged and averaged for the one-month period. The one-month mean results of warm water clouds in April 2003 has interesting features. The very thick cloud optical thickness appeared in the east coast of the North America, in the East Europe, and in the South-East Asia. The Atlantic Ocean and West to Middle Pacific oceans were covered by the moderately optically thick water clouds. The cloud effective particle radii were smaller on the continents and coastal areas than ocean area. The South-East Asia to the middle pacific area was the region of the existence of the smaller cloud effective particles.

GLI AND MODIS

The comparison between GLI products and MODIS products of warm cloud microphysical properties showed different features. The one-month mean of the GLI-derived cloud effective radii showed a single mode with a mode radius of 12 micrometers whereas the MODIS-derived results had bi-modes at 10 and 14 micrometers. Basically, the cloud effective radii are larger in MODIS than GLI especially over the open ocean area. The investigations of the difference are now undergoing. The possible reason for the differences can be due to the difference of the cloud phase algorithm and/or different wavelength of the short wave infrared channel, GLI (3.7 micron), MODIS (2.1 micron), that is used for the droplet size retrievals, and so on. On the other hand, the cloud optical thickness of GLI and MODIS showed almost the same values.

SUMMARY

The seven-month global observing data obtained from GLI aboard ADEOS-II satellite has analyzed by using data analysis system installed in JAXA. The global datasets of the cloud properties were released to the users since December 2003. The characteristics of the GLI-derived cloud properties qualitatively consist with the present scientific knowledge of the cloud statistics. However, the effective particle radius obtained from GLI and MODIS products showed a different feature. The investigation of the difference has just started.

REFERENCES

Coakley, J. A., R. L. Bernstein, and P. A. Durkee, 1987: Effect of ship-stack effluents on cloud reflectivity. *Science*, **237**, 1020-1022.

IPCC (the Intergovernmental Panel on Climate Change), 2001: Climate Change 2001: The Scientific Basis, J. T. Houghton, Y. Ding, D. J. Griggs, M. Noguer, P. J. van der Linden,D. Xiaosu, K. Maskell, and C. A. Johnson (Eds.), 896 pp., Cambridge Univ. Press, New York

Kawamoto K., T. Nakajima, and T. Y. Nakajima, "A Global Determination of Cloud Microphysics with AVHRR Remote Sensing.," *J. Climate* , **14**, 2054-2068. 2001.

Katagiri S. and T. Nakajima, "Radiative characteristics of cirrus clouds as retrieved from AVHRR.,", *J. Met. Soc. of Japan*, **82**, 81-99, 2004.

Nakajima T. Y. and T. Nakajima, "Wide-area determination of cloud microphysical properties from NOAA AVHRR measurement for FIRE and ASTEX regions.," *J. Atmos. Sci.* , 52, 4043-4059. 1995.

Radke, L. F., J. A. Coakley Jr., and M. D. King, 1989: Direct and remote sensing observations of the effect of ships on clouds. *Science*, **246**, 1146-1149.

Twomey, S., M. Piepgrass, and T. L. Wolfe, 1984: An assessment of the impact of pollution on global cloud albedo. *Tellus*, **36**, 356-366.

Measurements of clouds, and radiation from space for climate studies

Ehrhard Raschke
University of Hamburg, Germany
Visiting Professor at NIPR, Tokyo, Japan
and
Makoto Wada and Takashi Yamanouchi
National Institute for Polar Research, Tokyo, Japan

The technological advancements achieved during the past two to three decades enabled considerable progress in establishing space-borne observational systems for clouds and associated radiation fields. Measurements are now available for worldwide studies of climate variations. However they are still lacking in reliable accuracies and stability for global trend identification. This paper concentrates on recent results obtained on clouds and their effects on the radiation budget.

1. Introduction:

The early climatologists, as early astronomers for planets, were with highest priority interested to obtain quantitative information on the radiation budget fields at the top and bottom of the atmosphere, knowing that any spatial gradients of it force redistributions of energy. The equator to pole gradient forces steadily related heat transports in the atmosphere and in the oceans. Furthermore clouds in the troposphere are not only indicators of various dynamical processes. They modify the transfer of radiative energy and they are source of the ever needed precipitation. Therefore already the first meteorological satellites, which were successfully launched in the period between the years 1958 to 1970, carried (in comparison to the present situation) relatively simple sensors to measure clouds and also the components of the radiation budget at the top of the atmosphere. These early measurements formed already the presently accepted general picture on the radiation budget of our planet (Raschke, 1972), which however needs now details on its variations in space and time and on their uncertainty limits.

Since then the drastic advances in instrumental and computer technologies enabled the construction of more complicated instruments with enormous high data rates to be send down to earth and also rather detailed numerical models for the global climate system. The latter produce results on clouds and radiation fields for the present and even for future climate states, which however still do not agree with measurements of the same time period (see project CMIP: Bader (ed.), 2004; Potter and Cess, 2003). Future demands for improvement of climate and weather prediction and of the identification of regional or even (weaker) global climate trends call for much improved models and for more accurate and stable measured information (see NISTIR 2004; and recommendations of various projects of the WCRP).

This paper describes briefly the present status of space-borne cloud and radiation measurements and provides also a possible outline for the future.

2. Cloud observations from space

Tropospheric clouds, due to their composition of particles, modify the short-wave solar and longer-wave terrestrial (infrared) radiation in such ways, that multi-spectral imaging measurements contrast them against the mostly darker (solar) and warmer (infrared) ground. When simultaneous multi-spectral observations are available as with the presently used multi-spectral imager MODIS, this contrast allows not only to estimate the total cloud cover within given areas and often also at 2 to three different altitude ranges. They also allow to estimate the effective optical thickness and mean effective particle size and phase (ice or water). There are now many attempts reported to estimate also some aerosol characteristics from satellite data, since aerosols affect directly and indirectly (e.g. Lohmann and Feister, 2004) the radiative transfer properties and also precipitation efficiency of cloud fields.

The very recent operational network of polar and geostationary satellites provides – in conjunction with all other meteorological and climatological observations – a solid basis to establish longer time series which are superior to the earlier ones, which had to be based on relatively simple ones (one or two spectral intervals, or multi-spectral sounders with relatively course spatial resolution). Numerous new algorithm developments are now being discussed. Some allow for identification and even some characterisation of aerosols within cloud free areas. This information is required to identify quantitatively direct and indirect effects of aerosols on clouds and also on the planetary radiation budget.

Two such time series, covering already time periods of about 20 years are now available. The data series of the International Satellite Cloud Climatology Project (ISCCP: Rossow and Duenas, 2004; Zhang et al., 2004, or their website: http://isccp.giss.nasa.gov) begins during the year 1983. Besides of this satellite-borne information on cloud fields it also contains all supporting data (see Table 1 below), which are used in this retrieval algorithm, and all original and well calibrated radiance measurements. Thus re-analyses on the basis of more recent knowledge might always be possible.

Variables	**Data set of variables**
Cloud Cover, Optical Thickness, Top Temperature by Type	ISCCP satellite radiances
Cloud Particle Size	ISCCP-based Climatology
Cloud Vertical Structure	Combined ISCCP-Rawinsonde Climatology
Atmospheric Temperature and Tropospheric Humidity	TOVS, Oort Climatology for filling
Atmospheric Humidity (Upper Troposphere, Stratosphere)	SAGE Climatology
Atmospheric Composition	Actual record from Various Sources
Stratospheric Total Ozone	TOMS, TOVS for filling
Stratospheric Ozone Profiles	SAGE Climatology
Stratospheric Aerosols	SAGE
Tropospheric Aerosols	Baseline Current-day Climatology
Snow cover	NOAA product
Sea Ice cover	NSIDC product
Diurnal Cycle of Air Temperature over Land	Climatology based on surface weather reports and NCEP reanalysis
Surface Skin Temperature and Visible Reflectance	From ISCCP retrievals
Surface Spectral Albedo and Emissivity by Type	GISS GCM reconstruction by surface type and season

Table 1: Variables to be used in the cloud retrieval from the ISCCP radiance data

Quantity	**global**	**ocean**	**land**
Cloud amount [%]	67 *73*	71 *75*	57 *69*
Cloud-top temperature [K]	261 *261*	266 *264*	251 *256*
Cloud-top pressure [hPa]	587 *607*	631 *631*	489 *547*
Cloud optical thickness/	4.2	4.2	4.1
Effective emittance	*0.57*	*0.57*	*0.55*
Cloud water path [gm^{-2}]	62.0	58.6	69.6
Atmospheric water vapour [cm w.e.]	*2.51*	*2.60*	*2.23*

Table 2: Global cloud properties from 5 years of ISCCP / TOVS Path-B (italic)

Table 2 summarizes the major results and compares them with those derived from other – often concurrent measurements with operational sounders (TOVS Path-B – see e.g. Scott et al., 1999; Stubenrauch et al., 1999). This sounding technique, which is performed primarily to obtain operationally information on the vertical temperature structure of the lower and middle atmosphere, allows by proper combination of concurrent measurements in different spectral ranges (called “colour slicing”) a sharper contrasting of higher and medium level clouds against the background. This time series, mostly obtained from a single satellite, but in no case from geostationary orbit, covers a period from 1983 to 2001.

3. Radiation fields and cloud effects

3.1 Measured at TOA

Fields of the radiation budget components at TOA can be derived either from measurements with wide-field-of-view radiometers, which “see” the entire disc of the earth under the satellite, or from narrow-field-of-view radiometers. The latter enable budget analyses with a spatial resolution compatible with those of best global models (50 to 100 km grid length). Early measurements began already in 1959 onboard of always single satellites of the TIROS-, ESSA-, and later Nimbus- and NOAA-series (e.g. Raschke, 1972). The first multi-satellite system (ERBE, Earth Radiation Budget System; Barkstrom 1984) has been flown during the early 80th, with scanning and non-scanning radiometers. Further instrumental achievements enabled in particular various scanning techniques and more spectral information within the scope of the multi-satellite experiment CERES, where almost identical instruments are flown onboard of different operational and experimental satellites (Wielicki et al., 1996). A European development, ScaRaB (Scanner for Radiation Budget; Kandel et al., 1998), complemented these latter observations during shorter time periods.

These latter measurements from ERBE and CERES allowed first estimates of the cloud effect on the net solar and net terrestrial radiation budget at TOA by proper selection of measurements over cloud free areas. Global annual averages of the budget components are summarized in Table 3. These annual global averages show, that clouds reduce the absorption of solar radiation but keep also more thermal longwave radiation within the climate system.

Quantities at top of the atmosphere (TOA)	**Mean values**	**For cloudless earth**	**Effect of clouds**
Outgoing terrestrial radiation	-234 Wm^{-2}	-266 Wm^{-2}	+32 Wm^{-2}
Absorbed solar radiation	239 Wm^{-2}	288 Wm^{-2}	-49 Wm^{-2}
Net radiation	**+5 Wm^{-2}**	**+22 Wm^{-2}**	**-17 Wm^{-2}**
Albedo	30%	15%	+15%

Table 3: Global averages of the radiation budget components at TOA and the effects of clouds (last column) on the outgoing terrestrial radiation, computed from earlier ERBE data. The small positive value of the net radiation is considered within the error range of this analysis ***and should not interpreted as a heating of our planet.***

3.2 Computed at TOA

The ISCCP data sets – see Table 1 for all complementary data – allows for direct calculations of up- and downward radiation fluxes between TOA and the surface for both cloudy (as given by the ISCCP clouds) and cloud free atmosphere. The radiation fields at TOA are not identical with those observed simultaneously, showing regional differences between 10 to 20 Wm^{-2} for annual averages. But the general spatial patterns are quite similar showing also the already with early Nimbus data computed annual radiation deficits over the major terrestrial desert regions.

As an example we show here a global map of the cloud effect on the total radiation budget at TOA, whose numbers are differences between the net radiation at cloudy and at clear skies. Thus positive (negative) values mean, that the net radiation at cloudy skies is larger than at clear skies. The generally negative values mean, that cloudy generally reduce the net radiation budget, dominantly due to the reflective power for solar radiation (see Table 3).

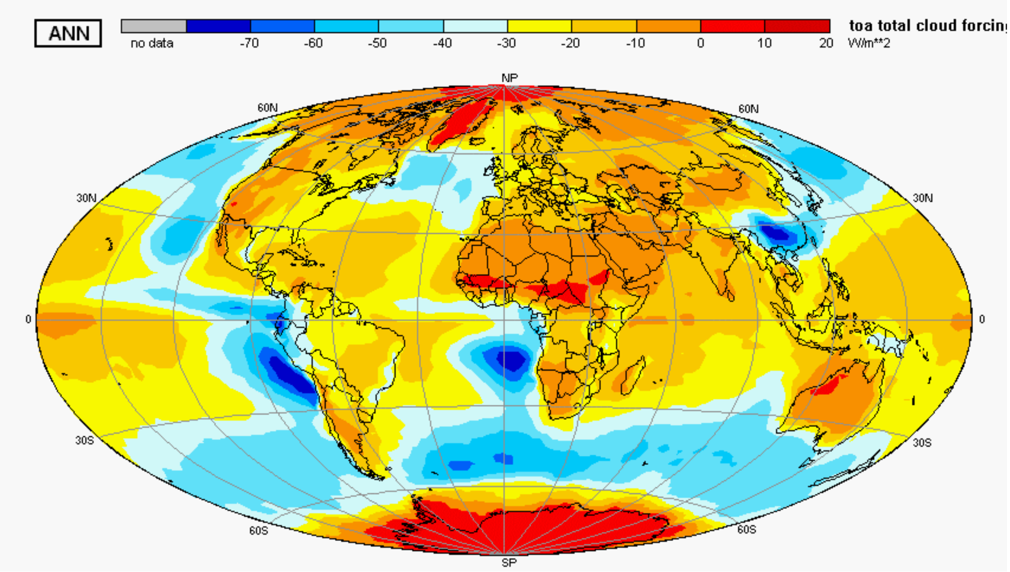

Fig. 1: Annual average of the effect of clouds on the net radiation budget *(in Wm*$^{-2}$*) during the period 1991 1995, computed as the difference between the net radiation at cloudy and clear skies. Over most areas clouds tend to reduce the net gain of radiative energy by the climate system (negative values), while over some small areas with high and persistent convection they tend to enhance it. Over both Polar Regions this effect is relatively more inaccurate due to large uncertainties in cloud identifications. Highest and lowest values: +13 and -80 Wm*$^{-2}$*; global average: -24 Wm*$^{-2}$*.*

3.3 Fields at surface

Radiation fields at the surface cannot be measured directly from space, but they can be inferred from such measurements with inclusion of various complementary data on the state of the atmosphere and of the ground (see e.g. Table 1). Numerous techniques have now been developed. Most recently Stackhouse et al. (November 2004, GEWEX NEWS) summarized their work within the CERES project. An analysis of the ISCCP results obtained for the years 1991 to 1995 has been provided by Raschke et al., (2005, in print). Most of these and other results are compared to simultaneous measurements with ground-bases radiometers for solar and terrestrial radiation, which are performed within different networks. These comparisons signal an uncertainty range for annual regional averages of the order of 10 to 20 Wm^{-2} where errors are possibly largest over both polar regions.

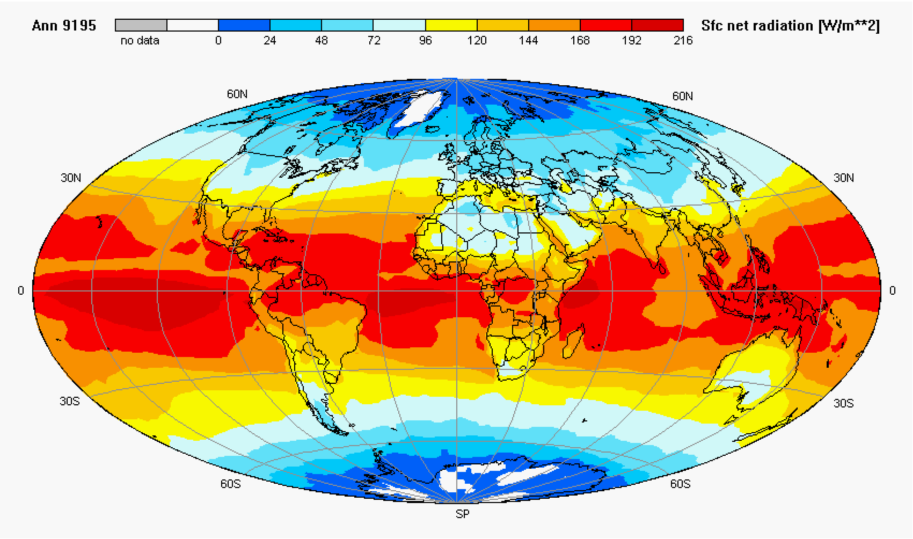

Fig. 2: Annual average of the total net radiation (or of the radiation budget) at the surface *during the period 1991 to 1995, in Wm^{-2}. All values, with a few exceptions over Greenland and Antarctica, are positive indicating, that the Earth's surface is everywhere heated by radiation. The small negative white areas are very close to zero. They are possibly caused by errors in both components over those regions, due to inaccurate cloud identification over those regions. Highest and lowest values: + 211 and –16 Wm^{-2}; global average: +116 Wm^{-2}.*

3.4 : The total radiation budget of the atmosphere

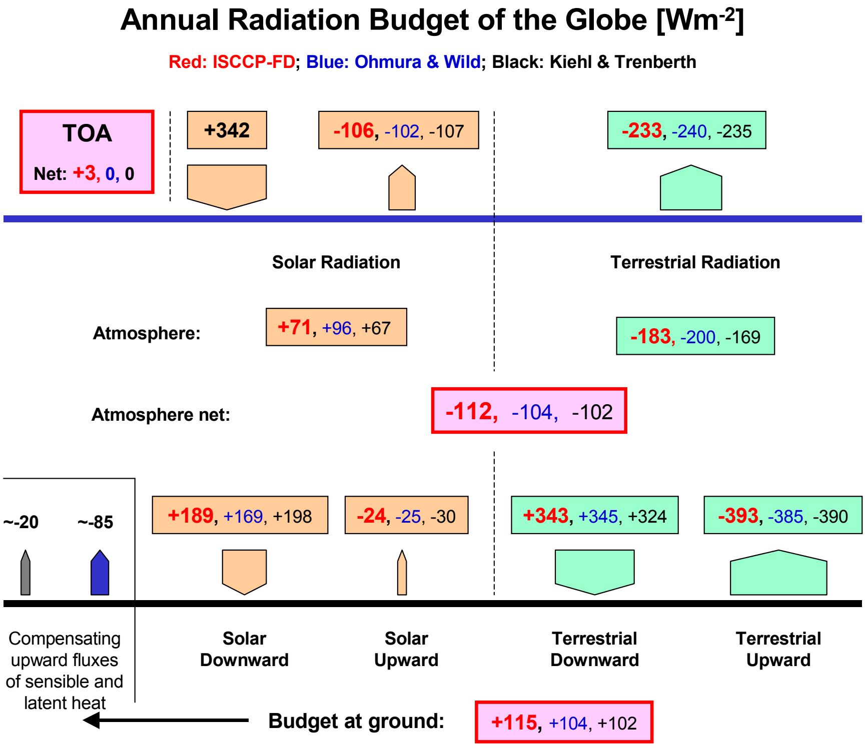

Fig. 3: Annual radiation budget of the climate system(in Wm^{-2}) calculated from the ISCCP data set (red numbers) and compared with results from Ohmura and Wild (blue numbers) and Kiehl and Trenberth (black numbers). Respective values for the total flux divergence in the atmosphere are –112, -104, -102 Wm^{-2}, respectively.

For global annual averages of the total radiation budget at TOA and at the surface quite similar values are found by these and other methods, however systematic differences occur in the two components. Particular high discrepancies occur the vertical divergences of both components urging for more intensive data validations. As an example, in Fig 3 are summarized the results of the ISCCP analysis by Raschke et al. (2005) and compared with others (Kiehl and Trenberth 1997; Ohmura and Wild, 2004, priv.comm.).

Fig. 4 summarizes the zonal averages of annual and seasonal values of the total radiation flux divergence within the atmosphere as computed from the ISCCP data set. All values are negative indicating, that within the mechanisms of the global heat engine the atmosphere is generally emitting radiation back to space, thus it must be heated from below by upward fluxes of latent and sensible heat. Note the large discrepancies between values for the solar and terrestrial vertical divergence, which were derived by those author teams. There are also significant regional differences in this budget.

Clouds, see Fig. 5, generally diminish this deficit at near-equatorial regions between about 30 degrees latitude, and enhance it elsewhere. The absorption of solar radiation in the clouds appears to be very low in this figure due to two causes: clouds reflect often more than 50% of the incident solar radiation back to space and they reduce considerably the amount of solar radiation into the lower tropospheric layers where most of the atmospheric water vapor rests. Various maps of these quantities will be shown during the presentation.

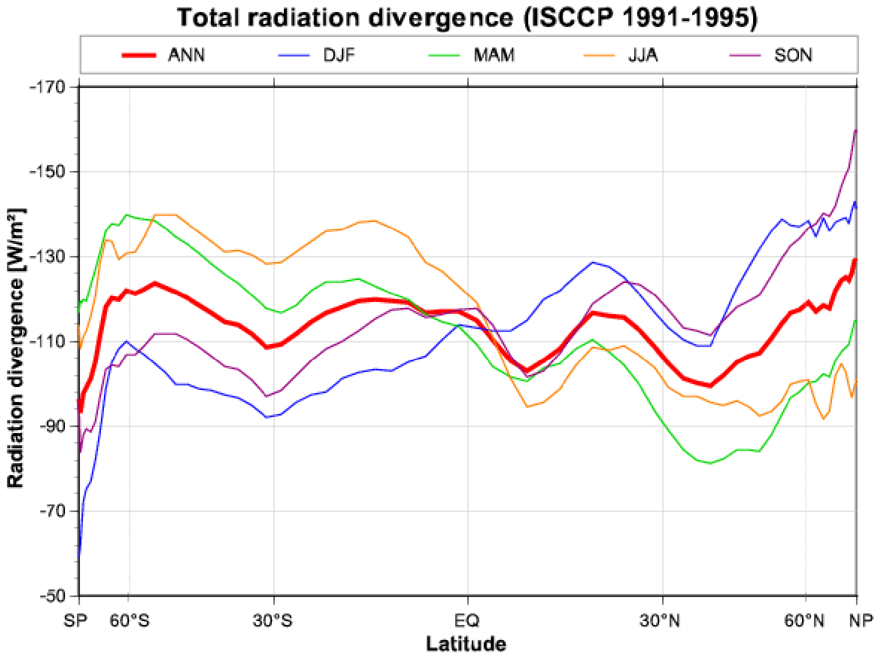

***Fig. 4:** Zonal averages of the total radiant flux divergence in the atmosphere during all seasons. These graphs are obtained for all seasons and for the annual average.*

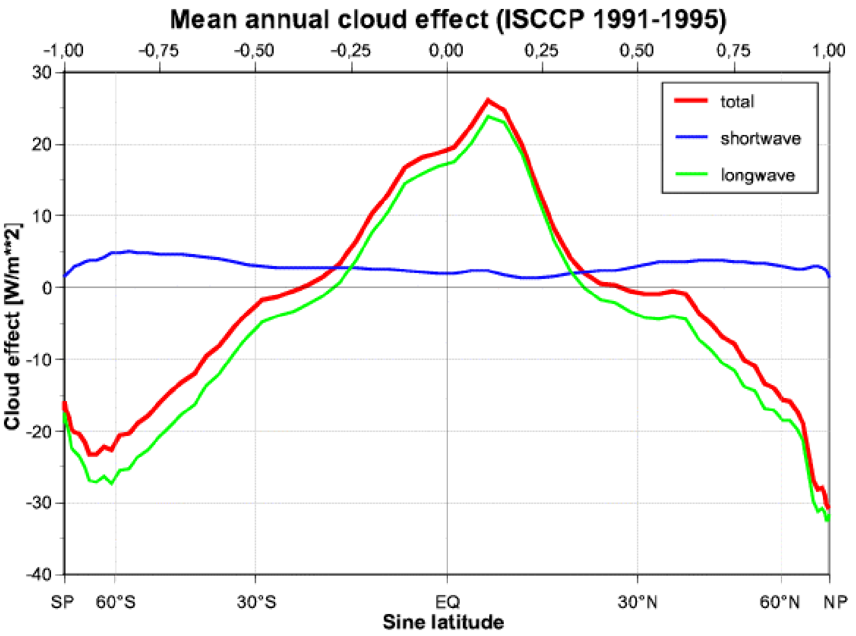

Fig. 5: Mean annual effect of clouds on the total radiant energy flux divergence in the atmosphere. *Positive values indicate that clouds contribute to the heating of the atmosphere. Clouds reduce the absorption of solar radiation below their bottoms and may slightly increase the absorption of radiant energy in the stratospheric ozone layer. The cloud effect in the infrared is due to partly compensating effects of emission from cloud tops and cloud bottoms at different altitudes and also the emission of lower atmospheric water vapor to ground.*

4. Some discussion

This paper can provide only a short overview on existing and hopefully future data sets, which are required to identify climate changes and to verify respective model results.

There is a need establish between different data sets more transparency about their weaknesses and strengths. In particular uncertainty range must be justified (e.g. Zhang et al., 2004) which should not exceed about 1 to 3 W m^{-2} for regional monthly averages and about one tenth of this limit for the annual stability to identify "trends", as they occur in the radiation budget quantities. As at present already the satellite ICE-Sat and other radar satellites, in future there will be dedicated active measurements with lidar and cloud radar, which will provide more information on he cloud geometry and internal structure, enabling then higher accuracies in calculating their radiative transfer properties and identifying even interactions between clouds and aerosols (e.g. Stephens et al., 2002). These new observational capabilities are a challenge for the research community.

5. References

Barkstrom, B.R., 1984: The Earth Radiation Budget Experiment (ERBE). *Bulletin of the American Meteorological Soc*iety **65:** 1170-1186.

Bader, D. (ed.), 2004: An Appraisal of Coupled Climate Model Simulations. Report UCRL-TR-202550, Lawrence Livermore National Laboratory, 73pp CMIP

Kandel, R., M. Viollier, P. Raberanto, J. Ph. Duvel, L. A. Pakhomov, V. A. Golovko, A. P. Trishchenko, J. Mueller, E. Raschke, R. Stuhlmann, and the International ScaRaB Scientific Working Group, The ScaRaB earth radiation budget dataset., *Bulletin of the American Meteorological Society,* **79**, 765-783, 1998.

Kiehl J., and K.E. Trenberth, 1997: Earth's Annual Global Mean Energy Budget. *Bulletin of the American Meteorological Society.***,** **78**, 197-208.

Lohmann, U., J. Feichter, 2004: Global indirect aerosol effects: a review. *Atm. Chem. Phys. Discuss.,***4,** 7561-7614

NISTIR 7047: Ohring G., B. Wielicki, R. Spencer, B. Emery, R. Datla (ed.), 2004: Satellite Instrument Calibration for Measuring Global Climate Change. US Department of Commerce, National Institute for Standards and Technology, 100pp

Potter, G.L., R.D. Cess, 2004: Testing the impact of clouds on the radiation budgets of 19 atmospheric general circulation models. *J. Geophys. Res*., **109, D02106**, doi:10.1029/2003JD004018

Raschke E., 1972: Die Strahlungsbilanz der Systems Erde-Atmosphäre – neuere Ergebnisse von Satellitenmessungen. *Zeitschrift für Geophysik,* **38:** 967-1000.

Raschke, E., A. Ohmura, W. B. Rossow, B. E. Carlson, Y-C. Zhang, C. Stubenrauch, M. Kottek, M. Wild, 2005: Cloud effects on the radiation budget based on ISCCP data (1991 to 1995). *Int. Journ. Climatology*, in press

Rossow, W.B. and E.N. Duenas, 2004 : The International Satellite Cloud Climatology Project (ISCCP) Web Site. *Bull. Am. Meteor. Soc.,* **85,** 167-172

Scott, N. A., Chédin, A., Armante, R., Francis, J., Stubenrauch, C. J., Chaboureau, J.-P., Chevallier, F., Claud, C., Chéruy, F., 1999. Characteristics of the TOVS Pathfinder Path-B Dataset. *Bulletin of the American Meteorological Soc*iety**, 80**: 2679-2701.

Stephens, G. L., D. G. Vane, R. J. Boain, G. G. Mace, K. Sassen, Z. Wang, A. J. Illingworth, E. J. O'connor, W. B. Rossow, S. L. Durden, S. D. Miller, R. T. Austin, A. Benedetti, C. Mitrescu, and The Cloudsat Science Team, 2002: The Cloudsat Mission and the A-Train - A New Dimension of Space-Based Observations of Clouds and Precipitation. *Bulletin of the American Meteorological Soc*iety**, 83:** 1771-1790.

Stubenrauch, C.J., W.B. Rossow, F. Cheruy, A. Chedin and N.A Scott, 1999: Clouds as seen by satellite sounders (3I) and imagers (ISCCP). Part I: Evaluation of cloud parameters. *Journal of Climate,* **12**: 2189-2213.

Wielicki, B.A., B.R. Barkstrom, E.F. Harrison, R.B. Lee, G.L. Smith and J.E. Cooper, 1996: Clouds and the Earth's Radiant Energy System (CERES): An Earth Observing System experiment. *Bulletin of the American Meteorological Soc*iety**, 77:** 853-868.

Zhang, Y-C., W.B. Rossow, A.A. Lacis, V. Oinas and M.I. Mishchenko, 2004: Calculation of Radiative Flux Profiles from the surface to top-of-atmosphere based on ISCCP and other global datasets: Refinements of the radiative transfer model and the input data. *Journal of Geophysical Research,* **109, D19105,** doi: 101029/2003JD004457**.**

2-2

Reflectance Band Ratios in Japan Using Satellite and Sky Observation Data

Y. Kawata, T. Umeki and K. Takemata

Earth and Social Information Core, Dept. of Computer Sciences
Kanazawa Institute of Technology,
Ogigaoka 7-1, Nonoichi, Ishikawa 921-8501, Japan

Abstract: We observed the aerosol optical properties, such as the optical thickness (τ_A) and Ångström exponent α over Kanazawa area, Japan for the period of seven months from Oct. 2003 to April 2004. using the sky radiometer. The reflectance ratios between the visible and short wave infrared bands were computed for the classes of the vegetation, urban, and the others using several data sets of Terra/MODIS and the sky observation data. The computed band reflectance ratios were compared with those by Kaufman et al. (1997)[1)] and us (2003)[2)].

Key Words: *Aerosol, Optical Thickness, Atmospheric Correction*

1. INTRODUCTION

In the atmospheric correction of the remotely sensed earth image data we need the information on the aerosol optical parameters, such as the optical thickness τ_a, Ångström exponent α, and the type of size distribution. A method for estimating them from the satellite-measured data itself is highly desirable. It was found by Kaufman et al.(1977)[1)] that there existed an empirical reflectance band ratio for a few land categories between the visible reflectance and middle IR reflectance as follows:

$r_{B1}/ r_{B7} = C_{1\,v}=0.50$ (vegetation) (1),
$r_{B3}/ r_{B7} = C_{3\,v}=0.25$ (vegetation) (2)
$r_{B1} / r_{B7} = C_{1u}=0.69$ (urban, and the other) (3),
$r_{B3} / r_{B7} = C_{3u}=0.42$ (urban, the other) (4),

where r_{B7}, r_{B1} and r_{B3} are the reflectance values in the band 7(2.15μm), band 1(0.645μm) and band 3(0.469μm) of Terra/MODIS. They obtained the reflectance band ratios using the ground and airborne measurement data in USA. Since the aerosol scattering effects are negligible in the band 7, we can obtain the surface reflectance in Band 7 by removing only molecular attenuation and water vapor absorption effects. The surface reflectance in band 1 and 3 can be easily found from the above reflectance band ratio. For given surface reflectance values for those classes, we can retrieve distributions of aerosol optical thickness in Bands 1 and 3 by using LUT(Look Up Tables) in which the theoretical radiances at the top of the atmosphere(TOA) are tabulated as a function of the surface reflectance and the aerosol optical thickness for given bands and angles of the incident and reflection.

In our previous study[2)], these reflectance ratios in Japan were found using the simultaneous sky measurement data and several image data sets of Terra/MODIS over Japan (May 06, 2002, April 07, April 16, May 09, and June 03 in 2003). as follows:

C_{1v}=0.554, C_{3v}=0.547 for vegetation (5),
C_{1u}=0.580, C_{3u}=0.489 for urban (6),
C_{1o}=0.503, C_{3o}=0.417 for others (7),

We should note that there is a large discrepancy in the value of C_{3v} between USA and Japan. Seasonal variations in the reflectance ratio were studied in this paper.

2. COMPUTATION OF REFLECTANCE RATIO

We made sky observations using the sky radiometer (Prede: POM-01) at our study site which is localted on the campus of Kanazawa Institute of Technology for a period of 7 months from Oct. 2003 to April 2004. The aerosol optical parameters, namely, the optical thickness $\tau_a(500)$ at 0.5μm and Ångström exponent α. are deduced by Sky-radiation Pack Code Ver.4. For example, the scatter diagram of them is shown in the case of Oct. 2004 in Fig.1. From Fig.1 it is said that we have aerosol particles with small size ($0.8<\alpha<1.7$) when the aerosol optical thickness is small ($0.2<\tau_a(500)<0.4$). Whereas, we have those with large size (α=0.5) when τ_a(500 is larger than 0.4. During the observation period we found 5 data sets of MODIS in which the study site is included and is seen, namely, on Oct.09, Oct. 20, Oct.25, Oct 27, and Nov. 01, 2003. We computed the surface reflectance values for the area near the study site from the MODIS band 1 and 3 images by removing the atmospheric scattering effects using the deduced aerosol optical thickness and . Ångström exponent values. In the atmospheric correction we assumed Haze M model(coastal aerosol) with refracted index, m=1.33 and the mid-lattitude winter atmosphere model. Then, we classified the sub-image of MODIS near the study site into 5 classes, namely, vegetation, urban, cloud & snow, sea, and the others, by using the maximum likelihood method. The reflectance band ratio values for three classes of vegetation, urban and the others were computed using corresponding surface reflectance values in band 1, 3 and band7. The scatter diagrams for the vegetation were shown in Fig.2. The reflectance band ratios for three classes were by this study as follows:

C_{1v}=0.561, C_{3v}=0.475 for vegetation (8),
C_{1u}=0.671, C_{3u}=0.525 for urban (9),
C_{1o}=0.616, C_{3o}=0.487 for others (10),

These reflectance ratios are different from those in the previous studies[1), 2)]. In this study the acquired dates of used data sets were in Oct. and Nov. 2003 and we assumed the mid-lattitude winter model, whereas they were in April to June 2003 and we assumed the mid-lattitude summer model in our previous study. It is difficult to say that the differences in reflectance band ratio between the current and previous studies is due to the seasonal changes without making sensitivity test on this matter in detail. We have not done it yet.

We retrieved the aerosol optical thickness values over land in Band 1 and 3 of MODIS data using pre-computed LUT of the theoretical radiance at TOP as a function of the reflectance for given angular conditions. The validation results of the retrieved aerosol optical thickness τ_a are shown in Fig.3, based on the new surface reflectance ratios found in this study.

3. CONCLUSIONS

We can conclude by this study as follows:

(1) We presented the surface reflectance ratios between the visible and infrared bands using both MODIS data sets and simultaneously observed sky data in the autumn.

(2) We found that the reflectance ratios for the autumn data are different from those for the spring-summer data. It is too early to say these differences due to the seasonal changes and we will continue to make further efforts on this subject.

ACKNOWLEDGEMENTS

This research was supported partially by CEReS, Chiba Uni., Joint Project Research 16-18. The MODIS data sets were provided by Yasuoka Lab., ISS, Univ. of Tokyo and Frontier Research Center, Tokyo Univ. of Infor. Sciences. ASTER data set was provided by ERSDAC, Japan. We appreciate very much for their kindness.

REFERENCES

1. Kaufman et al., 1997. The MODIS 2.1mm Channel-Correction with Visible Reflectance for Use in Remote Sensing of Aerosol, IEEE Trans. GRS, vol.35, no.5, pp.1286-1298.
2. Y. Kawata, H. Fukui, and K. Takemata, 2003. Retrieval of Aerosol Optical Parameters from Satellite Image Data over Lands, Intl. CEReS Symp. on Remote Sensing., CEReS, Chiba Univ., pp. 165-168.

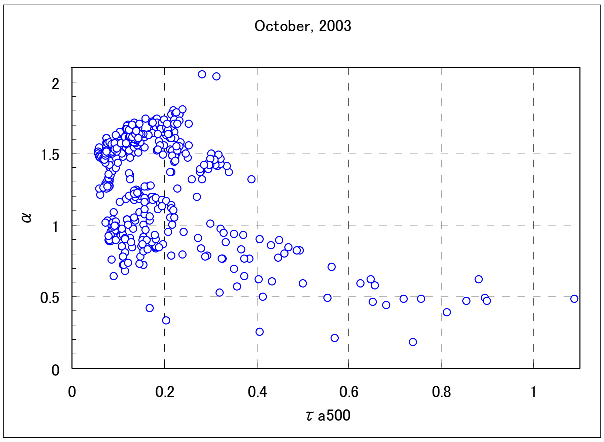

Fig.1. Scatter diagram of aerosol optical thickness τ_a(500nm) and Ångström exponent α.

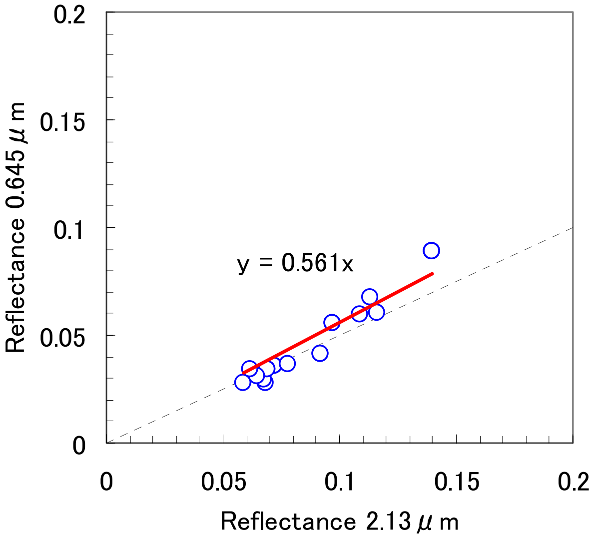

(a) C_{1v}=0.561

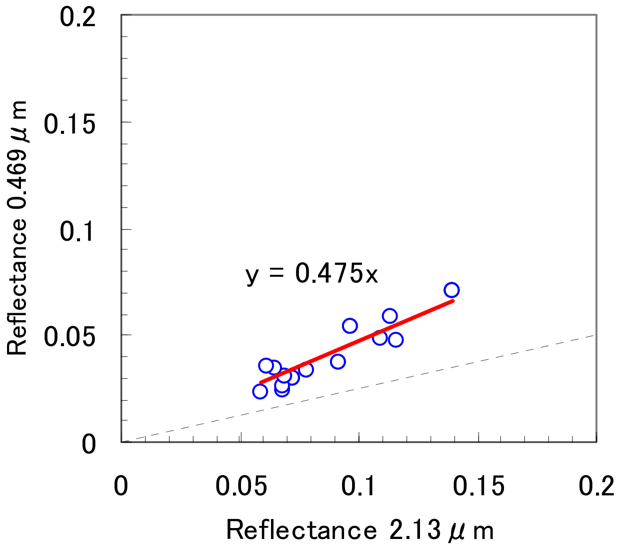

(b) C_{3v}=0.475

Fig.2. Scatter diagrams and Reflectance band ratio. for vegetation

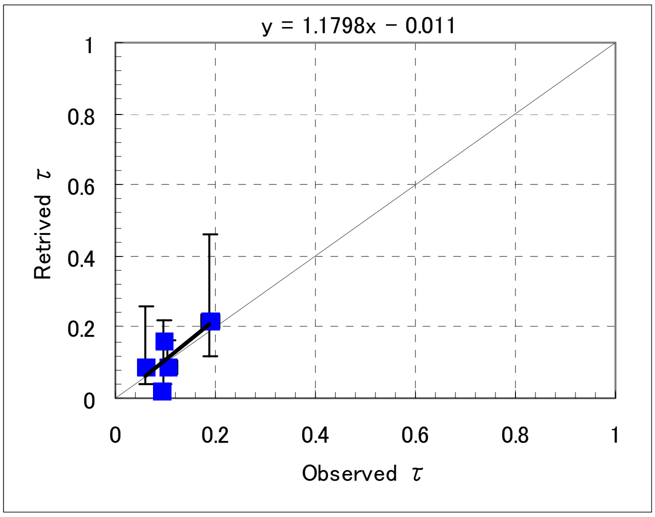

Fig.3. Observed and retrieved $\tau_a(500)$ using the autumn reflectance band.

SeaWiFS and MODIS-derived Product Verification using Normalized Water-leaving Radiance Model in the Western Equatorial Pacific Ocean

Katsutoshi Kozai[1], Anna Sasaki[2]

1 Kobe University Faculty of Maritime Sciences, 2 Kobe University Graduate School of Science and Technology

Abstract : The purpose of the study is to verify the SeaWiFS and MODIS-derived normalized water-leaving radiances and chlorophyll-a concentrations based on in situ sea surface spectral radiance observation. Utilizing ship's shadow for estimating sky radiance in the normalized water-leaving radiance model, we estimated normalized water-leaving radiance and compared with SeaWiFS and MODIS-derived corresponding products. It was found that SeaWiFS and MODIS-derived normalized water-leaving radiances and chlorophyll-a concentrations show good agreements with corresponding parameters derived from in situ spectral radiance observation.

Keywords : Western equatorial Pacific Ocean , Normalized water-leaving radiance , Chlorophyll-a concentration ,Sky radiance ratio

1. INTRODUCTION

In order to accurately extract chlorophyll-a as important indices of water quality and primary production, it is necessary to estimate upward radiances below the sea surface without an influence of surface reflectance. However the conventional in situ measurement of sea surface reflectance is not accurately enough to estimate chlorophyll-a concentration based on the spectral reflectance of the sea surface. The purpose of the study is to verify the SeaWiFS and MODIS-derived normalized water-leaving radiances and chlorophyll-a concentrations based on in situ sea surface spectral radiance observation during the cooperative air-sea interaction research cruise of R/V MIRAI belonging to JAMSTEC.

2． DATA AND METHOD

R/V MIRAI stationed at 138.5 degrees East and 2 degrees North from March 3 to 15, 2004 in the western equatorial Pacific Ocean. (Fig.1) During the research cruise we carried out in situ measurements of upward spectral radiance from sea surface using a spectral radiometer GER1500 with 512 bands ranging from 350 to 1050 nm and chlorophyll-a concentration synchronized with SeaWiFS and MODIS overpasses. Measurement times are 4 times a day (10, 11, 13, 14 hours (local time)). In order to estimate normalized water-leaving radiance (nLw) normalized water-leaving radiance model is used as follows[1)].

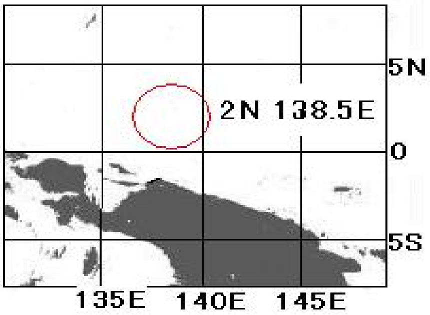

Fig. 1. R/V MR04-01 Stationary point within the circle. (Feb.22-Mar.22,2004)

$$nLw(\lambda) = R_L(\lambda)F_0(\lambda) \quad (1)$$

$$R_L(\lambda) = \frac{S_w(\lambda) - \rho(\theta)S_{sky}(\lambda)}{\pi S_G(\lambda)\rho_G(\theta,\lambda)} \quad (2)$$

$$S_{sky}(\lambda) = S_w(\lambda) * SR(\lambda) \quad (3)$$

$F_0(\lambda)$ is defined as an mean spectral solar irradiance, $S_w(\lambda)$, $S_{sky}(\lambda)$, $S_g(\lambda)$ are in situ spectral radiances from sea surface, sky and standard white board respectively. $\rho(\theta)$ and $\rho_G(\lambda)$ are Fresnel reflection coefficient and reflection coefficient of standard white board. $SR(\lambda)$ is the ratio between sky radiance and solar radiance. This ratio is defined based on upward spectral radiance from sea surface and the same radiance observed under shadowed sea surface, which is solely illuminated by sky radiance. Spectral sky radiance ratio is shown in Fig.2.

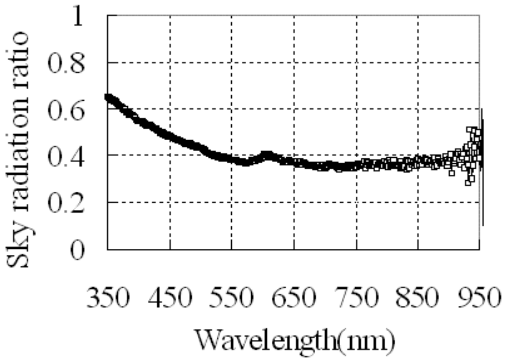

Fig.2 Spectral sky radiance ratio.

3. RESULTS AND DISCUSSION

Fig.3 shows the results of estimated nLw(λ) based on the nLw model above. Magnitude of nLw reaches maximum around 410 nm and shows minimum at the wavelength longer than 750 nm. Comparing with the nLw(λ) products derived from SeaWiFS and MODIS, the result of comparison is shown in Fig.4. Solid points are based on model-derived nLw and the ones derived from SeaWiFS and MODIS. White points are based on upward spectral radiance without using the nLw model[2)]. Model-derived nLw shows good agreement with SeaWiFS and MODIS-derived nLw.

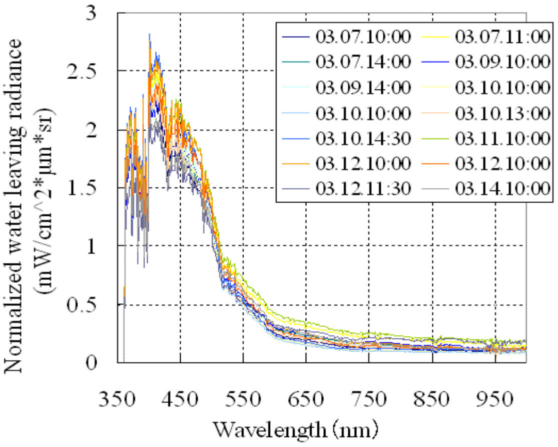

Fig. 3 Estimated normalized water-leaving radiance at the stationary point (Mar-7-14,2004).

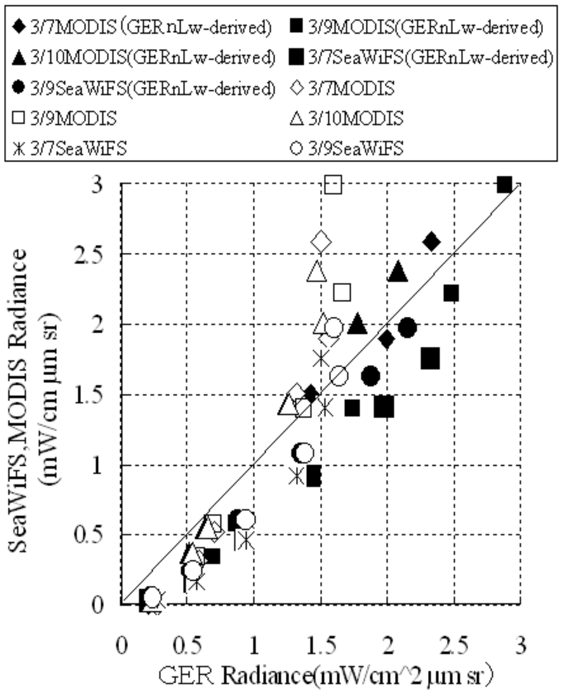

Fig. 4 Comparison between estimated normalized water-leaving radiance by GER-derived upwelling radiance and SeaWiFS and MODIS-derived normalized water-leaving radiance. (Solid points are based on model-derived nLw and the ones derived from SeaWiFS and MODIS. White points are based on upward spectral radiance without using the nLw model[2)].)

As far as the comparison of chlorophyll-a is concerned, the result of comparison between nLw-model-derived chlorophyll-a and chlorophyll-a without the nLw model is shown in Fig.5. Both concentrations are calculated based on OC4v4 algorithm[3)] which is the operational algorithm of SeaWiFS. OC4v4 algorithm is expressed as follows.

$$C=10.0\hat{}(0.366-3.067R_{4S}+1.930R^{2}_{4S}+0.649R^{3}_{4S}-1.532R^{4}_{4S}) \tag{4}$$

$$R_{4S}=\log_{10}(R^{443}{}_{555}>R^{490}{}_{555}>{}^{510}{}_{555}) \tag{5}$$

where C is chlorophyll-a concentration (mg/m^3), R_{4S} is defined as the logarithm of maximum ratio between radiances from two bands of SeaWiFS.

Chlorophyll-a derived from nLw model shows better agreement with the ones from SeaWiFS and MODIS (solid triangles and squares in Fig.5.) compared with the ones without using nLw model (cross marks).

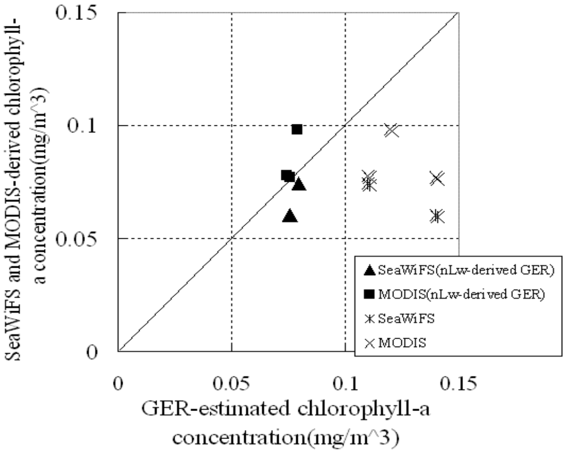

Fig. 5 Comparison between GER estimated chlorophyll-a concentration (solid triangles and squares: nLw model-derived chlorophyll-a, cross marks (x, ∗): chlorophyll-a without using nLw model) and SeaWiFS and MODIS-derived chlorophyll-a concentration

４. SUMMARY

By combining the normalized water-leaving radiance model with in situ spectral radiance observation utilizing the shadowed sea surface, we verified the normalized water-leaving radiance and chlorophyll-a products derived from SeaWiFS and MODIS.

It was found that SeaWiFS and MODIS-derived normalized water-leaving radiances and chlorophyll-a concentrations show good agreements with corresponding parameters derived from the normalized water-leaving radiance model with in situ spectral radiance observation.

ACKNOWLEDGEMENTS

We acknowledge the captain and crews of R/V MIRAI during the research cruise of MR04-01 (Feb.22 to Mar.22, 2004). We also acknowledge Marine Work Japan Inc. for their analytical skill of chlorophyll-a measurement.

REFERENCES

1) James L. Mueller, Roswell W .Austin : Ocean Optics Protocols for SeaWiFS Validation, Revision1, NASA Technical memorandum 104566, Vol. 25, pp45-46, pp53-54,1995.

2) Anna Sasaki and Katsutoshi Kozai : Validation of SeaWiFS data based on in situ spectral reflectance measurement of sea surface in the western equatorial Pacific Ocean, Proceedings of 36th Annual meeting of the Remote Sensing Society of Japan, pp.19-20, 2004.

3) O'Reilly, J.E., S. Maritorena, B.G., Mitchell, D.A., Siegel, K.L. Carder, S.A. Garver, M. Kahnu and C. McClain : Ocean color chlorophyll algorithms for SeaWiFS, J. Geophys. Res., vol. 103, No. C11, pp.24937-24953, 1998.

Uncertainty in cloud optical thickness estimation by GMS-5 S-VISSR algorithm and influence on the estimated radiative budget

H. Takenaka[1), T. Takamura[2), I. Okada[2)3), T. Y. Nakajima[2)4), J. R. Dim[2)

1) Graduate School of Science and Technology, Chiba University
2) Center for Environmental Remote Sensing, Chiba University
3) Japan Science and Technology Agency
4) Japan Aerospace Exploration Agency

Abstract

APEX (Asian Atmospheric Particle Environment Change Experiment) project aimed at performing simultaneous analysis of cloud, aerosol and atmospheric radiation by various observation methods(satellite, airplane, ground base) in East China sea. Comparison of the optical thickness from GMS-5 S-VISSR with those retrieved from Terra-MODIS shows some remarkable differences. Causes of such errors were investigated. One of them was a scientific problem deriving from the difference in cloud droplet effective radius. However this can not explain by itself all the error encountered in the estimation of the cloud optical thickness. The other cause of error checked was the quantization noise. And, this happens to be an engineering problem. In the error evaluation of the algorithm used, we realized that the quantization noise induced much of the optical thickness difference. Using the radiative transfer code "RSTAR5b" we examined the influence of this error in the estimation of the radiative budget.

1.Introduction

GMS-5 is a geostationary satellite enabling observations every hour over the equative at a latitude of 140°E. By using these observation data, high temporal resolution is attained in the estimation of Earth's radiative budget. Based on the GMS-5 S-VISSR (Stretched- Visible and Infrared Spin-Scan Radiometer) visible channel data and assuming plane parallel cloud, the radiative transfer code "RSTAR4b" [Nakajima T. and M. Tanaka, 1986,1988] was used

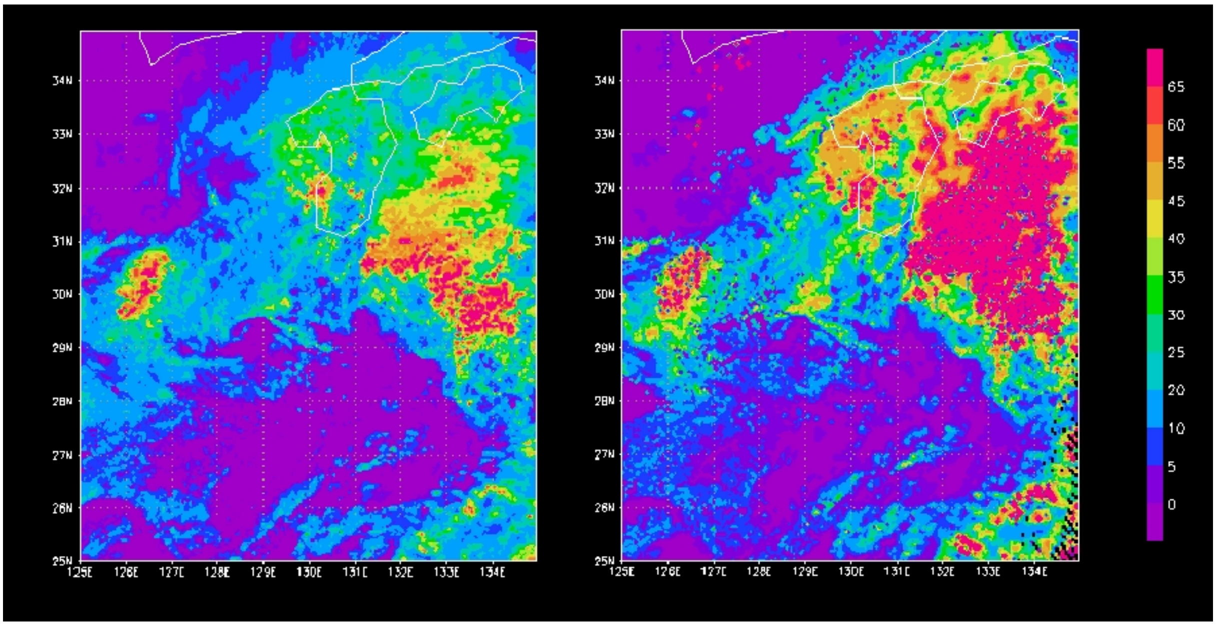

Fig. 1 : Cloud optical thickness estimation by GMS-5 S-VISSR (Left) and MODIS (Right) on April 9, 2001 in the study area (25°N—35°N and 125°E—135°E).

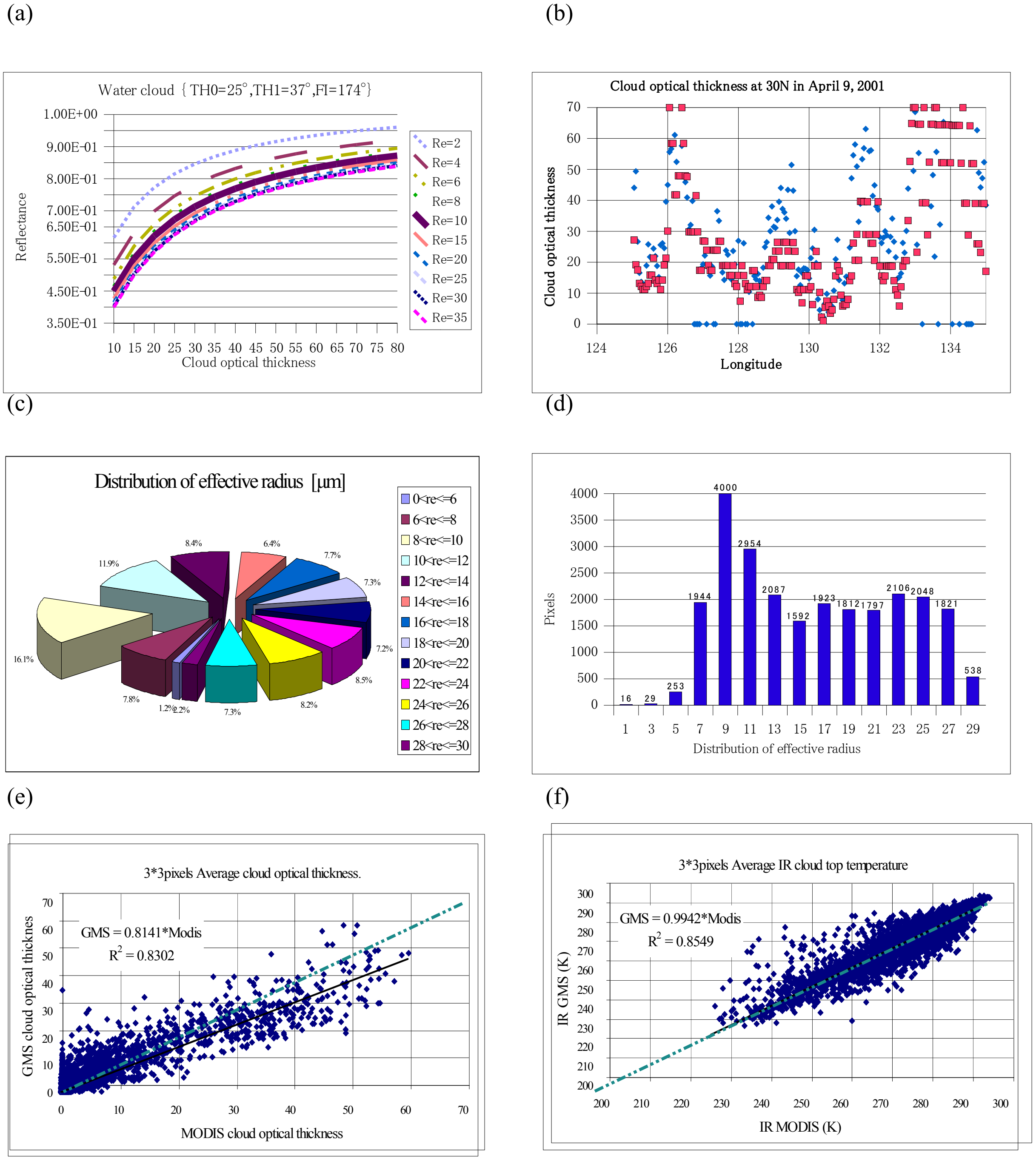

Fig. 2 : (a) Estimation curve of the cloud optical thickness with reflectance at GMS-5 S-VISSR ch1. The deep purple solid line shows the estimation from the algorithm used, with the water cloud droplet effective radius of 10μm. Assuming a solar zenith angle TH0=25 [degrees] , satellite zenith angle TH1=37 [degrees] and azimuthal angle FI=174 [degrees]. These angle values were determined from average data of April 9, 2001 (25°N-35°N and 125°E-135°E). (b) Cloud optical thickness at 30°N latitude of Fig. 1 (with intervals of 0.05°). Blue points (diamond) represent the cloud optical thickness from MODIS (0.05-degree data averaged from original 0.01-degree data), and red points (box) are those from GMS-5 S-VISSR. (c) Cloud droplet effective radius distribution (in %) from MODIS on April 9, 2001. The picked on the left of figure contains among other the10 [μm] effective radius. (d) Same as (c) but with total number of pixels per range. (e) Comparison of 3x3 pixels-average cloud optical thickness between MODIS and GMS-5 S-VISSR. (f) Comparison of corresponding to brightness temperature to Fig. 2e .

for retrieval of cloud optical thickness by the "solar reflection method" [T. Y. Nakajima, 2002] and the estimation of the radiative budget per hour. Analysis was conducted as in the APEX project where comparison of various observation data are made. Comparison of the retrieved optical thickness from GMS-5 S-VISSR with those from Terra-MODIS (Moderate Resolution Imaging Spectroradiometer) shows some remarkable differences. It seems that GMS-5 S-VISSR algorithm underestimates cloud optical thickness in certain conditions. Figure 1 is a comparison of the optical thickness data from MODIS and those from GMS-5 in the East Asia (25°N—35°N and 125°E—135°E) on April 9, 2001. Although distinction of cloud and the whole pattern look alike, the difference in absolute value can be noticed in the layers where optical thickness is high, while small optical thickness data show better correlation. MODIS data have a higher distribution of high optical thickness areas than GMS-5 S-VISSR data. The absolute value is fatally different.

2.Model analysis

There seems to be several reasons of difference of the cloud optical thickness between both satellite sensors. One of them was a scientific problem originating in the difference of an effective radius of cloud. Since GMS-5 S-VISSR does not have a water-absorbing channel (3.7micron), no effective radius can be retrieved from observation. For this reason, the cloud droplet effective radius has been assumed as 10μm (based on ISCCP : International Satellite Cloud Climatology Project) [Rossow et al., 1989]. Figure 2a is the estimation curve of cloud optical thickness with observed reflectance. The solid line represents a curve for GMS-5 S-VISSR estimation. Various studies have shown the dependence of reflectance on the cloud droplet effective radius; reflectance is smaller when the effective radius becomes larger, and it increases when the effective radius become smaller. This shows that even for the same reflectance, the optical thickness may have a different. Figure 2b presents the optical thickness from MODIS and GMS-5 S-VISSR at 30°N latitude in Fig. 1. The difference between MODIS and GMS-5 S-VISSR appears remarkably well. Although a clear judgment is difficult around of 126°E and in the area from 133°E to 134°E (GMS-5 S-VISSR shows exceeding value), it appears generally that GMS-5 S-VISSR data are underestimated in comparison to the MODIS data around of 129°E and 131°E. Figure 2c is the effective radius distribution from MODIS data (25°N-35°N and 125°E-135°E) and Figure 2d is the number of pixels on April 9, 2001. Since the effective radius can not be retrieved from S-VISSR (for the reason given earlier), we analyzed only MODIS data. This analysis shows that the effective radius mainly varies from 7 to 28 [μm], with the peak is at $8<re<=10$ [μm] (frequency of occurrence around 16.1%). The second highest frequency 11.9% corresponds to the range of $10<re<=12$ [μm]. The remaining frequencies are mostly around 7~8%. Though the near 10μm range has the highest absolute value, and looking at the whole distribution, the contribution is relatively small. There are indeed variations in the cloud droplet effective radius and, the 10μm fixed effective radius used for the S-VISSR retrieval of optical thickness can give some errors. The fixed value, may result in an uncertainty in the estimation of the cloud optical thickness from the GMS-5 S-VISSR algorithm. Figure 2e shows 3x3pixels-average cloud optical thickness comparison of MODIS and GMS-5 S-VISSR. The regression line is inclined toward MODIS side, which means that GMS-5 S-VISSR values are lower than MODIS data. Considering that the different effective radius values noticed on Fig. 2c, the optical thickness differences may be related to the variation of the effective radius. Figure 2f is a comparison of IR data 3x3pixels-average between GMS-5 S-VISSR and MODIS: the regression line is well in agreement; this means that the same clouds are observed. Furthermore and although the difference of the reflectance of Ice cloud and Water cloud was also considered without the effect of the ice non-spherical shape, the influence was small enough.

3.Consideration of Quantization

We found a problem in work to examine the look-up table carefully. It has the possibility of losing important information by quantization of the sensor installed in satellite. Furthermore, test have been performed to check the consistency of the algorithm. Chart 1 is the flow chart of “Reversible conversion test”. The problem is solved by assuming actual clouds and conducting comparison verifications with the output of the algorithm. This includes quantization. Figure 3a is the result of this “Reversible conversion test”. Red points (diamond) represents the 35μm effective radius and, the blue points (box) is the 2μm effective radius. The influence of quantization is shown by the stair-like shapes on the figure and, the domain, which cannot be distinguished due to large errors occurrences is visible as well. Figure 3b is the quantized reflectance (blue box points) and the relative error % (red diamond points). Although the quantization made so that the changes shows a smooth trend, the red line on this Figure shows that, the error is big. Figure 3c is the absolute difference between the assumed true cloud optical thickness and the algorithm output cloud optical thickness. It appears that the error due to assumption of an effective radius is increased by the quantization noise in some cases. Based on Fig. 2d, it is thought that the weighting towards the red points (diamond) side, caused by the drift of the effective radius towards larger values than 10μm, and this actually appears in regression line of Fig. 2e. These two error-elements overlap and cause the error in the optical thickness estimation of clouds. This error nonlinearly exceeds 30% in Fig. 3d. Although the important factor of error of the effective radius is essentially a physical matter, quantization noise is not consistent with physics. If this type of error appears nonlinear and shows a non-essentially physical trend, they will become a serious obstacle for the estimation algorithm of physical quantities.

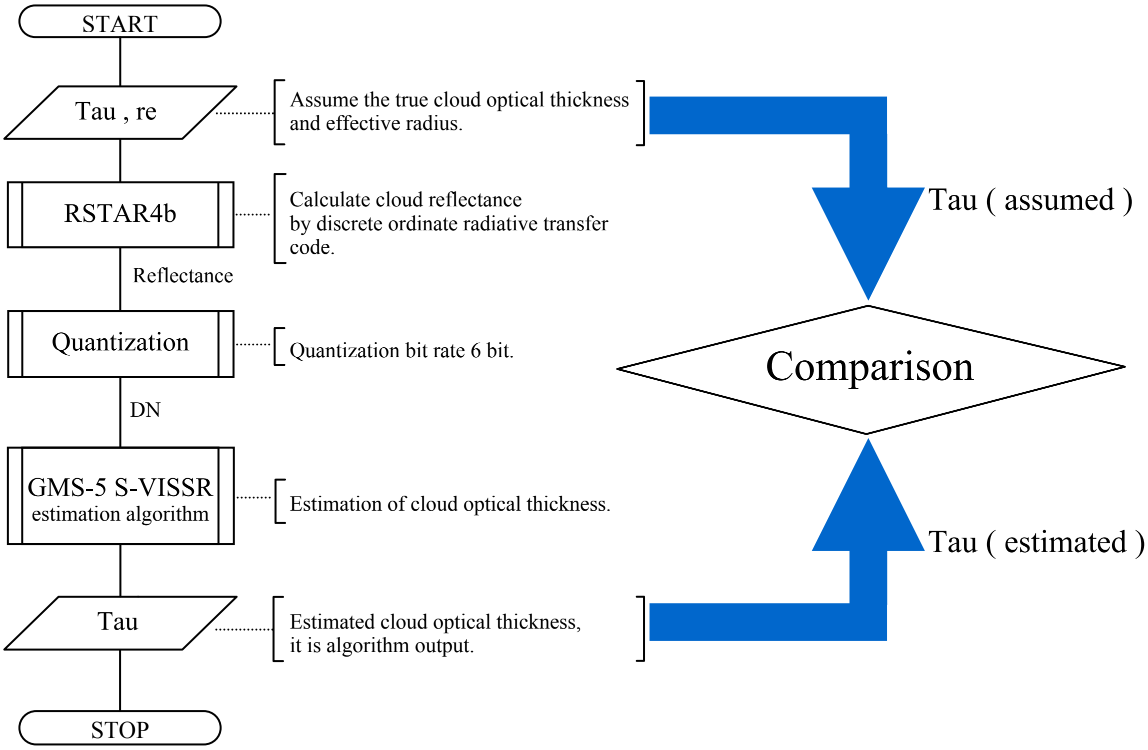

Chart.1 : The flow chart of the “Reversible conversion test”.

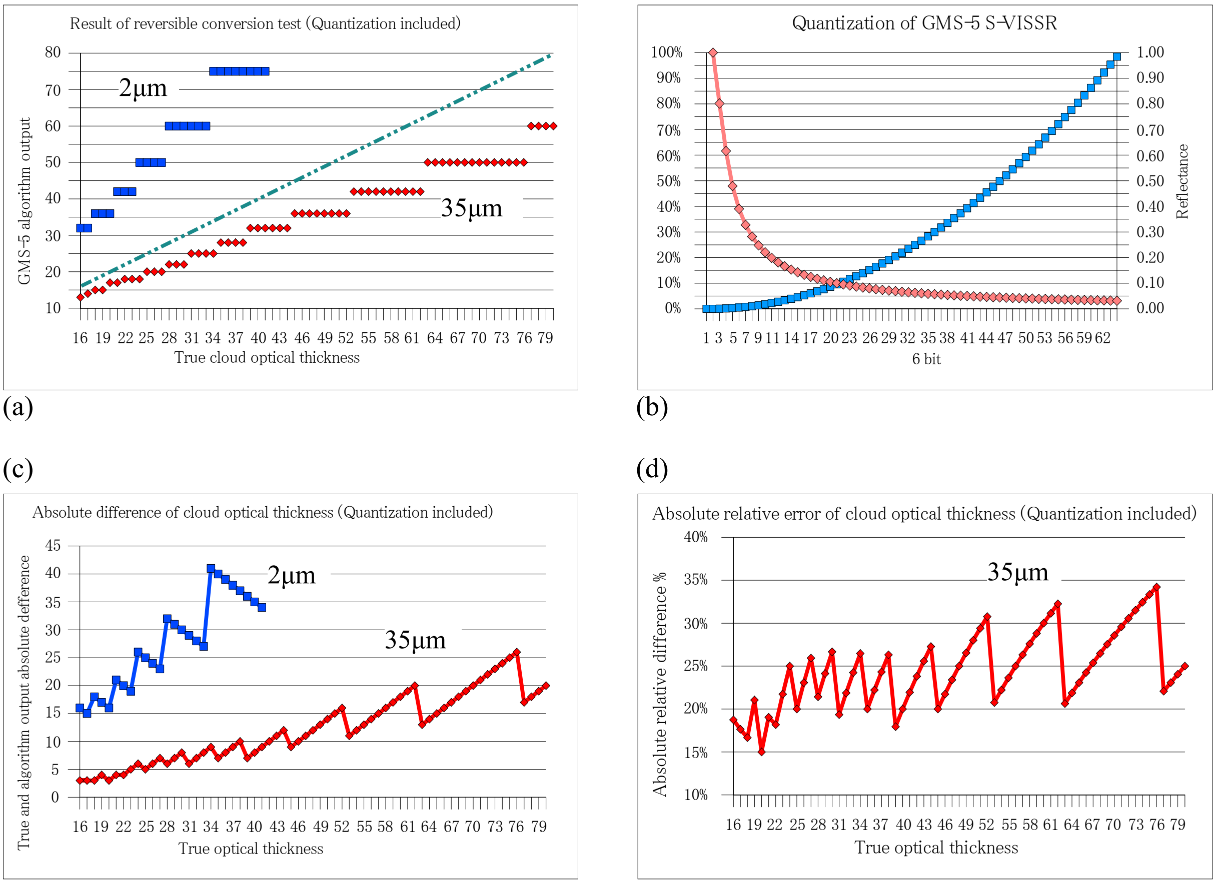

(a) (b)

(c) (d)

Fig. 3 : (a) Result of reversible conversion test on GMS-5 S-VISSR algorithm, including quantization noise. (b)Quantization of GMS-5 S-VISSR ch1: the Blue points (box) is the quantized reflectance, the red points (diamond) is the relative error of the reflectance. (c) Absolute difference of optical thickness between 10μm and 2μm than 35μm. (d) Absolute relative difference of cloud optical thickness at cloud droplet effective radius of 35μm including quantization noise on the worst case.

4.Influence on radiation budget

The cause of the differences became clear from the above-mentioned results. In this section, we investigate how much influence this error would have on the radiative budget. The radiative transfer code “RSTAR5b” was modified and used for calculation of radiative budget. Figure 4a is the estimated value of the downward shortwave flux at the surface, which includes each errors. When the cloud droplet effective radius is more than 10μm, radiative flux is overestimated, and vice versa. This is because, cloud optical thickness is overestimated when the effective radius is less than 10μm and underestimated when the radius is more than 10μm. The relative error on these conditions is set as on Fig. 4c. The proportion of the error increases with the cloud optical thickness, and this error may reach an inverse proportion for shortwave radiation at the surface. This error is nonlinear according to the quantization noise. The quantization noise making the error increase is well understandable. Fig. 4b is the estimated value of the upward shortwave flux at the TOA. If an effective radius of 35μm is assumed, the flux will be underestimated, and it is overestimated if a 2μm effective radius is assumed. Fig. 4d is the corresponding relative error. The error will decrease if the cloud optical thickness increases, this is because the error is relatively small compared to the increase of the reflectance of cloud. Fig. 4e is the albedo at the TOA, and Fig. 4f is the relative error. Since the downward shortwave flux at the TOA is fixed, this graph resembles the one of Fig.4d. And, the relative error of the energy absorbed by the Earth system is shown in Fig.5. The cloud optical thickness of 20 to 30 shows an error of 9% (overestimation).

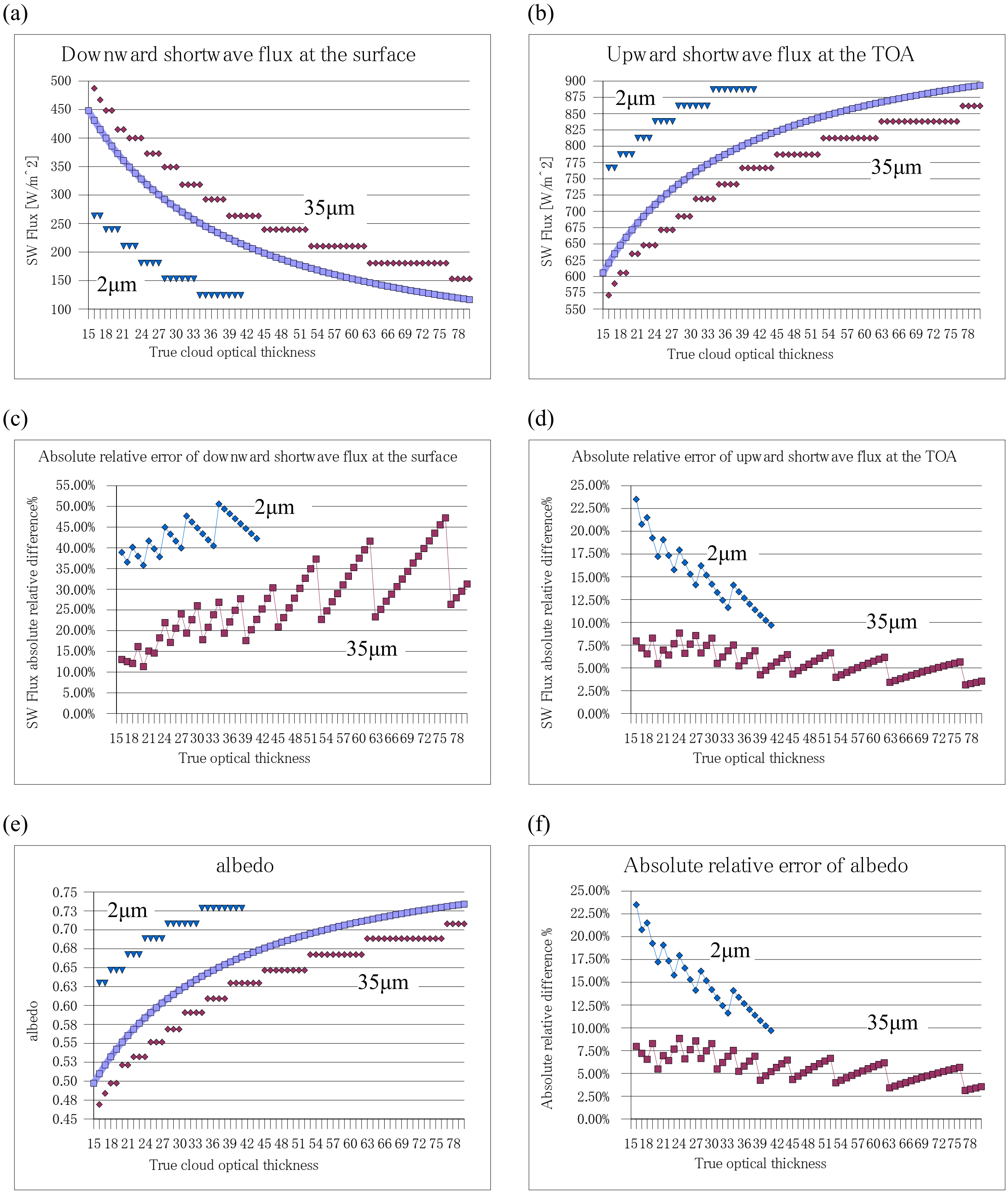

Fig. 4 : Error influence on the radiative budget. X axis is the assumed true optical thickness, Y axis corresponds to the radiative flux and albedo. The purple line is the estimation of the radiative budget by true cloud optical thickness. The red line includes errors by the 35μm effective radius, the blue line by the 2μm effective radius. These values were calculated by the radiative transfer code RSTAR5b, modified for short wave flux calculation. Calculation conditions are solar zenith angle = 25 degrees, an atmospheric model using US standard, surface albedo = 0.1 (assumed Lambert surface), and all clouds are assumed water cloud and

plane parallel. (a) The downward shortwave flux at the surface. (b) The upward shortwave flux at the TOA. (c) The downward shortwave flux absolute relative difference (%) at the surface. (d) The upward shortwave flux absolute relative difference (%) at the TOA. (e) The albedo from downward and upward shortwave flux at the TOA. (f) The albedo absolute relative difference (%) at the TOA.

5.Conclusion

When estimation and comparison of the cloud optical thickness are performed, the remarkable differences are noticed. The causes were investigated; one is an error by assumption of a fixed effective radius, the other is quantization noise. There is a possibility that a large difference is caused by them. These errors are nonlinear and exceed 30% according to the conditions of estimation of cloud optical thickness. The influence of these errors on the radiation budget was estimated. The both errors have some influence on the estimation of the radiation budget of the Earth.

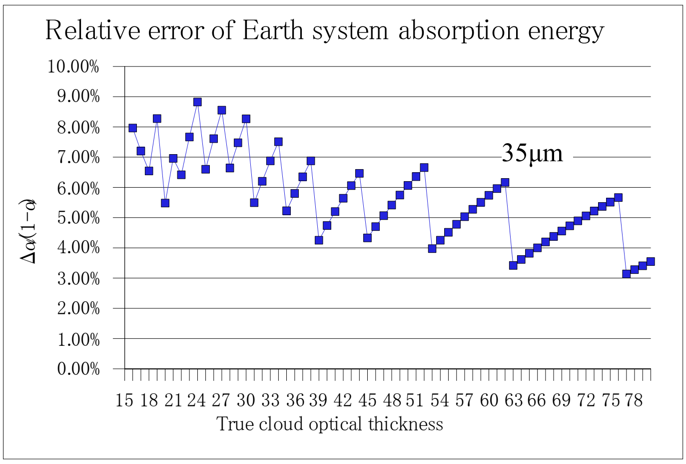

Fig. 5 : Earth system absorption energy relative error, including GMS-5 S-VISSR error due to differences in cloud droplet effective radius and quantization noise.

References

Nakajima, T. and M. Tanaka, 1986: Matrix formulations for the transfer of solar radiation in a plane-parallel scattering atmosphere, J. Quant. Spectrosc. Radiat. Transfer, 35.

Nakajima, T. and M. Tanaka, 1988: Algorithms for radiative intensity calculations in moderately thick atmospheres using a truncation approximation, J. Quant. Spectrosc. Radiat. Transfer, 40.

T. Y. Nakajima, 2002: Development of a comprehensive analysis system for satellite measurement of the cloud microphysical properties. EORC Bulletin Technical Report No.10.

Rossow, W.B., L. C. Garder, and A. A. Lacis, 1989: Global, seasonal cloud variations from satellite radiance measurements. Part I: sensitivity of analysis. J. Climate, 2.

Retrieval of aerosol optical properties over Chiba land area from Landsat/TM imagery

Part I: Determination of spatial distribution of aerosol optical thickness

Mitsuo Minomura, Yoshiyasu Todate, Hiroaki Kuze, Nobuo Takeuchi
Center for environmental remote sensing (CEReS), Chiba University,
1-33 Yayoi-cho, Inage-ku, Chiba 263-8522, Japan

Abstract:

Satellite remote sensing data provide information on two-dimensional distributions of both the surface albedo and optical thickness of the atmosphere. In this work, we report the method of separating the contributions of the surface albedo and aerosol optical thickness from Landsat-5 TM visible-band data taken over the Chiba urban area. We focus on the determination of surface albedo from the data observed on a relatively clear day. It is shown that when the aerosol optical thickness is small, the atmospheric correction is not greatly affected by the aerosol model employed. The resulting surface albedo distribution from the clear day, in turn, is used to determine the aerosol distribution from the turbid image in the same season.

keywords: Landsat TM, Atmospheric correction, Albedo, Aerosol model

1. Introduction

In the analysis of satellite remote sensing data, the atmospheric correction technique is useful to derive the accurate distribution of surface albedo values that are free from the “contamination” due to the atmospheric radiances [1-3]. From the viewpoint of the atmospheric studies, the precise knowledge of the surface albedo leads to the possibility of deriving the aerosol distribution from the satellite data. Over the ocean surfaces, the method has been applied to derive aerosol distributions [1]. Over the land surfaces, however, the application of this technique has been rather limited [2] because of the high variability of the surface albedo, in addition to the spatial variability in the aerosol properties.

In the present paper, we demonstrate that the separation of the surface and atmospheric (aerosol) contributions can be achieved by suitably choosing satellite datasets within a season. The test area is the Chiba area, inside the Tokyo metropolitan area along the east coast of the Tokyo Bay. The visible band images of Landsat-5/Thematic Mapper (TM) are analyzed by means of a fast atmospheric correction algorithm reported by Minomura et al. [3].

2. Theory

2-1. Relationship between surface albedo and optical thickness

The radiance observed by a satellite sensor is determined mainly by the surface albedo and atmospheric extinction. Both atmospheric molecules (Rayleigh scattering) and aerosol particles (Mie scattering) contribute to the extinction through the atmosphere. It is relatively easy to estimate the molecular contribution, and the temporal and spatial variability of the atmospheric extinction originates mostly from the aerosol effect. The aerosol optical thickness τ_a is one of the most effective parameters in the radiative transfer process.

The radiance L_{obs} observed by a satellite sensor is given as a digital number (*DN*), *e.g.* a value between 0 and 255 in the case of an 8-bit sensor. We can define L_{obs} as a function of the *DN*, which, in turn, is related to the target albedo ρ and the optical thickness τ_a:

$$L_{obs} = f(DN),\ DN = g(\rho\ ,\ \tau_a). \qquad (1)$$

Here the function f is determined from the sensor calibration, and the function g is given once the geometry of the satellite observation and the aerosol model are specified.

Figure 1 shows the relationship between ρ and τ_a calculated for Landsat-5/TM band 1. The geometry is for the image of Kanto area observed on January 14, 1999. The ρ-τ relationship is plotted for *DN* values of 50 and 60, the dominant range for band 1. This relationship has been calculated by the 6S code [4], employing three aerosol models (continental, maritime and urban) that are built in the code. From Fig. 1, it is clear that the result for the urban aerosol model is different from other two models. This is ascribable to the larger absorption coefficient incorporated in the urban model than in other models. For example, when the relative humidity is less than 70%, the single scattering albedo is 0.64 at 550 nm for the urban model, whereas it is about 0.9 for the continental and maritime models. Another important aspect found in Fig. 1 is that the difference among aerosol models appears in the region of large optical thickness. When τ_a is small, on the contrary, it is possible to retrieve the value of target albedo ρ that is more ore less independent of the aerosol model.

For the clear-sky case (no cloud), the main contribution to the aerosol optical thickness comes from the lower troposphere, especially from the boundary layer. Under such a condition, the assumption that a value of the optical thickness measured by a sun photometer (τ_{sp}) at a certain location within a satellite image represents the area is considered to be reasonable. This assumption is used here to derive the distribution of the surface albedo ρ. Hereafter this albedo distribution will be referred to as the "ρ map". In this manner, the process of the atmospheric correction is accomplished.

In the next step, this ρ map is used to evaluate the aerosol distribution from the satellite image observed on a relatively turbid day in the same season as the clear day. The functional relationship shown in Fig. 1 is used to obtain the value of τ_a from the known values of *DN* and ρ in this case. The resulting distribution of the aerosol optical thickness will be referred to as the "τ map".

2-2. Atmospheric correction

In the atmospheric correction of the clear-day image, the optical thickness is derived from the sun-photometer data (τ_{sp}) at the time of the Landsat-5 overpass. Figure 2 shows the *DN*-ρ transform function calculated by assuming three aerosol models (Continental, Maritime, and Urban) for TM band 1. The data were taken on January 14, 1999, when the aerosol optical thickness τ_{sp} was relatively small ($\tau_{sp}=0.1$ at 550 nm). The histograms of the raw *DN* and surface albedo ρ are also shown in Fig.2. It is seen that the difference in the aerosol model does not yield noticeable change in the *DN*-ρ relationship. Thus, the surface albedo ρ derived from this method is virtually independent of the assumed aerosol model.

The precision of the albedo ρ as determined by the satellite sensors is around 10^{-3} for the 8-bit Landsat-5/TM sensor. The resolution is different for other bands, due to the inherent gain of the sensor. In general, the *DN*-ρ relationship changes with the wavelength. At shorter wavelength, a quadratic relationship holds between *DN* and ρ when ρ is small. At longer wavelength, however, a linear relationship is seen between these parameters. Since the resolution of band 2 is insufficient to retrieve the optical thickness accurately, here the result is shown only for band 1. The ρ map is obtained from the image on a relatively clear day (January 14, 1999). This ρ map is used as a reference to retrieve the optical thickness distribution in the same season (see below).

2-3. Aerosol optical thickness (τ_a map)

The distribution of aerosol optical thickness (τ_a map) is obtained as follows. For each band and aerosol model, the (ρ,τ_a) pair is calculated for each *DN* and stored in a form of a lookup table (LUT). The optical thickness τ_a can be specified by the optical thickness at 550 nm (τ_{550}), since the aerosol model dictates the dependence on the wavelength. This simulation is conducted by the 6S code, the range of τ_a being varied from 0 to 1 with a step of 0.01. In the application of the LUT, an interpolation with a resolution of 0.001 is undertaken for τ_a. Figure 3 shows the functional relationship in the LUT for the continental aerosol model calculated for the band 1 data on December 13, 1998. This image was chosen as an example with a relatively large value of the aerosol optical thickness ($\tau_{sp}= 0.3$). For each pixel, we assume the albedo value given in the ρ map obtained from the clear-day image: thus, the aerosol optical thickness for that pixel can be determined from the pixel *DN* value using the LUT for each aerosol model. As also inferred from Fig. 3, the accuracy of τ_a can be estimated from the accuracy of ρ.

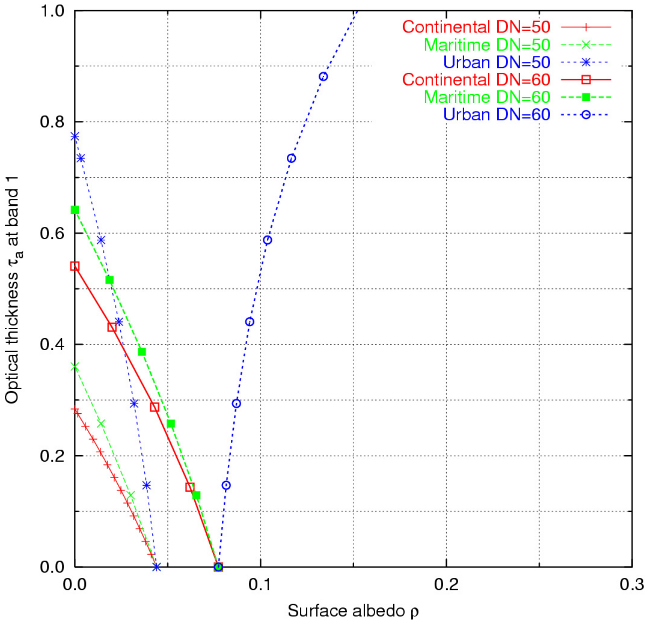

Fig. 1. The ρ-τ_a relationship for three aerosol models calculated for Landsat-5/TM band 1 image on January 14, 1999. Solid line is for Continental, dashed line for Maritime, and dotted line for Urban aerosol model. The curves are calculated for DN=50 (thin lines) and 60 (thick lines) which define the dominant DN range in the band 1 image. Urban aerosol model is characterized by a small single scattering albedo (strong absorption). When τ_a is small, the dependence on the aerosol model is insignificant.

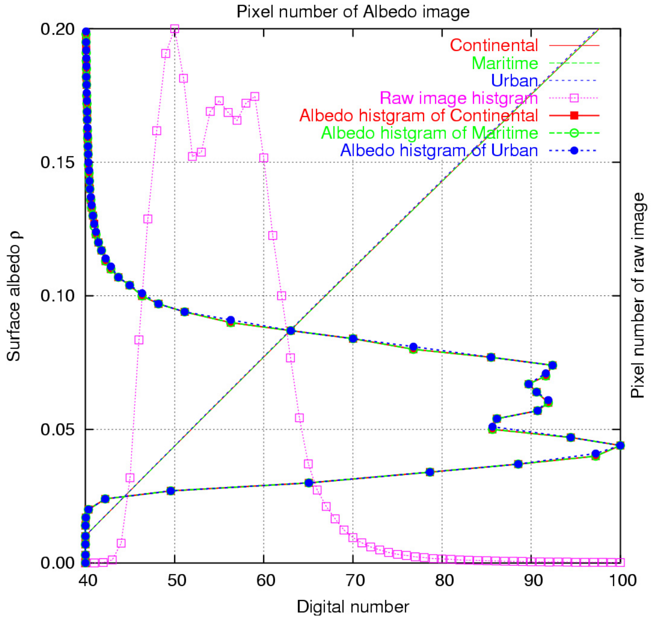

Fig. 2. The DN-ρ transformation curve for each aerosol model for a particular value of τ_a as measured by the sun photometer (τ_a=t_{sp}). Histograms of the band-1 image are shown for both DN and ρ. When the value of τ_a is small, a unique value of the surface albedo ρ can be determined regardless of the choice of the aerosol model.

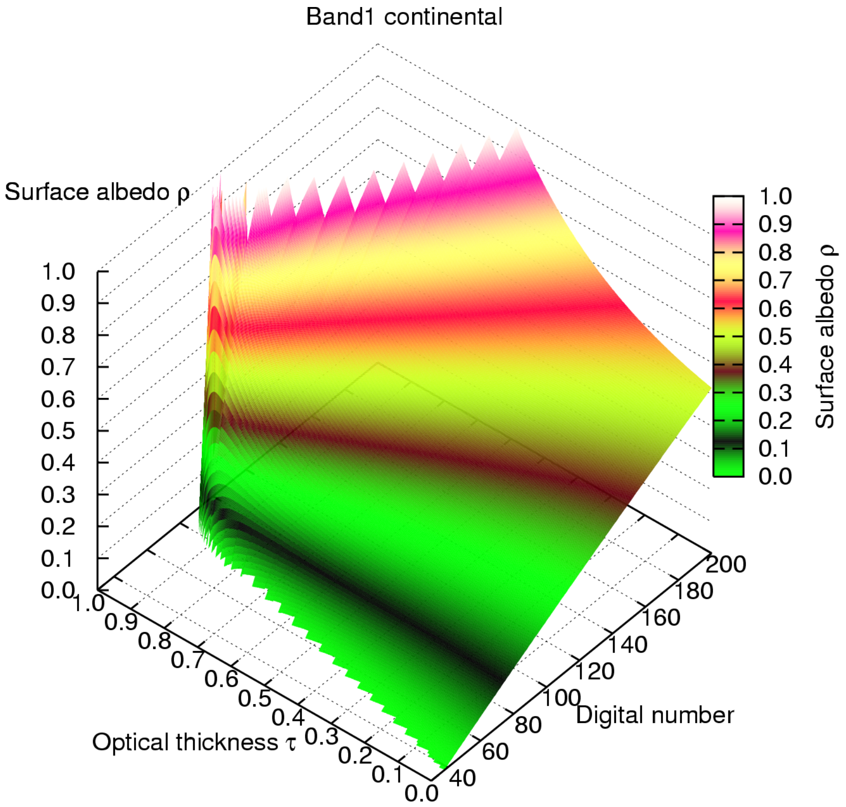

Fig. 3. The functional relationship among DN, ρ, and τ_a as calculated in a form of the lookup table (LUT). The curve is for the Continental aerosol model for the band-1 image observed on December 13, 1998.

3. Results and discussion

3.1 TM data and optical thickness

A target area chosen for the present study is a sub-scene of the Landsat-5/TM image (Path: 107, Row: 35), an image with 2001x2001 pixels centered at Chiba University (about 30 km southeast of Tokyo). The atmospheric correction is applied to a pair of datasets in the same season. First dataset is the one observed on January 14, 1999 (clear case). The correction of this dataset is used to obtain the ρ map (reference albedo map) of the winter season in the area. The second dataset obtained on December 13, 1998 (relatively turbid case) is used to derive the distribution of the optical thickness τ_a (τ_a map). For both cases, the values of aerosol optical thickness observed by the sun-photometer τ_{sp} are shown in Table 1 for band 1-4.

Table 1. Aerosol optical thickness τ_{sp} observed by the sun-photometer at 9:50 JST on each day. The values of τ_{sp} on January 14, 1999 (clear day) are smaller than those on December 13, 1998 (turbid day).

Date	Band 1	Band 2	Band 3	Band 4
Dec.13, 1998	0.294	0.241	0.192	0.140
Jan. 14, 1999	0.114	0.099	0.085	0.068

3.2 Albedo distribution (ρ map)

The ρ map (reference albedo) is derived from the data on January 14,1999. It is assumed that the values of τ_{sp} listed in Table 1 represent typical values in the TM scene. As seen from Fig. 2, more or less similar values of the surface albedo ρ can be obtained regardless of the type of the aerosol model assumed in the atmospheric correction process.

The ρ map obtained for band 1 is shows in Fig. 4 (the corresponding histogram of ρ has already been illustrated in Fig. 2). In this band, the dominant range of ρ is between 0.02 and 0.12, and these small values are mainly located in both the sea area in Tokyo Bay and inland. Pixels with high ρ values surround the Tokyo Bay, including the artificial island (named Sea Firefly) in the east side of the bay. A region with high ρ is also found in the sea area, presumably indicating the presence of haze. In order to avoid such an effect of local weather conditions, it is desirable to employ a number of images obtained on different days to construct the ρ map.

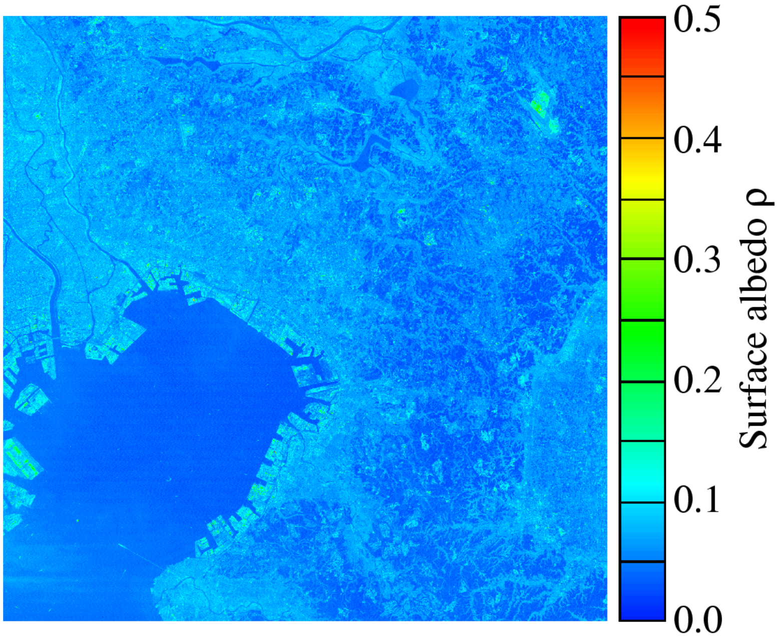

Fig. 4. Surface albedo map (ρ map) obtained from the atmospheric correction of the TM band-1 image observed on January 14,1999.

3.3 Retrieval of τ_a map

The aerosol distribution map (τ_a map) is constructed from the image observed on December 13, 1998. The aerosol models employed for this study are the continental and maritime models. Since the relationship among the parameters (Fig. 3) varies according to the model, the value of τ_a changes even if the same pair of the input parameter (*DN*, ρ) is used. The result is shown in Fig. 5, in which the value of τ_a is mapped in a range of 0 and 1: the region with $\tau_a>1.0$ is included in the region with $\tau_a=1$.

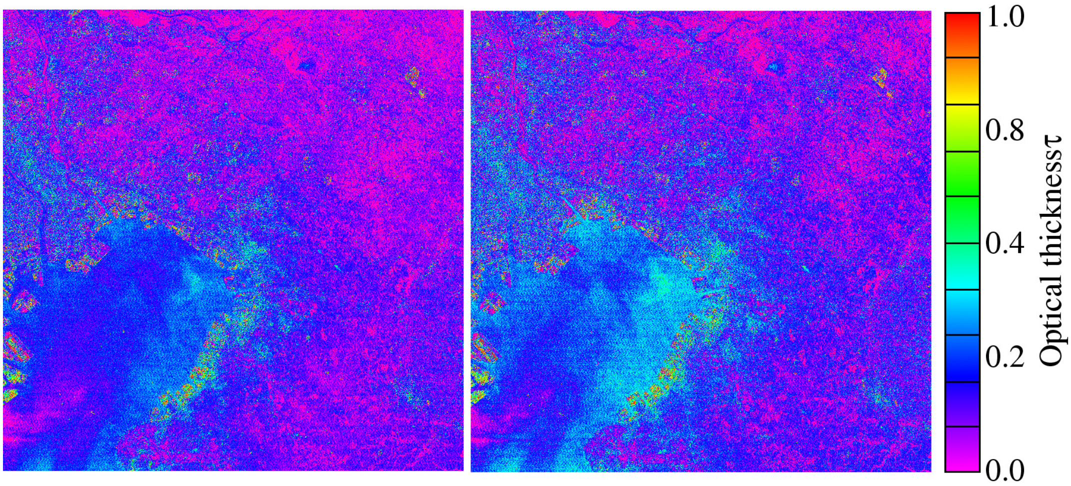

Continental

Maritime

Fig. 5. Aerosol optical-thickness map (τ_a map) from the TM band-1 image on December 13, 1998.

The optical thickness over the most part of the sea area in the Tokyo Bay is found to be 0.3 or smaller. The result over the sea area is of course not free from the effect of the wind, since the albedo is dependent on the wind speed. The optical thickness is somewhat larger along the seashore. The value of τ_a is under-estimated due to the presence of haze in the lower left part of Fig. 5. On the artificial island, we obtain $\tau_a > 1$ because of large ρ. High ρ values are also found in the urban area (near the center in Fig. 5) for both aerosol models. The distribution, however, is not necessarily correlated with the ρ map. In the vegetation areas inland, aerosol loading is relatively small, though the albedo values are similar to those in the sea region. It is possible that the aerosol model may change locally. During the winter season, the northwest wind prevails due to the pressure pattern (high in west ad low in east), leading to the relative dominance of the inland (polluted) aerosols rather than the maritime aerosols.

Figure 6 shows the histograms of the τ_a distribution for band 1 and band 2. Aerosol models are continental and maritime, and the resolution of τ_a is 0.01 in the simulation. The distribution turns out to be more compact for the continental model than for the maritime model, and sparser for band 2 than for band 1. This latter feature results from the higher gain in band 2, indicating the sensor gain is also important for the retrieval of τ_a.

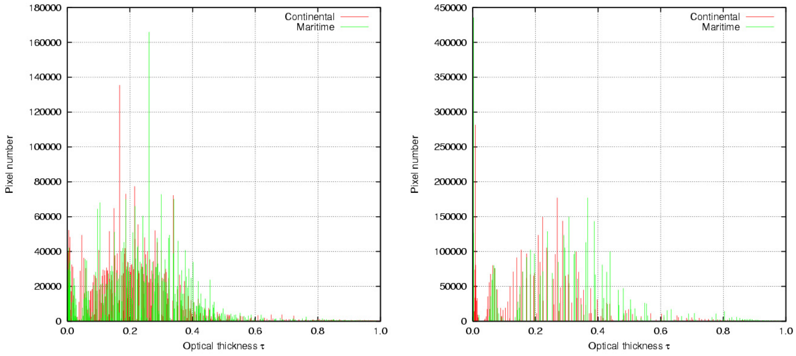

Band 1

Band 2

Fig. 6. Histograms of the τ_a distribution for TM band 1 and band 2.

4. Conclusions

We have discussed the derivation of the ground albedo map and the aerosol optical-thickness map from Landsat/TM data. In the determination of the ρ map (i.e. atmospheric correction), the dependence on the aerosol model is small when the optical thickness is small. This indicates that a reasonable "reference albedo map" can be retrieved using the satellite image observed on a relatively clear day. In the study of the τ_a map, on the other hand, the results are different for different aerosol models. Generally, the value of τ_a is smaller for the continental model than for the maritime model. High τ_a values are observed for the region with high albedo values. Finally, the result of this paper is developed in the Part II of this series paper [5] to further incorporate the study of aerosol size distribution from satellite data.

References

1) L. Stowe, A. Ignatov, R. Shing, Development, validation, and potential enhancements to the second-generation operational aerosol product at the National Environmental Satellite, Data and Information Service of the NOAA, J. Geophys. Res. 102, 16923-16934 (1997).

2) L.A. Remer, D. Tanre, Y. J. Kaufman, C. Ichoku, S. Mattoo, R. Levy, D.A. Chu, B. Holben, O. Dubovik, A. Smirnov, J.V. Martins, R.-R. Li, Z. Ahmad, Validation of MODIS aerosol retrieval over ocean, Geophys. Res. Lett.29(12), 1618 MOD3 1-4(2002)

3) M. Minomura, H. Kuze, N. Takeuchi, Atmospheric correction of visible and near-infrared satellite data using radiance components: an improved treatment of adjacency effect, J. Rem. Sen. Soc. Jpn., 21(3) 260-271 (2001)

4) E.F. Vermote, D. Tanre, J. L. Deuze, M. Herman, J. J. Mocrette, Second simulation of the satellite signal in the solar spectrum, 6S: An overview, IEEE Trans. Geosci. Remote Sensing 35 (3), 657-686 (1997).

5) K. Asakuma, M. Minomura, H. Kuze, N. Takeuchi, Retrieval of aerosol optical properties over Chiba land area from Landsat/TM imagery- Part II: Determination of aerosol size distribution - (this volume)

Characters of marine atmospheric boundary layer structure and aerosol profile observed by HSRL

Zhi-shen Liu   Zhao-ai Yan   Bing-yi Liu   Zhao-bin Sun

Ocean Remote Sensing Laboratory of Ministry of Education,
Ocean University of China, Qingdao, China

Abstract: This paper briefly discusses a YAG high spectral resolution lidar (HSRL) system developed by the Ocean Remote Sensing Laboratory of the Ministry of Education of China, Ocean University of China (OUC). In this system, iodine vapor filter was used to reject the returning signal of aerosol. We got backscattering ratio using HSRL and the result indicated that the correlation index of backscattering ratio of aerosol and the total returning signal is about 0.8. We also developed a new method to measure backscattering ratio using ordinary aerosol lidar. We compared two different methods to measure the altitude of boundary layer, and the validation experiments showed that the deviation is about 0.13km.

Key words: atmospheric aerosol; High Spectral Resolution Lidar (HSRL); iodine filter; backscattering ratio

1、 Introduction

Research on atmospheric aerosols have attracted extensive attention due to its role in human activities, climate change and biochemical circulation. Aerosol originated from atmospheric pollution is one of the most important factors in atmospheric pollution monitoring. Atmospheric aerosol has a great influence on the performance of visible remote sensing sensors and electro-optical system. Few data are available about the aerosol characteristics over the Eastern China Seas, where a large amount of dusts, which originate from the loess plateau exist in the atmosphere, thus making its distribution very complicated.

Atmospheric aerosols vary with time, location and altitude frequently. The components of aerosols, which make it difficult to measure their refractive index and extinction properties, are also very complicated.

The progress in modern lidar technology provides an effective means of measuring aerosols. The first attempt at detecting aerosols with lidar was initiated by Fiocco *et al.*, and many other measurements have been carried out since then. These measurements include Mie scattering lidar, Rayleigh-Mie lidar, differential absorption lidar (DIAL) and multiple-wavelength lidar. Sasano used DIAL technique to determine aerosol and molecular distribution, while She *et al* proposed to measure the vertical profiles of aerosol and atmospheric properties using the high spectral resolution Rayleigh-Mie lidar. They used two barium atomic filters to measure atmospheric temperature, density and aerosol scattering parameters in their system. Fischer used two

Fabry-Parot interferometers to detect the vertical distribution of winds and aerosols. Another new lidar technique for measuring aerosols is described in the following passages. This technique measures the Rayleigh scattering component of atmospheric molecules directly, where iodine filter was used to block the scattering component of aerosols to extract the contribution of Rayleigh component. Then scattering ratio measured by lidar was used to compute aerosol contribution. This kind of high spectral resolution method has potential application in the detection of aerosols in both troposphere and stratosphere, where aerosols are rare. We have built a YAG high spectral resolution lidar (HSRL) and detected atmospheric aerosols profile successfully.

2、Experimental setup and methodology

It is well known that Rayleigh scattering of air molecules, mainly due to Doppler broadening, yields a spectrum in the visible wavelength spreading over about 2.7GHz width at temperatures near 300K.The width of aerosol spectrum is confined to a region below 100MHz.The back scattering signals measured with lidar are composed of the contributions from both aerosol and molecules. At the marine boundary layer, the aerosol scattering signal is usually several orders of magnitude higher than molecular scattering. H Shimizu *et al* gave a typical sketch of atmospheric scattering spectrum and the typical variation of aerosol and molecular scattering with altitude was shown by McCormic.

To detect aerosol, it is necessary to separate the aerosol scattering and molecular scattering. Previously, measurement of atmospheric parameters (such as atmospheric density for different altitudes) and Rayleigh scattering theory were used for directly computing the contribution of molecular scattering, however, these theoretically calculated values have significant error due to the influence of many other parameters.

At present, high spectral resolution Fabry-Perot interferometers are used in HSRL lidar systems. But F-P etalon is very expensive, and it has such disadvantages as narrow field of view and low receiving efficiency, *etc*. At the beginning of the 1990s, a novel atomic or molecular absorption filter with high spectral resolution was developed. There are a number of advantages of molecular filters, including ultra-high Q value (10^5~10^6), narrow bandwidth (0.001nm), more-stable transmission characteristics, a much wider field of view (180°), and an ease of optical alignment. In addition, perhaps most important for the molecular filter method is its excellent ability to reject aerosol scattering. When operated at a frequency at the center of the absorption notch, the aerosol signal may be attenuated by better than 70 dB, allowing the aerosol scattering ratio to be measured. The excellent aerosol-rejection capability and the ease of optical alignment of molecular filter had been field tested, and the Wisconsin group replaced Fabry–Perot etalons with an iodine vapor filter in their lidar for the measurement of the aerosol-scattering ratio. Iodine molecular filter, which can work at low temperature and has several absorption lines near the output wavelength of double-frequency Nd:YAG laser (532nm), can serve as a high spectral resolution filter to take the place of Fabry-Perot interferometer . Iodine filters are also used in our experimental system as shown in Fig.1.

The schematic diagram for lidar transmitter, receiver, and frequency control is shown in Fig. 1.The master of the system is the two-wavelength diode pumped cw single-mode tunable Nd: YAG seed laser. The fundamental output at 1064 nm is used to seed a Continuum Powerlite 7000 Nd: YAG pulsed laser, as shown in the upper part of Fig. 1.The 532-nm output of the seed laser is sent to iodine filter cell 1,shown in the lower part of Fig.1, to control and lock the seed laser frequency.

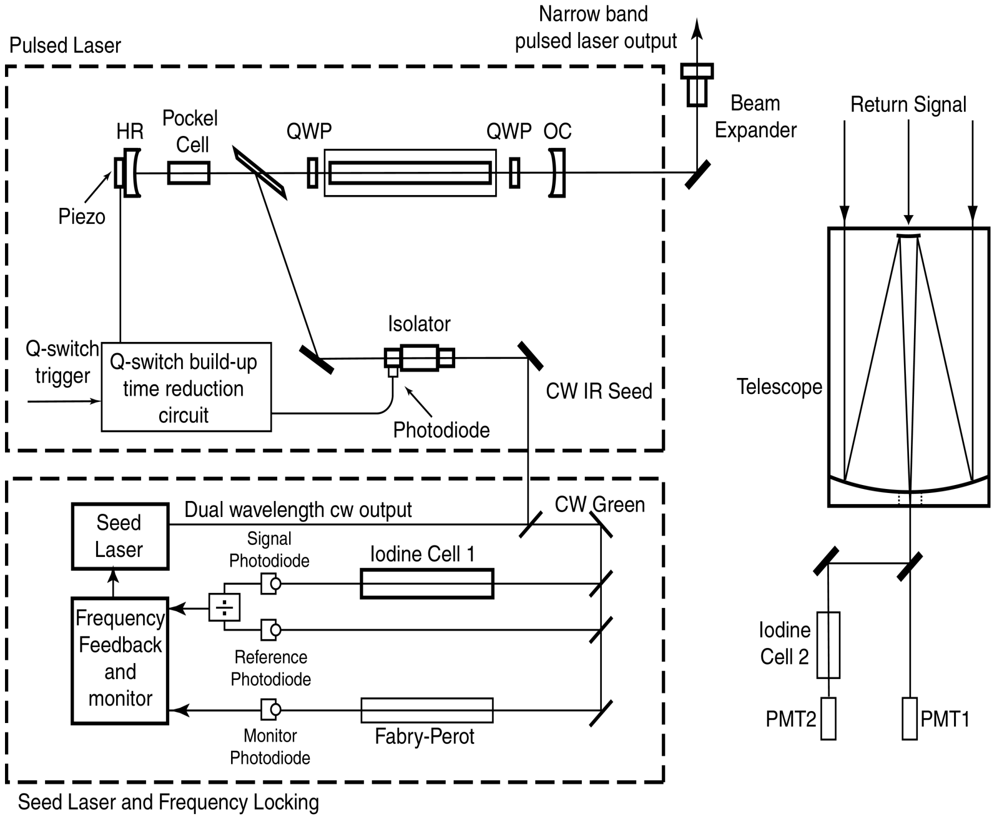

Fig. 1. Optical Diagram for injection-seeded Q-switched pulsed Nd:YAG laser transmitter on the left panels. The lidar receiver is shown on the right, where the iodine cell 2 is the frequency discriminator.

The received backscattered light is collected by a Cassegrain telescope with 300-mm aperture, and then passes through a temperature-controlled narrowband Daystar Corporation interference filter, bandwidth 0.15 nm, peak transmission 35.06%. As shown in the right of Fig. 1, the collected light is split into two channels; approximately 30% of it is detected directly by a photomultiplier in the reference channel, and the remaining light is passed through iodine filter cell 2 used for removing the aerosol component from the total backscattering signals and then detected by a second photomultiplier in the measurement channel. CR105 photomultipliers with gating control are used, and the signals from the two channels are digitalized by a dual channel 60-MHz, 14-bit analog-to-digital converter. Absorption line No. 1109 of the iodine is selected for our lidar system. Under the operating conditions, its normalized transmission function is shown in Fig. 2.

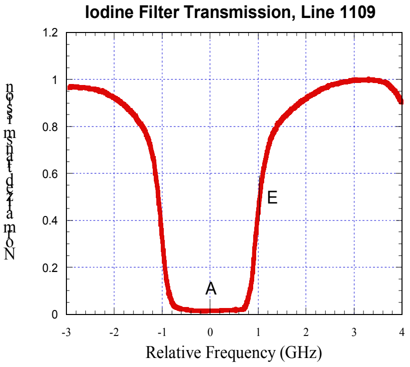

Fig. 2. Normalized transmission of absorption line 1109 of the iodine filter near 532 nm. The wave numbers at reference point A and operation point are 18787.796 cm^{-1} and 18787.830 cm^{-1} (1.02 GHz apart).

The detection iodine cell, which is stabilized through control of separately, has been constructed and found to have long-term stability. Since the vapor density is more sensitive to change in iodine vapor pressure, the temperature of the cell finger is controlled to near 65 °C within 0.01 °C rms, while its cell body is near 70 °C within 0.1 °C. The resulting transmission curve for the vapor filter near 532 nm is shown in Fig. 2, where the absorption line center at 18787.796 cm is marked A.

We can measure the aerosol backscattering ratio, $R_b = (\beta_a/\beta_m)$, using the system by locking the frequency of the injection seed laser to the point A at the 1109 line center of the I_2 filter where the aerosol backscattering will be mostly absorbed by the filter (measured to be 70dB). It is straightforward to show that the detected photo counts at a range r in the total scattering reference channel, N_R, and that in the measurement channel, N_M, are given in Eq. (1) and Eq. (2), adopting from Hair *et al.*, below:

$$N_R = k_R\left(\frac{\Delta r}{r^2}\right)[\beta_a + \beta_m]\exp\left(-2\int dr[\alpha_a(r') + \alpha_m(r')]\right) \qquad \text{Eq.1}$$

$$N_M = k_M\left(\frac{\Delta r}{r^2}\right)[f_a\beta_a + f_m\beta_m]\exp\left(-2\int dr[\alpha_a(r') + \alpha_m(r')]\right) \qquad \text{Eq.2}$$

Where:

$$f_a(\nu) = F(\nu)$$

$$f_m(T,P,\nu) = \int \Re(\nu' - \nu, T, P) F(\nu') d\nu'$$

$$\int \Re(\nu' - \nu, T, P) d\nu' = 1$$

Which are, respectively, the aerosol attenuation factor due to iodine filter at the receiving frequency $\nu = \nu_0$, the attenuation factor for Cabannes-Brillouin scattering by the iodine filter, and the expression showing that the normalized Cabannes-Brillouin scattering function, $\Re(\nu, T, P)$ is used here. $F(\nu)$ is the transmission function of the iodine filter for the return signal; it is correlation of the measured (cw) iodine filter function and laser line shape function. In Eq.1 and Eq.2, k_R and k_M are system constants, respectively, for reference and measurement channel, depending on total laser emission energy, optical efficiency and range factor; and Δr is the range resolution. β_a and β_m (α_a and α_m) are aerosol and molecular volume backscatter (extinction) coefficients, respectively.

Setting $f_a = 0$ in Eq.1, the atmospheric aerosol scattering ratio R_b can be expressed as:

$$R_b(r) = \frac{\beta_a(r) + \beta_m(r)}{\beta_m(r)} - 1 = \frac{k_M f_m N_R(r)}{k_R N_M(r)} - 1$$

In this manner, the aerosol scattering ratio R_b can be measured with accuracy better than 10%.

3、**Experimental results, comparisons and discussion**

We measured backscattering ratio using our HSRL in October and December 2004, the weather conditions including fine, fog and cloudy day, approximately 1Km off Qingdao seashore. The traditional method to extract the backscattering ratio using the aerosol lidar is to gain the ratio of real and standard atmosphere backscattering signal. As stated above, the signal N_M we received using HSRL is a signal without any influence of aerosol because the returning signal of aerosol has been rejected by iodine filter; in fact, it can basically represent the return signal profile of clear atmosphere. Therefore if there are similar conditions such as location, weather conditions, etc, we can get the backscattering ratio by our new method. (Shown in Fig.3 in cloudy day, Fig.4 in fine day, and Fig.5 in foggy day.)

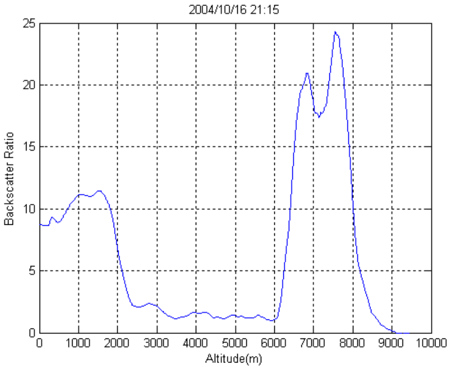

Fig .3 Backscattering Ratio β_a/β_m
(weather: cloudy)

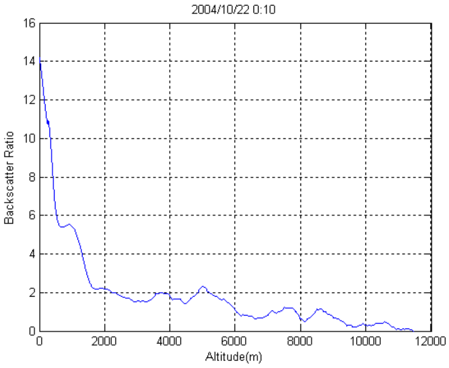

Fig.4 Backscattering Ratio β_a/β_m
(weather: fine)

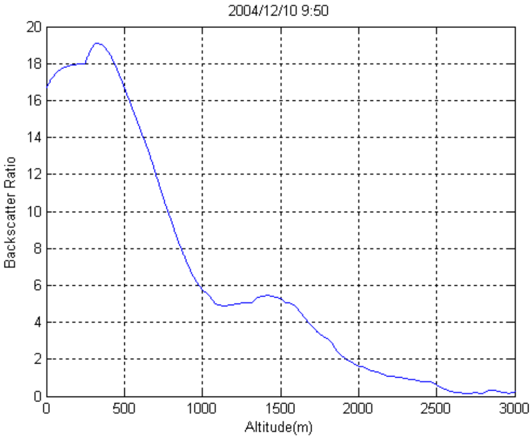

Fig. 5 Backscatter Ratio β_a/β_m (weather: fog)

β_m should be stable considering similar location and weather conditions, thus, what we need is measuring Nm just one time passing through iodine vapor filter by which we can get β_m of different time. Then we can get different R_b with different returning signal profile. (Shown in Fig.6, Fig.7, Fig.8)

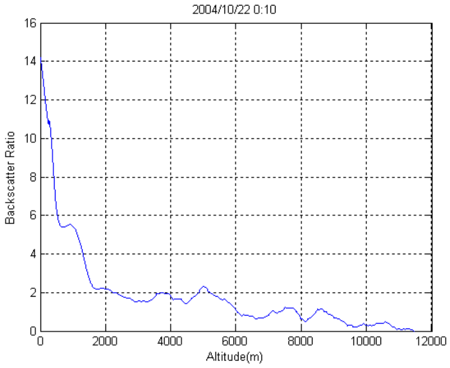

Fig.6 Backscattering ratio β_a/β_m , *Na and Nm at the same time*

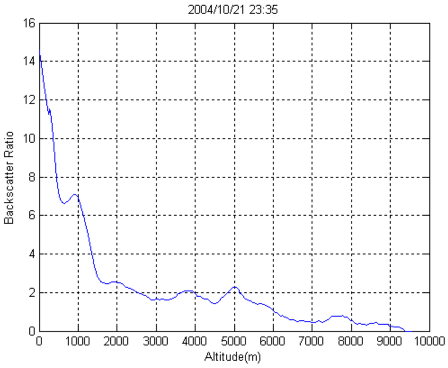

Fig.7 Backscattering ratio β_a/β_m

Na 23:35 October21, 2004;

Nm 00:10 October 22,2004

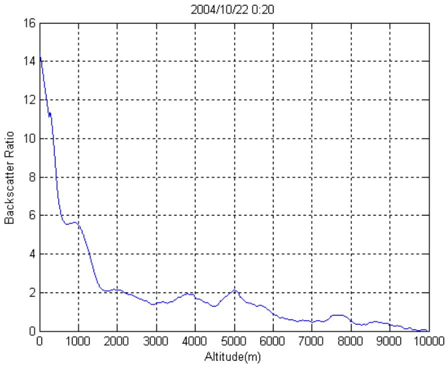

Fig.8 Backscattering ratio β_a/β_m

Na 00:20 October22, 2004;

Nm 00:10 October 22,2004

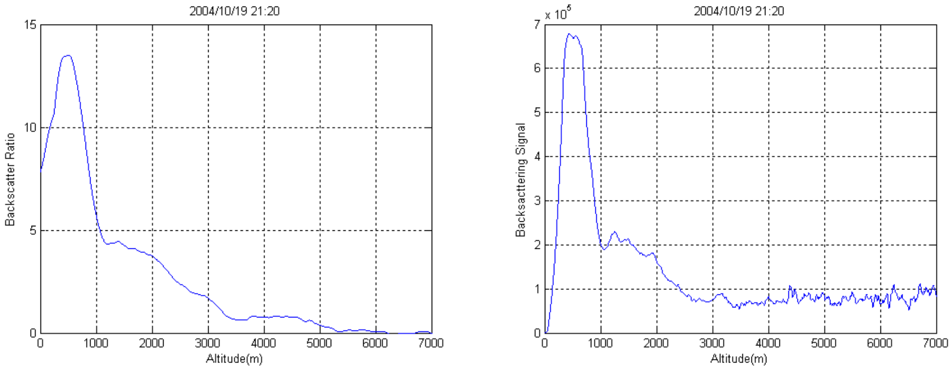

Fig.9 Correlation:0. 8881

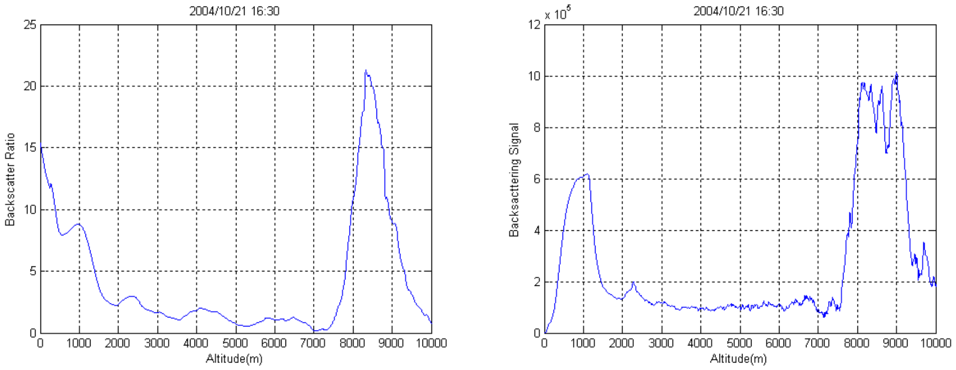

Fig.10 Correlation: 0.8093

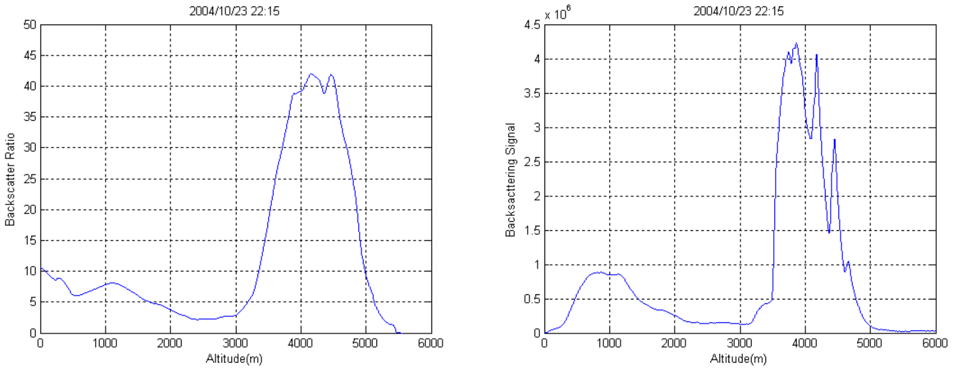

Fig. 11 Correlation: 0.8737

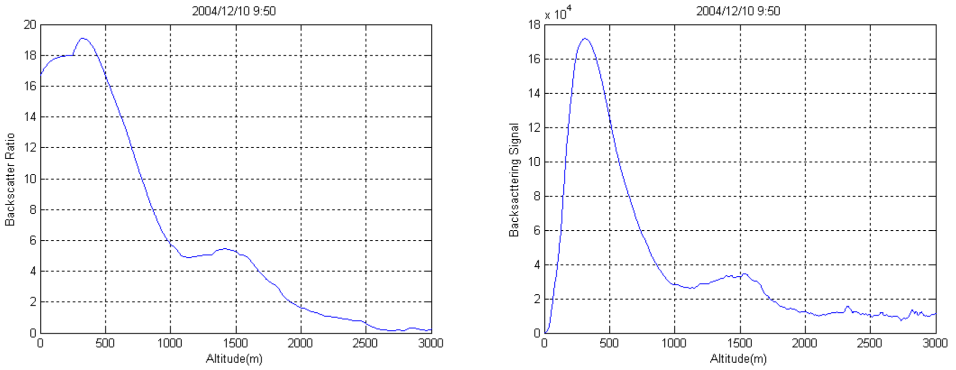

Fig.12 Correlation: 0.8611

We can also get the altitude of boundary layer (H) by the differential of backscattering signal. To validate feasibility of this method, we can compare a series of altitude of boundary layer using the profile of R_b. with differential method (shown in table 1)

Date	H determinated by R_b.（km）	H determinated by the differential of backscattering signal（km）
2004.10.15	1.25	1.45
2004.10.16	2.00	2.01

2004.10.19	0.85	0.73
2004.10. 21	1.44	1.26
2004.10.22	1.33	1.32
2004.10.23	1.87	2.05
2004.10.24	1.12	1.19

Table1: altitude of boundary layer with different method (Deviation: 0.13)

From table 1 above, we can get that the deviation is about 0.13km. Comparing the two methods, we can conclude that the differential method is feasible in determining the altitude of boundary layer.

References

1、ZhiShen Liu, Dong Wu, Jin-Tao Liu, *et al*, Low-Altitude atmospheric wind measurement from the combined Mie and Rayleigh backscattering by Doppler lidar with iodine filter,20 November 2002/vol.41,No.33/APPLIED OPTICS p7079-7086.

2、H. S. Shimizu, A. Lee, and C. Y. She, High spectral resolution lidar system with atomic blocking filters for measuring atmospheric parameters, Appl. Opt., 22, 1373--1391, 1983.

3、Z. S. Liu, W. B. Chen, T. L. Zhang, J. W. Hair, C.Y. She, “ Proposed ground-based incoherent Doppler lidar with iodine filter discriminator for atmospheric wind profiling,” in Application of Lidar to current Atmospheric Topics, Denver .A.J.Sedlacek, ed., Proc. SPIE. Vol.2833, 128-135 (1996).

4、R. J. Alvarez II, L. M. Caldwell, Y. H. Li, D. A. Krueger, and C. Y. She, "High Spectral Resolution Lidar Measurement of Tropospheric Backscatter-Ratio Using Barium Atomic Blocking Filter," J. Atm. Oceanic Tech. 7, 876-881 (1991).

5、E. W. Eloranta,, P. Piironen, "An I2-absorption filter based High Spectral Resolution lidar for measurements of the optical properties of aerosols and clouds", Atmospheric Propagation and Remote Sensing III, SPIE, Orlando, Florida, April 5-8, 1994.

6、P. Piironen, E. W. Eloranta, Demonstration of a high-spectral- resolution lidar based on an iodine absorption filter, Opt. Letter, 1994, Vol.19, No.3, 234-236.

7、S. Gerstenkorn and P. Luc, Atlas du spectre d’absorption de la molecule d’iode, Centre National de la Recherché Scientifique, Paris. 1978.

8、J. W. Hair, L. M. Caldwell, D. A. Krueger, Chiao-Yao She, High-spectral-resolution lidar with iodine-vapor filters: measurement of atmospheric-state and aerosol profiles, Appl. Opt. 2001, Vol.40, No.30, 5280-5294.

Characterization of Asian Tropospheric Aerosols with Multi-wavelength Mie-Raman Lidar and Skyradiometer

Toshiyuki Murayama*[a], Miho Sekiguchi[a], Detlef Müller[b], Katsuya Wada[a], and Yasuharu Saito[a]

[a]*Faculty of Marine Technology, 2-1-6 Etchujima, Koto, Tokyo 135-8533, Japan*
[b]*Institute for Tropospheric Research, Permoserstr. 15, 04318 Leipzig, Germany*

ABSTRACT

We have extensively observed tropospheric aerosols with lidar and Sun/sky radiometer in Tokyo. Recently, we have extended the lidar system to dual-wavelength Raman lidar (The primary laser wavelengths are 355 and 532 nm.). We found that the intensive optical properties such as Angstrom exponent and lidar ratios derived from the Raman lidar measurements are quite useful to characterize the aerosols resolving with height. As highlighted examples, we will show the case studies of Asian dust and Siberian smoke. For the smoke case (as spherical aerosol case), we retrieved the microphysical properties by applying an inversion with regularization. The results show an accumulation-mode dominate size-distribution and a low absorption; the effective radius and the single scattering albedo are ~0.22μm and ~0.95, respectively. The column-averaged microphysical properties derived from the skyradiometer are also consistent with the results. We also estimated the aerosol direct radiative forcing using the microphysical properties. Further systematic analyses and improvement of lidar system are now in progress.

Keywords: Raman lidar, Asian dust, Siberian forest-fire smoke, aerosol optical properties, aerosol radiative forcing

1. INTRODUCTION

Aerosols play an important role in the Earth's radiation budget through the scattering and absorption of light, and present a key uncertainty in the assessment of radiative forcing.[1] They also serve as cloud condensation nuclei and modulate the cloud properties. East Asia is considered as a region where emission of anthropogenic aerosol is rapidly increasing due to growing economy. Recently, the Asia-Pacific Regional Aerosol Characterization Experiment (ACE-Asia) showed that the spatial variability of aerosol composition and properties is rather high in this area.[2, 3] It is also shown that mineral dust has an indirect effect on clouds by serving as effective ice nuclei.[4-8] Therefore, it is highly important to study not only column-averaged but also height-resolved aerosol optical properties regularly, in order to assess their radiative impact. However, it is rather difficult to perform aircraft measurements frequently.

Nowadays, sophisticated multi-wavelength Raman lidars enable us to characterize tropospheric aerosols by the observable quantities themselves, and in further to retrieve microphysical properties from them.[9-11] From the point of view of feasibility, we installed a UV-Raman lidar system that emits the third harmonic frequency (355 nm) on the basis of a second Nd:YAG laser in addition to our existed lidar system at the Etchujima campus (35.66° N, 139.80° E)of Tokyo University of Marine Science and Technology (TUMSAT).[12] Thus

---

* mrayama@e.kaiyodai.ac.jp; phone +81-3-5345-7464; fax +81-3-5245-7339

our lidar system is capable of measuring backscatter coefficients at 355, 532, 1064 nm, extinction coefficients at 355 and 532 nm, particle depolarization ratio at 532 nm, and water–vapor mixing ratio, simultaneously. To our knowledge, this is the first dual-wavelength Raman lidar installed in East Asia. In this paper, we demonstrate how the dual-wavelength Raman lidar is useful for the characterization of aerosol optical properties depending on regional aerosol events. We outline the Raman lidar system and the analysis method in section 2. In section 3, we presents results of observations for the case of Asian dust and Siberian forest-fire smoke events in the spring of 2003 with emphasis on the aerosol characterization by observed aerosol optical properties. In section 4, we present the microphysical parameters of the smoke derived from the inversion code, comparison with the results from the skyradiometer analysis, and an application for estimating the aerosol radiative forcing using these results. Most of the results presented here are described in the reference 13.

2. LIDAR SYSTEM AND ANALYTICAL PROCEDURE

We installed a UV-Raman lidar system next to the existing Mie-Polarization-Raman lidar, which uses the laser beams at 532 (VIS) and 1064 nm (IR)[3,12] The schematic view of the full lidar system is shown in Fig. 1. The UV-Raman lidar system is a stand-alone system, which employs another Q-switched Nd:YAG laser with a third harmonics generator. The repetition frequency of the laser pulse is 10 Hz, which is synchronized with the VIS/IR system. The receiving telescope is of Schmid-Cassegranian type with 35.5-cm diameter and the field of view is 2 mrad. The optical axes of the laser beams and the telescopes were well co-aligned each other in the vertically direction. These conditions allow us to observe nearly the same volume in time and space with both lidar systems. Dichroic mirrors and following narrow interference filters, which bandwidths are 1-3 nm, are used to separate the backscattered light from Mie-Rayleigh scattering (355 nm) and from Raman scattering from nitrogen (387 nm) and water-vapor molecules (408 nm). Similarly the Raman signals at 607 nm and the Mie/Rayleigh signals at 1064 nm were separated from the signals at 532 nm in the VIS/IR lidar system. Photo-multiplier tubes are used for the detection. The data were stored every 4094 shots (~7 minutes) using transient recorders (TR20-160, Licel). Typical laser powers during operation are approximately 100, 100, 200 mJ per pulse for the 355, 532 and 1064 nm laser beams. Lower height data evaluation were limited by the incomplete overlapping between the telescope field of view and the laser beams below ~1-1.5 km. Only the backscatter ratio at 355 nm and the water-vapor mixing ratio are evaluated almost down to the surface because we can regard the geometrical form factor as identical for both elastic and inelastic Raman channels. It is not the case for the backscatter ratio at 532 nm presented here because we used different receivers for the 532 nm and 607 nm signals. At this moment, the operation of Raman channels is limited in nighttime.

We have analyzed averaged or integrated analog and photon-counting data for observations lasting a few hours when the vertical structure did not vary significantly. The extinction coefficient and the scattering ratio of the aerosols at 355 and 532 nm, and the mixing ratio are derived by the methods given the references 14-16. The atmospheric density profile was calculated from routine radiosonde observations at Tateno (36.05° N, 140.12° E) at 12 UTC. Normalization of the scattering ratio is made at an almost aerosol-free height, typically over 10 km. The backscatter coefficients are derived from the backscatter ratios. The backscatter coefficient at 1064 nm is obtained from the Mie-Rayleigh signal by using the method proposed by Fernald[17] and assuming a lidar ratio of 40 sr. The lidar-derived water-vapor mixing ratio is normalized so that the lowest value (~75 m above the lidar) matches to the surface observation at TUMSAT with assuming the error of ±10 %. The mixing ratio profile was converted to the relative humidity one using the temperature and pressure profiles obtained from the radiosonde data. Deviations of the mixing ratio and relative humidity obtained from the lidar at TUMSAT to the respective quantities derived with the radiosonde can be attributed to the spatial distance of the two sites and different measurement times, and the unknown error of the calibration factor of the lidar.

3. EXAMPLES OF OBSERVATION

3.1.Case of Asian dust

Fig. 2 presents the time-height cross-sections of the backscatter coefficient and total (particle + molecular) depolarization ratio at 532 nm on 12 March 2003. The depolarization ratio is an indicator of irregularly shaped particles. Fig. 3 shows the mean profiles for a measurement period from 1056 to 1306 UTC. We also indicated the Ångström exponent (AE) and the backscatter-related Ångström exponent (BAE) derived from the profiles of the extinction and backscatter coefficient at 355 and 532 nm, respectively. The error bars are based on statistical and estimated systematic errors. The aerosol layer between 3 and 5 km seems to be composed of two layers as indicated by the horizontal dashed lines A and B in Figure 2: layer A is rather narrow with the peak at 4.6 km, layer B is broader with the peak at 4.0 km. The lower layer B carries features of mineral dust as suggested from the high particle depolarization ratio (PDR>20 %), while the PDR in layer A is as small as 6 %. The mean lidar ratios at 355 (S_{355}) and 532 nm (S_{532}) were nearly same within the standard deviations: 48.6(±8.5) and 43.1(±7.0) sr, respectively in the dust-like layer (3.5-4.3 km). The value of PDR and S_{532} is similar to our previous observations.[3,18] The value of S_{355} is close to the lidar ratio observed for Saharan dust at 351 nm in southern Italy (~50 sr)[19], but smaller than what was observed in Leipzig, Germany (50-80 sr).[10] Mattis et al. also found that S_{355} is 10-30 % higher than S_{532}.[10] The difference in the lidar ratio values might be attributed to differences in shape, size or absorption properties of mineral particles.

In addition, we can see interesting differences of aerosol optical properties besides the large difference of the PDR in the layers A and B; a higher BAE in layer A (~1.2) than in layer B (~0.3) in Fig. 3, which suggests that layer A might be composed of finer aerosols. Since the relative humidity in the layers A and B are nearly identical (~40 %) as shown in Fig. 3, we can reject the assumption that hygroscopic growth of mineral dust reduces the depolarization ratio.

3.2.Case of Siberian forest-fire smoke

In the spring and summer of 2003, an unusually high number of forest fires occurred in Siberia.[11] Smoke plumes originating from these fires were transported over Japan with westerly wind. Fig. 4 shows a time-height plot of the backscatter coefficient and the total depolarization ratio at 532 nm on 21 May 2003. A high aerosol optical depth (τ_a) at the wavelength (λ) of 500 nm of more than 2.0 was observed in the daytime by collocated Sun photometer. The back trajectory analyses show that the airmass from 2 to 4 km trace back to regions of intense forest-fire from the west of Lake Baykal to the east of the border of China, Russia and Mongolia. The smoke layer sharply dropped off at ~4 km. The upper part (3-4 km) of the smoke layer showed a depolarization ratio of about 6 %. A similar feature was also observed in Suwon (37.14° N, 127.04° E), Korea.[20]

Fig. 5 shows the mean profiles of optical properties for a measurement from 1040 to 1349 UTC. A prominent layer between 2.5 and 4 km shows different optical properties separated at the peak (~3.2 km) from the intensive parameters, i.e., S_{532}, PDR, and AE. The upper part except the rim had the following features: i) BAE is high (~1.9) while AE is small (~0.7), ii) S_{532} (~65 sr) is apparently higher than S_{355} (~40 sr), iii) PDR (~6 %) is higher than that in the lower part. On the other hand, in the lower part, S_{532} and PDR drop to ~40 sr and ~3 %, respectively, while AE increases to be ~1.2.

The relationship between S_{355} and S_{532}, i.e., $S_{532}>S_{355}$, is consistent with the observation over central Europe of aged smoke from Canada during the Lindenberg Aerosol Characterization Experiment LACE98.[21] A part of this Siberian smoke was also detected over central Europe and confirmed the same relationship between S_{355} and S_{532}.[11] The non-zero depolarization ratio might be caused by soil material that was uplifted into the forest fire plume[22], or the nonsphericity of the particles due to coagulation of smoke particles.[23] The latter explanation sounds more presumable because no signature of mineral dust was found by a chemical analysis of aerosols sampled at the summit of Mt. Fuji (3,776 m above sea level and ~100 km west from Tokyo) in the same period.[24]

The relatively small AE (~0.7) in the wavelength range from 355-532 nm for the smoke layer is supported by the evidence observed by Sun/sky photometer for cases of heavy smoke events in South America and South Africa[25]: a significant positive curvature in the log(τ_a) versus log(λ) relationship, and in fact the analysis of the collocated TUMSAT skyradiometer (POM-01, Prede) also shows such relationship in the daytime.

4. DISCUSSIONS

4.1. Microphysical properties of the smoke aerosol retrieved from inversion

We applied the method of inversion with regularization only for the case of smoke to retrieve the microphysical properties using the backscatter coefficients at 355, 532, 1064 nm and the extinction coefficients at 355 and 532 nm.[9,21,26] We cannot apply currently the inversion code for Asian dust case which poses a high PDR, i.e., nonsphericity, because the inversion strongly relay on the assumption of spherical (Mie) particles. We found 0.22(±0.04) μm for the effective (surface-area mean) radius and 0.95(±0.06) for the single scattering albedo (SSA) at 532 nm around the peak of the smoke layer. Fig. 6 shows effective radius and single scattering albedo for selected height ranges. Comparison between a typical column-integrated volume size distribution derived from the skyradiometer[27] and that from the present inversion is indicated in Fig. 7. The results indicate that particles in the accumulation mode are dominant, which is a typical feature for this kind of aerosols. The relatively high SSA indicates low absorbing particles. It should be worthwhile to mention that the larger effective radius of 0.35(±0.07) μm with similar SSA of 0.97(±0.04) was retrieved with the same inversion code for the hemispheric transported smoke over Leipzig, Germany on May 29, 2003, which suggests the evolvement of the smoke aerosols.[28]

In comparison, we mention that the typical mean radius and the SSA of Asian dust plumes obtained by intensive airborne in situ measurements during the ACE-Asia are 2-3 μm and 0.96(±0.01) at 550 nm, respectively.[3,29]

4.2.Estimation of aerosol direct radiative forcing for the smoke case

There are relatively few literatures which presents the radiative forcing calculations using lidar data[22,30,31] Here we attempted to estimate the aerosol direct radiative forcing (ADRF) for the smoke case on 21 May 2003 base on the extinction coefficient profile from the lidar measurement at 532 nm and microphysical properties derived from the inversion. We used the radaitive transfer code FSTAR5C.[33] We estimated the ADRF in the shortwave radiation (0.2-4.0 μm) by assuming the flowing constant atmospheric condition; the temperature, pressure, relative humidity profiles from the radiosonde data at Tateno, 12 UTC. Daily mean ADRF is thus evaluated as –39 and –51 W/m^2 at the top of the atmosphere and the surface, respectively. Since we used wavelength independent refractive indices of particles from the inversion, we also calculated the ADRF using the column-averaged size distribution and refractive indices (wavelength dependent) retrieved from the skyradiometer analysis in the daytime. We found that both values agree each other if the mean refractive index is similar. The daily mean heating rate due to the aerosols is also obtained, which maximum reaches ~0.7 K per day just above the peak of the aerosol extinction profile.

5. CONCLUSIONS AND SUMMARY

The distinct optical signatures for mineral dust and aged smoke presented here well demonstrate how multi-wavelength Raman lidar including a depolarization channel is useful to characterize tropospheric aerosols resolving with height; for the Asian dust case we found a high PDR at 532 nm over 20 % and a small wavelength dependence of the lidar ratio between 355 and 532 nm (43-49 sr), for the smoke case we found that a small PDR of 5-8 % or less and a high wavelength dependence of the lidar ratio: S_{355} is ~40 sr, while S_{532} is ~65 sr. We successfully derived the climate-relevant microphysical parameters, e.g. effective radius and single scattering albedo, for the smoke case using the inversion code. We also attempted to evaluate the aerosol radiative forcing based on the height-resolved parameters using the radiative transfer code. Such an advanced Raman lidar is especially useful for the characterization of the complex aerosols found over East Asia and has a potential for application in global aerosol lidar networking in future.

ACKNOWLEDGEMENTS

This work is supported by Grand-in-Aid for Scientific Research on Priority Areas under Grant No. 14048232 from the Ministry of Education, Culture, Sports, Science and Technology, and Global Environment Research Fund for the project “Study of the dynamic transport mechanism and environmental effect of Kosa aerosol originated from the northern Chinese areas”, from the Ministry of the Environment. We also acknowledge partial supports from the projects “Variability of Marine Aerosol Properties (VMAP)” and “Asian Atmospheric particle Environment Change Studies (APEX)” of CREST of Japan Science and Technology Agency, and the joint research programs of CEReS, Chiba University (14-5), (15-7) and (16-4).

REFERENCES

1. IPCC (The Intergovernmental Panel on Climate Change), *Climate Change 2001: The Scientific Basis*, 896 pp., Cambridge Univ. Press, 2001.
2. B. J. Huebert et al., “An overview of ACE-Asia: Strategies for quantifying the relationship between Asian aerosols and their climate impacts”, *J. Geophys. Res., 108(D23)*, 8633, doi:10.1029/2003JD003550, 2003.
3. T. Murayama et al., “An intercomparison of lidar-derived aerosol optical properties with airborne measurements near Tokyo during ACE-Asia”, *J. Geophys. Res., 108(D23)*, 8651, doi:10.1029/ 2002JD003259, 2003.
4. T. Murayama, “Formation of ice cloud from Asian-dust particles in the upper troposphere”, *Proc. 4153*, pp.218-225, 2001.
5. T. Murayama et al., “Ground-based network observation of Asian dust events of April 1998 in east Asia”, *J. Geophys. Res., 106(D16)*, pp.18,345-18,359, 2001.
6. K. Sassen, “Indirect climate forcing over the western US from Asian dust storms”, *Geophys. Res. Lett., 29(10)*, 1465, doi:10.1029/2001GL014051, 2002.
7. K. Sassen, P. J. DeMott, J. M. Prospero, M. R. Poellot, “Saharan dust storms and indirect aerosol effects on clouds: CRYSTAL-FACE results”, *Geophys. Res. Lett., 30 (12)*, 1633, doi:10.1029/2003GL017371, 2003.

8. T. Sakai, T. Nagai, M. Nakazato, and T. Matsumura, "Raman lidar measurement of water vapor and ice clouds associated with Asian dust layer over Tsukuba, Japan", *Geophys. Res. Lett., 31*, L06128, doi:10.1029/2003GL019332, 2004.
9. D. Müller et al., "Comprehensive particle characterization from three-wavelength Raman-lidar observations: case study", *Appl. Opt., 40*, pp.4863-4869, 2001.
10. I. Mattis et al., "Dual-wavelength Raman lidar observations of the extinction-to-backscatter ratio of Saharan dust", *Geophys. Res. Lett., 29*, doi:10.1029/2002GL014721, 2002.
11. I. Mattis et al., "Unexpectedly high aerosol load in the free troposphere over central Europe in spring/summer 2003", *Geophys. Res. Lett., 30*, 2178, doi:10.1029/2003GL018442, 2003.
12. T. Murayama et al., "Application of lidar depolarization measurement in the atmospheric boundary layer: Effects of dust and sea-salt particles"*, J. Geophys. Res., 104(D24)*, pp.31,781-31,792, 1999.
13. T. Murayama, D. Müller, K. Wada, A. Shimizu, M. Sekiguchi and T. Tsukamoto, "Characterization of Asian dust and Siberian smoke with multi-wavelength Raman lidar over Tokyo, Japan in spring 2003", *Geophys. Res. Lett.*, *31*, *L23103*, doi:10.1029/2004GL021105, 2004.
14. A. Ansmann et al., "Combined Raman elastic -backscatter LIDAR for vertical profiling of moisture, aerosol extinction, backscatter, and lidar ratio", *Appl. Phys., B55*, pp.18-28, 1992.
15. D. N. Whiteman, S. H. Melfi, and R. A. Ferrare, "Raman lidar system for the measurement of water vapor and aerosols in the Earth's atmosphere"*, Appl. Opt, 31*, pp.3068-3082, 1992.
16. D. N. Whiteman, "Examination of the traditional Raman lidar technique. I. Evaluating the temperature-dependent lidar equations", *Appl. Opt., 42*, pp.2571-2593, 2003.
17. F. G. Fernald, "Analysis of atmospheric lidar observations: some comments", *Appl. Opt., 23*, pp.652-653, 1984.
18. T. Murayama, "Optical properties of Asian dust aerosol lofted over Tokyo observed by Raman lidar", in *Lidar Remote Sensing in Atmospheric and Earth Sciences (Proceedings of the 21th ILRC)*, edited by L. R. Bissonnette, G. Roy, and G. Vallée, pp.331-334, Defense R&D Canada – Valcartier, Québec, 2002.
19. F. De Tomasi, A. Blanco and M. R. Perrone, "Raman lidar monitoring of extinction and backscattering of African dust layers and dust characterization", *App. Opt., 42*, pp.1699-1709, 2003.
20. C. H. Lee et al., "Continuous measurements of smoke of Russian forest fire by 532/1064 nm Mie scattering Lidar at Suwon, Korea", in *Reviewed and Revised Papers presented at the 22nd International Laser Radar Conference*, G. Papparado and A. Amodeo Editors, *ESA SP-561*, pp.535-538, 2004.
21. U. Wandinger et al., "Optical and microphysical characterization of biomass-burning and industrial-pollution aerosols from multiwavelength lidar and aircraft measurements", *J. Geophys. Res., 107(D21)*, 8125, doi:10.1029/ 2000JD000202, 2002.
22. M. Fiebig et al., "Optical closure for an aerosol column: Method, accuracy, and inferable properties applied to a biomass-burning aerosol and its radiative forcing", *J. Geophys. Res., 107(D21)*, 8130, doi:10.1029/2000JD000192, 2002.
23. J. V. Martins et al., "Sphericity and morphology of smoke particles from biomass burning in Brazil", *J. Geophys. Res., 103(D24)*, pp.32051-32057, 1998.
24. N. Kaneyasu, National Institute of Advanced Industrial Science and Technology, *private communication*, 2004.

25. T. F. Eck et al., “Wavelength dependence of the optical depth of biomass burning, urban, and desert dust aerosols”, *J. Geophys. Res., 104(D24),* pp.31,333-31,349, 1999.
26. I. Veselovskii et al., “Inversion with regularization for the retrieval of tropospheric aerosol parameters from multiwavelength lidar sounding”, *Appl. Opt., 41*, pp.3685-3699, 2002.
27. T. Nakajima et al., “Use of sky brightness measurements from ground for remote sensing of particulate polydispersions”, *Appl. Opt., 35*, pp.2672-2686, 1996.
28. I. Mattis et al., “Siberian forest-fire smoke observed over central Europe in spring/summer 2003 in the framework of EARLINET”, in *Reviewed and Revised Papers presented at the 22nd International Laser Radar Conference*, G. Papparado and A. Amodeo Editors, *ESA SP-561*, pp.857-860, 2004.
29. T. L. Anderson et al., “Variability of aerosol optical properties derived from in situ aircraft measurements during ACE-Asia”, *J. Gephys. Res., 108(D23)*, 8647, doi:10.1029/2002JD003247.
30. J. Redemann et al., “Case studies of the vertical structure of the direct shortwave aerosol radiative forcing during TARFOX”, *J. Geophys. Res., 105(D8)*, pp.9971-9979, 2000.
31. J. G. Won et al., “Estimation of direct radiative forcing of Asian dust aerosols with Sun/sky radiometer and lidar measurements at Gosan, Korea”, *J. Metorol. Soc. Jpn., 82, 1*, pp.115-130, 2004.
32. T. Y. Nakajima, T. Nakajima, T. Aoki, A. Higurashi, A. Tanaka, M. M. Verstraete, Y. Hashibe, *GSS Reference Hand book (Rstar Reference Handbook)*, *JAXA EORC Bulletin*, *15*, 2004.

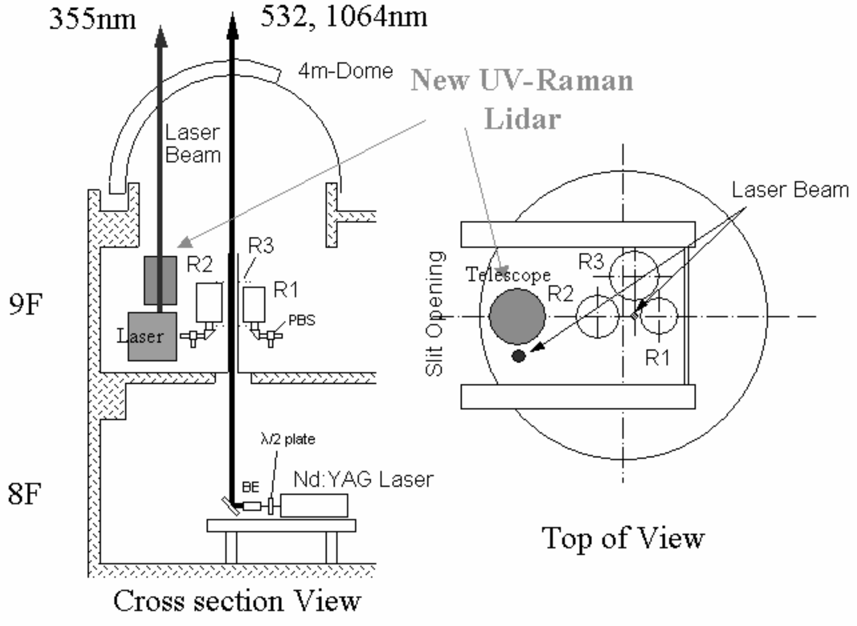

Fig. 1. Schematic view of the TUMSAT multi-wavelength Raman lidar system.

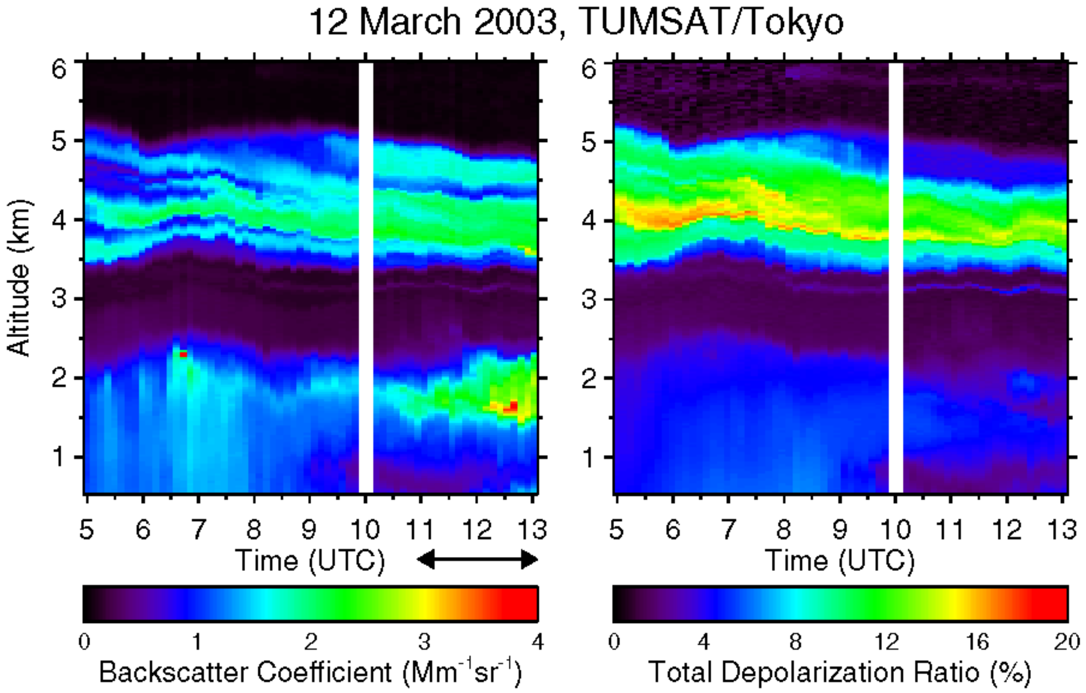

Fig. 2. Time-height cross section of aerosol backscatter coefficients and total depolarization ratio at 532 nm over TUMSAT in Tokyo, Japan on 12 March 2003.[13]

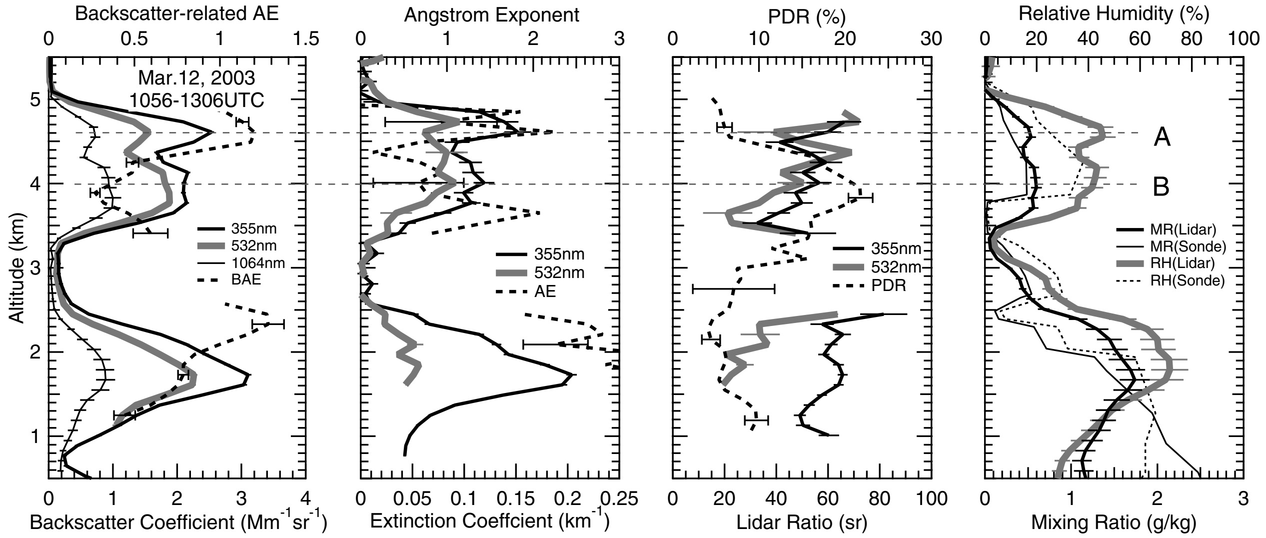

Fig. 3. Mean profiles of aerosol optical properties and water-vapor mixing ratio for the measurement from 1056 to 1306 UTC on 12 March 2003.[13] BAE and AE denote Backscatter-related Ångström Exponent and Ångström Exponent for the extinction coefficient between 355 and 532 nm, respectively. The mixing ratio and relative humidity obtained from radiosonde at Tateno (12 UTC) are shown for reference.

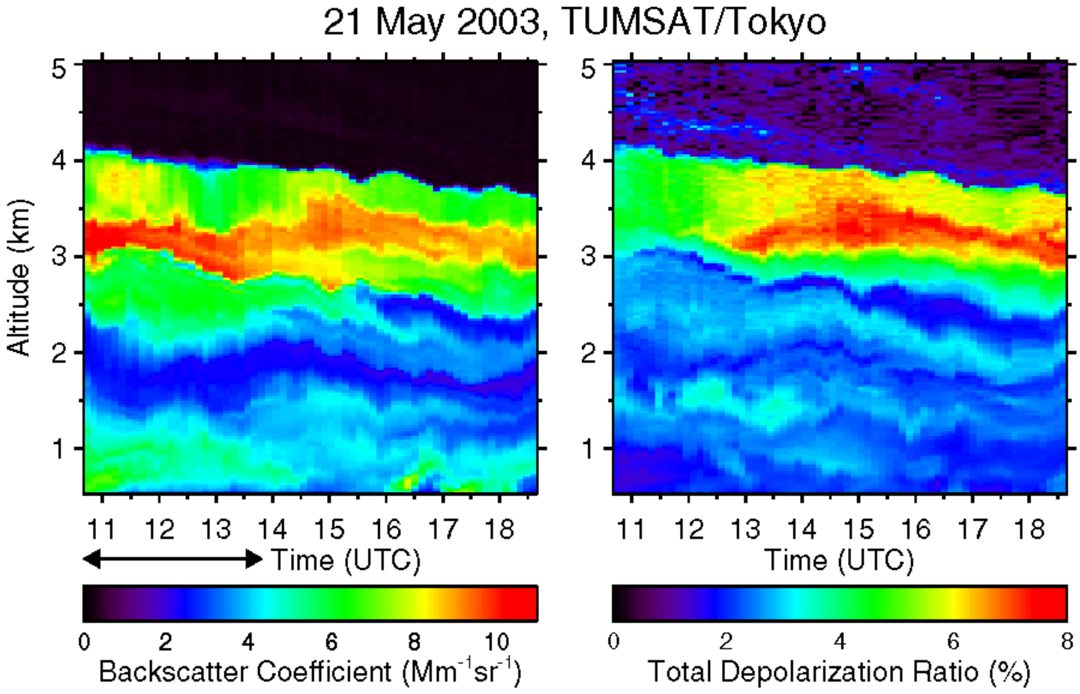

Fig. 4. As in Fig. 2, except for 21 May 2003.[13]

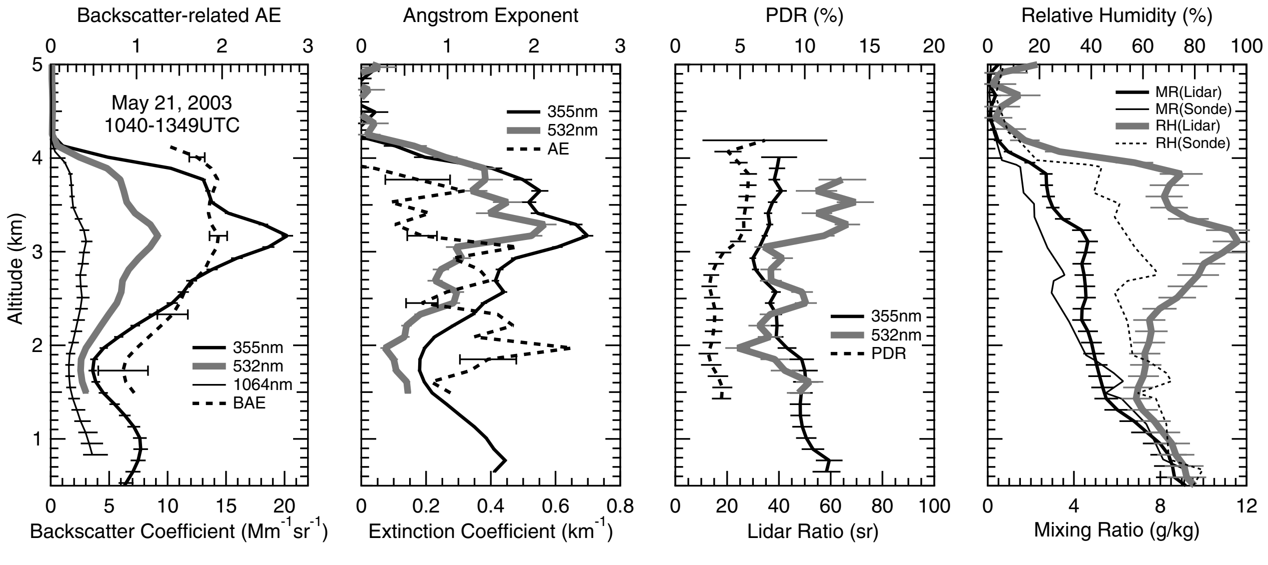

Fig. 5. As in Fig. 3, except for the period from 1040 to 1349 UTC on 21 May 2003.[13]

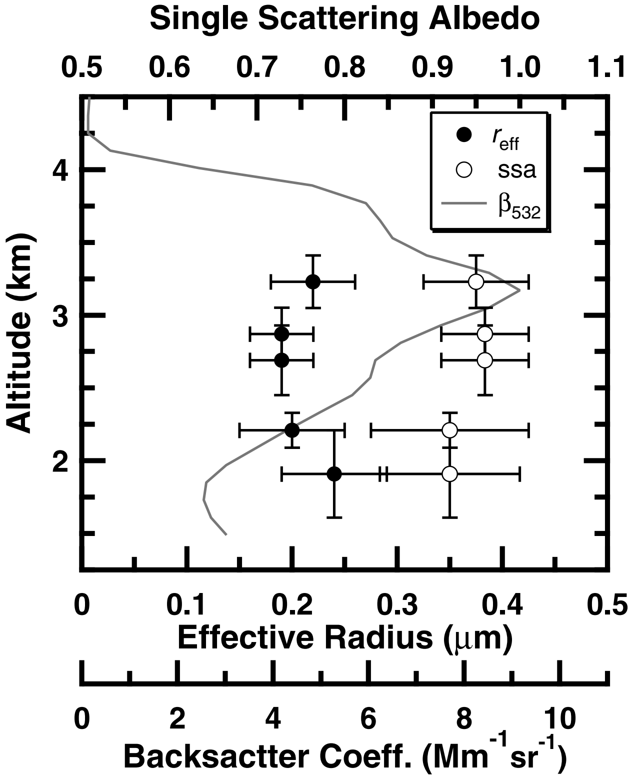

Fig. 6. Vertical variation of the effective radius and single scattering albedo at 532 nm retrieved from the Raman lidar observation shown in Fig. 5.[13]

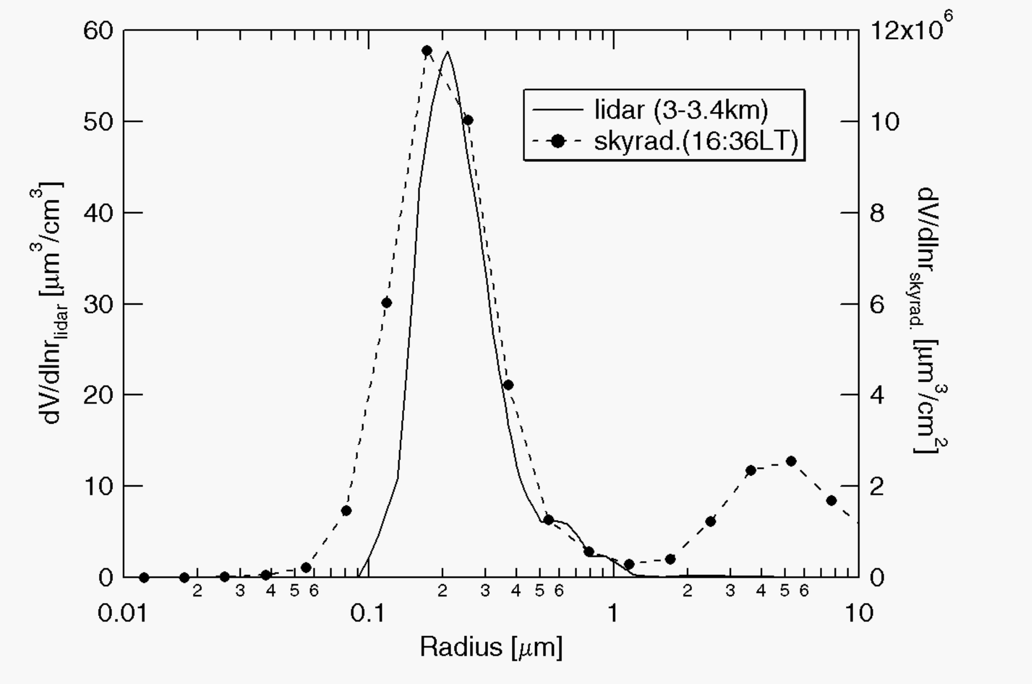

Fig. 7. Comparison between the volume size distributions retrieved from the Raman-lidar and skyradiometer inversions on 21 May 2003.

A Study of Optical Properties of Urban Aerosols in China

Jinhuan Qiu

Institute of Atmospheric Physics, Chinese Academy o Sciences, Beijing 100029, China

ABSTRACT

Some broadband radiation methods are developed to retrieve aerosol optical depth, imaginary part of its refractive index, aerosol single scatter albedo and its meteorological extinction coefficient profile. These methods include:

1. Broadband extinction method (Qiu: J. Atmos. Sci., 1998; Qiu: Tellus, 2001; Qiu: J. Appl. Meteo., 2003) to retrieve aerosol optical depth from pyrheliometer data;
2. Broadband diffuse solar radiation method (Qiu et al.: Tellus, 2004) to retrieve the aerosol imaginary part and single scatter albedo. In the method, the solar diffuse radiation is determined from joint pyrheliometer and pyranometer data in order to avoid paranometer shading ring effect.
3. Method to derive so-called scaling height of tropospheric aerosol and its meteorological (yearly/seasonally/monthly mean) extinction efficient profile, using joint aerosol optical depth and surface visibility (Qiu et al.: Journal of Aerosol Science, in press). The scaling height is defined using an assumption of exponent-type aerosol extinction coefficient profile. The scaling height and exponent-type extinction coefficient profile are determined from ground-measured aerosol optical depth and surface visibility data.

These methods are used to retrieve aerosol optical depths, aerosol imaginary part (AIP) and its single scatter albedo (SSA), and aerosol extinction coefficient profiles over 14 sites in China. These sites locate over 14 cities of Urumqi, Geermu, Harbin, Shengyang, Beijing, Zhengzhou, Kunming, Shanghai, Wuhan, Guangzhou, Lanzou, Ejinaqi, Lhasa and Sanya, which cover most areas in China. Yearly/seasonally/monthly mean characteristics of these optical parameters are emphatically analyzed. Some main results and conclusions are as follows:

(1) **Variation Trend of aerosol optical depths**

During 1980-1993, aerosol optical depths have increasing trends for all sites. But after 1994 and for such sites as Beijing, Harbin and Lanzhou, the depths have decreasing trends.

(2) Asian sand-dust event effects

Over most areas in China, sand-dust events mainly originated from Inner Mongolia and Xinjiang deserts are an important aerosol pollution source. It is found from the monthly-averaged AODs that the AODs in the spring are larger for most cities, especially in northern China.

(3) Characteristics of aerosol imaginary part and its single scatter albedo

The total yearly-mean AIPs during 1993-2001 change from 0.0207 to 0.0301 for 6 cities in Northern China, and the corresponding single scatter albedo (SSA) from 0.851 to 0.803 with a mean

value of 0.832. The AIP is larger during winter (warming period in northern China), especially for Shenyang site, owing to coal-burning increase. The AIP during summer is usually smaller. There are different variation trends in AIP and SSA. Over Harbin site the AIP (respectively, SSA) has an evidently increasing (respectively, decreasing) trend during 1993-2001. Over Zhengzhou site, the AIP has an increasing trend during 1993-1995 but evidently decreasing after 1997.

(4) Characteristics of scaling height of tropospheric aerosol and its mean extinction coefficient profile

Characteristics of seasonally/yearly mean scaling heights and aerosol extinction profiles over 11 sites in China during 1994-2001 are analyzed.

It is found that the aerosol scaling heights over different sites are very variable. The yearly mean scaling heights changes between 1.30 (Shenyang) and 2.67km (Wuhan). The aerosol scaling heights for different seasons are also very variable. The heights during spring are larger for all sites, especially in northern China, due to Asian dust storm events. The 11-site-mean yearly-mean aerosol scaling heights change between 1.85 and 2.11km during 1994-2001, being close to MODTRAN rural aerosol scaling height (2.04km), and they have an increasing trend with the yearly increasing rate of 0.031km, implying a shifting-up trend of aerosol particles in the troposphere.

The yearly-mean tropospheric aerosol extinction coefficient profiles are very variable for different sites. Shenyang is the capital of Liaoning province, a heavy-industry center in China. Here the aerosol pollution in the near to surface atmosphere is relatively more serious, resulting in the larger surface aerosol extinction coefficient and then the lower surface visibility. Another characteristic of aerosol extinction coefficient profile over the Shenyang site is its stronger decrease with an increase of the height. The Geermu site locates over Qinghai-Tibet Plateau, having the sea level of 2808m. Here, the surface visibility is usually larger than 30km; the surface aerosol extinction coefficient is relatively smaller, there are relatively more aerosol particles in the upper troposphere, especially during spring.

Optical, Physical and Chemical Properties of Aerosols around Japan Based on the R/V Shirase Shipboard Measurements

M. Shiobara[1)], M. Yabuki[1)], K. Hara[1)], and H. Kobayashi[2)]

[1)] *National Institute of Polar Research, Tokyo, Japan*
[2)] *University of Yamanashi, Kofu, Japan*

Abstract

In order to investigate the optical, physical and chemical properties of marine boundar layer aerosols and its relation to the origin of aerosols for estimating the direct radiative effect of aerosols in East Asia, shipboard aerosol measurements were carried out around Japan. The instrumented Research Vessel *Shirase* made counterclockwise coastal cruises from Yokosuka via the Western-North Pacific, the Sea of Japan, and the East China Sea in early autumns of 2002, 2003, and 2004. This paper includes results not only from optical measurements using an Optical Particle Counter, an Integrating Nephelometer, and a Particle Soot/Absorption Photometer but also chemical analysis of aerosols collected by an impactor-filter system. Water-insoluble aerosols were measured with a Coulter Counter. It was found that different features of optical, physical and chemical properties of aerosols in the marine boundary layer around Japan were strongly related to the origin and history of air mass.

1. Introduction

Aerosols play an important role in the global climate system due to their radiative effect to the Earth's radiation energy balance. Though it is well known that aerosols have two-fold significant effects characterized by "direct" and "indirect", the quantity of both effects is still uncertain. The direct effect is for aerosols to affect directly on the radiation budget by scattering and absorbing solar radiation in the atmosphere. Therefore the aerosol optical properties are essential for quantitative estimation of the direct effect of aerosols.

The aim of this study is to investigate the spatial variation of aerosol optical, physical and chemical properties and its relation to the origin of aerosols for estimating the direct effect of aerosols in East Asia. For this purpose, we carried out the aerosol measurement on board the instrumented R/V *Shirase* during the Japanese Antarctic Research Expedition (JARE) Training Cruise with counterclockwise coastal round cruises from Yokosuka via the Western-North Pacific, the Sea of Japan, and the East China Sea in early autumns of 2002, 2003, and 2004 (Shiobara et al., 2004a and 2004b; Yabuki et al, 2004). In this paper, results from the shipboard aerosol measurement in 2002 and 2003 are shown and compared for discussion on the optical, physical and chemical properties of aerosols in the marine boundary layer around Japan.

2. Measurements

Shipboard aerosol measurements were carried out on board the Antarctic R/V *Shirase*, an icebreaker operated by Japan Maritime Self-Defence Force, cruising around Japan prior to the voyage for the Antarctic research activity. The R/V *Shirase* made coastal round cruises counterclockwise from Yokosuka for the period from 28 August to 29 September in 2002, 4 September to 4 October in 2003, and 1 September to 5 October in 2004.

Aerosol optical properties were measured with an optical particle counter (OPC; RION KC01D), an Integrating Nephelometer (IN; Radiance Research M903), and a Particle Soot/Absorption Photometer (PSAP; Radiance Research). The OPC measured the number density of particles for five radius ranges of $r > 0.15$, 0.25, 0.5, 1.0, and 2.5 μm: the data were corrected for the coincidence loss. The IN measured the scattering coefficient at the wavelength of $\lambda = 530$ nm. The PSAP measured the absorption coefficient at $\lambda = 565$ nm. The extinction coefficient and the single scattering albedo at 565 nm were calculated by assuming that the scattering coefficient was inversely proportional to the wavelength (*i.e.*, Angstrom Parameter = 1). Considering the contamination by the exhaust from the ship engine, the data were excluded when the wind blew from the sector of 60- 240° relative to the ship heading.

Aerosol particles and acidic gases were collected using a 3-stage mid-volume impactor with back-up filter in series of 2-stage alkaline impregnated filters during the cruise. Air sampler was set on the central front of the upper deck. The collected samples were kept in freezer until analysis in laboratory. After extraction by ultra pure water (18.3 MΩ; Milli-Q), each water-soluble constituent was analyzed with an ion chromatograph.

Aerosol particles were also collected on Nuclepore filters with the 0.4-µm pore size to measure the size distribution of water-insoluble particles. The size distribution was measured with a Coulter Counter (Beckman-Coulter Inc. Multisizer III) after collected samples were dispersed into electrolyte with an ultrasonic cleaner.

Figure 1 shows the cruise tracks for 2002 (left panel) and 2003 (right panel). The region (A) in the left panel and the regions (B) and (C) in the right panel are selected for extracting the different feature of aerosol properties to be referred to in the following discussion.

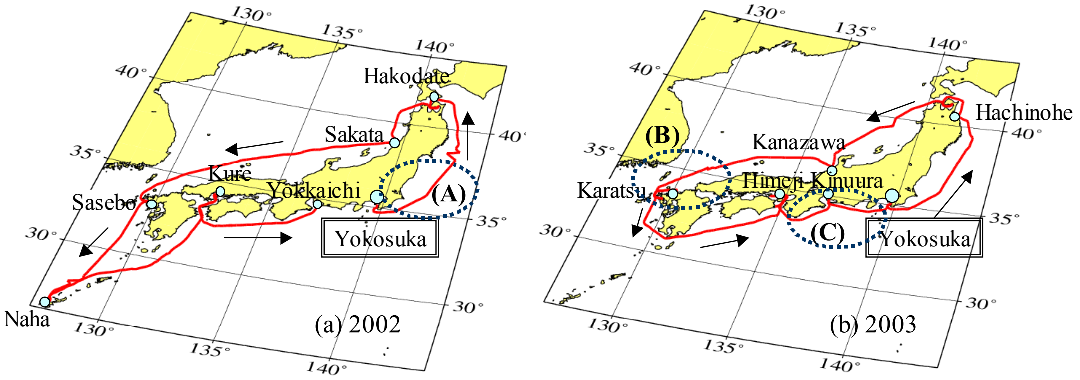

Figure 1. Cruise tracks of the R/V *Shirase* JARE Training Cruise for (a) 2002 and (b) 2003.

3. Results and discussion

3.1. Weather condition and air trajectories

The weather conditions during the 2002 cruise are briefly described below. Although a typhoon was moving north in the western part of Japan in the end of August 2002, the weather was rather fine under a high pressure system centered in the North-Western Pacific Ocean, that is, the meteorological situation was typical for Japan's summer until 2 September. Then a high pressure system located in the north of China was coming strong, and yielding stationary fronts over Japan by competing with another high pressure system over the ocean for 7 – 12 September when R/V *Shirase* was cruising in the Sea of Japan and the East China Sea. Since 14 September, during the latter half of the cruise from Naha, cyclones accompanied by fronts were alternately passing through the southern part of the mainland. That was a normal weather pattern of the summer – autumn transition season in Japan.

The weather conditions for September and early October of 2003 were rather normal with alternately traveling cyclone and high pressure systems. Another significant feature of meteorological situation during the 2003 cruise is that two typhoons, Typhoon 14 and Typhoon 15, have passed in the vicinity of Japan Islands. Passing of these typhoons caused atmospheric disturbance and air mass exchange along with strong wind and precipitation. Thus the atmospheric situation for the 2003 cruise was quite different from the 2002 cruise while the summer of 2002 had remained in early September.

Figure 2 shows the results from the 5-day backward trajectory analysis calculated from 1000 m above sea level for some selected cases along the ship track of the 2002 cruise (left panel) and the 2003 cruise (right panel). The NOAA HYSPLIT4 Model (Draxler and Rolpf, 2003) with the vertical motion mode was employed for this analysis. During the cruise in 2002, the trajectories indicated that the air mass was transported from the various areas; e.g., from remote Pacific Ocean during the Pacific Ocean leg (Region (A) in Fig. 1), from Chinese Continent during the Sea of Japan leg, and sometimes across the Mainland Japan. On the other hand, in the case of 2003, the air mass mostly passed over the continent (and the Mainland) by the northwesterly wind.

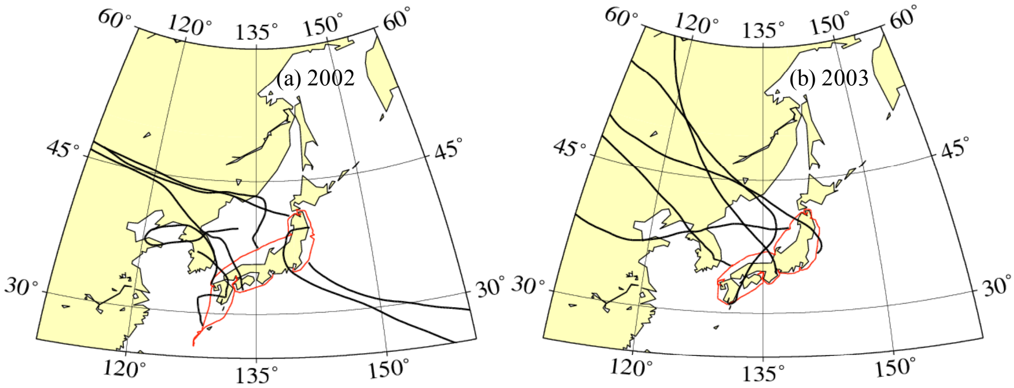

Figure 2. Five-day backward trajectories with the vertical motion mode for (a) the 2002 cruise and (b) the 2003 cruise.

3.2. Chemical properties of water-soluble aerosol particles

Selected chemical compositions for anthropogenic aerosols and natural sources are shown in Fig. 3. Describing in general on the size and composition of aerosols for both cruises in 2002 and 2003, sea-salt (Na$^+$, top panels), and NO_3^- (second top panels) were mostly distributed in coarse modes (D = 2-6 μm and >6 μm). In contrast, nss- (non-sea-salt) SO_4^{2-} (second bottom panels) was present in fine (D = 0.2 – 2 μm) and Aitken (D<0.2 μm) modes. Particulate oxalate (bottom panels) was mostly distributed in both coarse (D = 2-6 μm) and fine (D = 0.2-2 μm) modes.

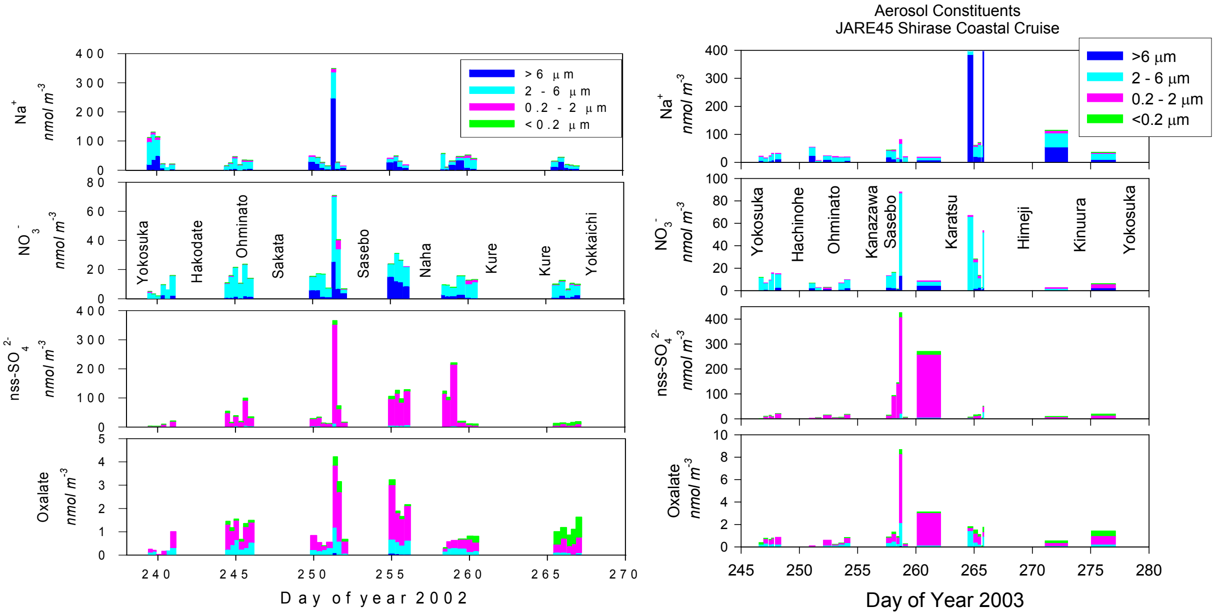

Figure 3. Variations of aerosol constituents (Na$^+$, NO_3^-, nss-SO_4^{2-}, and oxalate) during the 2002 (left panel) and 2003 (right panel) cruises.

During the cruise of the region (A) in 2002, sea-salt particles were dominant and the concentrations of anthropogenic species such as particulate NO_3^-, non-sea-salt (nss-) SO_4^{2-} and oxalate were quite low. According to the trajectory analysis described earlier, the air mass in the region (A) is identified as clean maritime air from the remote Pacific Ocean.

On the other hand, the most significant chemical feature of anthropogenic aerosols is found in the results from cruises off shore the west of Kyushu Island both in 2002 and 2003. From the 2002 cruise, the concentrations of anthropogenic species such as NO_3^-, nss-SO_4^{2-}, and oxalate in the region around Sasebo and Naha were evidently higher than those in the region (A). The backward trajectory suggested that human activities in Chinese continent, Korean Plateau and Japan Islands might affect to the quality of air masses in the marine boundary layer during the cruise off shore Kyushu Island. Also from the 2003 cruise, the highest concentrations of anthropogenic species were observed in the region (B) corresponding to high number concentration of aerosol particles, especially in fine particles. Despite of clear sky on 17 September, the atmospheric visibility at Sasebo was lower than 10 km due to heavy haze. The backward trajectory exhibited that air mass loading anthropogenic species had passed in boundary layer – lower free troposphere over Korea, Yellow Sea, the northeast area of China for the previous five days.

3.3. Size distribution of water-insoluble aerosol particles

Figure 4 shows the volume-size distribution of water-insoluble aerosol particles to see difference in the results from the Pacific Ocean cruise (28-29 August 2002) and the East China Sea cruise (12-13 September 2002). The error bars mean standard deviations of blank samples. During the 28-29 August cruise, corresponding to the region (A), water-insoluble particles were not significantly detected. As shown in earlier, during the cruise of the region (A), the air was transported mainly from the central Pacific Ocean, so that water-insoluble aerosols such as soil and solid dust were not expected in the air mass.

On the other hand, the result from the 12-13 September cruise shows evidently a different size distribution. As soil particles generally show a log-normal size distribution, the measured size distribution can be decomposed to a log-normal distribution for soil particles and a power-law distribution. From the curve fitting for the 12-13 September measurement, the existence of the log-normal size distribution with the geometrical mean radius of 1.35 μm and the geometrical standard deviation of 1.55 was found. During the 12-13 September cruise, the air was transported mainly from Korea and the northeast of China, and possibly included soil particles originated in these areas. However, it should be noted that uncertainty in the absolute values of the volume-size distribution still remains due to uncertainty of the extraction efficiency of particles deposited on a filter into electrode and due to smash of extracted particles by ultrasonic cleaning.

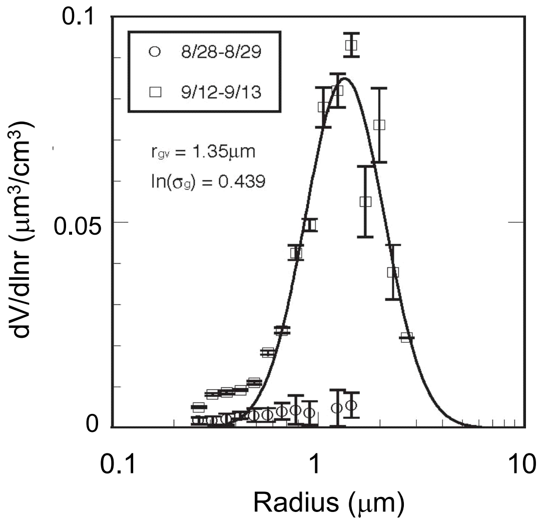

Figure 4. Volume-size distribution of water-insoluble particles measured by a Coulter Multisizer for the Pacific Ocean cruise (8/28-8/29, circles) and the East China Sea cruise (9/12-9/13, squares). The curve shows a log-normal size distribution fit to the 9/12-9/13 result.

3.4. Optical and physical properties

Figures 5 and 6 depict spatial variations of (a) the extinction coefficient at 565 nm, (b) the single scattering albedo at 565 nm, and (c) the ratio of the number density of the 0.15-0.25 μm radius bin to that of the 0.25-0.5 μm radius bin, for the 2002 and 2003 cruises, respectively. The present study focuses on the three regions (A, B and C) as shown in Fig. 1. In the region (A), the air mass was transported from central Pacific Ocean without passing over land surfaces. In addition, large and non-absorbing particles were dominant as indicated in Fig. 5 (b) and (c). The main source in this region might be identified as maritime aerosols. In the region (B), a strong haze event was observed. The absolute value of the extinction coefficient indicated the highest in the whole cruise of 2003. It was correlated with the increase of fine particles. As described in the previous section, simultaneous measurements of chemical constituents of aerosol particles revealed that the concentrations of anthropogenic species such as nss-SO_4^{2-}, oxalate, and NO_3^- gradually increased in the region (B). Also, the backward trajectory showed the outflow from Korea and Chinese continent. In the region (C), the single scattering albedo was relatively low due to the increase of absorbing particles. Based on the trajectory analysis, it is suggested that the air in the region (C) was polluted by human activity in the Mainland.

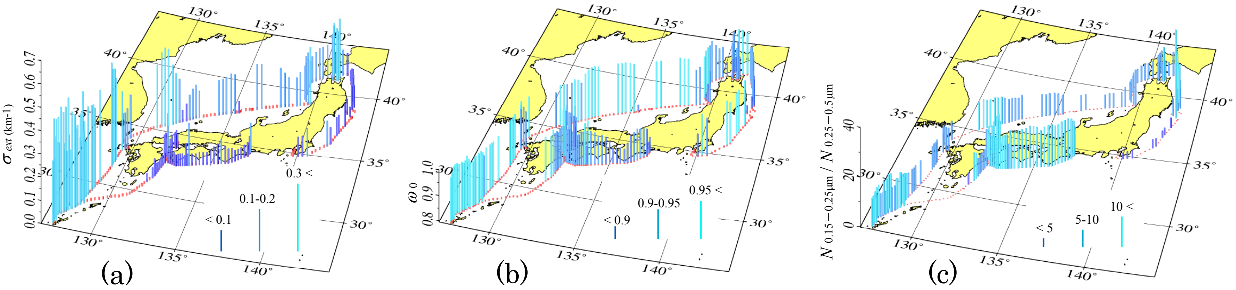

Figure 5. (a) The extinction coefficient, (b) the single scattering albedo, and (c) the number density ratio of the 0.15 – 0.25 μm radius bin to the 0.25 – 0.5 μm radius bin for the 2002 cruise.

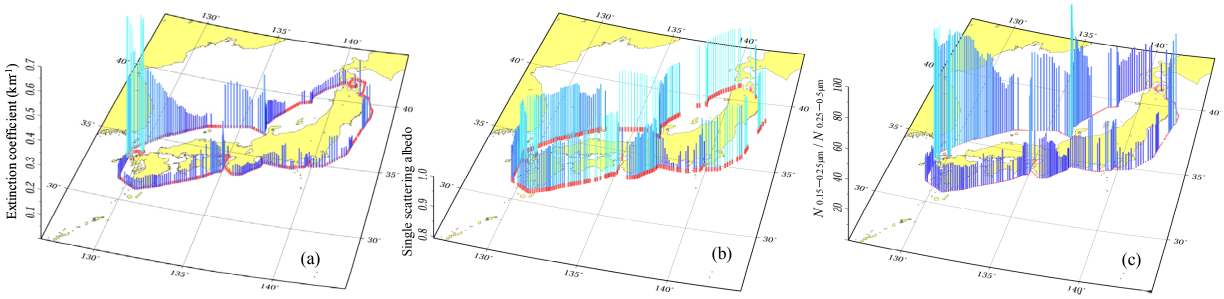

Figure 6. Same as Figure 4 but for the 2003 cruise.

The complex refractive index was retrieved by a method proposed in Yabuki et al.(2003). The procedure was applied for simultaneous measurements of the aerosol size distribution, scattering coefficient and absorption coefficient with OPC, IN and PSAP. Generally speaking for the result, the averaged imaginary part of the refractive index during the 2003 cruise was about 0.005. This value was twice as large as that for the 2002 cruise. With regard to the selected regions in Fig. 1, the values of the imaginary part in the regions (A, B and C) were ranged in 0-0.001, 0.001-0.004, and 0.004-0.015, respectively. The values of the real part ranged in 1.38-1.40 for the region (A) and 1.51-1.57 for the region (C). Existence of sea-salt rich aerosol particles is reflected on such low values of the imaginary index in the region (A) as supposed from the chemical analysis described earlier. The complex refractive index for the region (A) was nearly consistent with that for maritime aerosols. Slightly high but rather low imaginary values in the region (B) under the haze condition might be affected by reduced absorption of aerosol particles due to the increase of the scattering matters with water-soluble particles such as sulfate. High values of both real and imaginary indices in the region (C) were possibly caused by aerosol particles mixed with soil dust and anthropogenic pollution.

4. Summary

We described optical, physical and chemical properties of aerosols in the marine boundary layer around Japan Those aerosol properties were quantitatively obtained from optical and chemical measurements on board the R/V *Shirase* in 2002 and 2003. The result shows some characteristic features of aerosol properties and their difference in spatial distribution. Summarizing the result, we can understand that the marine boundary layer aerosol mainly consists of maritime sea-salt particles from remote ocean, soil dust and sulfate aerosol from Chinese Continent, and the anthropogenic aerosol produced in Japan and neighboring countries including Korea and China. The mixing state of these aerosols is strongly related to the air mass origin and history. The trajectory analysis must be helpful for understanding the fraction of mixing of each aerosol. The practical values of the aerosol optical parameters obtained in this study are expected to improve the accuracy in estimating the aerosol direct radiative forcing in the East Asia.

Acknowledgments

The present study was done with the Grant-in-Aid for Scientific Research in Priority Areas, Gr. No. 14048228, supported by the Ministry of Education, Culture, Sports, Science and Technology. Aerosol measurements on board the R/V *Shirase* were carried out as part of the JARE-44, 45 and 46 Training Cruise Program operated by Japan Defense Agency. This work was partly arranged for a collaborative research program of CEReS, under Project III led by Prof. Kuze of Chiba University.

References

Draxler, R.R. and G.D. Rolph, 2003: HYSPLIT (HYbrid Single-Particle Lagrangian Integrated Trajectory) Model access via NOAA ARL READY Website (http://www.arl.noaa.gov/ready/hysplit4.html). NOAA Air Resources Laboratory, Silver Spring, MD.

Shiobara, M., K. Hara, M. Yabuki, and H. Kobayashi, 2004a: Optical and chemical properties of the marine boundary layer aerosol around Japan from the R/V Shirase 2002 shipboard measurement. Submitted to *J. Meteorol. Soc. Japan*.

Shiobara, M., N. Kaneyasu, K. Hara, M. Yabuki, H. Kobayashi, K. Osada and T. Murayama, 2004b: Field experiments for the direct effect of aerosols: Results from R/V Shirase and Chichi-jima. *Atmospheric Environmental Impacts of Aerosols in East Asia (AIE) Research Report 2003, March 2004, Ed. M. Kasahara,* 115-122.

Yabuki, M., M. Shiobara, H. Kobayashi, M. Hayashi, K. Hara, K. Osada, H. Kuze, and N. Takeuchi, 2003: Optical properties of aerosols in the marine boundary layer during a cruise from Tokyo, Japan to Fremantle, Australia. *J. Meteorol. Soc. Japan*, **81**, 151-162.

Yabuki, M., M. Shiobara, K. Hara, and H. Kobayashi, 2004: Optical properties of aerosols in the marine boundary layer around Japan. *Nucleation and Atmospheric Aerosols 2004: 16th Int l Conf., Ed. M. Kasahara and M. Kulmala,* Kyoto Univ. Press, 772-775.

Observation on Radiative Properties of Aerosol Particles Over the Urban Area of Nagoya

Pradeep Khatri[1], Yutaka Ishizaka[2], and Tamio Takamura[3]

[1] *Graduate School of Environmental Studies, Nagoya University, Furo-cho, Chikusa-ku, Nagoya, 464-8601, Japan*
[2] *Hydrosphoric Atmospheric Research Center, Nagoya University, Furo-cho, Chikusa-ku, Nagoya, 464-8601, Japan*
[3] *Center for Environmental Remote Sensing, Chiba University, Yayoi-cho, Inage-ku, Chiba shi, Chiba, 263-8522, Japan*

ABSTRACT

In order to understand the effects of anthropogenic air pollutants on atmospheric heat budget, the radiative properties of aerosols were investigated over the urban area of Nagoya. Measurements included size distributions of aerosols greater than 0.3 μm in diameter, scattering coefficients and absorption coefficients. The mean values with standard deviations for hourly averages of scattering coefficients, absorption coefficients and single scattering abledos were reported to be $52.3 \pm 39.3 \mathrm{Mm^{-1}}$, $24.6 \pm 18.3 \mathrm{Mm^{-1}}$ and 0.66 ± 0.13 respectively. Such low values of single scattering albedos suggest that aerosols of the urban area of Nagoya are highly absorptive in nature, which have a potential to warm our climate. Comparison of our results with other polluted cities of US and China were also performed. Mass scattering efficiency of dry aerosols and mass absorption efficiency of black carbon over the urban area of Nagoya were found to be around $4.7 \mathrm{m^2 g^{-1}}$, and $14.6 \mathrm{m^2 g^{-1}}$ respectively. Before and after the rain events, diurnal variations of radiative properties were observed. Such diurnal variations were suggested to be driven by local pollutants rather than meteorological changes throughout the day. The prominent peaks of black carbon concentrations and absorption coefficients during morning were suggested to be the effects of local sources such as burning and vehicles whereas peaks of scattering coefficients observed during afternoon were found to be the effects of photochemically driven aerosol production. Two different effects of rain events on scattering coefficients were also observed. It was estimated by the observation data that the rain events reduced scattering coefficients by washing out coarse and accumulation mode aerosols, whereas the continuous rain events increased scattering coefficients by condensing water vapor to non-washed aerosols of the atmosphere.

Keywords: Air pollutants, scattering coefficients, absorption coefficients, black carbon, single scattering albedo

1. INTRODUCTION

An estimate of the total global radiative forcing due to the direct and indirect effects of atmospheric aerosols has become a subject of debate in recent years. Unlike well-mixed greenhouse gases, the climatic impact of anthropogenic aerosols is still subject to large uncertainties [*Penner et al.,* 2001]. Spatial and temporal variations of aerosols with short life time in the atmosphere, seasonal nature of aerosol emissions, insufficient information regarding the mixing state of aerosols in the atmosphere and nonuniform relative humidity dependency of physical and optical properties of different aerosol species have arisen difficulties to accurately model the radiative forcing of aerosols in a global scale. For this reason, it is very necessary to measure and study the aerosol radiative properties at various locations around the Earth.

Several field campaigns such as ACE1, ACE2, INDOEX, TARFOX, LACE98 and APEX were designed to investigate the aerosol properties at different parts of the Earth to reduce existed scientific uncertainties. However the role of aerosols over polluted urban areas that contain highly absorbing boundary layer particles is still not very well investigated. To our knowledge, there have not been measurements of aerosol radiative properties reported for the urban area of Nagoya ($35^0$7'N, $136^0$58'E). The existence of costal industrial zones at around Nagoya port with heavy industries such as iron and steel, an oil refinery, petrochemicals, gas production, power generation, and so on emit a large amount of anthropogenic aerosols. Further, air pollution by automobile exhaust is also high in Nagoya. The major components of Nagoya urban aerosols are reported to be organic aerosols and elemental carbon [*Kadowaki*, 1990]. *Kasahara et al.* [2000; Personal communication] also reported of around 51% of elemental carbon in this region. Aerosols with high fraction of light absorbing black carbon have a potential to warm our climate. In recognition of this situation, it is of interest to study optical properties of aerosols over the urban area of Nagoya.

2. INSTRUMENTATION AND DATA

Aerosol measurements were made at the 5th floor of Hydrospheric-Atmospheric Research Center (HyARC) of Nagoya University located in the east section of the city. The experimental place is unique in that traffic is for the most part prohibited on campus and therefore the measurements don't include short-term peaks from very nearby mobile sources, but instead reflect the broad average conditions over the eastern Nagoya. A nephelometer (Model M903, Radiance Research) was used to measure the light scattering coefficient(σ_{sp}) at 530nm. The instrument was calibrated prior to the experiment using clean (particle-free) air as well as CO_2 for the span gas. The light absorption coefficient (σ_{ab}) was measured at 565nm using a Particle Soot Absorption Photometer(PSAP) (Radiance Research). At the same time mass concentration of black carbon was measured using a 7-wavelength "Spectrum" aethalometer (Model AE 30, Magee Scientific). Number concentrations of aerosol particles larger than 0.3 μm in diameter were measured using Laser Particle Counter (LPC) (Model TF-500,Kanomax). Meteorological data were obtained from Nagoya Regional Observatory, JMA.

3. RESULTS AND DISCUSSION

3.1. TIME SERIES OF AEROSOL RADIATIVE PROPERTIES

Figure1 shows statistical analysis of daily scattering coefficient and black carbon concentration(μg/m^3) of aerosols from July 23, 2004 to September 5, 2004. The measured scattering coefficients ranged from 5 Mm^{-1} to 222 Mm^{-1}, resulting in a mean value with standard deviation of 52.3±39.3Mm^{-1}. Similarly the measured black carbon (measurement made by aethalometer at 880nm wavelength) concentration ranged from 0.1 μg/m^3 to 8.0 μg/m^3, resulting in a mean value with standard deviation of 1.7±1.25 μg/m^3. The measured scattering coefficients showed excellent correlation with total number of particles measured by LPC (R^2=0.98). There was not a clear relationship between total particle number concentration, scattering coefficient and black carbon concentration with wind speed. On the other hand, particle number concentration and scattering coefficients showed relationship with wind direction. Statistical analysis results showed that westerly winds reaching the observation site were characterized by relatively high particle number concentrations and high scattering coefficients whereas south south easterly and south easterly winds reaching the observation site were characterized by comparatively low particle number concentrations and low scattering coefficients. Not surprisingly, the coastal industrial zones which is the main source of anthropogenic aerosols are located at the west side of observation site whereas pacific ocean is located at the south south east and south east direction of the observation site.

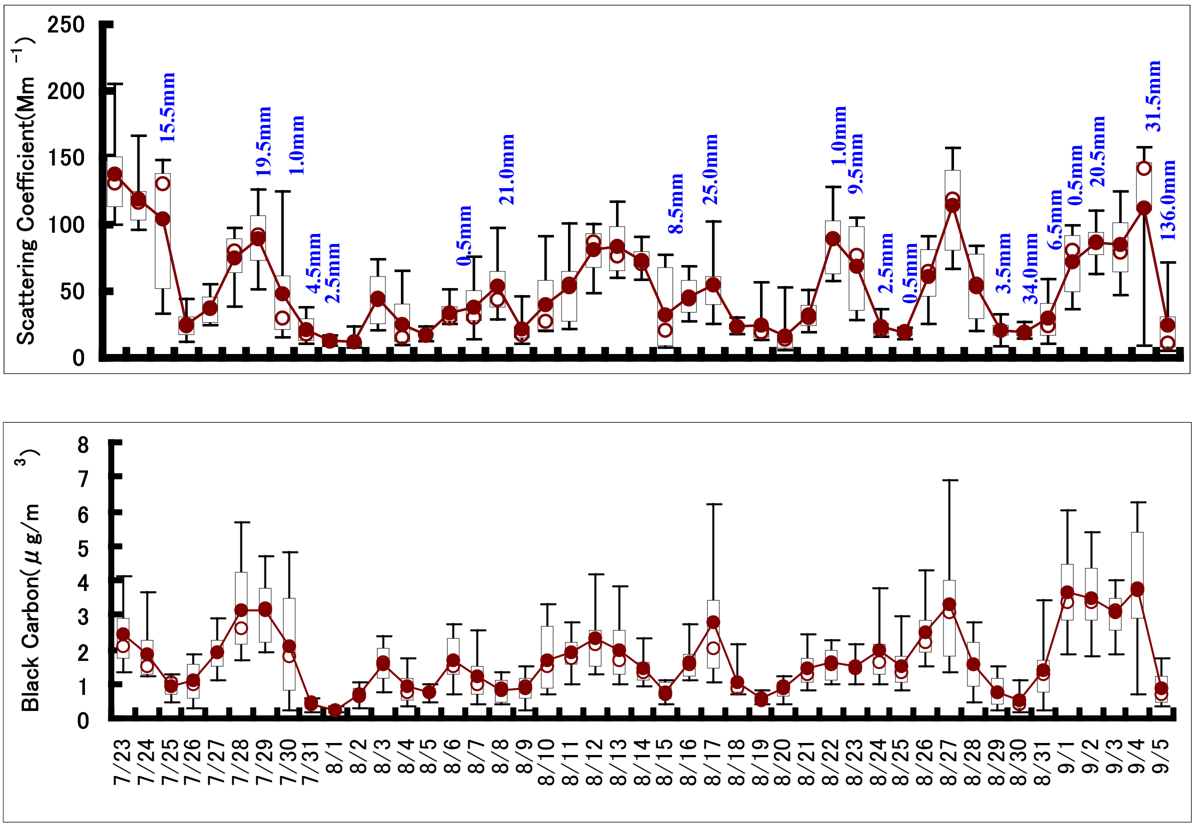

Figure 1. Time series of the scattering coefficients (Upper) at 530nm and mass concentrations of black carbon (Lower) at urban area of Nagoya, between 23 July and 5 September. Boxes are determined by the 25th and 75th percentiles, and whiskers are determined by the 5th and 95th percentiles. Close circles with the solid line and open circles show the daily mean and median of hourly averaged data respectively.

Two effects of rain events were observed during the entire study period. The first effect showed the decrease of scattering coefficients and the second effect showed the increase of scattering coefficients. Sharp decrease of scattering coefficient on 26 July after a light rain event on 25 July, the lowest scattering coefficient detected on 2 August followed by a continuous decrease of scattering coefficients from 28 July due to frequent rain events observed on 28 July, 29 July, 30 July, 31 July, and 1 August and decrease in scattering coefficients from 22 August till 25 August followed by frequent rain events on 22 August, 23 August, 24 August, and 25 August were suggested due to washout of atmospheric aerosols by rain events. The second effect showed the increase of scattering coefficient during rain events. Most probably rain events occurred on 29 August and 30 August had greatly washed out the aerosols of the atmosphere and the increase of scattering coefficients from 30 August to 2 September were due to the effects of relative humidity. It should be noted that nephelometer was not completely drying the aerosol, and therefore a significant amount of measured light scattering was due to condensed water. More or less similar effects of rain events were observed on mass concentrations of black carbons. *Chen et al.* [2001] suggested that elemental carbon from atmosphere is removed primarily through precipitation scavenging after it is internally mixed with salts (such as sulfate) and becomes soluble. The precipitation scavenging of black carbon suggested that black carbon might have internally mixed with sulfate in the urban area of Nagoya.

With the estimated absorption efficiency of black carbon as 14.6 m^2/g in the urban area of Nagoya (see section 3.3), absorption coefficients were calculated from mass concentration of black carbon to estimate single scattering albedos of aerosols. The mean value with standard deviation of the overall experimental period was found to be 0.66±0.13. Note that the average single scattering albedo may increase by certain percentage after correcting absorption coefficient data measured by PSAP instrument for both light scattering and instrument overestimation as described by *Bond et al.* [1999] and after correcting angular truncation of nephelometer. This part of work is on progress and will be reported during the presentation. The previous study reported the single scattering albedo of around 0.55 from the analysis of physical and chemical properties of urban aerosols of Nagoya [*Kasahara et al.,* 2000; Personal communication]. Overall, it was found that aerosols of Nagoya are highly absorptive in nature, which have a potential to warm the climate.

3.2. DIURNAL VARIATION OF AEROSOL RADIATIVE PROPERTIES

Before and after the rain events all the aerosol properties exhibit a characteristic diurnal cycle. Figure 2 shows the statistical analysis of scattering coefficients and black carbon concentrations grouped by hour of a day. Statistical analyses were carried out only for the non rainy days. The peaks in mean scattering coefficients were observed at 1100-1500 JST with the highest peak at 1300 JST. The cycle is even more pronounced when looking at the 75th and 95th percentile populations.

It was suggested that number concentration of aerosol particles were reduced during morning and night time as a result of coagulation and highly reduced sources and OH productions when there was little or no solar insolation [*Iziomon and Lohmann*, 2003]. During afternoon, sulfate formation from SO_2 emissions from local power plants or refineries, photochemically driven productions of organic or N-containing particles were possible. The highest values of total particle number concentrations and scattering coefficients were noticed under clear skies relative to cloud sky and all sky conditions in increasing difference in the afternoon. It was observed that the frequency of westerly winds reaching the observation site was higher in afternoon that morning and night This suggested that photochemically driven aerosol production was the main reason for high peaks of scattering coefficients observed at afternoon in our study location. Further mass scattering efficiency of aerosols below $4.7m^2g^{-1}$ during afternoon (see section 3.3) suggested that sulfate aerosols were dominant.

The pronounced morning peaks of black carbon concentrations observed at 0500-0800JST might be the effects of local sources such as burning and vehicles.

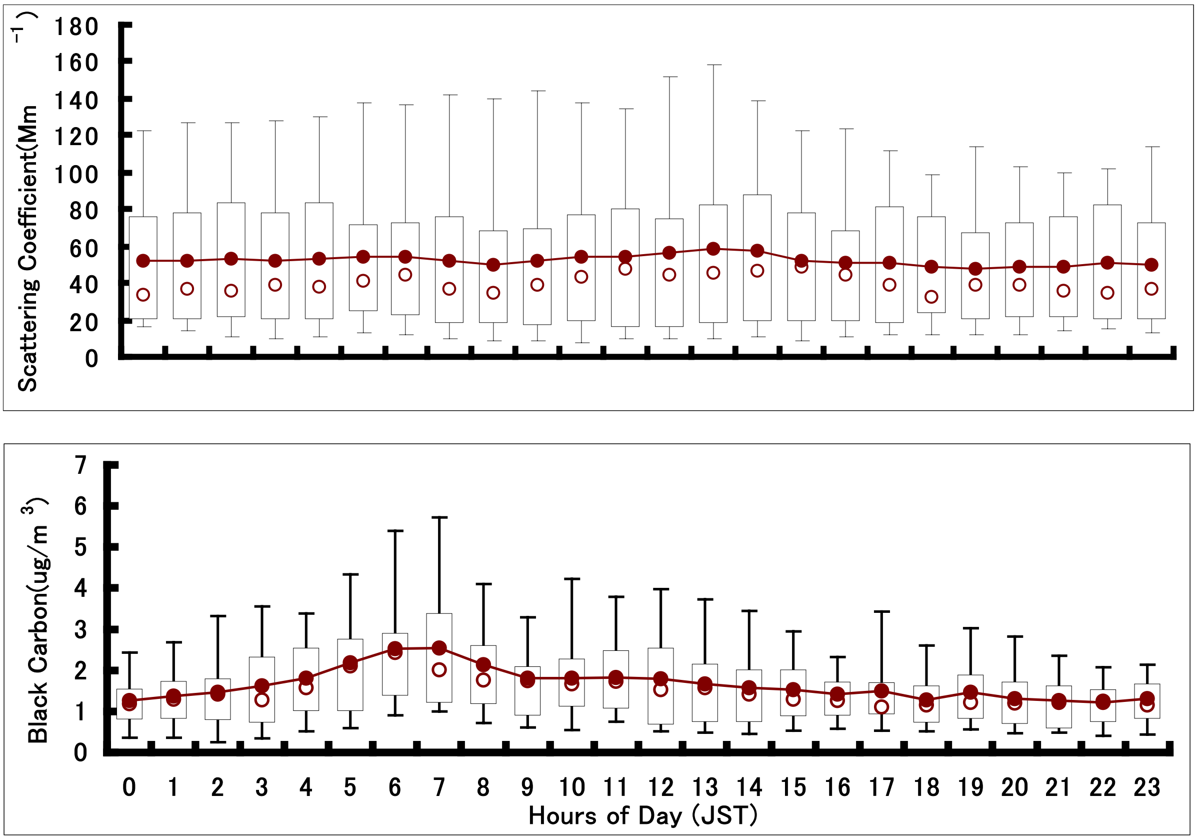

Figure 2. Statistical analysis showing hourly averages of scattering coefficients (Upper) at 530nm and mass concentrations of black carbon (Lower) over the non rainy days of field campaign from 23 July to 5 September. Boxes are determined by the 25th and 75th percentiles, and whiskers are determined by the 5th and 95th percentiles. Close circles with the solid line and open circles show the daily mean and median of hourly averaged data respectively.

The calculated daily cycles of hourly averaged single scattering albedos from the information of daily cycles of hourly averaged scattering coefficients and hourly averaged absorption coefficients showed quite similarity with hourly averaged absorption coefficients but inversely related. This suggested that the single scattering cycle was being driven more by the variability in absorption coefficient than the variability in scattering coefficients.

3.3. MASS SCATTERING EFFICIENCY OF DRY AEROSOLS AND MASS ABSORPTION EFFICIENCY OF BLACK CARBON

From the hourly averaged size distributions of relatively dry aerosols with ambient RH less than 60%, we calculated the mass concentrations of aerosols considering the density of dry aerosols as 1.7gcm^{-3}. Calculated mass concentrations were plotted against the scattering coefficients as shown in figure 3(left). An excellent correlation between mass concentration of aerosols and scattering coefficients with R^2=0.93 was found. The estimated mass scattering efficiency was 4.7m^{2}g^{-1}. This value could be considered as the upper limit mass scattering efficiency of urban aerosols in Nagoya because the minimum detection size range of LPC instrument was 0.3 μ m and masses of aerosols below 0.3 μ m weren't included. Since aerosols of the afternoon hours were comparatively dry and ambient relative humidity generally dropped below 60%. Thus the reported mass scattering efficiency could be considered as the representative value of aerosols of afternoon. The value falls within the range of sulfate scattering efficiency values of 2.4 to 4.7 m^{2}g^{-1} reported in previous publications [*Andrae et al.,* 2002]. Based upon this finding, it could be suggested that sulfate

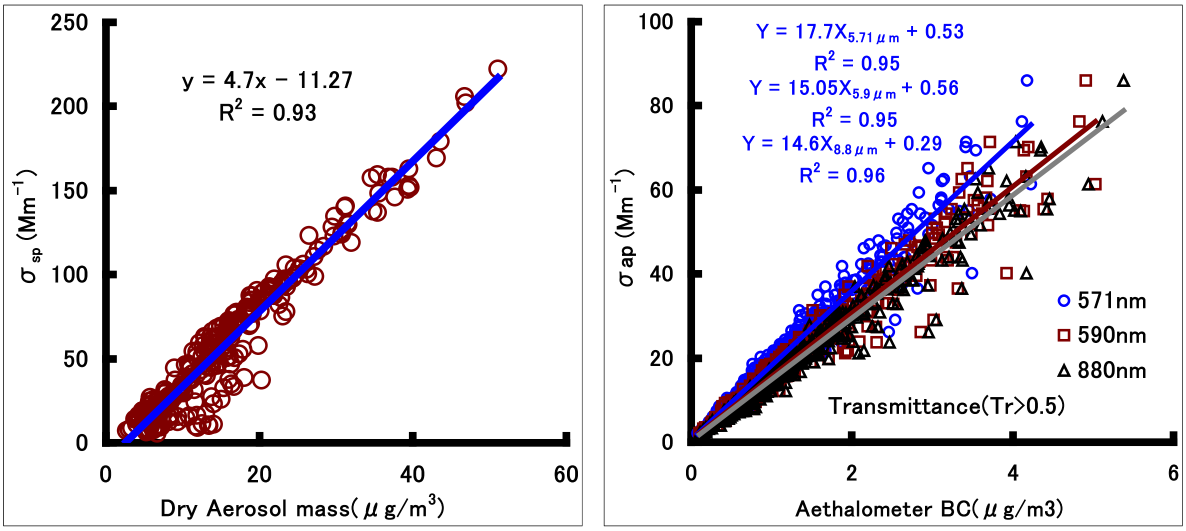

Figure 3. Mass scattering efficiency of dry aerosols with relative humidity less than 60% (Left) and mass absorption efficiency of black carbon (Right).

formation from SO_2 emissions from local power plants or refineries was the main phenomenon to increase particle number concentration and scattering coefficients during the afternoon in urban location of Nagoya.

Absorption coefficients measured by PSAP were correlated with mass concentrations of absorbing aerosols measured by aethalometer at 571nm, 590nm, and 880nm. Excellent correlations were observed between two types of measurements and the best correlation was observed between PSAP absorption coefficient and aethalometer black carbon (measured at 880nm) and value of absorption efficiency of black carbon was found to be 14.6 m^2g^{-1} with R^2=0.96. The estimated mass absorption efficiency of black carbon in this study falls within the range of reported mass absorption efficiency of 5-20 m^2g^{-1} [*Liousse et al.,* 1993]. Further, this value is comparable to the values of mass absorption efficiencies of other urban locations reported in literatures.

4. CONCLUSION

The measurement of aerosol radiative properties was performed over the urban area of Nagoya from 23 July 2004 to 5 September 2004. The measured scattering coefficients ranged from 5 Mm^{-1} to 222 Mm^{-1}, resulting in a mean value with standard deviation of 52.3 ± 39.3Mm^{-1}. Similarly the measured black carbon (measurement made by aethalometer at 880nm wavelength) concentration ranged from 0.1 μ g/m^3 to 8.0 μ g/m^3 , resulting in a mean value with standard deviation of 1.7 ± 1.25 μ g/m^3. Mass absorption efficiency of black carbon was found to be 14.6 m^2g^{-1} . Since PSAP data with Transmission (Tr>0.5) were not available for the entire field experiment, hourly averaged absorption coefficients of the entire field campaign were estimated from the information of black carbon concentrations and mass absorption efficiency of black carbon. The absorption coefficients ranged from 1.5 Mm^{-1} to 116.6 Mm^{-1} , resulting in a mean value with standard deviation of 24.6 ± 18.3 Mm^{-1}.

Light scattering coefficients of our study location was found to be comparable to the measurements of scattering coefficients observed in several urban areas of the United States over varying time periods during the 1970s which ranged from 30 to 210 Mm^{-1} [*Waggoner et al.,* 1981]. On the other hand, the mean light scattering coefficients of the urban area of Nagoya was roughly 2 times lower than the mean value of 120 Mm^{-1} measured in Atlanta (a relatively polluted city in the USA) during August 1999 as a part of Atlanta SuperSite Experiment [*Carrico et al.,* 2003], roughly 6 times lower than the mean value of 353Mm^{-1} measured in Linan, China (Agriculture Yangtze delta region of China) during November 1999 [*Xu et al.,* 2002], and roughly 9 times lower than the mean value of 488 Mm^{-1} measured in Beijing, China during June 1999 [*Bergin et al.,* 2001].

Light absorption coefficients of our study location was found to be comparable to the absorption coefficients made at several urban locations of US over varying time periods during the 1970s which ranged from 27 to 118 Mm^{-1}[*Waggoner et al.,* 1981]. The mean value of absorption coefficients of our study location was higher than the mean value of 16 Mm^{-1} in Atlanta, US reported by *Carrico et al.* [2003], comparable to the mean value of 23 Mm^{-1} in Linan, China reported by *Xu et al.* [2002], and roughly 4 times lower than the mean value of 88 Mm^{-1} in Beijing, China reported by *Bergin et al.* [2001].

The diurnal pattern of scattering coefficients in the urban area of Nagoya was characterized by peak values during afternoon, which was suggested due to photochemicaly driven aerosol productions. The pronounced morning peaks of black carbon concentrations and absorption coefficients observed during morning were suggested due to the effects of local sources such as burning and vehicles.

Overall, aerosols of Nagoya are characterized by high absorbing aerosols, which result to very low single scattering albedo and have a potential to warm our climate by absorbing solar radiation.

5. ACKNOWLEDGEMENT

The authors would like to express sincere thanks to Mr. Tomokazu Takahashi, Ms. Mandira Adhikari and Mr. Kazuo Yamamoto of Hydrospheric Atmospheric Research Center, Nagoya University for their sincere help during field observation.

6. REFERENCES

Andreae, T. W., M. O. Andreae, and C. Ichoku, Light scattering by dust and anthropogenic aerosol at remote site in the Negev desert, Israel, *J. Geophys. Res., 107(D2)*, 10.1029/2001JD900252, 2002.

Bergin, M. H., G. Cass, J. Xu, C. Fang, L. Zeng, Y. Tong, C. S. Kiang, and W. L. Chameides, Aerosol radiative, physical and chemical properties in Beijing during June, 1999, *J. Geophys. Res., 106*, 17,969-17,980, 2001.

Bond T. C., T. L. Anderson, and D. Campbell, Calibration intercomparison of filter-based measurements of visible light absorption by aerosols, *Aerosol Sci. technol.,* 30, 582-600, 1999.

Carrico, C. M., M. H. Bergin, J. Xu, K. Baumann, and H. Maring, Urban aerosol radiative properties: Measurements during the 1999 Atlanta Supersite Experiment, *J. Geophys. Res., 108(D7),*8422, doi:10.1029/2001JD001222, 2003.

Chen, L. -W. A., B. G. Doddridge, R. R. Dickerson, J. C. Chow, P. K. Mueller, J. Quinn, and W. A. Butler, Seasonal variations in elemental carbon aerosol, carbon monoxide and sulfur dioxide: Implications for sources, *Geophys. Res. Lett., 28(9)*, 1711-1714, 2001.

Iziomon, M. G., and U. Lohmann, Characteristics and direct radiative effect of mid-latitude continental aerosols: the ARM case, *Atoms. Chem. Phys.,* 3, 1903-1917, 2003.

Kadowaki, S., Characterization of carbonaceous aerosols in the Nagoya urban aera. 1. Elemental carbon and organic carbon concentration and the origin of organic aerosols, *Environmental science and technology*, pp. 741-744, 1990.

Liousse, C., H. Cachier, and S. G. Jennings, Optical and thermal measurements of black carbon aerosols content in different environments: variation of the specific attenuation cross-section, sigma (σ), *Atmos. Environ.,27(8)*, 1203-1211, 1993.

Penner, J., R. Leaitch, D. Murphy, J. Nganga, G. Pitari, Aerosols, their direct and indirect effects, in *Climate Change: The Scientific Basis*, edited by J.Houghton, Y. Ding, D. J. Griggs, M. Noguer, P. J. van der Linden, X. Dai, K. Maskell, C. A. Johnson, pp. 289-348, Cambridge Univ. Press, New York, 2001.

Waggoner, A. P., R. E. Weiss, N. C. Ahlquist, D. S. Covert, S. Will, and R. J. Charlson, Optical characteristics of atmospheric aerosols, *Atmos. Environ.*, 15, 1891-1909, 1981.

Xu, J., M. H. Bergin, X. Yu, G. Liu, J. Zhao, C. M. Carrico, and K. Baumann, Measurement of aerosol chemical, physical and radiative properties in the Yangtze delta region of China, *Atmos. Environ.*, *36(2)*, 161-173, 2002.

Dust storm observations in Mongolia in spring 2004

Jugder DULAM (Ph.D) and Erdenetsetseg BAASANDAI
Institute of Meteorology and Hydrology

ABSTRACT

A study on dust storms observed over the territory of Mongolia from January to May in 2004 was carried out. Asian regional and local weather maps at surface and 500-hPa level, and NOAA satellite images were used for the study. The study focused on formation, intensity and movement of dust events originated in Mongolian Gobi Desert area. Atmospheric circulation factors causing formation of dust events are reviewed.

During the spring, there were 10 cases of strong dust events and 6 moderate or weak dust events in Mongolia. About 6 of them arrived at and Japan via NE China and the Korean Peninsular. Favourable and unfavourable conditions including winter and spring snowfall for the formation of intense dust storms were studied. Snowfall amount was 1-12 mm over the Gobi Desert area from January to February, and there was no snowfall over the some areas of the Gobi Desert in those months. Monthly precipitation amount in January and February fluctuated around the climate normal between 1961 and 1990, and less than that. March and April of 2004 were the driest months in Mongolia including the Gobi Desert areas. Monthly precipitation amounts were about 0-5 mm over the most areas of Mongolia in those months. Monthly precipitation amounts were less than the climate normal over the Gobi Desert area in Mongolia in the period from March to May.

Soil wet was small in winter and spring, and it was favourable for the formation of dust storms in those periods. NOAA satellite images discover dust clouds over NE Asia in spring.

1. Introduction

The Gobi Deserts of Mongolia is a source area for the formation of dust storm in East Asia (Natsagdorj et al., 2003). Occurrences of dust storms are different every year especially in spring season. Some spring is relatively fine for dust events depending on atmospheric circulation pattern, amount of precipitation, soil condition etc. The spring of 2003 was comparatively wetter than other years and formation of dust storms was with less frequent both in Mongolia and Inner Mongolia of China (Chung et al., 2004).

The study aim was to investigate dust storms in spring 2004 in relation with precipitation amount, soil condition and atmospheric front. In addition, transportation of dusty air and indication of dust aerosols on the satellite images were compared with ground visual observations on dust storms.

2. Data used

Dust storm observations, snow cover, monthly amount of precipitation and its anomaly over the territory of Mongolia from January to May 2004 were used in the study. In addition, some examples of NOAA satellite images were included in the study.

3. Basic conditions for the formation of dust storms in Mongolia from January to May 2004

Snowfall and precipitation in January to May in 2004

Monthly amount of precipitation and its anomaly are shown in the Fig.1 and Fig.2. Monthly precipitation anomaly was less than normal over the 40-50% of the territory of Mongolia from January to March and 80-90 % from April to May. Monthly amount of precipitation was 0.1-12 mm in January to February and 0.1-37 mm from March to May. According to the precipitation data, the territory of Mongolia had received the small amount of precipitation in winter and spring 2004.

Small amount of snowfall and precipitation over the Gobi Desert areas was positive effect for the formation of dust storms.

Snow cover in January to March

Snow cover maps from January to March are shown in Fig.3. Snow depth was 0-5 cm over the Gobi Desert areas in January and February 2004. The Gobi Desert areas were no snow cover from March to May 2004. This situation is contribution for the soil dryness and formation of dust storms.

<u>Soil wet</u> Soil wet in the Gobi Desert area is not measured in Mongolia. However, precipitation and snow cover data show that soil wet was not enough and soil was dry in the Gobi Desert area in Mongolia in spring 2004. In addition, the Gobi Desert area is with scarce vegetation.

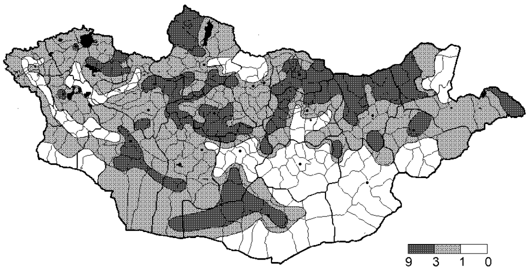

6 дугаар зураг. 1 дүгээр сард орсон тунадасны нийлбэр, мм

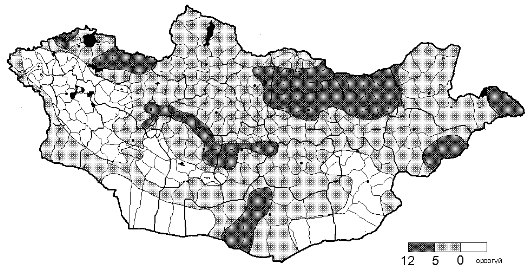

6 дугаар зураг. 2 дугаар сард орсон тунадасны нийлбэр, мм

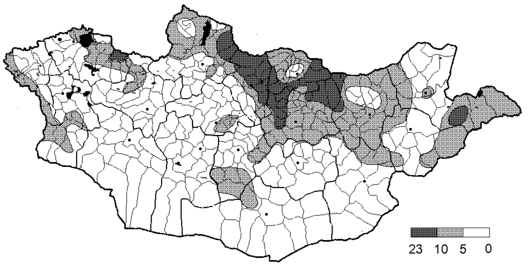

6 дугаар зураг. 3 дугаар сард орсон тунадасны нийлбэр, мм

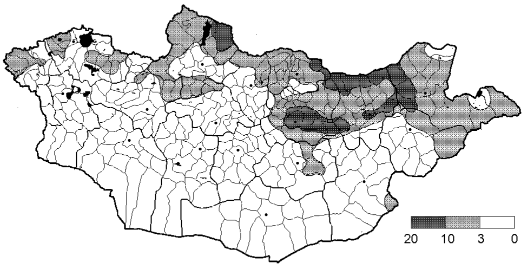

5 дугаар зураг. 4 дүгээр сард орсон хур тунадасны нийлбэр мм

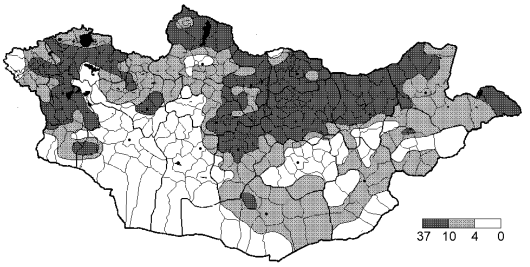

6 дугаар зураг. 5 дугаар сард орсон хур тунадасны нийлбэр, мм

Fig.1. Monthly amount of precipitation in Mongolia from January to May 2004.
From the top, January (left), February (right), March (left), April (right), May (left)

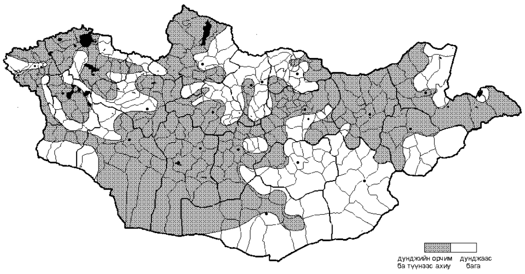

7 дугаар зураг. 1 дүгээр сард орсон тунадасны хазайлт

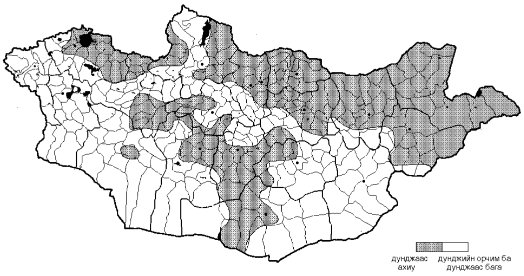

7 дугаар зураг. 2 дугаар сард орсон тунадасны хазайлт

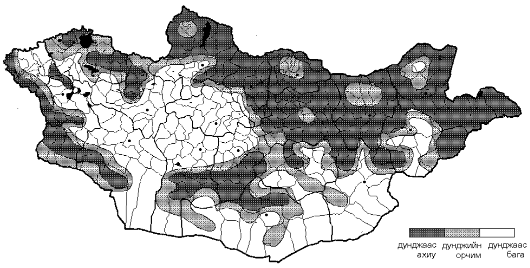

7 дугаар зураг. 3 дугаар сард орсон тунадасны хазайлт

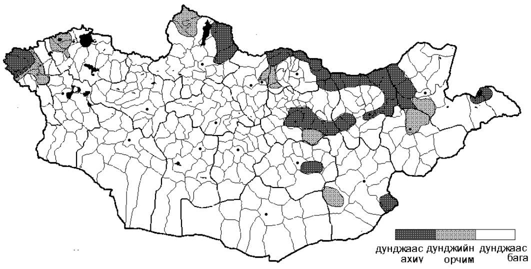

6 дугаар зураг. 4 дүгээр сард орсон тунадасны хазайц

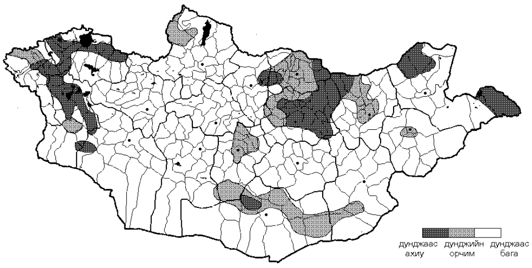

7 дугаар зураг. 5 дугаар сард орсон хур тунадасны хазайлт

Fig.2. Precipitation anomaly in Mongolia from January to May 2004.
From the top, January (left), February (right), March (left), April (right), May (left)

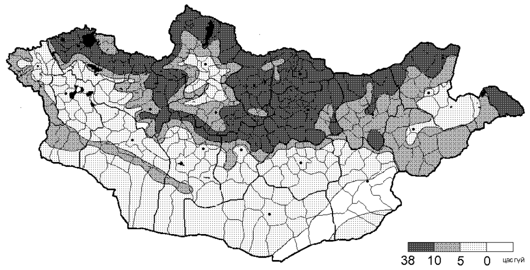

3 дугаар зураг. Цасны дундаж зузаан, см
/2004 оны 1 дүгээр сарын 31-ний байдлаар/

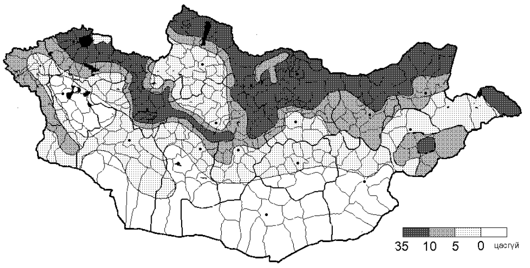

3 дугаар зураг. Цасны дундаж зузаан, см
/2004 оны 2 дугаар сарын 29-ний байдлаар/

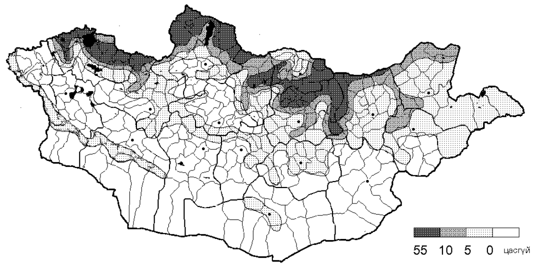

3 дугаар зураг. Цасны дундаж зузаан, см
/2004 оны 3 дугаар сарын 31-ний байдлаар

Fig.3. Snow cover in Mongolia from January to March 2004. From the top, January (left), February (right), March (left)

4. Dust storm observations in Mongolia from January to May 2004

Dust storm observations

However, soil condition in the Gobi Desert areas was drier due to the small amount of precipitation and snowfall, frequency of dust storms observed in Mongolia in spring 2004 was not many. Dust storm observations are shown in Table 1. Severe dust storms, which covered large areas, were included in Table 1. Strong winds that were 16-28 m/c could produce severe dust storms in the Gobi Desert areas with dry and loose dusty/sandy soil.

Table 1. Dusty days in Mongolia in spring 2004

2004/ Month	Day	Synoptic situation	Number of stations with dust storms	Gusty wind m/s	Commentary
February	23-24	Cold front over Mongolia on 23	19	12-28	Arrived at Japan on 26 Feb.
February	27	Cold front over Mongolia on 27	14	14-22	
March	8-9	Cold front over Mongolia on 8-9	38	12-28	Arrived at Japan on 11 March.
March	27-28	Cold front over Mongolia on 27-28	14	10-28	
April	13-14	Cold front over Mongolia on 14	36	12-24	Arrived at Japan on 17 April.
April	16-17	Zonal Cold front over Mongolia on 17	25	12-34	
April	20	Cold front over Mongolia on 20	22	12-19	Arrived at Japan on 22 April
April	27-28	Cold front over Mongolia on 27-28	23	10-24	
May	1-2	Cyclone and cold front	39	9-24	
May	4	Cold front over the east of Mongolia on 4	16	12-20	Arrived at Japan on 7 May.
May	6-8	Cyclone sector on 6 and cold front on 7-8	21	10-20	Arrived at Japan on 11 May.
May	11	Cyclone and cold front on 11	12	12-20	
May	18	Cold front over Mongolia on 18	16	12-34	

NOAA images

Detection of dust storms using satellite images is one of useful methodologies for observations because ground network is sparse in Mongolia. Also it is important for the monitoring transportation and movement of dust storms over a region included bordering and nearby countries. Dust aerosols appeared on the NOAA Satellite images are shown in the Fig. 4.

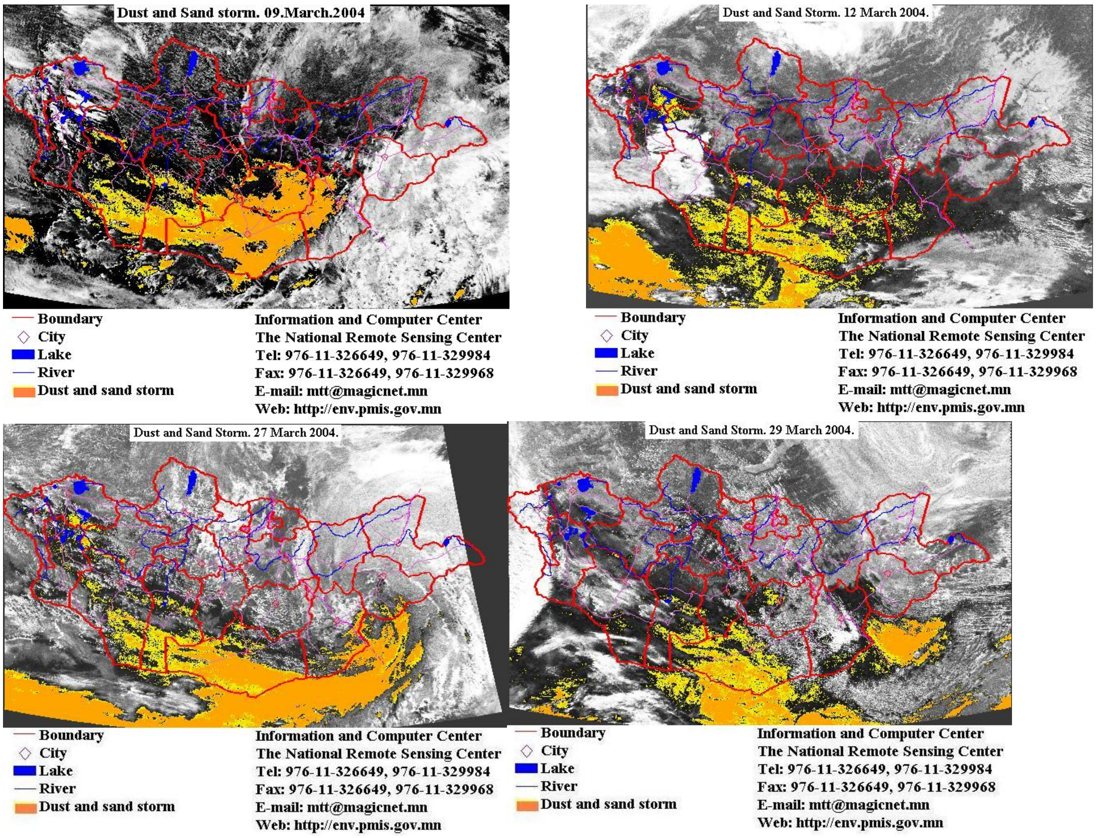
Dust and Sand storm. 09.March.2004

Dust and Sand Storm. 12 March 2004.

Dust and Sand Storm. 27 March 2004.

Dust and Sand Storm. 29 March 2004.

Fig.4. Dust aerosols appeared on the NOAA satellite images on 9, 12, 27, 29 March 2004.

5. Atmospheric situations causing formation of dust storms

In association with atmospheric cold fronts and upper air troughs arriving at the territory of Mongolia all dust storm events occurred in Mongolia in spring 2004 (Table 1). Air pressure differences in the cold frontal zone generate gusty winds and dust storms over the Gobi Desert area in Mongolia.

6. Conclusions

Passages of cold fronts, small amount of snowfall or precipitation and soil dryness were basic cause for formation of dust storms in dusty and sandy areas in the world. Snowfall, precipitation amount, soil condition and atmospheric situations are dissimilar every year and they differently influence on the formation of dust storms in Mongolia. For the winter and spring 2004, precipitation was small and soil condition was dry in the Gobi Desert areas in Mongolia. These situations were favorable for the formation of dust storms in the Gobi Desert areas.

In addition, it is necessary to measure dust concentrations and vertical distributions of aerosols in the source areas. For this purpose, NE Asian countries need to establish a joint-project and researchers need to implement a joint-study.

References

Agro-meteorological and environmental bulletin, 2004: Institute of Meteorology and Hydrology, Mongolia, No.1-15.

Chung Y.S., Kim H.S., Park K.H., Jugder Dulam and Tao Gao, 2004: Dust-storm observations in China, Mongolia and Korea from March to May 2003, *Journal of the Korean Meteorological Society*, 40, 3, 2004, p.241-257.

Natsagdorj L., D. Jugder and Y.S. Chung, 2003: Analysis of dust storms observed in Mongolia during 1937-1999, *Journal of the Atmospheric Environment*, Volume 37, Issues 9-10, (March 2003) Pages 1401-1411, Elsevier Science Ltd., Printed in the England.

The Radiation Monitoring Network of Chinese Ecosystem Research: (CERN)

Yuesi Wang

Institute of Atmospheric Physics, Chinese Academy o Sciences, Beijing 100029, China

Abstract:

Solar radiation is the original dynamical system of the earth. It is an essential parameter of Earth-climate physical process, and controls all courses of life-form on the earth. Energy from the sun sustains all life on the earth, and sustains all climate dynamic system. The differences of climate in the world are caused by different receivers of radiation energy on the surface of the earth. Ground-based radiation measurements are essential in forecasting the climatic change trends, evaluating the solar radiation transport theory in the atmosphere, assessing climate model computations, estimating retrial results by satellite, and surface radiation balance research. Radiations are also absolutely necessary parameters in environmental study.

Chinese ecosystem research network (CERN) was established in 1988. It consisted of 29 ecological research stations at beginning and expended to 36 stations in 2003, including 14 stations for agriculture, 9 for forest, 2 for grassland, 5 for desert, 1 for marsh, 2 for lake and 3 for marine ecosystems, representing diverse ecosystems. CERN has been placed as a base for ecological monitoring, research and demonstration in china. The CERN is engaged on monitoring the water, soil, atmosphere and biological elements of major ecosystems, the important ecological processes such as the energy and matter flow, and land use and land cover changes in the surrounding areas of the stations, by the standardized methods and organization. The goal of radiation monitoring is to obtain high quality dataset of radiation and ancillary measurements to develop climate model, adjust satellite retrieval, research on climate change and environment. The station map is showed in Fig 1. The routine observations of solar spectral radiation were carried out at 28 stations by the Chinese Academy of Sciences from 1 January 1989. The observational instruments are model TBQ-4-1 (Jinzhou ,china) and as follows. (1) There are three sensors with sensing wavelength ranges of 270–3200nm, 400–3200 nm, and 700–3200 nm, respectively. The main technical characteristics of the sensors are: sensitivity is 5–10 mV kW^{-1} m^2, response time is ≤1s(1/e), and stability is ≤2%.

The data on global irradiation on a horizontal surface in 28 stations of CERN during the 6-year period 1998–2003 are analyzed. The object of this study is obtained the global radiation time series and spatial variation characteristic in China.

In this topic, we want discuss distribution properties of global radiation in CERN. The main contents as fellow:

1, distribution properties of yearly global radiation
2, distribution properties of monthly global radiation
3, the global radiation extremum value

We rebuild radiation measurement system of CERN from August 2004.In the new observe

system Global radiation was measured using a Kipp&Zonen model CM-21, reflect radiation using CM6B, ultraviolet radiation using CUV3, Net radiation using QMN101, sunshine duration using CSD2, and soil heat flux using HFP01SC (Delft, The Netherlands). The Photosynthetically active radiation was measured with a Licro quantum sensor LI-190Sz (Lin-coln, Nebraska, USA). This station was completed with a data acquisition system (Vaisala M520 data-logger, and a storage module, Finland). The signals were conditioned with the respective instrument factors into units of W/m^2 and $\mu Em^{-2}s^{-1}$(quantum $mol^{-1}s^{-1}$ or $\mu molm^{-2}s^{-1}$). Global radiation measurements have an estimated experimental error of ±2-3%, while the Photosynthetically active radiation sensor has a relative error of lees then 5%. All radiation values were measured by one-minute interval, and the hourly values were driven from minute value by integrating them. The global radiometers were calibrated against a reference pyranometer, which is calibrated a standard pyrheliomter, while the LI-190SA pyranometer is calibrated against calibration lamps at factory. All this calibrated work was done at the beginning and the end of data collected. In this observe system HMP45D used for temperature and humidity, WAA151 used for wind speed, WAV151 used for wind direction, DPA501 used for atmospheric pressure, 8 pieces of QMT110 used for profile of soil temperature (0cm, 5cm, 10cm, 15cm, 20cm, 40cm, 60cm, 100cm)(Vaisala, Finland), and RG13 used for precipitation (Casella, USA).

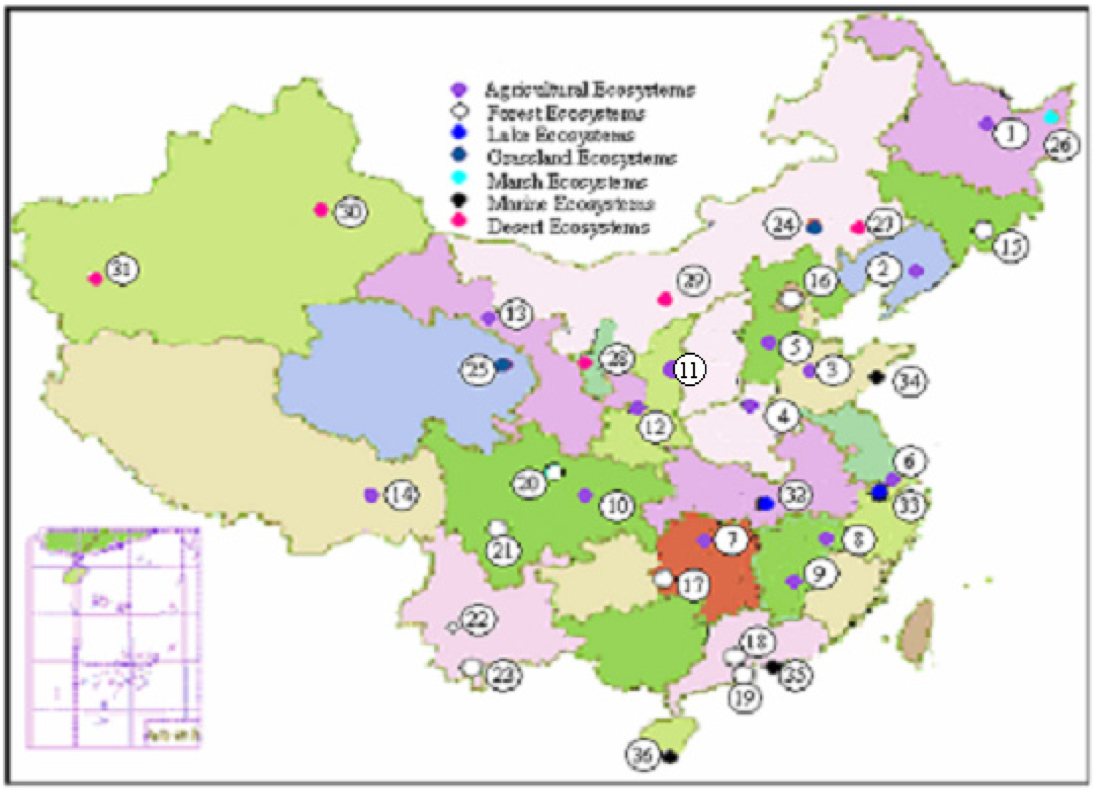

Fig.1 Distributions map of ecosystem research stations of CERN

1-14th Stations are Research stations for Agricultural Ecosystems; 15-23rd stations are Research Stations for Forest Ecosystems; 24-25th stations are Research Stations for Grassland Ecosystems; 26th station is Research Station for Marsh Ecosystem; 27-31st stations are Research Stations for Desert Ecosystems; 32-33rd stations are Research Stations for Lake Ecosystems; 34-36th stations are Research Stations for Marine Ecosystems

Introduction

CERN has been operating as a network of surface radiation monitoring observatories for over 10 years. The determination of a global climatology of the radiation budget at the surface of the Earth is fundamental to understanding the Earth's climate system, climate variability and climate change resulting from human influence. Estimation of the surface radiation budget from satellite observation can't be obtained without high accuracy surface-based measurements at various sites in contrasting climatic region for calibrating and validation. Long-term observations are essential for the study on climate variation trend and radiations transform theory.

The original motivation for the CERN is provide data for climatic change, ecology system study and the relationship between these two fields. The goals and objectives were prescribed as fellow:

Monitor regional radiation fluxes at the surface
Get the radiation variation trend
Provide data for ecology system study
Provide data for calibrating satellite estimates of the surface radiation budget.

Instruments and database

The routine observations of solar spectral radiation were carried out at 28 stations by the Chinese Academy of Sciences from 1 January 1989(Donghu station no data). The observational instruments are model TBQ-4-1 (Jinzhou, china) and as follows. (1) There are three sensors with sensing wavelength ranges of 270–3200nm, 400–3200 nm, and 700–3200 nm, respectively. The main technical characteristics of the sensors are: sensitivity is 5–10 mV kW^{-1} m^2, response time is ≤1s(1/e), and stability is ≤2%.These instruments are fixed in the old observation system.

The instrument fixed in new observation system is showed as fellow.

Global radiation was measured using a Kipp&Zonen model CM-11 (wavelength ranges of 300–3200nm) (Delft, The Netherlands). The PAR photon flux was measured with a Licro quantum sensor LI-190Sz(wavelength ranges of 400–700nm) (Lin-coln,Nebraska,USA).Reflect radiation is measured by a Kipp&Zonen model CM-6B.Ultraviolet radiation is measured by a Kipp&Zonen model CUV3(wavelength ranges of 290–400nm).Net radiation is measured by a Kipp&Zonen model QMN101(wavelength ranges of 300–10000nm).This station complete with data acquisition system(Vaisala M520 data-logger, and a storage module, Finland). Global radiation measurements have an estimated experimental error of 2-3%, while the PAR sensor has a relative error of lees then 5%. All radiation values were measured by one-minute interval, and the hourly values were driven from minute value by integrating them.

A metrology observation system is also fixed in this system. (Vaisala automatic weather station with wind speed, wind direction, temperature, humiditity, rainfall, atmospheric pressure, and soil temperature)

The data used in this topical is get from the old observation system in 28 station from 2001 to 2003.

Results and discussion

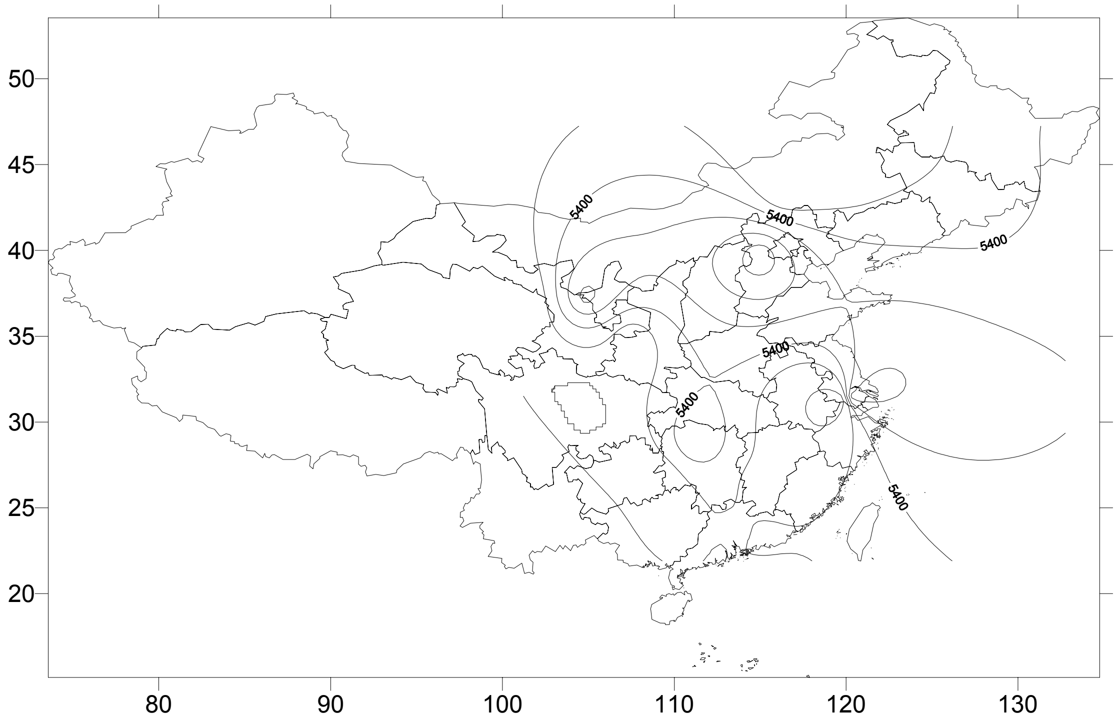

Fig.2 The distribution of annual global radiation in 2003(CERN)

The figure of global radiation annual variation characteristic show that there are four low center, namely, Yanting of Sichuang,Huitong of Hunan,Changshu of Jiangsu ,and Beijing. There is a high central of global radiation in Inner Mongolia. The global values of inner land are higher than that of inshore province, and dry area values of global radiation is higher than global radiation in humidification circumscription. There is a lower values appears in Sichuang,this phenomena is caused by there are many rainy and more cloudy day in this area, at the same time pollution concentration is higher in this area.

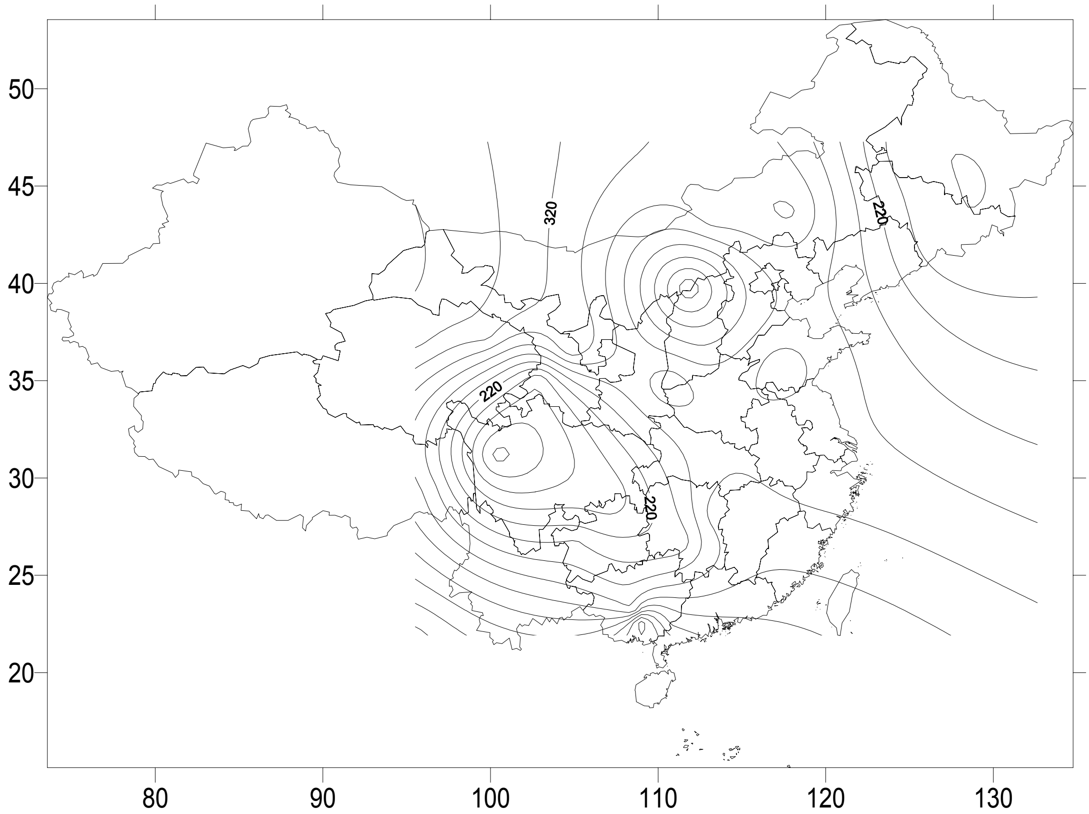

Fig.3 The distribution global radiation in January 2003

In winter the distribution characteristic of global radiation is similitude as that in annual global variation characters. In the eastern area, the value of south area is bigger than the north area. The distribute properties is depend on the law of sun revolution. The lower values in Sichuang is caused by cloudy and pollution concentration.

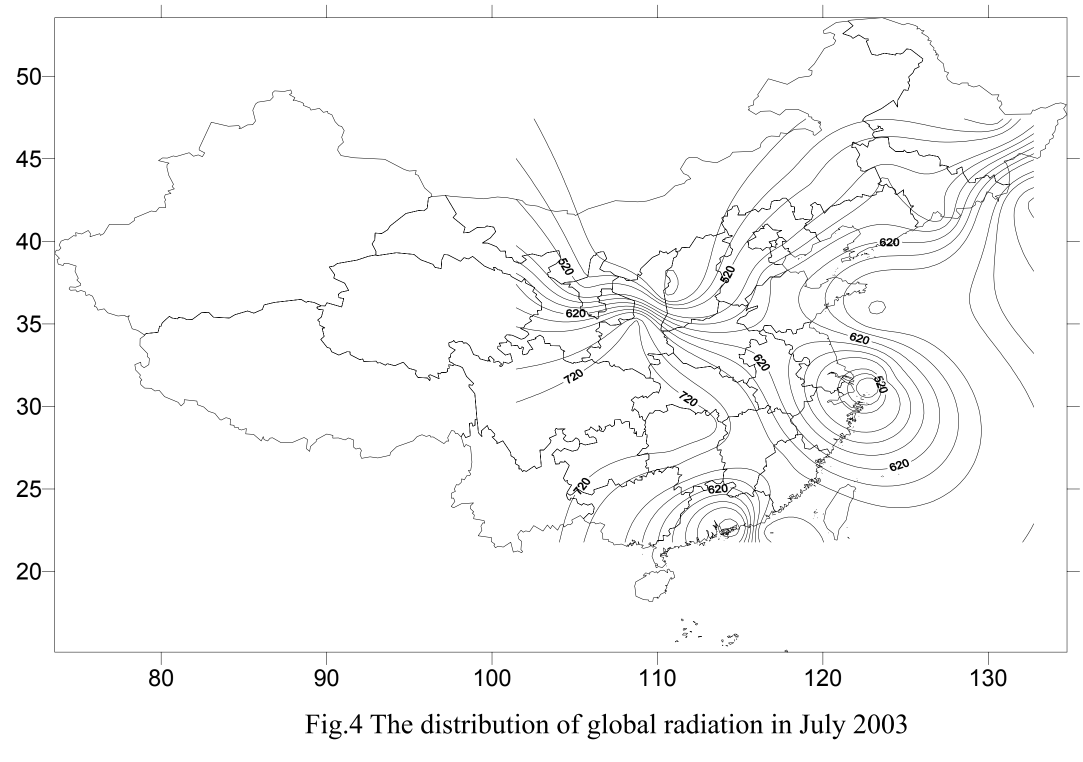

Fig.4 The distribution of global radiation in July 2003

The isoclines of global radiation, which stretch from northeast to southwest, are higher in northwest hinterland than that in coastland except Sichuan province.

Conclusions

The global radiation on ground of Inner Mongolia and Xinjiang is higher than other area of China. Contrariwise, it is very low in Sichuan province, which is decided by the climate of local area. The global radiation measured by CERN radiation observation system is consistent with the observation results from ninety-eight radiation-observing stations distributed over our country. Thus, the observation stations we have established are so representative that the results can reflect the characteristics of global radiation on the mainland of China.

EARLINET: The First Continental-Scale Lidar Network for Vertical Aerosol Profiling

Ulla Wandinger

Leibniz Institute for Tropospheric Research, Leipzig, Germany

Abstract. An overview on the establishment and the objectives of the European Aerosol Research Lidar Network is given. Major results of the intensive observational period from May 2000 to November 2002 are presented. The air-flow-related aerosol modification across Europe and the observation of special events are discussed. These results describing the European haze plume in three dimensions and the regional to continental aerosol transport are based on the network observations in combination with extensive backward trajectory analysis.

Key words: lidar, networking, aerosol measurements, vertical profiling

INTRODUCTION

The European Aerosol Research Lidar Network (EARLINET) is the first continent-scale lidar network for monitoring of anthropogenic haze [Bösenberg et al., 2003]. The main objectives of EARLINET are the establishment of a comprehensive and quantitative statistical data base of the horizontal and vertical distribution of aerosols on the European scale, and the use of these data for studies related to the impact of aerosols on a variety of environmental and climate-relevant problems.

METHODOLOGY AND QUALITY ASSURANCE

During the intensive observational period from May 2000 to November 2002, coordinated lidar measurements (three observations per week, Monday afternoon and evening, Thursday evening) were performed at 20 EARLINET stations distributed over most of Europe. In addition to the regular schedule, individual observations addressed special situations such as Saharan dust outbreaks, long-range transport of forest-fire aerosols, smog episodes, and diurnal cycles in the planetary boundary layer. Typical measurement wavelengths are 355, 532 and/or 1064 nm; most of the systems operate in the UV. Thirteen stations have implemented the Raman technique for an independent retrieval of aerosol extinction and backscatter coefficient profiles.

Because the network consists of individual lidar systems designed at research institutes for different purposes, an extended quality-assurance program based on the intercomparison of individual lidar systems [Matthias et al., 2004a] as well as retrieval algorithms [Böckmann et al., 2004; Pappalardo et al., 2004] was conducted to ensure a homogeneous data set. Evaluated data in terms of profiles of aerosol backscatter and extinction coefficients are stored in a platform-independent common data base. Backward trajectories for each station for two daily arrival times and six pressure levels provided by the German Weather Service complement the data set.

STATISTICAL ANALYSIS

EARLINET provided statistical findings on the temporal and spatial distribution of boundary-layer heights and of aerosol extinction and backscatter coefficients in the planetary boundary layer (PBL) and in the free troposphere as well as on the wavelength dependence of the optical properties [Mattis et al., 2004; Matthias et al., 2004b]. From Raman lidar observations at 10 stations a data base of extinction-to-backscatter ratios has been established. For moderately polluted sites in central Europe mean PBL extinction coefficients of the order of 200 and 100 Mm^{-1} at 355 and 532 nm, respectively, are found. The values are a factor of 2 lower at maritime sites at the western rim of the continent and up to a factor of 2–3 higher at polluted south-eastern European stations. Mean PBL heights range from 1200 to 2000 m, with lowest values at the coast and highest at continental sites, and show a strong seasonal dependence especially over the continent. In northern Europe, the free troposphere contributes 10–20% to the total aerosol optical depth. In southern Europe 25–40% of the aerosols are found above 2 km height. This high value is mainly attributed to the transport of Saharan dust across the Mediterranean (see below). Extinction-to-backscatter, or lidar, ratios vary strongly depending on the observed aerosol types. Values of 50–60 sr are found for industrial-pollution aerosols. Lidar ratios are of the order of 30–50 sr at stations which are mainly influenced by maritime air masses. In Saharan dust, values of 40–80 sr are observed.

AIR-FLOW-RELATED MODIFICATION OF AEROSOL PROPERTIES

Changes in the aerosol optical properties of the European haze plume related to anthropogenic activities can be observed when clean air crosses the densely populated, highly industrialized continent with the prevailing westerly winds [Wandinger et al., 2004]. Air flows across the predominantly flat terrain in the northern part of Europe show an increase of the optical depth at 355 nm from 0.05 at the most western station at Aberystwyth, Wales, to values of 0.3–0.4 in central Europe (Hamburg, Leipzig) and 0.6 at Belsk, Poland. During easterly flows optical depths of 0.5–0.6 are measured at the central European sites, and the values are as high as 0.9 when air from the Black Sea region arrives with south-easterly flows at the most eastern stations of Belsk, Poland, and Minsk, Belarus.

The Alps represent a major orographic barrier between the northern and southern part of EARLINET. In southern Europe, the diverse orography which can lead to a complex aerosol layering due to sea breezes and mountain-induced winds [Perez et al., 2004] complicates the investigation of air-flow-related changes of the aerosol properties. However, even in this part of Europe the influence of anthropogenic activities, e.g., when air masses cross Italy from northwest to southeast, can be documented.

SPECIAL OBSERVATIONS

A variety of special observation programs have been performed within EARLINET. One of the major projects was the characterization of Saharan dust outbreaks towards Europe. In southern Europe as many as 50 dust events per year have been monitored. Up to 10 dust plumes per year reach central Europe. In these situations the dust, which is mainly found in the free troposphere, often dominates the aerosol properties of the whole troposphere. Dust optical depths of up to 0.8 at 532 nm have been found in central Europe [Ansmann et al., 2003]. Because dust particles are relatively large and non-spherical their optical properties differ significantly from other aerosol types [Mattis et al., 2002; De Tomasi et al., 2003; Balis et al., 2004; Murayama et al., 2004].

Wild fires have been identified as another import source of aerosols in the free troposphere. Smoke from forest fires can be transported in the free troposphere over very long distances and remain in the atmosphere for several weeks. In May–July 2003 aerosol extinction in the free troposphere was a factor of 3–4 higher than in the respective months of the years 2000–2002 because of severe forest fires in Siberia and Canada [Mattis et al., 2003].

REFERENCES

A. Ansmann, J. Bösenberg, A.P. Chaikovsky, A. Comerón, R. Eixmann, V. Freudenthaler, P. Ginoux, L. Komguem, H. Linné, M.Á.L. Márquez, S. Manoj, V. Matthias, I. Mattis, V. Mitev, D. Müller, S. Nickovic, J. Pelon, L. Sauvage, P. Sobolewsky, A. Stohl, O. Torres, G. Vaughan, U. Wandinger, and M. Wiegner: Long-range transport of Saharan dust to northern Europe: The 11-16 October 2001 outbreak observed with EARLINET. J. Geophys. Res. 108, 10.1029/2003JD003757, 2003.

D.S. Balis, V. Amiridis, S. Nickovic, A. Papayannis, C. Zerefos: Optical properties of Saharan dust layers as detected by a Raman lidar at Thessaloniki, Greece. Geophys. Res. Lett. 31, 10.1029/2004GL019881, 2004.

C. Böckmann, U. Wandinger, A. Ansmann, J. Bösenberg, V. Amiridis, A. Boselli, A. Delaval, F. De Tomasi, M. Frioud, I.V. Grigorov, A. Hågård, M. Horvat, M. Iarlori, L. Komguem, S. Kreipl, G. Larchevêque, V. Matthias, A. Papayannis, G. Pappalardo, F. Rocadenbosch, J.A. Rodrigues, J. Schneider, V. Shcherbakov, and M. Wiegner: Aerosol lidar intercomparison in the framework of the EARLINET project. 2. Aerosol backscatter algorithms. Appl. Opt. 43, 977-989, 2004.

J. Bösenberg et al.: EARLINET: A European Aerosol Research Lidar Network to establish an aerosol climatology. MPI Report No. 348, Max Planck Institute for Meteorology Hamburg, Germany, 2003.

F. De Tomasi, A. Blanco, M.R. Perrone: Raman lidar monitoring of extinction and backscattering of African dust layers and dust characterization. Appl. Opt. 42, 1699-1709, 2003.

V. Matthias, V. Freudenthaler, A. Amodeo, J. Balin, D. Balis, J. Bösenberg, A.P. Chaikovsky, G. Chourdakis, A. Comerón, A. Delaval, F. De Tomasi, R. Eixmann, A. Hågård, L. Komguem, S. Kreipl, R. Matthey, V. Rizi, J.A. Rodrigues, U. Wandinger, and X. Wang: Aerosol lidar intercomparison in the framework of the EARLINET project. 1. Instruments. Appl. Opt. 43, 961-976, 2004a.

V. Matthias, D. Balis, J. Bösenberg, R. Eixmann, M. Iarlori, L. Komguem, I. Mattis, A. Papayannis, G. Pappalardo, M.R. Perrone, and X. Wang: Vertical aerosol distribution over Europe: Statistical analysis of Raman lidar data from 10 European Aerosol Research Lidar Network (EARLINET) stations. J. Geophys. Res. 109, 10.1029/2004JD004638, 2004b.

I. Mattis, A. Ansmann, D. Müller, U. Wandinger, and D. Althausen: Dual-wavelength Raman lidar observations of the extinction-to-backscatter ratio of Saharan dust. Geophys. Res. Lett. 29, 10.1029/2002GL014721, 2002.

I. Mattis, A. Ansmann, U. Wandinger, and D. Müller: Unexpectedly high aerosol load in the free troposphere over Central Europe in spring/summer 2003. Geophys. Res. Lett. 30, 10.1029/2003GL018442, 2003.

I. Mattis, A. Ansmann, D. Müller, U. Wandinger, and D. Althausen: Multiyear aerosol observations with dual-wavelength Raman lidar in the framework of EARLINET. J. Geophys. Res. 109, 10.1029/2004JD004600, 2004.

T. Murayama, D. Müller, K. Wada, A. Shimizu, M. Sekiguchi, and T. Tsukamoto: Characterization of Asian dust and Siberian smoke with multi-wavelength Raman lidar over Tokyo, Japan in spring 2003, Geophys. Res. Lett. 31, 10.1029/2004GL021105, 2004.

G. Pappalardo, A. Amodeo, M. Pandolfi, U. Wandinger, A. Ansmann, J. Bösenberg, V. Matthias, V. Amiridis, F. De Tomasi, M. Frioud, M. Iarlori, L. Komguem, A. Papayannis, F. Rocadenbosch, and X. Wang: Aerosol lidar intercomparison in the framework of EARLINET: 3. Raman lidar algorithm for aerosol extinction, backscatter and lidar ratio. Appl. Opt. 43, 5370-5385, 2004.

C. Perez, M. Sicard, O. Jorba, A. Comerón, J.M. Baldasano: Summertime re-circulations of air pollutants over the north-eastern Iberian coast observed from systematic EARLINET lidar measurements in Barcelona. Atmos. Environ. 38, 3983-4000, 2004.

U. Wandinger, I. Mattis, M. Tesche, A. Ansmann, J. Bösenberg, A. Chaikowski, V. Freudenthaler, L. Komguem, H. Linné, V. Matthias, J. Pelon, L. Sauvage, P. Sobolewski, G. Vaughan, and M. Wiegner: Air-mass modification over Europe: EARLINET aerosol observations from Wales to Belarus, J. Geophys. Res., in press, 2004.

Ultraviolet Radiation Measurement in the South of Sinkiang Using a Compact Zenith-sky Spectrometer

Pinhua Xie, Yihuai Lu, Yujun Zhang, Ang Li, Jianguo Liu and Wenqing Liu

Anhui Institute of Optics and Fine Mechanics, Chinese Academy of Sciences, Hefei, Anhui, 230031

Abstract

Terrestrial levels of solar UV radiation determine the impact on human health. Ozone depletion and associated increases in solar UV radiation reaching the earth's surface are therefore major environmental issues. The quality (spectrum) and quantity (intensity) of terrestrial UV radiation vary with factors including the elevation of the sun above the horizon and absorption and scattering by molecules in the atmosphere, notably ozone, and by clouds.

Here we report the measurement of UV radiation in the south of Sinkiang, the northwest part of China, using a compact zenith-sky spectrometer in summer 2004. The measurement site, as an area of 1090 meters altitude near the planetary boundary layer, has more extreme climatic conditions and air with less anthropogenic pollution. The spectral power distribution and the diurnal variation of ambient UV radiation from 290nm to 380nm were measured during days of clear sky. The zenith-sky spectrometer consists of a small telescope pointing zenith direction with a field of view of 13 mrad, a fibre-coupled compact spectrometer with 0.6 spectral resolution and a CCD detector. A filter (ZWB_3) was used to block the light above 400nm to reduce stray light. Due to the high spectral resolution, the stratospheric O_3 slant columns were analyzed from the UV spectra by Differential Optical Absorption Spectroscopy methodology at the same time. The compact zenith-sky spectrometer gains in terms of field-operability, mobility and flexibility as well as being a cost-effective alternative to the normal zenith-sky system with expensive spectrometer and CCD detector. Additionally, the vertical profile of temperature, humidity and pressure were measured under 30km height by sounding radio.

Key Words: solar UV radiation, slant column density of O3, zenith-sky spectrometer

1. INTRODUCTION

Ultraviolet (UV) radiation is part of the electromagnetic spectrum. Although solar UV radiation constitutes only about 5% of terrestrial sunlight, it holds the greatest interest in the biological effects which strongly impact on human health and plant life. Ozone layer acts as the protector of the earth by its strong absorption of UV radiation. Therefore ozone depletion and associated increases in UV radiation are major environmental issues and attract the attention of scientific community and governments [1][2][3][4].

This paper reports a measurement of UV radiation in the south of Sinkiang in China with a compact zenith-sky spectrometer. The preliminary results are discussed, including relative UV spectral power distribution, diurnal variation of UV radiation, slant column density of O_3 as well as the vertical profile of temperature, humidity and pressure.

2. MEASUREMENT

The measurement site locates in the south of Sinkiang with 1090 meters altitude near the planetary boundary layer (northwest part of China). It represents the area with more extreme climatic conditions and air with less anthropogenic pollution. The measurement was performed from June 29th to July 2nd and on July 7th, 2004. During most time period, it was sunny with clear sky.

A schematic diagram of the zenith-sky spectrometer is shown in Figure 1. The system is based on a single holographic grating spectrograph, fiber-coupled to a telescope which collects the zenith-sky sunlight and a CCD detector. A portable computer was used to collect data from the CCD detector with 12 bit A/D. The spectral resolution is 0.68 nm over a wavelength range of 290~380 nm. The telescope consisting of one quartz lens and a filter collect the ultraviolet light scattered from zenith sky. The field-of view of the telescope is about 13 mrad. A filter (ZWB_3) is used to blocking visible light above 400nm to reduce the stray light.

Normally the devices used to measure terrestrial UV radiation consist of complex spectrometer (e.g. double monochromator) and diffuser input optics with sufficient accuracy, resolution and reproducibility. Our system is very compact and at low cost. Still it can give useful information about the variation of UV radiation during daytime as well as measuring the stratospheric O_3.

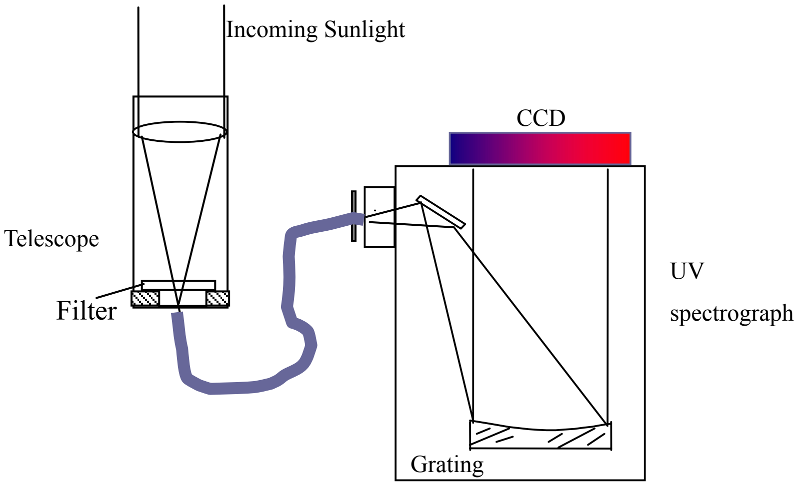

Fig.1 Schematic diagram of the zenith-sky spectrometer

3. RESULTS

3.1 UV radiation

Figure 1 shows the spectral power distributions of UV radiation from 290 nm to 380nm at different daytime. The UV radiation reaches the peak level around noon time 13:00 (21° SZA). This can also be clear seen from Figure 2, which shows the diurnal variation of UV radiation (integration radiation of 290-380nm) on July 2, 2004. The UV radiation changes very smoothly except for some small undulations over the smooth trend. This could be caused by clouds in the sky. Around 13:00, few clouds appeared in the sky.

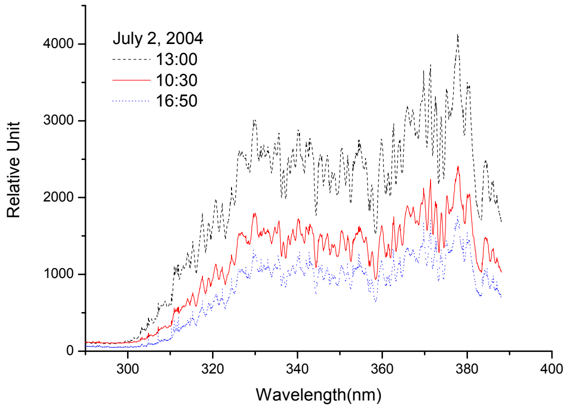

Figure 2. Spectral power distribution of clear sky, terrestrial UV radiation measured in July 2, 2004

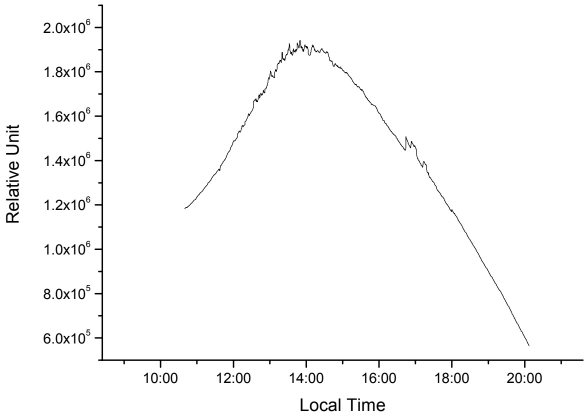

Figure 3. Variation of ambient UV radiation from 290-380nm on July 7, 2004 in Sinkiang.

3.2 O_3 Slant column density

The measurement technique, which is called differential absorption spectroscopy, is used for highly structured NO_2 and O_3 absorption in UV/Vis spectral range[5][6][7]. During sunrise and sunset, the observed scattered sunlight passes through a long slant path, which enhances the absorption. The observation was carried out from the morning to the evening (SZA from 21.2 º to 67.6º). The spectra at 21.2 º SZA (noon time) are used as reference spectra. The ratio of zenith sky spectra of noontime and other time is taken to eliminate the Fraunhofer line structure and this ratio spectrum gives the effect of absorption of O_3 column relative to the reference spectrum. The ration is used to determine the SCDs of O_3. Figure 4 shows the measured spectrum with O_3 absorption structures and the O_3 differential cross section after same DOAS data processing procedure (e.g. high pass and low pass filter). We found good agreement between them. The SCDs of O_3 are calculated by DOAS method. Figure 5 shows the SCD of O_3 measured on July 7, 2004.

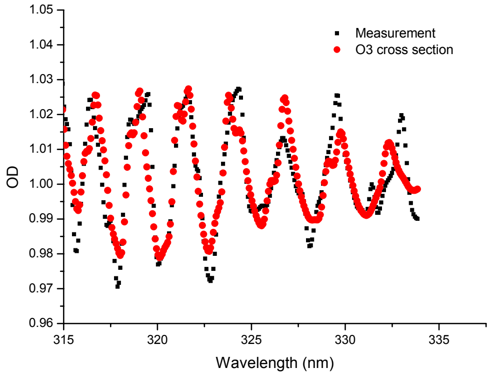

Figure 4. Comparison of observed and calculated OD of O_3.

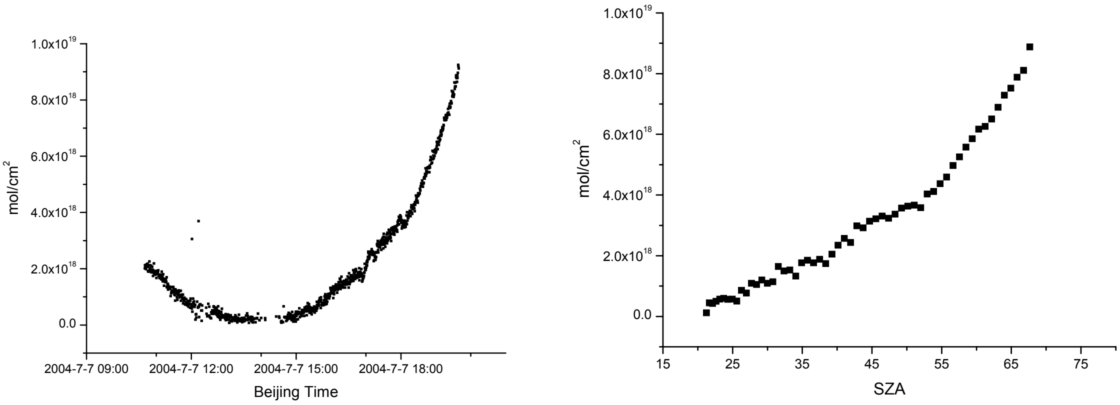

Figure 5. Measurement of O_3 on July 7, 2004.

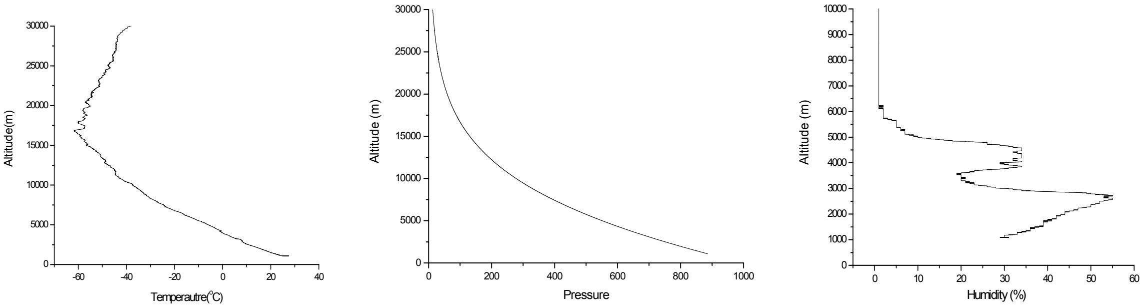

Figure 6. Vertical profile of temperature, pressure and humidity on July 7, 2004.

3.3 Vertical profile of temperature, pressure and humidity

During the measurement time, vertical profile of temperature, air pressure and humidity was obtained by sounding radio, as shown in Figure 6. The top of troposphere is about 17km altitude. The humidity reached zero at about 6km altitude.

4. CONCLUSIONS

A compact zenith-sky spectrometer was used to measure UV radiation and O_3 SCDs, both of which are very important atmospheric parameters needed long term observation. The measurement in Singkiang in summer of 2004 gives relative spectral power distribution and diurnal profile of UV radiation as well as the SCDs of O_3. The compact device demonstrates its gains in speed, cost and portability.

For the future work, the compact device will be further temperature controlled and calibrated for absolute measurement of UV radiation. SCDs of O_3 will be combined with air mass factor (AMF) calculated from radiative transfer model to obtain the total O_3 amount. The accuracy of the measurement will be further compared with other instruments (e.g. spectroradiometer and Dobson spectrophotometer).

5. REFERENCES

[1] B. L. Diffey, Sources and measurement of ultraviolet radiation, Methods 28 (2002) 4–13

[2] M. Steinmetz, Continuous solar UV monitoring in Germany, Journal of Photochemistry and Photobiology B: Biology 41(1997)181-187

[3] J.M. Sabburg, A.V. Parisi, M.G. Kimlin, Enhanced spectral UV irradiance: a 1 year preliminary study, Atmospheric Research 66 (2003) 261–272

[4] P.C. Wang, B.Y. Wu and W.X. Zhang, Analysis on the factors affecting surface UV radiation, Chinese Journal of Atmospheric Science, Vol.23, No.1(1999) 1-8

[5] J. F. Noxon, Nitrogen dioxide in the stratosphere and troposphere measured by ground based spectroscopy. Science, 1975, 189, 547-549

[6] U. Platt, “Differential Optical Absorption Spectroscopy (DOAS)”. In M. W. Sigrist M.W. (Ed.), Monitoring by Spectroscopic Techniques. John Wiley & Sons, New York. 1994

[7] G.S. Meena, D.B. Jadhav and C.S. Bhosale, Total column density variations of NO2 and O3 by automatic visible spectrometry over Pune, India, Current Science, Vol. 85, No.2, 25, 2003

Progress and Outstanding Challenges in Estimating Surface Radiation Budgets by Methods of Remote Sensing

R. T. Pinker

Department of Meteorology, University of Maryland, College Park, MD 20742

ABSTRACT

Attempts to obtain information on shortwave surface radiative fluxes from satellite observations have been made since the very early stages of satellite explorations. During the last two decades the methodologies to obtain such fluxes have advanced to a level where results have been found to be of sufficient quality to address a wide range of climate issues. The current inference schemes have capabilities to derive not only the total down-welling shortwave fluxes, but also fluxes absorbed in the atmosphere and at the surface both under clear and cloudy conditions, and diffuse and spectral fluxes. The framework for advancing the development of such capabilities was provided by the Global Energy and Water Cycle Experiment (GEWEX) program aimed at understanding and modelling the global hydrological cycle and programs such as the Coordinated Enhanced observing Period (CEOP) activity. The satellite based flux estimates have proven to be very valuable for evaluating large scale models that require information on radiative fluxes at global and regional scales. Yet, many outstanding issues of these data sets as related to spatial sampling, temporal sampling, adequate representation of the diurnal cycle, spectral resolution of the observations and the quality of the auxiliary information used to drive the inference schemes (such as information on aerosols), need to be addressed in a systematic manner. Since satellite estimates are now available for periods of at least twenty years, there is also interest in assessing the temporal variability of the radiative balance and implications for climate change studies. In this presentation, reviewed will be the current status of available information on shortwave radiative fluxes, discussed will be current issues related to outstanding problems, and presented will be examples of collaborative activities in progress.

Key Words: surface radiation budgets; satellite inference of radiation budgets

INTRODUCTION

Since the early seventies, attempts to derive radiative fluxes from satellite observations have been in progress (VonderHaar et al., 1973; Raschke and Preuss, 1979). A comprehensive effort to obtain such information at global scale was initiated by the Global Energy and Water Cycle Experiment (GEWEX) program of the World Climate Research Program (WCRP) (Chahine, 1992; Sorooshian, 2003) aimed at: improvement of the understanding and modeling of the hydrological cycle on time scales from diurnal to interannual; evaluation of land surface parameterizations; and testing their implications for global climate and weather forecast models. Such information is also required at the boundary of the upper ocean since radiative fluxes influence the sea surface temperature and precipitation.

Capabilities to derive radiative fluxes at global and regional scales for extended time periods from geostationary and polar orbiting satellites have been demonstrated (Stuhlman et al. (1990); Pinker and Laszlo (1992); Brison et al. (1994); Chou (1994); Whitlock et al. (1995); Pinker et al. (1995); Rossow and Zhang (1995); Gupta et al. (1999, 2001); Ceballos et al. (2004); Pinker et al. (2003); Zhang et al. (2004)). The global scale effort was facilitated by the joint NOAA/NASA PATHFINDER activity (Dodge and

Ohring, 1992) under which uniform and long -term observations taken from numerous satellites have been processed into reduced resolution, global coverage homogeneous information. The various versions of the International Cloud Climatology Project (ISCCP) data (Schiffer and Rossow, 1985) that are a sub-set of the PATHFINDER data, have been extensively used for inferring global scale distributions of clouds, cloud properties, and surface radiative fluxes (Zhang et al., 1995; Pinker and Laszlo, 1992; Stackhouse et al., 2002). The WCRP GEWEX Surface Radiation Budget (SRB) project was specially tasked to produce, validate, and assess long-term surface and atmospheric radiative budgets on a global scale (Stackhouse et al., 2002). The satellite estimates have been evaluated extensively by the producers of the data as well as by independent investigators. The ground truth as available from the Swiss Federal Institute of Technology, Global Energy Balance Archive (GEBA) (Ohmura et al., 1998), and various other sources as compiled at the NASA Langley Data Center have been used. Many ground-based observational networks are now available (BSRN; SURFRAD; ARM; SKYNET; AERONET) that provide information needed for evaluation. Extensive evaluations are also conducted against fluxes at the top of the atmosphere using observations from ERBE (Barkstrom et al., 1984), SCARAB (Hollmann et al., 1999) and CERES (Wielicki, 1999).

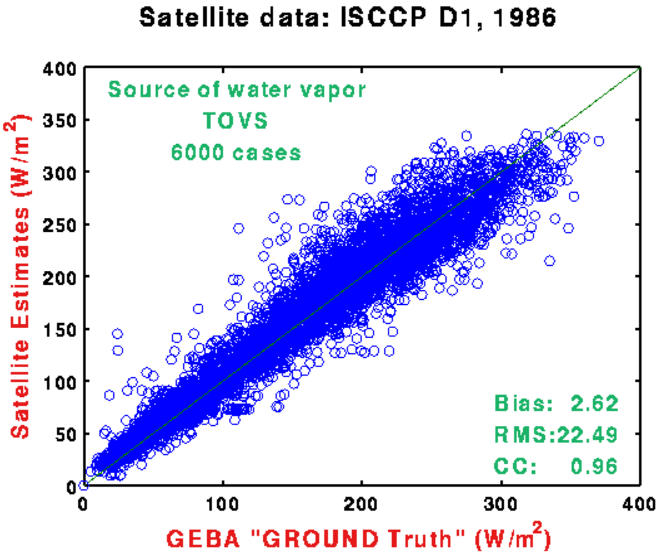

Figure 1. Comparison of University of Maryland SRB model (Version 2.1) retrieved monthly mean surface downward shortwave fluxes against ground truth from GEBA for the entire year of 1986, using satellite observations from ISSCP D1.

The satellite based estimates of radiative fluxes at global scale have already been used in a wide range of applications (Hahmann et al., 1995; Bony et al., 1997; Machado et al., 1998; Sui et al., 2001). New types of experiments for improving weather prediction at regional scale are in progress. Improving weather and seasonal climate prediction requires information on initial states of the atmosphere, oceans and land. Sparse observations need to be assimilated from various observing platforms into atmospheric initial states via 4-dimensional data assimilation (4DDA) to blend observations with the background fields of an LSM. Yet, errors remain in soil moisture/temperature and surface energy/water fluxes, due to biases in the surface forcing. Under the North American Land Data Assimilation System (NLDAS) project (Mitchell et al., 2004) quality controlled, spatially and temporally consistent, real-time and retrospective forcing data of rainfall and radiation as obtained from observations and satellite based estimates of radiative fluxes (Pinker et al., 2003) have been used to support LSM activities. This activity is a first real-time operational prototype of a continental-scale uncoupled land 4DDA assimilation executed daily at the National Centers for Environmental Pedictions (NCEP) that utilizes real-time streams of hourly to daily precipitation and insolation fields (from satellites and/or ground observations). It is hoped that such an approach will reduce the errors in the storage of soil moisture and energy which are often present in NWP models and which degrade the accuracy of forecasts.

In parallel to the NLDAS activity, a Global Land Data Assimilation System (GLDAS) is being developed jointly by scientists at NASA's Goddard Space Flight Center (GSFC) and NOAA's National Centers for Environmental Prediction (NCEP) (Rodell et al., 2003). Its purpose is similar to that of NLDAS but runs globally and produces results in near-real time (typically within 48 hours of the present). The global land surface fields provided by GLDAS will be used to initialize weather and climate prediction models and will promote various hydrometeorological studies and applications. As yet, radiation fields are not produced globally in real time based on satellites but rather use clouds and parameterization of their effects. Similar activities are in progress in the European LDAS Community (ELDAS) (Meetschen et al., 2004).

Other programs of relevance that promoted the use of satellite estimates of radiative fluxes are the various GEWEX Continental Scale studies such as LBA (Nobre et al., 2001), BALTEX (Raschke, 1998) or GAME (Nakajima, 2001; Takamura et al., 2001; Sekiguchi et al., 2003). The Coordinated Enhanced Observing Period (CEOP) program (Grassl, 2002) supports research objectives in climate prediction and monsoon system studies, and surface radiation is an important element of the program. CEOP has been endorsed as the first element of the new Integrated Global Water Cycle Observation Theme approved by the Integrated Global Observing System Partners (IGOS-P) (http://www.ceop.net/).

The goal of research on satellite based inference schemes is to determine the atmospheric and surface radiative fluxes at a level of precision needed to predict transient climate variations and climate trends, improve capabilities to predict changes in water resources and soil moisture and aid in the development of global models to a level that will allow them to determine if the Earth's energy budget and water cycle are changing. In this presentation addressed will be issues that still require attention before such goals can be achieved.

SELECTED INFORMATION ON SURFACE RADIATIVE FLUXES

- First WCRP Surface Radiation Budget Global Data Sets, Short-wave Radiation Parameters March 1985-December 1988, NASA Earth Observing System Distributed Active Archive Center, NASA Langley Research Center, Hampton, VA (Whitlock et al., 1995), at monthly time scale.
- Global Data Sets for Land-Atmosphere Models, ISLSCP Initiative 1: 1987-1988, Volume 1-5, NASA Goddard DAAC Science Data Series, at three hourly intervals (Sellers et al., 1996).
- ISLSCP Initiative II consists of a 10-year core global data collection spanning the years 1987 to 1995 at spatial resolutions of one-quarter to one degree. http://islscp2.sesda.com/ISLSCP2_1/html_pages/islscp2_home.html
- Global Ecosystem Database, Disk B, National Environmental Satellite, Data, and

Information Center National Geophysical Data Center, Boulder, Colorado November 1997. Monthly averaged on Photosynthetically Active Radiation, for the period July 1983-July 1988.

The most recent global scale and long term data sets on satellite surface radiative fluxes can be found at: http://www.gewex.org/srb.html; http://atmos.umd.edu/~srb/pathfinder; and http://isccp.giss.nasa.gov/

ADDRESSING SELECTED OUTSTANDING PROBLEMS

1. Spatial Inhomogeneity

Satellite observations are incomplete in space or/and in time. In order to use such observations to monitor climate, in climate modeling, or to drive general circulation models, there is a need to subject them first to some type of optimal interpolation, to obtain homogeneous information. The magnitude of errors in available estimates of surface radiative fluxes due to this deficiency is not well established and requires attention.

An approach was developed to obtain homogeneous data sets, and the methodology was applied to the widely used International Cloud Climatology Project (ISCCP) DX and D1 data. These provide observations independently for each geostationary and polar orbiting satellite, sampled at 30 km. Data gaps, degraded spatial resolution near boundaries of geostationary satellites, and different viewing geometries in areas of satellite overlap, could result in inhomogeneous estimates of radiative fluxes. An Empirical Orthogonal Function (EOF) iteration scheme was introduced for homogenizing the radiative fluxes (Zhang, Pinker and Stackhouse, 2004). When compared against ground truth over Europe, Africa and United States for a period of about four years, the rms error was reduced by about 2 W/m^2 when compared to unsmoothed results.

2. Aerosol effects

Aerosols scatter and absorb solar radiation and their effect on the hydrological cycle has been of concern (Ramanathan et al., 2002). Information on aerosol optical properties is therefore important for accurate modeling of the surface radiation budget. In recent years, progress has been made to derive aerosol optical depth (AOD) from a variety of sources. To estimate uncertainties in SRB due to aerosols, a methodology was developed to merge satellite observations, chemical models, as well as ground observations. The method keeps the large-scale spatial and temporal variation patterns as derived from satellites and models, and simultaneously regulates the magnitude using ground measurements (Liu, Pinker and Holben, 2004). Specifically, the following data were used:

- **GOCART model simulation:** A three-dimensional chemical transport model (Chin et al., 2000, 2002; Ginoux et al., 2001) capable of reproducing prominent spatial and temporal variations, especially in areas with strong signals (biomass burning and dust).
- **MODIS satellite retrieval:** The MODerate resolution Imaging Spectroradiometer (MODIS) provides information on AOD (King et al., 2002). Used are the MODIS Level-3 monthly mean AOD data.
- **AERONET ground measurement:** The AERONET is a globally distributed federated network of ground-based observations representing a wide variety of atmospheric conditions using state-of-the-art sunphotometers (Holben et al., 1998;

Eck et al., 1999). Used are AOD monthly mean data from 159 sites in operation during the analysis period.

The derived AOD distribution used is presented in Figure 1. The impact was tested in a region frequented by dust. A "control run' was made with "nominal values of AOD, assigned according to land use. A second run was performed with the realistic AOD information. Results are presented in Figure 2. As evident, over the ocean adjacent to the coast of Africa, aerosols can reduce surface fluxes by as much as 12 W/m^2.

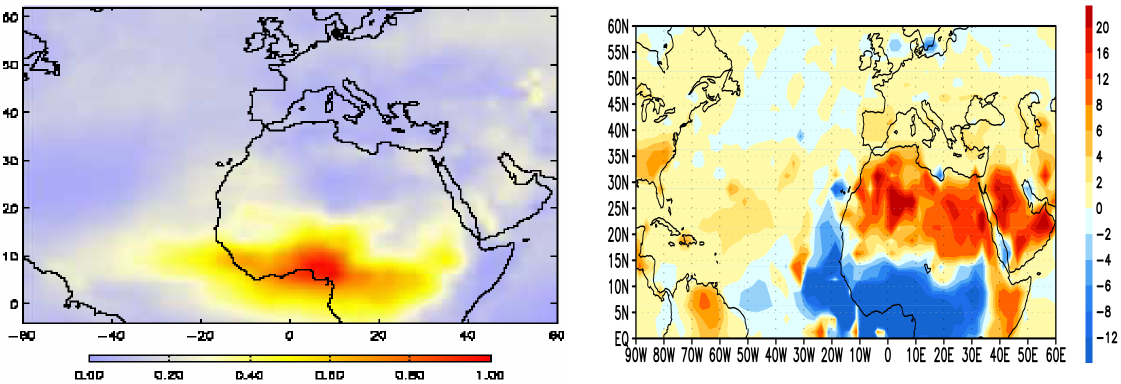

Figure 2. Monthly mean values of aerosol optical depths as derived from the combined estimates from MODIS, GOCART and AERONET for February 2001 (left) and the impact on SRB when compared to nominal AOD (right)

3. Calibration uncertainties

Parameters derived from satellite observations depend on the quality of calibration of the satellite measurements. Sensitivity of surface shortwave downward fluxes to different calibration methods for the visible sensor aboard the GOES-8 geostationary satellite were investigated (Wonsick and Pinker, 2004). One calibration method was developed at the National Oceanographic and Atmospheric Administration (NOAA) National Environmental Satellite Data and Information Service (NESDIS) (Weinreb et al., 1997). The second evolved from a study conducted at the NASA Langley Research Center, in which data from research satellites carrying onboard calibration systems were used as reference sources to develop new calibration coefficients for GOES-8 (Minnis et al., 2002). Evaluated were differences in absolute reflectance, derived cloud cover, and estimated surface shortwave fluxes as compared to ground measurements. Differences in visible reflectance ranged from -0.5 to 3%. The average difference in monthly mean cloud amount was ~3%, and the average difference in monthly mean shortwave downward flux was 5 W/m^2. Differences in bias and RMS in evaluation against ground station measurements were less than 2 W/m^2. Neither calibration method was shown to consistently outperform the other. This evaluation yields an estimate of the errors in fluxes that can be attributed to calibration. In the case of the ISCCP data, homogeneity of the satellite observations is achieved by normalizing all the geostationary satellites used to polar orbiting satellites, which enjoy a long history of calibration know-how (Desormeaux et al., 1993).

A MULTI-SATELLITE APPROACH

In the past, emphasis has been on the use of geostationary satellites to capture the diurnal variability in cloud distributions that determines the amount of energy received at the surface during the course of a day. Many of these satellites are limited in their capability to accurately detect cloud or aerosol optical properties that are important elements of the radiation budget. The MODIS instrument onboard the Terra and Aqua satellites and the Midori II GLI observed with 36 spectral bands with the capability for measuring atmospheric and surface properties at higher accuracy and consistency. It is important to utilize such observations to evaluate the performance of algorithms applied to satellites that do not provide direct information on cloud and aerosol optical characteristics. The "Atsk 13" SRB algorithm that was developed for use with GLI observations was implemented with the MODIS prototype data at 1^0 resolution as well as with the pixel level MODIS swath data as illustrated in Figure 4. Work is in progress on the evaluation of surface radiative fluxes from such multiple-source observations and various algorithms in the domain of the GMS satellite, using ground truth as available from the SKYNET.

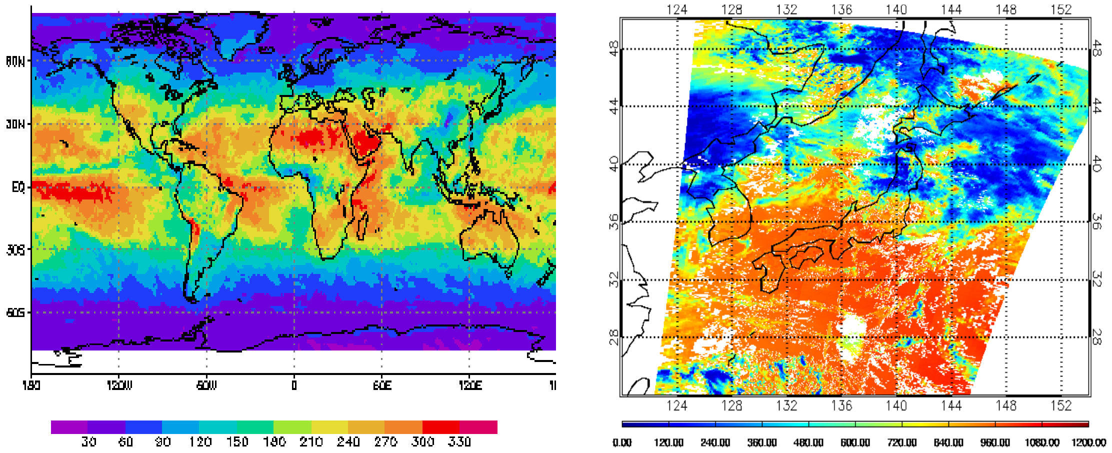

Figure 3. Monthly mean shortwave surface downward flux (W/m^2) with MODIS V004 data at 10 resolution for September 2001 (left) and pixel level MODIS data for July 4, 2001 over Japan (right). Cloud fraction, cloud optical thickness, aerosol optical thickness, precipitable water, total column ozone amount, spectral surface albedo and solar zenith angle are from MODIS data.

SUMMARY

Global data sets on surface radiative fluxes have been developed by several groups and are being used extensively in a wide range of climate applications. In the United States, Europe and Brazil, work has started on providing such information in an operational mode for use as forcing functions in numerical weather prediction models. Yet, uncertainties in available estimates of SRB are not fully known and require further attention. Many new satellite missions have been launched that can help to address specific issues related to uncertainties. For instance, MODIS on Terra and Aqua satellites (King et al., 2002) and the GLI instrument on ADEOS-II observe the earth in an unprecedented number of spectral intervals and at high spatial resolution. Such observations can be utilized for assessing limitations of the operational satellites with limited spectral capabilities. New observations from a suite of sensors on the METEOSAT Second Generation (MSG) mission, to be made with the Spinning Enhanced Visible and Infra-Red Imager (SEVIRI) and with the Geostationary Earth Radiation Budget (GERB), will facilitate improvements in existing methodologies to derive surface radiative fluxes. Level 1.5 data from SEVIRI and GERB have half hourly observations in all 12 SEVIRI channels and two GERB channels. The two instruments are collocated and therefore, it would be possible to test narrow-to-broadband transformations that are needed when narrow-band observations are used to infer broadband fluxes. New angular models based on CERES should be also helpful in reducing uncertainties in the derived fluxes. Application of high quality satellite based radiative fluxes to process studies in models can help to improve: extended range forecasts; water resource variability; simulations of climate response to anthropogenic forcing and provide input to other climate related programs such as CLIVAR (http://www.clivar.org/).

Acknowledgements: Thanks are due to H. Wang, H. Liu, and M. Wonsick, Graduate Students, University of Maryland for their contributions. Support under NASA grants EOD/IDS NAG59634 and NAG56464 to the University of Maryland and JAXA grant AEO1208001 are greatly appreciated. The ISCCP D1 and the GEBA data were obtained from the NASA Langley Research Center Atmospheric Sciences Data Center.

References

Barkstrom, B. R., 1984. The Earth Radiation Budget Experiment (ERBE). *Bull. Amer. Meteorol. Soc.*, 65:1170-1185.

Bony S, Y. Sud, K. M. Lau, J. Susskind, and S. Saha, 1997. Comparison and satellite assessment of NASA/DAO and NCEP-NCAR reanalysis over tropical oceans: Atmospheric hydrology and radiation. *J. Climate,* **10 (6),** 1441-1462.

Brest, C. L., W. B. Rossow, and M. Roiter, 1997. Update of Radiance Calibrations for ISCCP. *J. Atmos. Ocean Tech.,* **14,** 1091-1109.

Brisson, A., P. Le Borgne, A. Marsouin, and T. Moreau, 1994. Surface irradiance calculated from Meteosat sensor data during SOFIA-ASTEX. *International Journal of Remote Sensing,* 15, 197-203.

Ceballos J. C., M. J. Bottino, J. M. de Souza, 2004. A simplified physical model for assessing solar radiation over Brazil using GOES 8 visible imagery, *J. Geophys. Res.-Atmospheres,* 109 (D2): Art. No. D02211.

Chahine, M. T., 1992. GEWEX is International, *GEWEX NEWS*, Vol. 2, No. 2, 2.

Chou, M.-D., 1994. Radiation Budgets in the Western Tropical Pacific, *J. Climate*, 7 (12), 1958-1971.

Desormeaux, Y., Rossow, W. B., C. L. Brest, G. G. Campbell, 1993. Normalization and calibration of geostationary satellite radiances for the International Satellite Cloud Climatology Project. *Journal of Atmospheric and Oceanic Technology*, 10 (3): 304-325.

Grassl, H., 2002. CEOP-Global Monitoring for Improved Prediction. *CEOP Newsletter* No. 2.

Gupta, S. K., N. A. Ritchey, A. C. Wilber, C. H. Whitlock, G. G. Gibson, P. W. Stackhouse, Jr., 1999. A climatology of surface radiation budget derived from satellite data. *J. Climate,* 12 (8), 2691-2710 Part 2.

Hahmann, A. N., Ward, D. M., Dickinson, R. E., 1995: Land-surface temperature and radiative fluxes response of the NCAR CCM2 Biosphere-Atmosphere Transfer Schemes to modifications in the properties of clouds. *J. Geophys. Res.-Atmos,* **100 (D11),** 23239-23252.

Hahn C. J., Rossow W. B., Warren S. G., 2001. ISCCP cloud properties associated with standard cloud types identified in individual surface observations. *J. Climate*, **14 (1),** 11-28. King, M. D., Kaufman, Y. J., Menzel, W. P., and Tanré, D., 1992: Remote sensing of cloud, aerosol, and water vapor properties from the Moderate Resolution Imaging Spectrometer (MODIS). *IEEE Transactions on Geosciences and Remote Sensing,* **30**, 2-27.

Hollmann R., J. Feng, H. G. Leighton, J. Mueller, and R. Stuhlmann, 1999. ScaRaB as a valuable tool for BALTEX and MAGS: Satellite applications for energy budgets and the hydrological cycle. *Advances in Space Research*, 4 (7): 955-958 1999

Kineman, J. J. (Ed), 1997. Global Ecosystems Database Disc-B: including Database, User's Guide, and Dataset Documentation, USDOC/NOAA National Geophysical Data Center, Boulder, CO. GED: 1B. 640MB on 1 CDROM.

King, M. D., W. P. Menzel, Y. J. Kaufman, D. Tanré, B. C. Gao, S. Platnick, S. A. Ackerman, L. A. Remer, R. Pincus, and P. A. Hubanks, 2003. Cloud and Aerosol Properties, Precipitable Water, and Profiles of Temperature and Humidity from MODIS**.** *IEEE Trans. Geosci. Remote Sens*., 41*, 442-458.*

Meetschen, D., B. van den Hurk, F. Ament, and M. Drusch, 2004. Optimized surface radiation fields derived from METEOSAT imagery and a regional atmospheric model. *J. Hydromet.,* in press.

Minnis, P., L. Nguyen, D. R. Doelling, D. F. Young, W. F. Miller, and D. P. Kratz, 2002: Rapid Calibration of Operational and Research Meteorological Satellite Imagers. Part I: Evaluation of Research Satellite Visible Channels as References. *J. Atmos. Oceanic. Tech,*.**19**, 152-168.

Mitchell, K., D. Lohmann, P. Houser, E. Wood, A. Robock, J. Schaake, B. Cosgrove, J. Sheffield, L. Luo, Q. Duan, D. Lettenmaier, R. T. Pinker, D. Tarpley, W. Higgins, J. Meng, A. Bailey, F. Wen, 2004. The Multi-institution North American Land Data Assimilation System (N-LDAS): Leveraging multiple GCIP products in a real-time and retrospective distributed hydrological modeling system at continental scale, *J. Geophys. Res*.-Atmospheres, 109 (D7): Art. No. D07S91 APR 9.

Nakajima, T., 2001. An overview of the GAME radiation acitivites-2000: Proceedings: The Fifth International Study Conference on GEWEX in Asia and GAME (Vol. 2), GAME Publication No.31 (2), 363-366, Nagoya, Japan.

Nobre, C. A., D. Wickland, and P. I. Kabat, 2001. The large scale biosphere-atmosphere experiment in Amazonia (LBA), *Global Change Newsletter 45:* 2-4.

Ohmura, A., E. G. Dutton, B. Forgan, C. Frohlich, H. Gilgen, H. Hegner, A. Heimo, G. Konig-Langlo, B. McArthur, G. Muller, R. Philipona, R. T. Pinker, C. H. Whitlock, K. Dehne, and M. Wild, 1998. Baseline Surface Radiation Network (BSRN/WCRP): New Precision Radiometry for Climate Research, *Bull. Amer. Met.* Soc., *79*, 2115-2136.

Ohring, G. and D. C. Dodge, 1992. The NOAA/NASA Pathfinder Program. Current Problems in Atmospheric Radiation, IRS '92, Deepak Publishing, pp. 405.

Pinker, R. T. and I. Laszlo, 1992. Modeling of surface solar irradiance for satellite applications on a global scale. *J. Appl. Meteor.,* **31**, 194-211.

Pinker, R. T., I. Laszlo, C. H. Whitlock and T. P. Charlock, 1995. Radiative Flux Opens New Window on Climate Research. *EOS,* 76, No. 15, April 11.

Pinker, R. T., J. D. Tarpley, I. Laszlo, K. E. Mitchell, P. R. Houser, E. F. Wood, J. C. Schaake, A. Robock, D. Lohmann, B. A. Cosgrove, J. Sheffield, Q. Duan, L. Luo, and R. W. Higgins, 2003. Surface Radiation Budgets in Support of the GEWEX Continental Scale International Project (GCIP) and the GEWEX Americas Prediction Project (GAPP), including the North American Land Data Assimilation System (NLDAS) Project JOURNAL OF GEOPHYSICAL RESEARCH-ATMOSPHERES 108 (D22): Art. No. 8844 NOV 19 2003

Ramanathan, V., Crutzen, P.J., Kiehl, J. T., Rosenfeld, D., 2001. Aerosol, climate and the hydrological cycle. Science, 294, 2119 – 2124.

Raschke, E., U. Karstens, R. Nolte-Holube, R. Brandt, H.-J. Isemer, D. Lohmann, M. Lobmeyr, B. Rockel, and R. Stuhlmann, 1998. The Baltic Sea Experiment, BALTEX: A brief overview and some selected results, *Surveys of Geophysiscs,* 19, 1-22.

Raschke, E., and H. J. Preuss, 1979. The determination of the solar radiation budget at the earth's surface from satellite measurements, *Meteor. Rdsch.*, 32:18-28.

Rodell, M., P. R. Houser, U. Jambor, J. Gottschalck, K. Mitchell, C.-J. Meng, K. Arsenault, B. Cosgrove, J. Radakovich, M. Bosilovich, J. K. Entin, J. P. Walker, D. Lohmann, and D. Toll, 2004. The Global Land Data Assimilation System, *Bull. Am. Met. Soc.,* 85 (3): 381+.

Reynolds, R. W., T. M. Smith, 1995. A high resolution global sea surface temperature climatology. *J. Climate*, **8,** 1571-1583.

Rossow, W. B. and Y.-C. Zhang, 1995. Calculation of surface and top of the atmosphere radiative fluxes from physical quantities based on ISCCP data sets. 2. Validation and first results. *J. Geophys. Res*., 97, 1167-1197.

Schiffer, R. A., and Rossow, W. B., 1985. ISCCP Global Radiance Data Set: A New Resource for Climate Research. Bull. Amer. Meteor. Soc., 66, 1498-1505.

Sekiguchi, M., T. Nakajima, K. Suzuki, K. Kawamoto and A. Higurashi. 2003. A study of atmospheric radiation budget in Asia, Proceedings: The Fifth International Study Conference on GEWEX in Asia and GAME (Vol. 3), GAME Publication No.31 (3), 778-783, Nagoya, Japan.

Sellers, P. J., Collatz, J., Hall, F. G., Meeson, B. W., Closs, J., Corprew, F., McManus, J., Myers, D., Sun, K.-J., Dazlich, D., Kerr, Y., Koster, R., Los, S., Mitchell, K., Try, P., 1996. The ISLSCP Initiative I Global Datasets: Surface Boundary Conditions and Atmospheric Forcing for Land-Atmosphere Studies, Bulletin of the American Meteorological Society: Vol. 77, No. 9, 1987-2006.

Sorooshian, S., 2003. GEWEX support reaffirmed at recent WCRP/JSC meeting. *GEWEX NEWS,* Vol. 13, No. 2, May 2003.

Stackhouse, P. W., Jr., S. K. Gupta, S. J. Cox, J. C. Mikovitz, and M. Chiaachio, 2002. New results from the NASA/GEWEX Surface Radiation Budget Project: Evaluating El Nino effects at different scales, *11th Conference on Atmospheric Radiation, American Meteorological Society*, Ogden, UT, June 3-7.

Stuhlmann, R., M. Rieland, and E. Raschke, 1990. An improvement of the IGMK model to derive total and diffuse solar radiation at the surface from satellite data, *J. Appl. Meteor.*, 29, 586-603.

Sui, C. -H., M. M. Rienecker, X. Li, K. -M. Lau, I. Laszlo, and R.T. Pinker, 2002. The impacts of daily surface forcing in the upper ocean over tropical Pacific: A numerical study, *J. Climate*, 16 (4): 756-766.

Takamura, T., I. Okada, N. Takeuchi and T. Nakajima, 2001. Estimation of surface solar radiation from satellite data and its validation using SKYNET data. Proceedings: The Fifth International Study Conference on GEWEX in Asia.

Weinreb, M. P., M. Jamison, N. Fulton, Y. Chen, J. X. Johnson, J. Bremer, C. Smith, and J. Baucom, 1997: Operational calibration of Geostationary Operational Environmental Satellite-8 and -9 imagers and sounders. *Applied Optics,* **36,** pp 6895-6904.

Whitlock, C. H., T. P. Charlock, W. F. Staylor, R. T. Pinker, I. Laszlo, A. Ohmura, H. Gilgen, T. Konzelman, R. C. DiPasquale, C. D. Moats, S. R. LeCroy and N. A. Ritchey, 1995. First Global WCRP Short-wave surface Radiation Budget Data Set. *Bull. Amer. Meteor. Soc.* **76**, No. 6, 1-18.

Wielicki, B. A., Barkstrom, B. R., Harrison, E. F., et al. 1996. Clouds and the earth's radiant energy system (CERES): An earth observing system experiment. B. Am. Meteorol. Soc., 77 (5), 853-868.

Wonsick, M. A. and R. T. Pinker, 2004. Satellite Estimates of Surface Shortwave Fluxes: Sensitivity to Sensor Calibration AGU Joint Assembly 2004, Montreal, Quebec, May 17-21, 2004

Zhang Y. C., Rossow, W. B., Lacis A. A., 1995. Calculation of surface and top of the atmosphere radiative fluxes from physical quantities based on ISCCP data sets. 1. Method and Sensitivity to input data uncertainties. *J. Geophys. Res-Atmos*, **100 (D1),** 1149-1165.

Zhang, Y-C., W. B. Rossow, A. A. Lacis, V. Oinas and M. I. Mishchenko, 2004. Calculation of radiative flux profiles from the surface to top-of-atmosphere based on ISCCP and other global datasets: Refinements of the radiative transfer model and the input data, *J. Geophys. Res.,* 109, D19105, doi:10.1029/2003JD004457.

Zhang, B., R. T. Pinker, and P. W. Stackhouse, 2004. An EOF Iteration approach to obtain homogeneous radiative fluxes from inhomogeneous satellites observations. Manuscript in preparation.

Seasonal and Long-term Variations of Shortwave Radiation in China

Tadahiro Hayasaka[1], Kazuaki Kawamoto[1], Jianqing Xu[2] and Guangyu Shi[3]

[1]Research Institute for Humanity and Nature, Kyoto 602-0878, Japan
[2] Frontier Research System for Global Change, Yokohama 236-0001, Japan
[3]Institute of Atmospheric Physics, Chinese Academy of Sciences, Beijing 100029, China

1. Introduction

Surface radiation budget is one of the most important factors in the earth's climate system. The changes in surface radiation as well as radiation at top of the atmosphere due to anthropogenic emissions of aerosols and greenhouse gases have been recently studied by using ground-based measurements, satellite measurements, and climate model simulations (IPCC, 2001). Downward shortwave radiation at the surface is complicatedly related to atmosphere including clouds, aerosols, water vapor and other constituents, and thus surface radiation measurements are important although the number of station with high quality operation is limited. Calculation based on satellite cloud data can evaluate surface SW surface radiation in a wide area for the past two decades. However, those calculation also has some limits such as plane-parallel atmosphere assumption and spatial and temporal resolution of cloud data. It is therefore worthwhile to compare and comprehensively evaluate surface SW radiation among the various data set.

In the present study, we compare the monthly averaged surface SW radiation data between two satellite derived data set and pyranometer measurements in China for 11 years. In addition to those data, SW radiation data calculated by using parameterization with meteorological data other than pyranometer measurements are also used to check the quality of pyranometer data. The pyranometer measurements need careful operation such as keeping level and clean glass dome as well as precise calibration. Therefore it is quite important to compare the data obtained by independent methods. After checking the quality of the pyranometer data, we will discuss the seasonal and long-term variations of surface shortwave radiation in China.

2. Comparison of surface shortwave radiation data.

Ground based measurement data, i.e., pyranometer measurements and parameterization from meteorological data are compared with each other, and also with the 1km grid data derived from satellite observations. All these data were compared month by month. A simple lenear regression analysis was carried out for the comparison.

Chinese Meteorological Administration (CMA) has been measuring downward SW radiative flux at more than 120 stations in which more than 60 stations continue the measurements since late 1950's or early 1960's. All of the data were originally acquired every hour and daily data were reported. In this study monthly average data based on daily average data were used for the analysis. Calibration before early 1990s was carried out every 5 year by using the Eppley blackbody cavity radiometer PMO-6 which is calibrated in Meteorological Research Institute, Japan Meteorological Agency. Recently CMA has been directly attending the intercomparison with the international calibration standard of World Radiation Center in Davos, Switzerland.

There are several products of surface SW radiation data set derived from satellite cloud data. We used NASA/GEWEX SRB product provided by NASA Langley Research Center, for which the algorithm is originally based on Pinker and Laszlo (1992). The SRB data used here are daily average and 1 degree by 1 degree in spatial resolution, which are calculated from ISCCP DX cloud data and objective analysis meteorological data.

Monthly average data of surface SW radiation are also obtained from operational meteorological data by using parameterization method. The surface SW radiation is basically estimated with water vapor amount, tubidity coefficient, and sunshine duration as a proxy of cloud amount (Xu et al., 2005).

Figure 1 shows examples of the comparison among the three data set. SSAT and SXU correspond to satellite derived data and parametrization data, respectively. The period for the comparison is 1984-1994. It is shown that satellite derived data have a negative bias against pyranometer data in the arid area Golmud (upper panel) and a positive bias in the large city area Shanghai (lower panel). On the other hand, parametarization data are rather consistent with pyranometer data at both stations.

We compared pyranometer data with satellite derived data at 65 stations, and with parameterization data at 15 stations. It is found from the comparison that SRB data overestimate SW radiation in large city areas, while underestimates it in desert areas. These discrepancies are ascribed to aerosol assumption in the calculation of SW radiation from satellite cloud data. Absorbing aerosols in the sub-cloud layer, which is not observed from space, is important for SW radiation on the surface. On the other hand, incorrect assumption on the aerosol loading seems to be the reason of the negative bias in Golmud. Other factors for the discrepancy is effect of cloud inhomogeneity. However, this effect seems to be small if the cloud properties are averaged for the results retrieved from various viewing angle radiance data (Iwabuchi and Hayasaka, 2002).

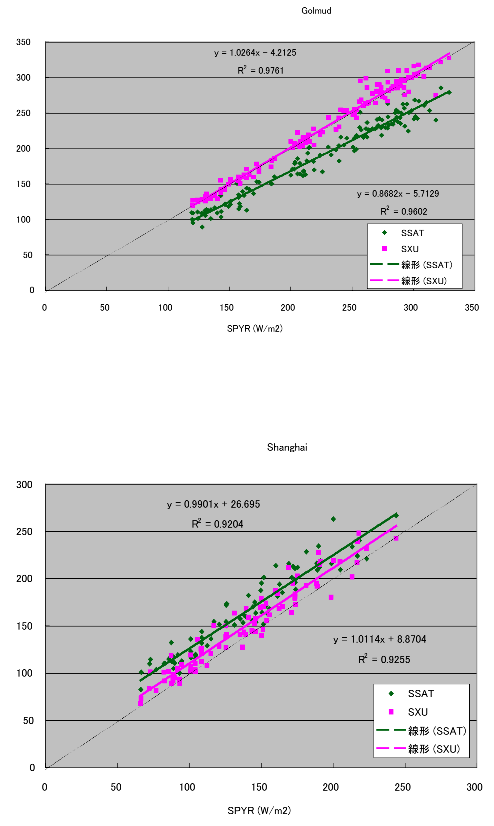

Fig. 1. comparison among the three data set. SPYR, SSAT and SXU correspond to pyranometer data, satellite derived data and parametrization data, respectively.

3. Seasonal and long-term variations of shortwave radiation

Figure 2 shows a typical distribution of shortwave radiation obtained from SRB data. It is found that shortwave radiation over China has seasonal variations as follows. In spring and summer, large values of SW radiative flux extend over desert and semi-desert area in the north part of China, whereas those in the southern part are small. These properties are associated with front system. It is inferred from ISCCP cloud analysis that low-level cloud amount is more important in spring rather than optical thickness, while optical thickness as well as cloud amount is also important in summer. In autumn and winter, spatial variation of SW radiative

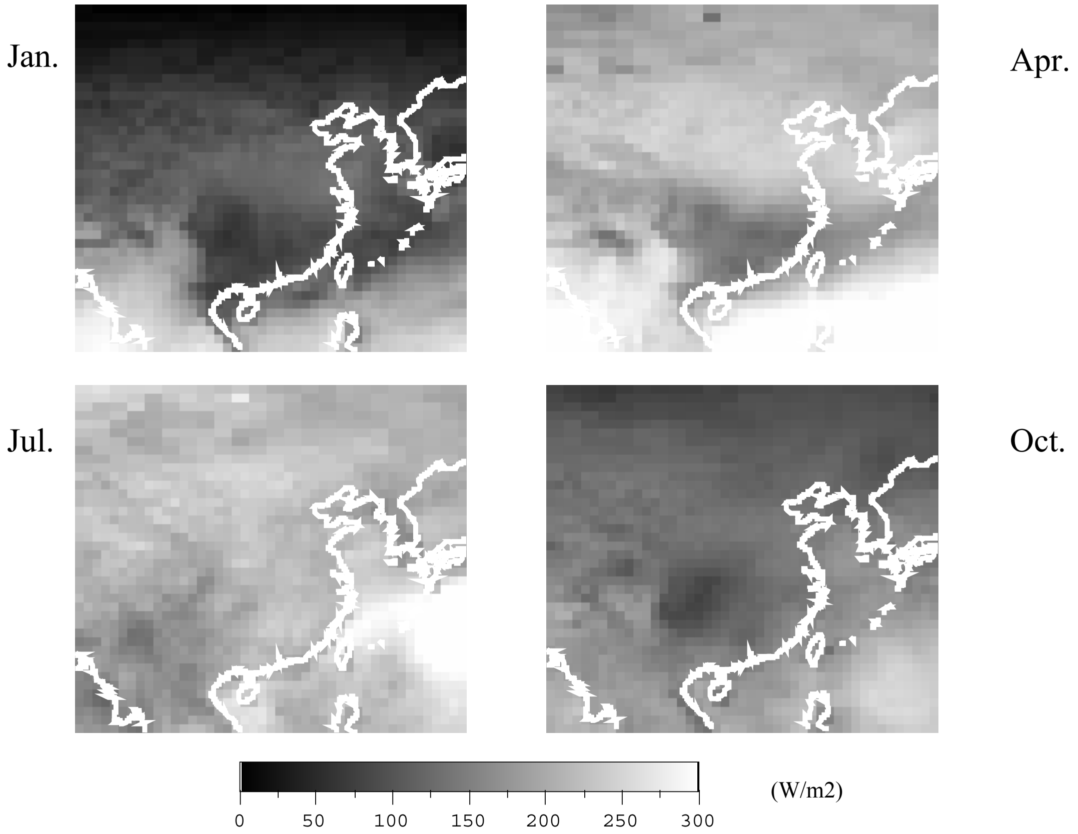

Fig. 2. Shortwave sueface radiative flux in 1995 over China estimated from SRB data

flux is small except for the minimum value around Sichuan basin where heavy aerosol loading is always observed.

It is inferred from ISCCP cloud analyses that low-level cloud amount is more important in spring rather than optical thickness, while optical thickness as well as cloud amount is also important in summer. It is also found that spatial variations of these cloud properties change year to year.

We retrieved cloud amount, optical thickness and effective particle radius of low-level clouds from NOAA/AVHRR GAC data, based on the reflection method (Kawamoto et al., 2000). This method basiclly uses visible and near infrared channels, by comparing the data and theoretical calculations. In order to avoid the errors in the retrieval due to cloud inhomogeneity, data with scanning angle less than 25 degree were used (Iwabuchi and Hayasaka, 2002). Results of AVHRR analysis suggest that aerosols strongly affect not only cloud amount but also effective particle radius and optical thickness, for example, small cloud particles and large optical thickness are observed around Sichuan basin corresponding to aerosol optical thickness distribution. In autumn and winter, effective particle radius is smaller than summer. Low-level cloud system is affected by aerosols in boundary layer and thus aerosol indirect effects become more important. Therefore the seasonal variation as shown in Fig. 2 may reflect the indirect effect of aerosol.

Long-term variation of SW radiation was analyzed for 1971-2000 by using mainly pyranometer measurement data after chacking the quality of the data as dissucused above. It is found from preliminary analysis that SW radiation almost all over China has a tendency to decrease for 1971-2000, but looks to increase in south region for 1991-2000.

4. Summary

Downward shortwave radiative flux on the surface in China were evaluated by using pyranometer data, calculated results by parameterization with ground-based meteorological data such as sunshine duration and water vapor. The results are also compared with NASA/GEWEX SRB data set for 1984-1994. These radiation data are in general consistent with each other for monthly average values although SRB has positive bias for large city areas whereas negative bias for the desert area in the west part of China. One of the reasons for these biases is ascribed to inappropriate assumption of aerosols in the SRB.

The amplitude of seasonal variation of shortwave radiation is large in the northeast region, while it is small and complicated, i.e., it is not a simple seasonal variation . As for long-term variation of SW radiation, the decrease tendency was observed in almost all stations. The synthetic analysis by using various data set should be discussed because the satellite data are limited after 1980s and pyranometer measurements have some difficulties in keeping quality of data due to the calibration and operation.

Acknowledgments.

We would like to thank Drs. P. W. Stackhouse Jr. and S. Gupta for providing GEWEX/SRB data set calculated from ISCCP data.

References

IPCC, 2001: Climate Change 2001, The Scientific Basis, edited by J. T. Houghton et al., Cambridge Univ. Press, New York.

Iwabuchi, H. and T. Hayasaka, 2002: Effects of cloud horizontal inhomogeneity on the optical thickness retrieved from moderate-resolution satellite data. *J. Atmos. Sci.*, **59**, 2227-2242.

Kawamoto, K., T. Nakajima and T. Y. Nakajima, 2001: Aglobal determination of cloud microphysics with AVHRR remote sensing. *J. Climate*, **14**, 2054-2068.

Pinker, R. T. and I. Laszlo, 1992: Modeling surface solar irradiance for satellite applications on a global scale. *J. Appl. Meteor.*, **31**, 194-211.

Xu, J., T. Hayasaka, K. Kawamoto and S. Haginoya, 2005: An estimation of downward surface radiation over China. *J. Meteor. Soc. Japan* (in press).

Properties of long-time digital camera records in Changchun and Ulaanbaatar

Kisei Kinoshita (1), Hiroyuki Kikukawa (2), Naoko Iino (3),

Wang Ning (4), Zhang Gang (4), Jugder Dulam (5),

Tsatsaral Batmunkh (5) and Satoshi Hamada (1)

(1) Faculty of Education, Kagoshima University, Kagoshima, 890-0065, Japan
(2) Faculty of Fisheries, Kagoshima University, 890-0056, Japan
(3) Department of Mechanical Engineering. Kagoshima University, 890-0065, Japan
(4) Environmental Science Department, Northeast Normal University, Changchun, China
(5) Institute of Meteorology and Hydrology, Ulaanbaatar 210646, Mongolia

Abstract : Digital cameras to record fixed wide views with one-hour interval are operating in Changchun, China since the middle of March 2003, and in Ulaanbaatar, Mongolia since the middle of March 2004, to study visibility and air turbidity affected by Asian dust. Digital video cameras with ten-minute interval are also in operation there. We discuss the results of the observation in the spring and summer of 2004, and the optical properties of the digital photo records.

Key Words: Asian dust, digital image ,interval recording, turbidity, visibility

1. Introduction

Long-time visual recordings by using digital cameras are very effective for the studies of atmospheric phenomena as reviewed in [1] concerning volcanic cloud observation. In order to observe the Asian dust phenomena from the ground in Northern Asia, digital photo and video cameras have been set at Northeast Normal University in Changchun, Jilin Province, China since 18 March 2003, and also at the Institute of Meteorology and Hydrology, Ulaanbaatar, Mongolia since 16 March 2004. Digital photo cameras were also set at two stations, Bulgan and Dalanzadgad in southern Gobi, Mongolia in the spring of 2004. The ground observation at these stations, shown in Fig. 1, are important to study the rise and the transport of the dusty air in the northern roots toward Northern Pacific, as often observed in the satellite imagery [2]. On the other hand, the web-camera recording in Kagoshima, southwest Japan, started in the end of 2000, preceded by video recording since 1987 and extended to southern islands including Mayon volcano, Philippines, as summarized in [3].

The results of ground observations and satellite imagery of dust events in 2003 were already reported in [4]. In this report, we discuss the ground observation results in Changchun, Ulaanbartar and two stations in southern Gobi in 2004, with special attention to the optical properties and the performance of digital cameras. Preliminary results concerning the dust events supplemented with the satellite imagery are reported in [5, 6].

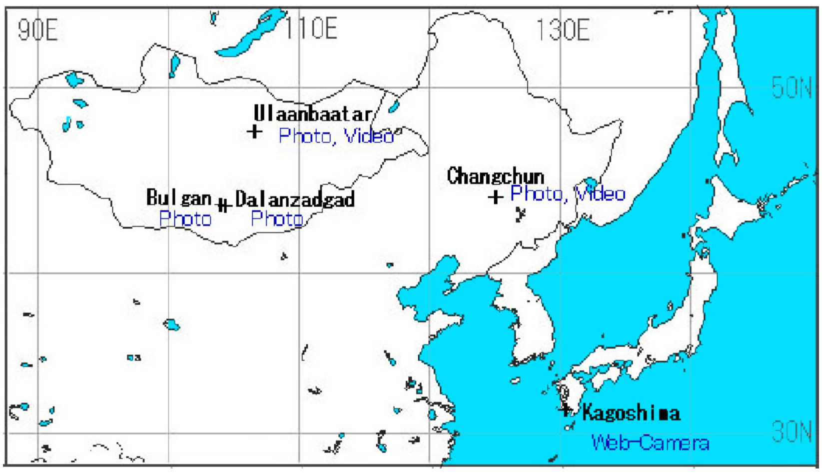

Fig. 1. Location map of observation stations.

2. Observation in Changchun and digital RGB analysis

Interval recordings by digital photo and video cameras in Changchun in 2004 started in the evening on March 9. On the next day, very dusty air was observed almost all the day. The recordings continued until August 21, by changing medias on May 24. The cameras were set at the window toward the north on the fifth floor in a building of Environmental Science Department, College of Urban and Environmental Sciences, Northeast Normal University. Fig. 2 (a), (b) and (c) are typical images by photo camera Casio QV-R4 of clear sky, cloudy and dusty scenes in the daytime in the middle of March. The differences in color and the brightness change according to the vertical angle are obvious in the images.

(a) clear sky: 13 March at 11 CST (b) cloudy: 16 March at 12 CST (c) dusty: 10 March at 14 CST

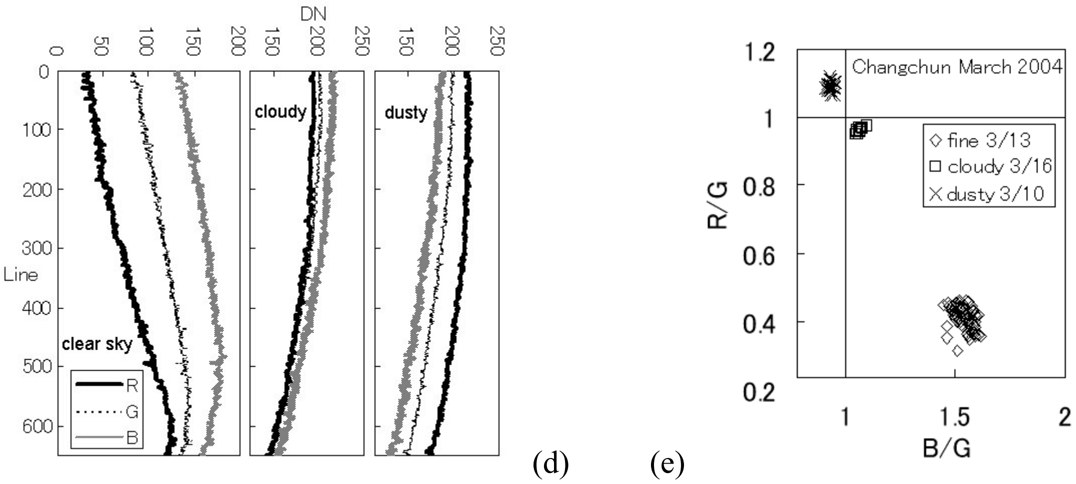

Fig. 2. The photo scenes (a-c) at the Changchun station, RGB profiles (d) along a common vertical line shown in (c), and the scatter diagram (e) of R/G vs. B/G at the upper part of the line indicated in (a) for three scenes.

These images are taken by the format 1280 pixels * 960 lines in the normal mode. Quantitative study can be done by taking the RGB (Red, Green and Blue) profiles in 8 bit, such as shown in Fig.2(d), along a common vertical line in the sky shown in Fig. 2(c). In the case of clear sky, the relationship among three color-components is B > G > R and the difference of each is significantly large especially in the sky region far away from the horizon. For cloudy sky, the differences become small, especially between G and R, but never change the relation. For dusty sky, the above relationship is reversed as B < G < R, and the differences increase with dusty levels. A scatter diagram of the values B/G and R/G normalized by the Green component in the upper part of the vertical line, shown in Fig. 2(a), are exhibited in Fig. 2(e), where three clusters are clearly separated corresponding to the air turbidity.

We may also study the decrease of the visibility in dusty air in the photo data. Fig. 3(a) is a comparison of the views near the horizon in Fig. 2 (a, b and c). The RGB values along a line there are displayed in Fig. 3 (b, c and d). The decrease of the contrast between the buildings far away and the background sky is obvious for cloudy and dusty scenes.

In order to see the air turbidity from the color information of the sky, the white-balance of the color was set to the daylight (outdoor) mode. The zooming of the camera was set as wide as possible.

All of the photo records were edited by html to see a few days from dawn to dusk at a glance, keeping original jpeg images without change, after renaming to indicate the place and the date-time and separating nighttime scenes.

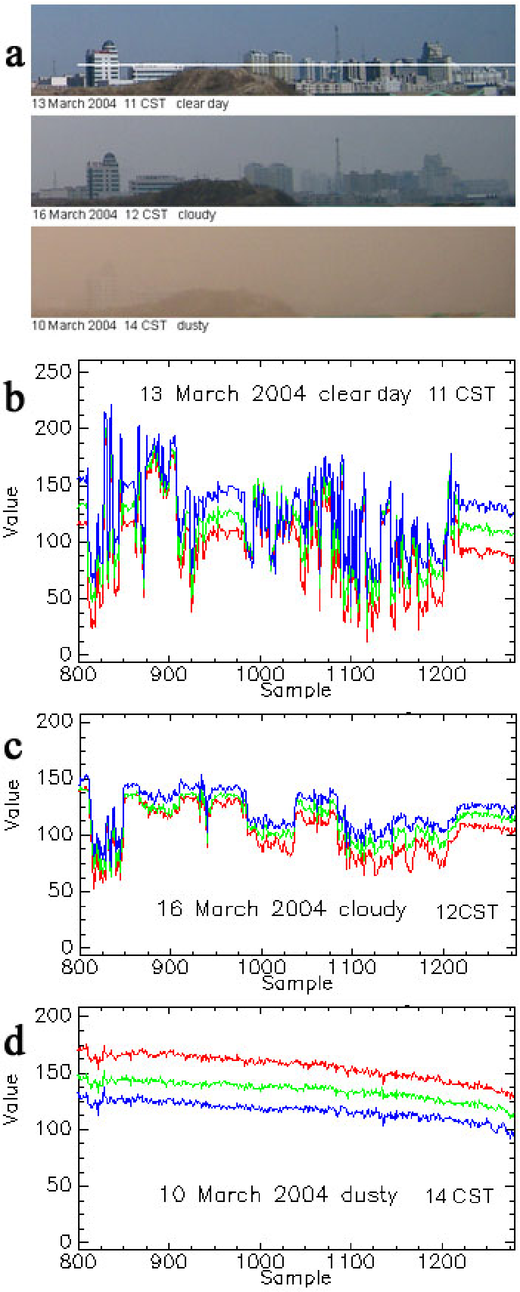

Fig. 3. (a) Parts of photo scenes near the horizon in Fig. 2 (a-c). (b-d) RGB values along the line indicated in (a).

Fig. 4. A list of photos on June 29 in Changchun, as indicated by ch040629hh with CST (=UTC+8) for hh.

Thus, we may have quick look images of seasonal change of daytime hours as well as weather changes in day and time. Fig. 4 is a sample of a photo list in a fine and longest day in the end of June. We see that the development and decrease of cumulus clouds around the mid-day.

In Changchun, a video camera Sony DCR-TRV40E has been operating with ten-minute interval, with somewhat close-up because of the limitation of the window frame for wider view. In Fig. 5, we compare the photo and video records in dusty and clear days in March. We see that the difference of the air turbidity is remarkable, though the color contents somewhat depend on the cameras.

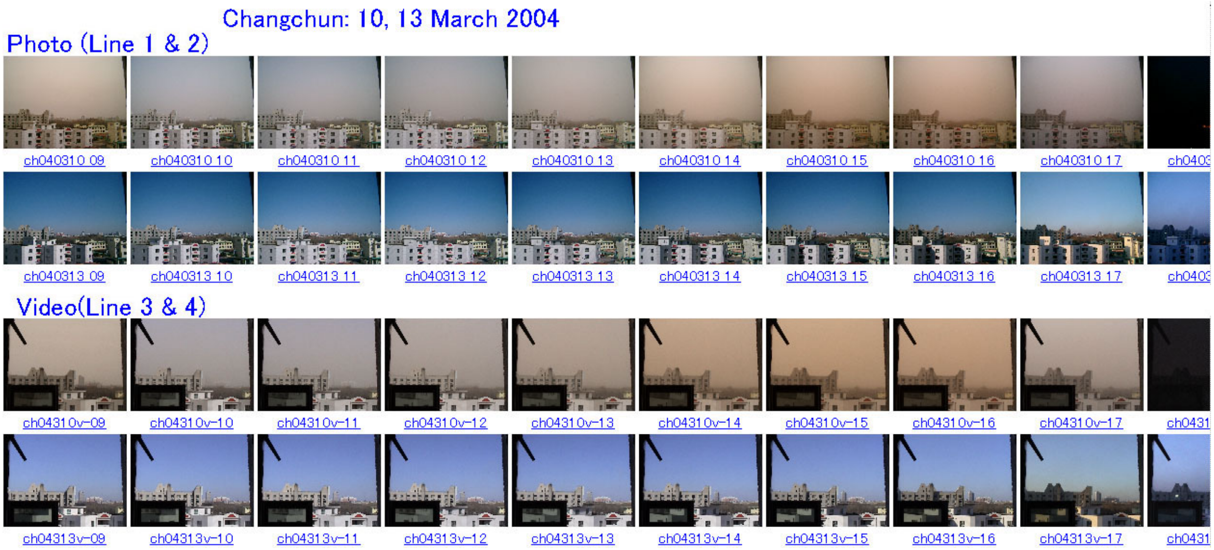

Fig. 5. Comparison of photo (line 1 and 2) and video (line 3 and 4) records on 10 and 13 March, corresponding to dusty and clear days respectively in Changchun.

3. Observation in Ulaanbaatar

In Ulaanbaatar, a photo camera with wide view, Ricoh Caplio G4wide, and a video camera Sony DCR-TRV900 with semi-fish eye converter lens Kenko x0.45 have been set at a window toward the west on the third floor of Institute of Meteorology and Hydrology (IMH). A tall bank building in front of the window somewhat disturbs the view as shown in Fig. 6, which is a semi-fish eye view of the video camera. The photo camera has been tilted by 90 degrees, so as to take wide vertical view. In 2004, photo records were obtained during 16 March and 20 June with one-hour interval, and video records between 16 March and 2 June with ten minutes interval as in Changchun. The video records were converted into mpeg files for each day separately from dawn to dusk. Fig. 7 is a quick look list of photos for seven days in the middle of

Fig. 6. A semi-fish eye video scene at IMH, Ulaanbaatar..

April from the sunrise to dusk for a day in a line. The filename of each photo indicates the place (UB) and the date-time, where Mongolian standard time (MST= UTC+8) is used. In these photos, we see the mirror images of rising sun around 6 MST, and the direct images of falling sun in the afternoon partly shielded by the bank building. In Fig. 7, light dusts were occasionally seen on 13-14 and 17-19, while very fine sky is seen in many other days and times.

Fig. 7. A sample of quick look scenes at IMH, Ulaanbaatar, for 13-19 April, 2004, 6-19 MST.

4. Observation in southern Gobi

At Bulgan and Dalanzadgad in southern Gobi, photo cameras Casio QV-R4 and Sharp MD-PS1 were set at the windows toward the south and the west respectively on the ground floors in the meteorological stations there, with the zoomings of the cameras as wide as possible. At the Bulgan station isolated in Gobi desert, the camera was powered by a battery-pack outside. We got the records there for 26 days since 18 March. (At the other stations in general, the cameras have been powered by AC converters connected to AC power sources through uninterrupted power supplies.) At the Dalanzadgad station, restart of the camera was necessary for many times, and the photos were obtained during 27 March and 17 June, lacking the records of March 31, April 1-7 and 14-19, May 6, 12-13 and 20-31, and June 8-10. The white-balance of MD-PS1 had to run by automatic mode only.

Fig. 8 shows quick look images for two days in the afternoon in the end of March at two stations. We may see dusty air to the south of these stations in the afternoon on 27 March.

Fig. 8. Quick look images at Bulgan (BL) and Dalanzadgad (DZ), in the afternoon on 27-28 March 2004.

5. Remarks

Interval digital records of photo and video cameras are useful for the studies of dusty air and many other aspects of weather changes. Studies of Asian dust in conjunction with satellite imagery and other related data are in progress, as partly reported in [5, 6]. Three photos per day at local standard time 9, 12 and 15 hours at Changchun and Ulaanbaatar are archived in http://volceye.edu.kagoshima-u.ac.jp/webcam/archive/ .

References

[1] K. Kinoshita, C. Kanagaki, A. Minaka, S. Tsuchida, T. Matsui, A. Tupper, H. Yakiwara and N. Iino: Ground and Satellite Monitoring of Volcanic Aerosols in Visible and Infrared Bands, Proc. CEReS Int. Symp. Remote Sensing, Chiba, Japan, pp.187-196, 2003.

[2] Kagoshima Kosa Analysis Group: Satellite Imagery of Asian Dust Events, Kagoshima Univ., 159 pp. 2001; N. Iino, K. Kinoshita, R. Iwasaki, T. Masumizu, T. Yano: NOAA and GMS observations of Asian dust events during 2000-2002, Proc. SPIE Vol. 4895 Applications with Weather Satellites, SPIE, Bellingham, WA, USA, pp. 18-27, 2003.

[3] Kagoshima Univ. Volcanic Cloud Research Group: Volcanic Eruption Clouds in the Western Pacific - Ground and satellite based observations and analyses -, Kagoshima Univ., 142pp., 2004.

[4] K. Kinoshita, N. Wang, G. Zhang, S. Hamada, S. Tsuchida, A. Tupper and N. Iino: Continual observation of Asian dust in Changchun and Kagoshima, 2nd International Workshop on Sandstorms and Associated Dustfall, Nagoya, 2003.

[5] K. Kinoshita, N. Iino, S. Hamada, H. Kikukawa, T. Batmunkh, D. Jugder, N. Wang,G. Zhang and A. Tupper: Automatic image recording network of sand storm and dusty airs in northern Asia, International Radiation Symposium: Current Problems in Atmospheric Radiation, August 23-28, Busan, Korea, 2004.

[6] K. Kinoshita, S. Hamada, N. Iino, H. Kikukawa, J. Dulam, T. Batmunkh, N. Wang and G. Zhang: Interval Camera Recordings of 2004 Asian Dusts in Mongolia, Northeast China and Southwest Japan, 4th ADEC Workshop, Jan. 26-28, 2005, Nagasaki, Japan.

Analysis And Impact Study Of Global Positioning System Radio Occultation Precipitable Water Vapor Over East Asia Region

D.Rajan and GR.Iyengar

Department of Science & Technology, New Delhi, India

Abstract.

The Asian summer monsoon governs the very pulse of life on the whole continent. Understanding and predicting the variability of this monsoon is, therefore, extremely challenging for the well-being of billions of people and the diverse flora and fauna inhabiting the Asian region. This Asian land mass is unique in the sense of its geographical distribution, where the observation by remote sensing techniques are essential. The lack of accurate measurements of atmospheric parameters over the oceans and other remote regions contributes greatly to the uncertainties in the initial state of weather over this region. Meeting the ever-increasing demand of the atmospheric parameters over this landmass is a challenging task for researchers in the field of environmental remote sensing. The science and applications that develop from space observing systems will have far-reaching impact on mankind's ability to sustain a vigorous and fruitful life in the Asian region.

The Global Positioning System (GPS) is developing into a powerful source of information in this field of science with the application of the remote sensing techniques. In this study, a detailed analysis of the GPS METeorological parameters (GPS/MET) is carried out for the Asian summer monsoon period 2001 and March 2002. The results of the GPS/MET quality are described in detail in comparison to other source of meteorological parameters.

Key words: (Radio occultation, monsoon, Remote sensing, Spectral Statistical Interpolation, Data assimilation, Precipitable Water Vapor)

INTRODUCTION

The Asian land mass is unique in the sense of its geographical distribution of oceans, forests, mountains, valleys, deserts, etc. The advent of remote sensing technique has added new dimensions to the study this distribution in depth. In recent years, there has been a substantial increase in the understanding of this unique landmass by the use of remote sensing techniques.

The implementation of the GPS network of satellites with the development of small, high-performance instruments to receive GPS signals have created the opportunities for active remote sounding of the earth's atmosphere by radio occultation at comparatively low cost. With the development of the GPS satellite network, it becomes possible to measure precipitable water vapor, accurate temperature, pressure, etc using radio occultation. Since the first launch of GPS/MET instrument package, namely receiver, a major goal has been to demonstrate the potential value of these GPS radio occultation measurements in numerical weather analysis and prediction. Many studies have revealed that the quality of the GPS/MET retrieved temperature/moisture measurements as compared to other types of data, such as operational global analysis, radio-sondes and satellite data (Ware et al., 1996; Kursinski et al., 1995, 1996; Rocken et al, 1997; Kuo et al., 1998) is reasonably good. These detailed studies suggest that

GPS/MET occultation measurements are accurate and have the potential to be useful in numerical weather prediction and climate studies.

BACKGROUND OF THE GPS OBSERVATION

Detailed numerical weather prediction requires observational data of good quality and of high spatial/temporal resolution. Due to various limitations, important variables such as tropospheric water vapor are often inadequately covered by conventional observations from radio-sondes or by meteorological satellites systems. The GPS is developing into a powerful tool for the moisture content for use in fine-scale regional models and the global models. Recent years have seen great advances in GPS meteorology and related fields. The GPS was developed by the United States Department of Defense primarily for military uses. It consists of 24 GPS satellites that are evenly distributed in six orbit planes around the earth. The altitude of each GPS satellite is 20200 km. Almost all the Low Earth Orbiting (LEO) satellites are at about 750 km altitude. Each GPS satellite is equipped with a transmitter with highly stable frequency. The GPS receiver can be located (i) on the LEO satellite (ii) at the earth stations to transmit data ranging from 1.2 to 1.6 GHz (L-band signals) to ground-based or space-based receivers. Basically the GPS system measures time delays between the transmission and reception of the electromagnetic signals. During an occultation, the satellites move in such a way that the electromagnetic ray connecting them traverses the atmosphere.

The receivers are also located on the ground. Geographical Survey Institute (GSI), Japan, established GPS Observation NETwork called GEONET with about 1000 GPS ground stations spread over its territory. Back in 1997, Japan launched a GPS project, an application of precipitable water from a nationwide GPS array (GEONET) for data assimilation in Numerical Weather Prediction (NWP), and an improvement of geodetic accuracy of GPS based on NWP database. Today the Japanese GEONET, which consists of more than 1200 GPS permanent stations, is one of the largest GPS networks of the world. The details of the GPS project over this East Asian region, is given in Table-1. In addition, there are a few on-going assessments of prototype missions available for us-namely GPS/MET, the German Challenging Minisatellite Payload (CHAMP), and Argentine SAC-C. Some of the developed operational missions are Constellation of Observing System for Meteorology, Ionosphere, and Climate (COSMIC), METOP/GRAS, NPOESS/GPSOS. GPS ground measurements are the only means to obtain integrated precipitable water vapor values under all weather conditions.

The GEONET database offers datasets with high spatial resolution and a very dense time scale. The data from June to September, 2001 & March 2002 are obtained from the web page of the Chiba University for this study. This database contains the following meteorological parameters: (i) Zenith Total Delay (ZTD), (ii) Precipitable Water Vapor (PWV), (iii) water vapor mixing ratio (q), (iv) Relative Humidity (RH), (v) precipitation, (vi)air pressure, (vii) air temperature, (viii) zonal component of wind, and (ix) vertical component of wind. The parameters are analyzed and the accuracy of these GPS/MET parameters is statistically examined in this study. For this study a 3 dimensional Spectral Statistical Interpolation (SSI) weather analysis scheme is used. The detailed explanation of this spectral statistical analysis technique is given below.

UNIQUE FEATURES OF GPS RADIO OCCULTATION

Some important features of GPS RO are (i) Highly accurate averaged temperature profiles with an accuracy of up to 0.1° K (ii) assured long-term stability (ii) all-weather operations (iii) global 3-dimensional coverage (iv) high vertical resolution (less than 100 m) in the lower troposphere (v) independent of height, pressure, and temperature (vi) the GPS RO instrument is very compact (not more than size of shoe box), (vii) low-power, low-cost sensors required.

SPECTRAL STATISTICAL INTERPOLATION ANALYSIS

In spectral analysis the actual state of the atmosphere is represented by an expansion of a series of space dependent functions with time dependent coefficients. The analysis procedure consists of determination of these coefficients, which make series expansion a best fit with the observed data. The meteorological data from various observing platforms from all over the globe is received at the regional telecommunication hub, New Delhi through the Global Telecommunication System (GTS). The Spectral Statistical Interpolation (SSI) is a three-dimensional variational analysis scheme, here after called as SSI. The observation residuals are analyzed in spectral space on sigma surfaces, In the SSI scheme the objective function to be minimized is defined in terms of the deviations of the desired analysis from the first guess field (6hr forecast) and the observations, weighted by the inverse of the forecast and the observational error variances respectively. The objective function is based on the Parish (1992) concept of minimizing a cost function consisting of a cost function of mainly two parts as follows $J = J_{ges} + J_{obs}$, the two terms in J on the right hand side of this equation deal with the best fit of the first guess field and the observations with the analysis respectively. The analysis variables are chosen to simplify background term, for speedy convergence and to include balance. The analysis variables can be transformed to model variables. The analysis variables in this scheme are vorticity (ζ), fast or unbalanced part of divergence (D), temperature (T) and logarithm of surface pressure (ln Ps) and mixing ratio (ω).

For this experiment the year 2001 data of various types viz SYNOP/SHIP, BUOY, TEMP, PILOT, AIREP, SATOB, INSAT, GMS, GOES, and METEOSAT are assimilated. These observations falling within ± 3 hours of the respective hour of assimilation are being used in the corresponding hours of assimilation. Thus four times (00, 06, 12, 18 UTC) assimilation cycle is made. Once the initial condition is prepared, the prediction equations are integrated and weather predictions are obtained. The impact of (i) PWV obtained from NOAA/TOVS, (ii) moisture obtained from INSAT, (iii) specific humidity from GMS with this SSI technique has been documented, in Rajan et al (2000, 2001, 2002a, 2002b).

ANALYSIS OF GPS OBSERVATION

GPS/MET is one of the most cost-effective remote sensing systems tested recently at the National Oceanic and Atmospheric Administration (NOAA). Here the GPS/MET data has been obtained from the Chiba university website dbx.cr.chiba-u.jp. The primary results have been listed here.

There are more than 980 reports available for each of the 3 hourly (00, 03, 06, 09, 12, 15, 18, 21) observations in a day. The reports are spread from 24. 06° N to 45.4° N in the north south direction, and 122.94° E to 145.8° E in the east west direction. Each report has GPS meteorological parameters with a particular latitude, longitude, altitude and pressure level. This information is available in the pressure level from 1000 hPa to 800 hPa only. The air temperature is attaining minimum value at 21 hrs rather than 00 hrs. The PWV variations are too large in this sample database. The mean monthly PWV average is 35 mm, with maximum of 84 mm, and minimum of 1.5 mm. The corresponding maximum Relative Humidity (RH) of 84 % is observed in the summer monsoon period. The RH reaches the maximum of 99.14 % with an average value of 76 % in the month of September. It seems that for the year 2001, September is wetter than earlier monsoon months. The earlier study indicates that GPS PWV estimates are accurate to a millimeter level and look very promising for use in NWP models. The statistical study about the diurnal variations of the PWV at the location 43°N, 142°E shows in Fig-1. The PWV attains its maximum value at 15-18 hrs of a typical day 01 June 2001. The mean monthly moisture variable, specific humidity (q) is computed as 22 g/kg with standard variations of 6 g/kg for the month of August 2001. In August, the vertical distribution of GPS-PWV and SSI-PWV over Fuji Mountain in Japan is shown in the Fig –2. It is clearly seen that the GPS PWV has best fit with the SSI-PWV. The monthly distribution (June, July, August and September) of PWV over ‘Chiba’ is shown in the Fig-3. The geographical distribution of mean August month SSI-PWV is plotted in the Fig-4. From this, it is noted that the gradient over the latitude 40° to 45° N is much more than that over Japan’s land areas.

This GEONET GPS station measures the delay that the ratio signal from GPS satellite suffers as it propagates through the atmosphere. When several satellites are seen from the stations, the delays are combined or ‘mapped’ into a zenith total delay (ZTD) (Niell, 1996). The largest part of ZTD is the ‘dry’ delay (90 %) due to the dry air gases; the remaining delay or ‘wet’ delay depends on the moisture content of atmosphere and is therefore highly variable. The average value of the ZTD is 2.65. The PWV can be derived from ZTD using an approximate formula that requires information on the pressure and temperature at the GPS station (Bevis et al., 1994). They can be derived for high frequency and from a dense network, and are not affected by rain or cloud. In this sense any type of weather does not affect all GPS measurements at the time of observation. The disadvantage of having only one piece of information along the vertical can be alleviated with the aid of the data assimilation technique used in NWP. It is seen that there is a small wet-bias in GPS data with respect to radio-sonde, SSI, and numerical model predictions. The azimuthal variations in slant-wet delay contain information on relative variations in water vapor.

SUMMARY AND OUTLOOK

Individual GEONET observation soundings when compared with radio-sondes, SSI analysis and prediction from numerical models, provide additional insight on the PWV component of monsoon studies over this East Asian region. The present preliminary study shows better agreement of GEONET PWV over many locations. The location of the typhoon (# 11) on 20-22 August 2001 is very clearly brought out from GEONET-PWV observation associated with heavy rainfall observation over this region. The combination of GEONET, SSI's PWV offers the possibility to understand new concepts on water vapor cycle in the atmosphere. In the current scenario, an altimetry space mission (TOPEX) is one of the first satellites to have a GPS receiver on-board. This study reported here will be extended to a GPS/MET long-term study for the period 1996 to 2002.

ACKNOWLEDGEMENTS

Acknowledgements are due to GEONET database of Chiba University provided by the GPS Meteorology project of Ministry of Education, Sports, Science and Technology (MEXT), Japan. Thanks are due to Dr.Kondoh, Akihiko, CEReS, Japan. The author acknowledges the support and encouragement given by Dr B.K.Basu and AK. Bohra.

REFERENCES

Bevis. M., S.Businger, S.Chiswell, T.A.Herring, R.A Anthes, C. Rocken and R.H. ware, 1994: GPS meteorology: mapping zenith wet delay onto precipitable water, *Journal of Applied Meteorology*., **33,** 379-386.

Kuo, Y.H., X.Zou, S.J.Chen, Y.R.Guo, W.Huang, R.Anthes, D.Hunt, M.Exner, C.Rocken and S.Sokolovskiy 1998: A GPS/MET sounding through an intense upper-level front. *Bulletin of American Meteorological Society*., **79**, 617-626.

Kursinski, E. R., G.A.Hajj, W.I. Bertiger, S.S.Leroy, T.K. Meehan, L.J.Romans, J.T.Schofield, D.J.McCleese, W.G.Melbourne, C.L.Thornton, T.P. Yunck, J.R. Eyre and R.N.Nagatani 1996: Initial results of radio occultation observations of earth's atmosphere using the Global Positioning System. *Science.,* **271**, 1107-1110.

Kursinski, E.R., G.A. Hajj, K.R.Hardy, L.J.Romans and J.T.Schofield, 1995: Observing tropospheric water vapor by radio occultation using the Global Positioning System. *Geophysical Research Letter*., **22**, 2365-2368.

Niell, A., 1996: Global mapping function for the atmosphere delay at ratio wavelengths. *Journal of Geophysical Research*., **101**, 3227-3246.

Parrish, D.F. and J.C. Derber, 1992: The National Meteorological Center's spectral statistical interpolation analysis system. *Monthly Weather Review*., **120**, 1747-1763.

Rajan. D., A.K. Bohra, A.K. Mitra, R.K. Paliwal, V.S. Prasad and V.B. Bhatia 2002(a): Moisture profiles from satellite data over Indian Ocean area. *International Journal of Remote Sensing*., **23** (15), 2951-2969.

Rajan. D., A.K. Mitra, S.R.H. Rizvi, R.K. Paliwal, A.K. Bohra and V.B. Bhatia, 2001: Impact of Satellite Derived Moisture in a Global Numerical Weather Prediction Model, *Atmosfera*., **14,** 203-209.

Rajan. D., B. Simon, P.C. Joshi, V.B. Bhatia, A.K. Mitra and R.K. Paliwal 2002(b): Impact of NOAA/TOVS derived moisture profile over ocean on global data assimilation and medium range weather forecasting, *Atmosfera*., **15**, 223-236.

Rajan. D., S.R.H. Rizvi, V.B. Bhatia and H.V. Gupta 2000: Intercomparison of satellite derived OLR and total precipitable water content over India and their impact on the analysis-forecast system. *Indian Journal of Radio & Space Physics*, **29**, 341-348.

Rocken, C., R.Anthes, M.Exner, D.Hunt, S.Sokolovskiy, R.Ware, M.Gorbunov, W.Schreiner, D.Feng, B.Herman, Y.Kuo and X.Zou 1997: Analysis and validation of GPS/MET data in the neutral atmosphere. *Journal of Geophysical Research*., **102**, 29849-29866.

Ware, R., M. Exner, D.Feng, M. Gorbunov, K.Hardy, B. Herman, Y.Kuo, T.Meehan, W.Melbourne, C.Rocken, W. Schreiner, S.Sokolovskiy, F.Solheim, X.Zou, R.Anthes, S.Businger and K. Trenberth 1996: GPS soundings of the atmosphere from low earth orbit: Preliminary results. *Bulletin of American Meteorological Society*., **77**, 19-40.

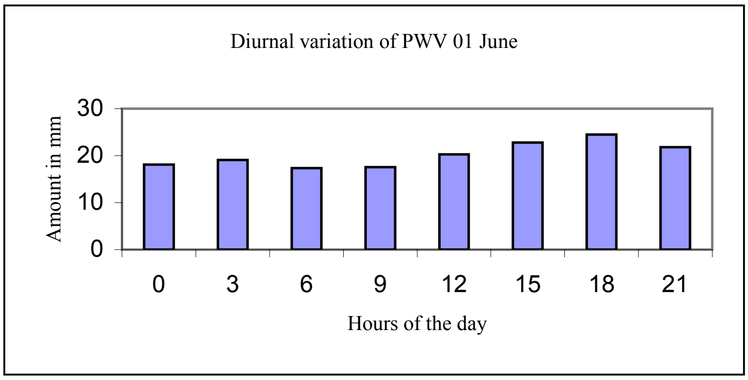

Figure-1

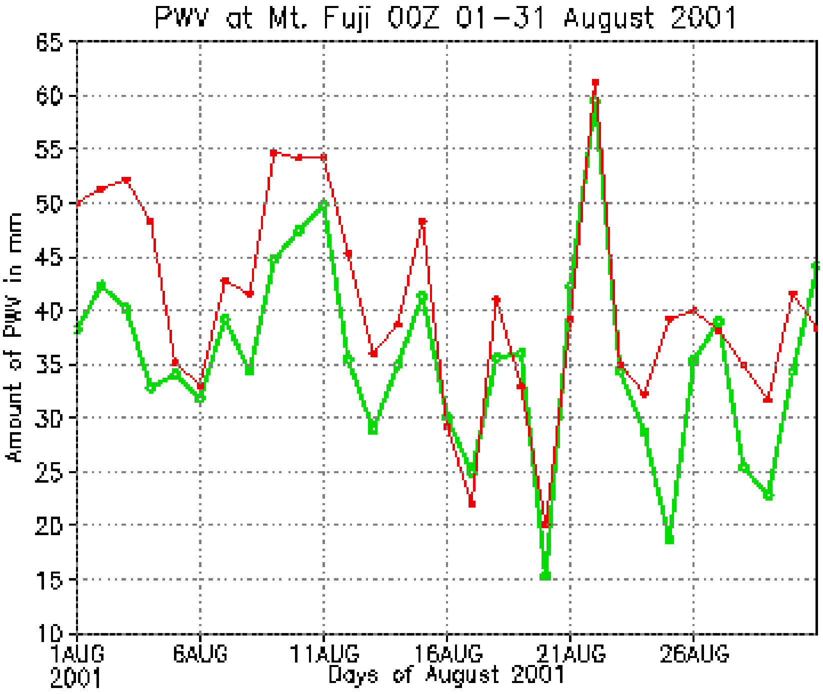

Figure-2

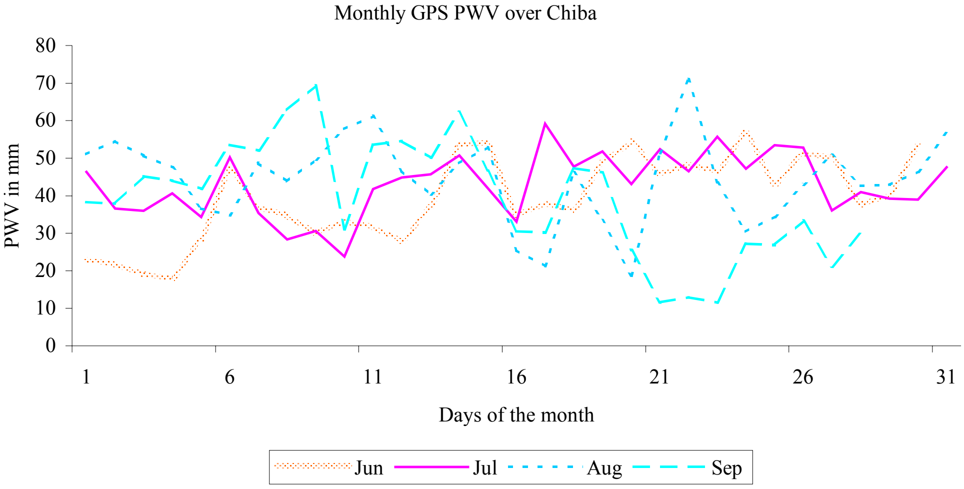

Figure-3

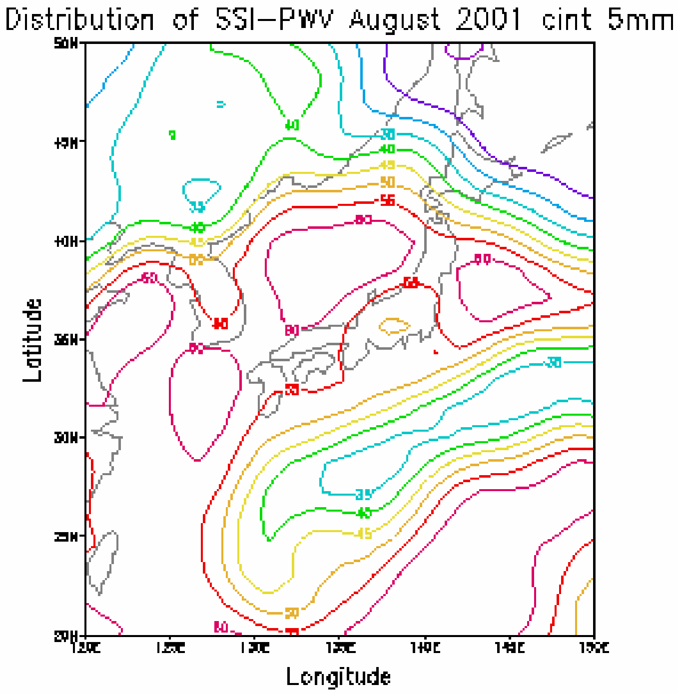

Figure-4

Table-1

Year	Event
1988	The first workshop on GPS tropospheric delay
1993	COntinuous Strain MOnitoring System (COSMOS) with GPS and GSI- 110 sites
1994	GEONET –partial service started
1994 -october	GPS Regional Array for Precise Surveying/physical earth service GRAPES –210 sites
1995-1997	GPS tomography experiment method
1996-1997	Feasibility study of GPS/MET Japan
1997-2000	GPS/MET Japan (First period)
1999	GEONET-610 sites
2000-2003	GPS/MET Japan (Second period)
2003	International workshop on GPS meteorology
2004	Today more than 1400 sites.

Optical and Microphysical Properties of the 2003 *Yamase* Clouds Estimated from Satellite Remote Sensing and Shipboard Observation

Shoji ASANO[1], Masaya KOJIMA[1], and Tamio TAKAMURA[2]

1) *Center for Atmospheric and Oceanic Studies, Tohoku University*
(*E-mail: asano@caos-a.geophys.tohoku.ac.jp, kojima@caos-a.geophys.tohoku.ac.jp*)
2) *Center for Environmental Remote Sensing, Chiba University*
(*E-mail: takamura@ceres.cr.chiba-u.ac.jp*)

Abstract: '*Yamase*' clouds are one of typical marine boundary-layer clouds, for which the present state-of-the-art performance of weather prediction models and general circulation models is not good enough to simulate properly the clouds, mainly because of coarse spatial-resolution of those models. *Yamase* clouds frequently appear over the North-Western Pacific Ocean east off the Sanriku district in summer under easterly cool winds, called *Yamase*, blown out from Okhotsk anti-cyclones. In order to validate numerical simulation and satellite remote sensing of *Yamase* clouds, we have carried out cloud observations on board the *Koufu-maru* of the Hakodate Marine Observatory in June of recent years. Here we discuss the optical and microphysical properties of the *Yamase* clouds, estimated from the shipboard observation and satellite remote sensing during the 2003 *Koufu-maru* cruise, in which for the first time we observed the evolution features of *Yamase* clouds from their formation to decade. Remote sensing using the contemporary AVHRR data from NOAA-17 in the morning orbit revealed that the *Yamase* clouds were rather thin, stratiform low-level clouds with an area-averaged optical thickness and effective particle radius of about 12 and 13 μm, respectively, and with a mean liquid-water-path of about 110 gm^{-2}.

(*Key Words*: *Yamase clouds*, marine boundary-layer clouds, cloud microphysical properties, satellite remote sensing, NOAA-17/AVHRR data, shipboard observation, 2003 *Yamase* event)

1. INTRODUCTION

Marine stratiform clouds appearing in the maritime atmospheric-boundary-layer (ABL) play a significant roll in the Earth's radiation budget due to their large horizontal extent, long lifetime, and high reflectivity for solar radiation. The state-of-the-art performance of such models as numerical weather prediction and general circulation models is not good enough to simulate properly the low-level stratiform clouds, mainly because of coarse spatial-resolution of these models. Generally, the marine stratiform clouds occur in a wide regional scale under some characteristic synoptic weather condition, but within the vertically thin ABL. Recently, many studies have tried to simulate the boundary-layer clouds by using various cloud resolving models. However, even high-resolution models still have difficulties to reproduce 'correct' features of cloud structure and physical properties; the simulated cloud structure and properties tend to differ for different models and/or resolutions [1]. Moreover, there are very few observational data available to validate the model performance. The cloud physical properties are generally different for different cloud types and different stages of the cloud lifetime, so they are highly variable with time and space. Satellite remote sensing is an efficient technique to observe wide-area distributions of cloud properties. However, it is critically important to validate the performance of satellite remote sensing through comparison with in-situ measurements.

'*Yamase*' clouds are one of typical marine boundary-layer clouds, that appear over the ocean east off the Sanriku area (the east of the Northern District of the Main Island of Japan) in early summer season under easterly cool winds, i.e., the so-called *Yamase* [2], blown out from Okhotsk anti-cyclones. We are studying the formation processes of *Yamase* clouds through numerical simulations by using a non-hydrostatic cloud-resolving model [1, 3]. The preliminary results suggest that the model-produced clouds strongly depend on the used spatial resolution as well as parameterizations of such physical processes as turbulence, cloud and radiation processes. Further, we are going to retrieve the cloud properties such as optical thickness and effective particle radius of *Yamase* clouds from the AVHRR data of NOAA satellites. To validate the results from the numerical simulation and satellite remote sensing of *Yamase* clouds, we have carried out a few times of shipboard observations in June of the latest years. Here we present the cloud optical and microphysical properties estimated from satellite remote sensing and the shipboard observation for the *Yamase* event in June 2003. The 2003 summer in the northern Japan is remembered as an unusually cool summer with severe shortages of insolation and crop damage due to the *Yamase* weather.

2. SHIPBOARD *YAMASE* OBSERVATION

The cloud observations on board a ship have been carried out within the Yamase Intensive Experiment (YIE) conducted by the Sendai District Meteorological Observatory and the Hakodate Marine Observatory (HMO) of the Japan Meteorological Agency, in collaboration with the Center for Atmospheric and Oceanic Studies (CAOS) of Tohoku University. The marine observation vessel *Koufu-maru* of the HMO operated the shipboard YIEs in an area east off the Sanriku [4] in June of the recent years. In addition to the routine marine weather observations and intensive GPS-sonde launchings, the CAOS-group conducted cloud observations for measuring cloud parameters by using various radiometric instruments as well as an aerosol particle-counter aboard the *Koufu-maru*. The measured parameters can be used in validation of the products from satellite remote sensing and numerical simulations. Among these parameters, cloud liquid-water-path (*LWP*) and cloud-base height are particularly useful parameters for the validation; they were measured by a dual-frequency microwave-radiometer (Radiometric Co., WVR-1100) and a laser ceilometer (ImpulsePhysik, LD-25), respectively. Further, the temperature, humidity and wind profiles measured by GPS-sondes can be compared with the model-simulated profiles.

In the 2003 YIE, we fortunately encountered a *Yamase* event, in which, for the first time, we observed a series of the formation and evolution processes of *Yamase* clouds from the evening of 22 June through the evening of 24 June 2003. The *Koufu-maru* stayed near the point (39ºN, 143ºE) for operating the YIE from the afternoon of 22 June to the morning of 25 June. Figure 1 shows time variation of the temperature and humidity profiles in the lower troposphere during the *Yamase* event. In the figure, the cloud-base heights measured by the ceilometer and the wind profiles measured by the GPS-sondes are also plotted. Over the location of *Koufu-maru*, the lower part of ABL became cool and humid with the inflow of *Yamase* wind in the evening of 22 June, and very low *Yamase* clouds (might be fogs) appeared with the cloud-base heights of a few tens meters in the night of 22 June through the morning of 23 June. During the daytime of 23 June, the cloud-base was lifted up, at highest, to 300 m with the development of mixing in the ABL, although the cloud layer became rather thin and patchy; the cloud-base height gradually decreased during the night down to about 100 m in the morning of 24 June. In the daytime of 24 June, the cloud-base was again lifted up, and finally it reached the heights higher than 1 km in the night, when the ABL was well mixed with an almost constant equivalent temperature up to about 1.2 km. In the morning of 25 June, the low-level *Yamase* clouds disappeared over the *Koufu-maru* site. The mean cloud-base height averaged over the duration was about 270 m, and the corresponding mean *LWP* was about 60 gm^{-2} for the *Yamase* cloud measured on board the *Koufu-maru*. The observational data of time variations of the atmospheric profiles and associated cloud fields will be useful for validation of simulations of the *Yamase* event.

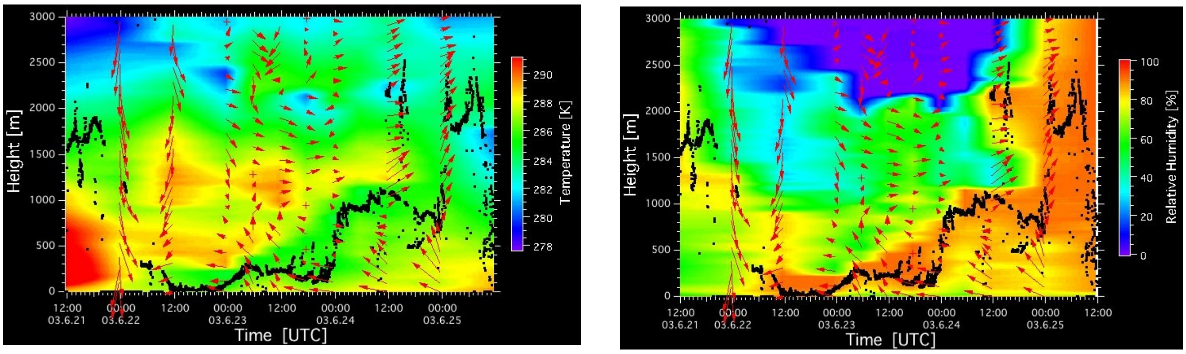

Fig. 1. Time variation in UTC of the temperature (*left*) and relative humidity (*right*) profiles, interpolated from those measured by the GPS-sondes launched from the *Koufu-maru*, in the marine lower atmosphere from 21 June to 25 June 2003. In the figure, the cloud-base heights (*black dots*) measure by the ceilometer and the wind profiles (*red arrows*) measured by the GPS-sondes are also superimposed.

3. SATELLITE REMOTE SENSING

The cloud optical thickness (τ_c) and effective particle radius (r_{eff}) of the *Yamase* clouds have been retrieved from the contemporary NOAA/AVHRR data in a wide area in the Western North Pacific region. The AVHRR data used in the present study were processed from the High Resolution Picture Transmission data of NOAA-17 satellite in the local morning orbit; the data are being archived at Tohoku University, Sendai. Simultaneous data of the visible and near-infrared reflected radiances in the AVHRR channels 1 (0.58 - 0.68 μm) and 3A (1.57 - 1.78 μm), respectively, were used to retrieve τ_c and r_{eff}. The infrared channel data in channels 4 (10.3 – 11.3 μm) and 5 (11.5 – 12.4 μm) were used to discriminate low-level water clouds from higher-level clouds by estimating the cloud-top temperatures. In the satellite data analysis, we employed the atmospheric profiles from the NCEP/NCAR reanalysis data, and the sea surface temperatures from the NGSST (new generation sea surface temperature) products released from the CAOS [5]. From the retrieved τ_c and r_{eff}, the liquid-water-path *LWP* can be estimated by using the approximate relation, $LWP{=}2\rho\tau_c r_{eff}/3$, where ρ is the density of liquid water. The performance of satellite remote sensing was validated by comparing the satellite-derived *LWP* and the shipborne WVR-measured *LWP* for the collocated scenes. During the 2003 YIE cruise, we had two scenes for which the *Koufu-maru* site was completely covered by low-level clouds and the NOAA-17 satellite simultaneously observed the clouds over the site. For the two cases, the satellite-derived *LWP* and the WVR-measured *LWP* agreed with each other within an uncertainty of 20 gm^{-2}. Therefore, the satellite remote sensing of the low-level clouds can be regarded as reasonable and reliable.

Figure 2 shows an example of the retrieved τ_c and r_{eff} for the low-level clouds in the morning of 24 June 2003. The easterly surface winds are also depicted by the arrows superimposed on the panels. The figure shows a wide distribution of optically thin and uniform, stratiform low-level clouds in the Western North Pacific region. However, in some locations, the cloud distribution exhibits band-like features and cellar structures, particularly, in the leeward places. The retrieved τ_c and r_{eff} are, in general, positively correlated each other with larger r_{eff} for larger τ_c, and vice versa; this suggests that the cloud was, as a whole, in a developing stage. However, the opposite correlations between τ_c and r_{eff} were also noticed in some places, where there might be dominated by drizzle and precipitation formation or ship-track clouds [6]. The cloud distribution features and the τ_c vs r_{eff} correlations changed in time and location during the *Yamase* event.

From the five days' remote sensing during 23 June to 27 June, the occurrence probability of the retrieved τ_c, r_{eff} and *LWP* were analyzed for the low-level clouds in a wide area of about 400 km×400km, east off the Sanriku district. Figure 3 shows the frequency histograms of the retrieved τ_c, r_{eff} and *LWP*. It is shown that most clouds were fairly thin with optical thicknesses between 4 and 20

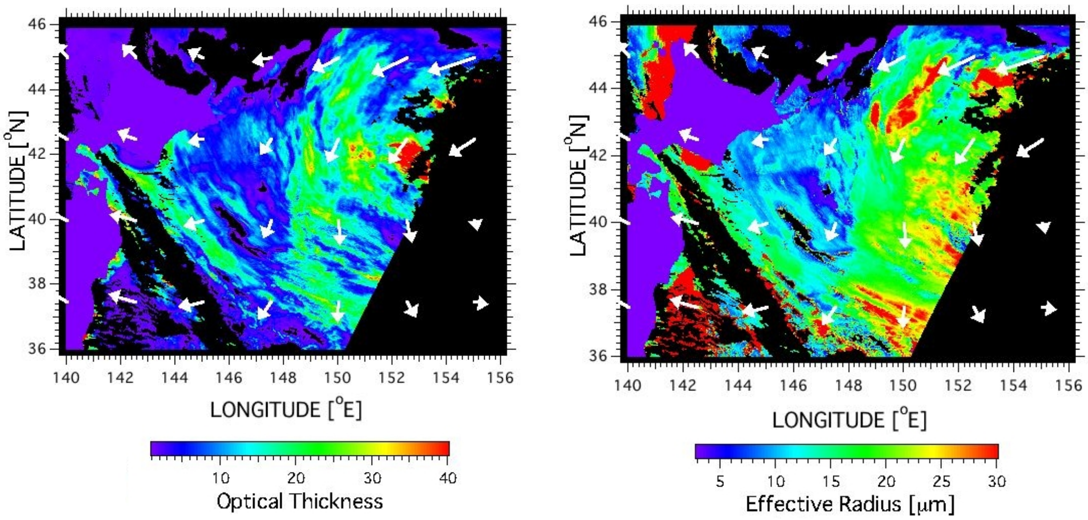

Fig.2. Optical thickness (*left*) and effective radius (*right*) retrieved from the AVHRR data of NOAA-17 for the low-level clouds on 24 June 2003. The black areas indicate the areas of no data and/or covered by higher clouds. The white arrows indicate wind velocity at 1000 hPa from the NCEP/NCAR reanalysis data.

(mean nalue of 12) and with rather uniform particle radii between 8 and 16 μm (13 μm). The mean value of *LWP* averaged over the area was about 110 gm^{-2}.

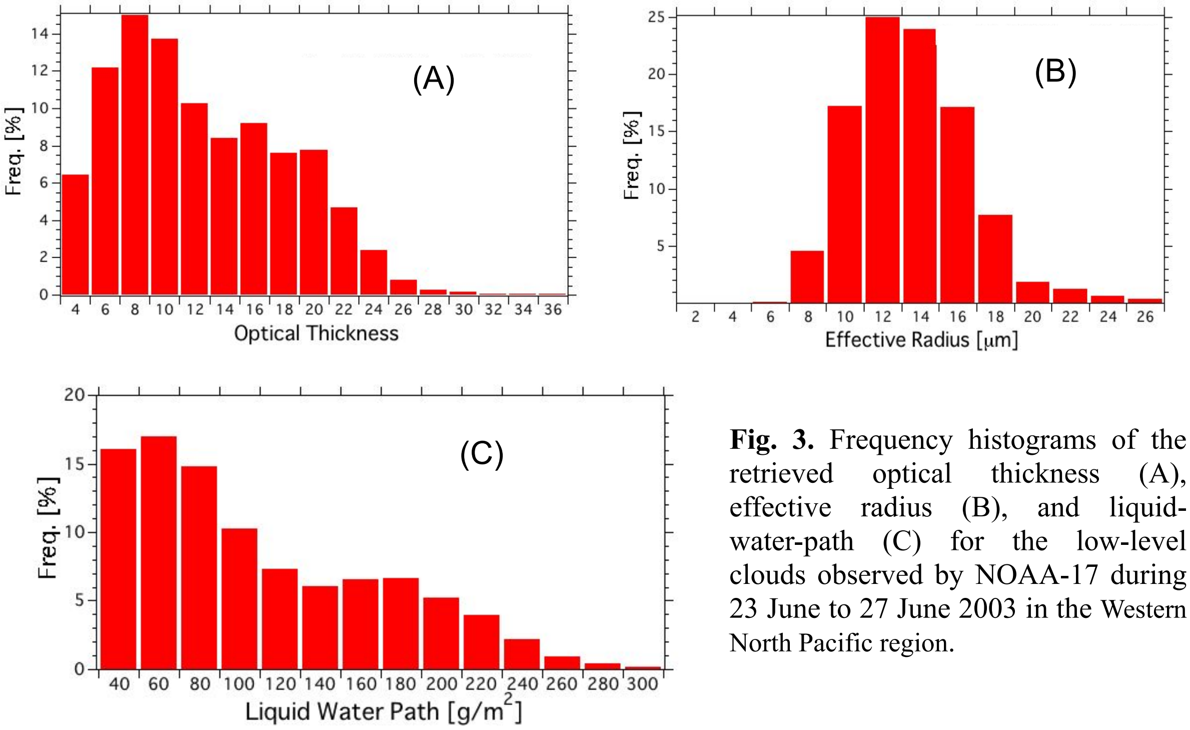

Fig. 3. Frequency histograms of the retrieved optical thickness (A), effective radius (B), and liquid-water-path (C) for the low-level clouds observed by NOAA-17 during 23 June to 27 June 2003 in the Western North Pacific region.

4. Concluding remarks

We have investigated the optical and microphysical properties of *Yamase* clouds in June 2003 by means of the shipboard observation on *Koufu-maru* and remote sensing using the contemporary AVHRR data from NOAA-17 satellite. For the first time, we could observe the evolution features of maritime low-level clouds in *Yamase* event from their formation to decade. The present results can be used to validate numerical simulations of the 2003 *Yamas*e event by using non-hydrostatic cloud-resolving models. The shipboard experiment should be continued to accumulate more observational data usable to validate and improve the performance of numerical models and satellite remote sensing of low-level clouds for different weather conditions and different places.

Acknowledgements: The shipboard observations were carried out within the YIE under the cooperation with the Sendai District Meteorological Observatory and the Hakodate Marine Observatory. We are grateful to Drs. F. Sakaida and H. Iwabuchi for their kind assistance in the analysis of NOAA/AVHRR data. The study was partly supported by the CEReS Joint Research Program and by the Research Revolution 2002 Project.

REFERENCES:

[1] R. Nagasawa, T. Iwasaki, S. Asano, K. Saito, and H. Okamoto, 2004: A numerical study of low-level cloud formation in 'Yamase' with a nonhydrostatic multi-nested regional climate model, *J. Meteor. Soc. Jpn* (submitted).

[2] H. Kawamura (*Ed.*), 1995: YAMASE, *Meteorol. Res. Note* (Japan Met. Soc.), No. 183, 179pp (*in Japanese*).

[3] T. Iwasaki, S. Asano, H. Okamoto, and R. Nagasawa, 2002: A cloud study system using a nonhydrostatic multi-nested regional climate model. *Proc. EarthCARE Workshop* (Harumi, Tokyo, 17-18 July 2002), 171-174.

[4] S. Asano, M. Kojima, Y. Yoshida, and T. Takamura, 2003: Validation experiment for satellite remote sensing and numerical models of low-level clouds: Shipboard observation of YAMASE clouds, *Proc. CEReS Int l Symp. Remote Sensing* (Chiba Univ., 16-17 December 2003), 135-138.

[5] See, *http://www.ocean.caos.tohoku.ac.jp/~merge/sstbinary/actvalbm.cgi*.

[6] S. Asano, M. Shiobara, and A. Asano, 1995: Estimation of cloud physical parameters from airborne solar spectral reflectance measurements for stratocumulus clouds, *J. Atmos. Sci.*, **52**, 3556-3576.

IMPROVING ALONG-BEAM SPATIAL RESOLUTION OF RADAR MEASUREMENTS

Nick Schutgens, Hiroshi Kumagai

NICT
National Institute of Information and Communication Technology
4-2-1 Nukui-kitamachi, Koganei, Tokyo, 184-8795
Japan

We consider the possibility of improving the range or along-beam spatial resolution of a pulse radar through oversampled observations. Radar observations are related to the state of an atmospheric volume, about half a pulse-length in size along the beam. The sampling distance of observations (gate separation) may however be much shorter. As a consequence, such observations become strongly correlated. Still, they will also contain independent information. We have constructed a deconvolution algorithm and study its efficiency using simulated observations based on actual 95 GHz (SPIDER) observations. Initial results show that the success rate of the algorithm depends on the number of independent samples N_{indep} on which the observation is based, and the noise level of the receiver as well as the abundance of oversampled observations. This work is relevant to the space missions CloudSat and EarthCARE.

Keywords: radar – CloudSat – EarthCARE – range weighting – deconvolution

INTRODUCTION

It is usually assumed that the range or along beam resolution of a radar is determined by its pulse-length. A careful analysis involves the range weighting function $|W|$, which determines the relative contributions of different parts of the atmosphere to the voltage measured at the receiver. This range weighting function depends on both the emitted pulse-shape and the receiver filter characteristics. Total expected power is given by the well-known expression (e.g. Doviak & Zrnic 1993):

$$P(r_0) = \frac{g^2 \lambda^2 P_t^2}{(4\pi)^3} \frac{\pi \theta_1^2}{8 \ln 2} \int_0^\infty \frac{|W(r_0 - r)|^2}{r^4} \eta(\mathbf{r}) dr, \tag{1}$$

where the pre-factors are related to calibration and the beam pattern, while r is the distance and $\eta(r)$ the atmospheric backscatter profile along the beam . We have ignored attenuation as it is not relevant to the present study. The range or along beam resolution is often defined as the width of $|W(r)|^2$ at the 3 dB or 6 dB level. For a radar with a matched receiver filter, the width at 6 dB corresponds to about half a pulse-length. This would be the extent of atmosphere that significantly contributes to the power observed in a single radar range gate.

Consequently, many radars only sample the reflectivity profile at gate separations comparable to ½ a pulse-length. Still, several radars have used or will use shorter gate separations, particularly when the pulse-length is fairly long (e.g. 1000 m). This is called oversampling. Examples are windprofilers and the cloud profiling radars that will be employed on the upcoming space mission CloudSat (NASA) and the proposed space mission EarthCARE (ESA/JAXA). Typically, they sample at ¼ or ⅛ of the pulse-length.

Equation (1) is mathematically speaking a convolution, with $|W|^2/r^4$ the convolution kernel. Is it possible to perform a deconvolution, given enough observations $P(r_0)$ at various distances, and derive a backscatter profile $\eta(r)$ that has a higher spatial resolution than the original observations? If so, what restrictions are there to the signal-to-noise ratio of the observations? What should be the gate separation of the oversampled observations? We will attempt a preliminary answer to these questions in this note.

METHOD AND DATA

Equation (1) can be solved numerically through a matrix inversion after discretization. Unfortunately matrix inversions are unstable operations, so we apply Tikhonov regularisation (Tikhonov & Arsenin 1977). That is, we try to minimize the following expression by finding a suitable η,

$$\left\|\mathbf{A}\bullet\eta-\mathbf{P}\right\|+\lambda^2\left\|\eta\right\| \tag{2}$$

where **P** is a vector containing the observed profile and η is a vector of the backscatter profile we want to retrieve. The matrix **A** contains information on W^2/r^4 . When the regularisation parameter $\lambda = 0$, instability of the procedure often causes unphysical spikes in the solution. For small $\lambda \neq 0$, the second term will act as a filter and suppress these high frequency components in the numerical solution that are unphysical. The exact choice of λ is a study in itself. Usually Expression (2) is minimized for many different values of λ , after which the optimal value is chosen based on some criterion that compares the various solutions (Hansen 2001). In this note, we only present results for the quasi-optimality criterion. Other criteria (i.e. L-curve, generalised cross-validation) were examined as well, but were generally found to be inferior.

We will test this method using simulated radar observations based on actual ground-based 95 GHz SPIDER observations, sampled to 1 km horizontal resolution based on prevailing wind-speeds. The simulated observations include correct Rayleigh fading statistics of receiver power, as well as correct correlations between range gates. For the radar, we have used EarthCARE design parameters, which include a pulse-length of 1000 m, a gate separation of 100 m (5 times oversampling) and a noise level of -20 dBz.

The number of independent samples N_{indep} is either 10^4 or 10^5. The case $N_{indep}=10^4$ agrees with along-track integration over 10 km for the space-borne EarthCARE radar (satellite speed ~ 7 km/s). The case $N_{indep}=10^5$ is included to show the effect of the number of independent samples. For satellite observations, this would imply along-track integration over the ridiculous length of 100 km. But note that ground-based radars can easily achieve $N_{indep}=10^5$ for 1 km horizontal resolutions (wind-speed ~ 30 m/s).

DECONVOLUTION OF OBSERVED POWER PROFILES

We will look in detail at the results for a single profile observed on January 10, 2003 at 1:08 AM. We have looked at other profiles as well, and have also conducted less detailed studies over larger datasets but always found similar results.

In Fig 1, we show the original SPIDER profile (gate separation of 82.5 m, but interpolated to 10 m) as a solid line. Based on this, a thousand observations for EarthCARE parameters were generated. The blocky dotted line represents the average observation, corrected for average noise level. Each observed profile was then deconvolved. The average reflectivity of the deconvolved profiles is shown by black dots. The horizontal lines extending from these dots represent the 1 σ variation over those 1000 samples.

In the figure, we see that the deconvolution is very reliable for high reflectivities, but not for low reflectivities. Since Eq. 1 and 2 are linear in η, high and low should be interpreted relative to typical signal and noise power levels in the profile. When the Number of Independent samples increases, the reliability of the deconvolution increases as well.

Note that reliability is not the same as accuracy. The averages and standard deviations in Fig. 1 and 2 were computed without any attempt to remove obviously unphysical solutions from among the 1000 samples.

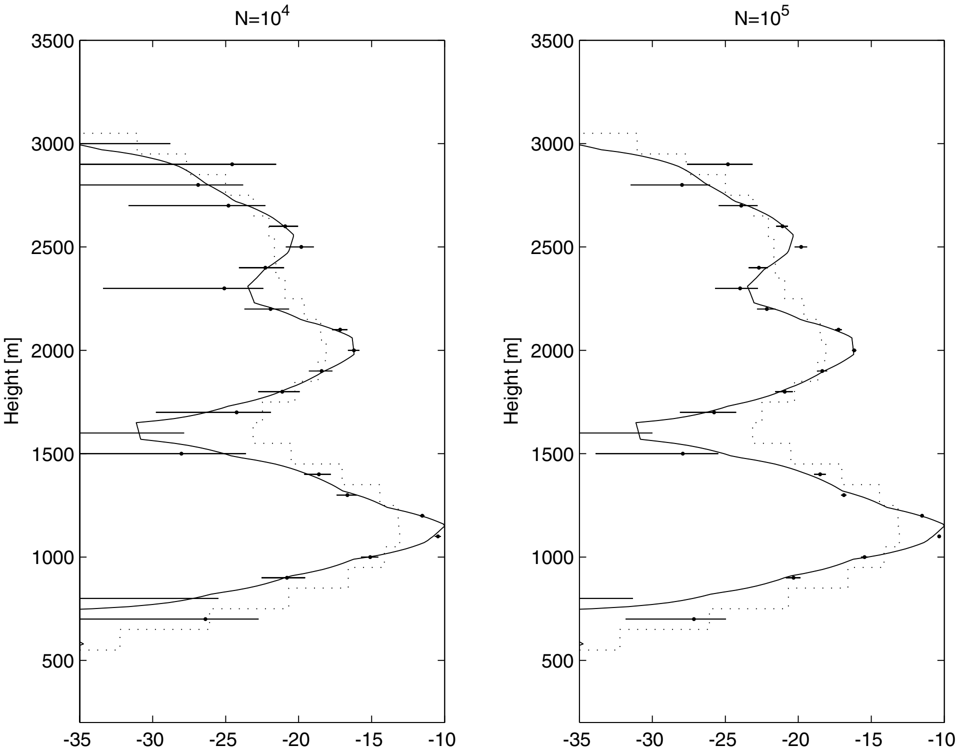

Figure 1 For a gate separation of 100 m (5 times oversampling), the effect of N_{indep} is shown.

Figure 2 shows that the gate separation is also an important factor, as accuracy improves when the oversampling is increased. Even though these oversampled observations are strongly correlated, they still contain useful independent information.

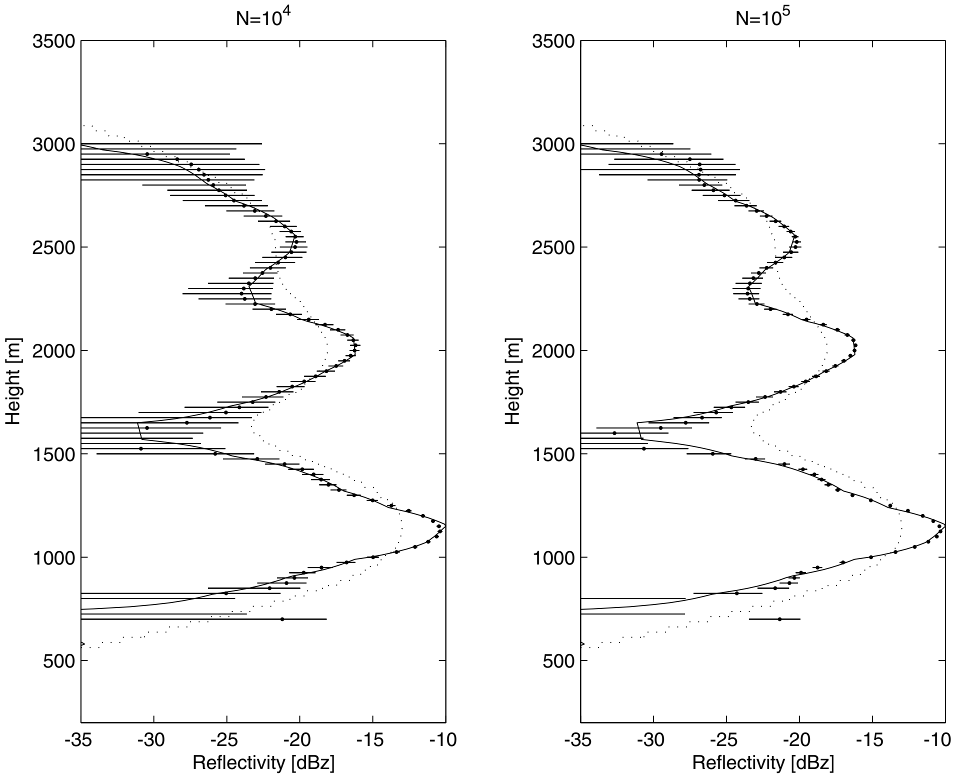

Figure 2 For a gate separation of 25 m (20 times oversampling), the effect of N_{indep} is shown.

SUMMARY

Signal-to-noise ratios increase with increasing pulse-lengths, but at the cost of reduced range resolution. Oversampled observations can improve the range resolution, but this requires a deconvolution. Our results so-far show that such a deconvolution is possible, but not always reliable. Further research will concentrate on more reliable deconvolution techniques (better criteria for the regularisation parameter) and estimates of the reliability of a particular deconvolved profile without additional knowledge.

REFERENCES

Doviak RJ, Zrnić DS, “Doppler radar and weather observations”, Academic Press inc.

Hansen PC, “Regularization tools a mathlab package for analysis and solution of discrete ill posed problems” , version 3.1, downloadable from http://ww.imm.dtu.dk/~pck .

Tikhonov AN, Arsenin VY, “Solutions of ill-posed problems”, Winston & sons, 1977.

Aerosol Properties over Asia with ADEOS-1 & -2/POLDER

Itaru Sano (1), Sonoyo Mukai (1),
Yasuhiko Okada (2), and Masayoshi Yasumoto (3)

1. Faculty of Science and Technology, Kinki University, Japan
2. Faculty of Science, Kobe University, Japan
3. RIST, Kinki University, Japan

The major properties of atmospheric aerosols are the optical thickness (AOT: τ_λ) and the Ångström exponent (α) which is calculated from the spectral tendency of optical thickness of aerosols as below:

$$\alpha = -ln(\tau_{\lambda 1}/\tau_{\lambda 2}) \, / \, ln(\lambda_1/\lambda_2), \qquad (1)$$

where wavelengths λ_1 and λ_2 take values of the central wavelength of observing channels, respectively. The values of α are closely related to the aerosol size distribution. For example, the small values of α indicate the large particles, and the large values represent small particles such as artificial aerosols. In general, the values of Ångström exponent (α) from ~0 to 1 shows coarse particles (such as sea salt solution, and soil dusts), on the contrary, $1 < \alpha < \sim 2.5$ indicates small particles (such as sulfate, biomass burning etc.).

Figure 1 and 2 show the aerosol optical thickness and Ångström exponent on 13 April 2003. These results are derived from ADEOS-2/POLDER polarization as well as radiance data. Although the details of retrieval procedure have been interpreted in the previous paper [1], the basic idea of our aerosol retrieval is that the scattering behavior of aerosols plays a sufficient role in the polarization field of the Earth atmosphere-surface system in the near infrared wavelengths. The area loading lots of Asian dust flown from China is circled by the solid curve in Figure 1. It is clear that Asian dusts distribute over from the Yellow sea to Japan. Note that there are some uncertainties to distinguish the heavy aerosol loading from the thin cloud.

It is found that aerosol optical thickness in the dust event is more than double of clear value, and Ångström exponent takes small values in dust event.

These space-based aerosol properties are validated from the ground based AERONET data in a global scale. It is of interest to mention that the annual change of aerosol characteristics is found from comparison of POLDER products from ADEOS-1 with those from ADEOS-2.

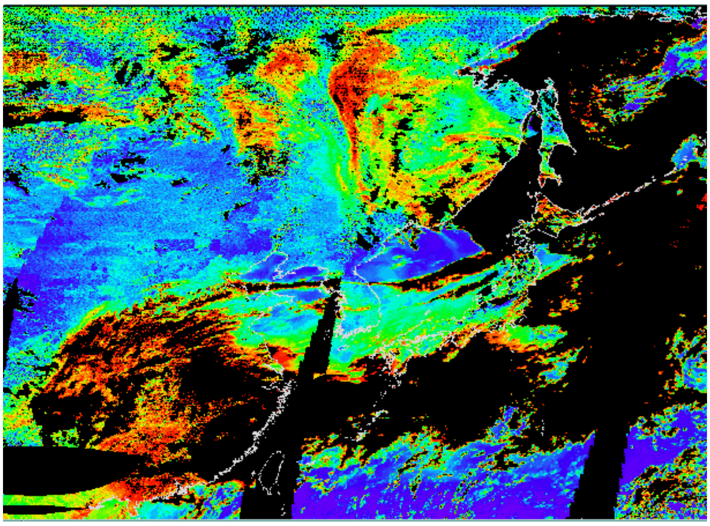

Figure.1. Distribution of aerosol optical thickness at a wavelength of 0.55 μm over East Asia on 13 April 2003 derived from ADEOS-2 / POLDER.

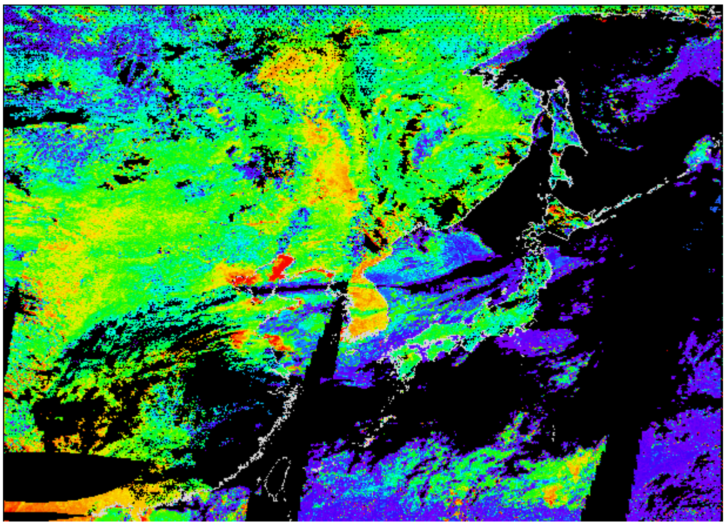

Figure.2. Distribution of Ångström exponent on 13 April 2003 derived from ADEOS-2 / POLDER

The ADEOS-2/POLDER data were provided by CNES / France.

REFERENCES

[1] I. Sano, "Optical properties and Angstrom exponent of aerosols over the land and ocean from space-borne polarimetric data", *Adv. Space Res.*, **34**(4), pp 833-837, doi:10.1016/j.asr.2003.06.039, (2004).

Observations of Cloud Properties Using the Developed Millimeter-Wave FM-CW Radar at 95 GHz

Toshiaki TAKANO (1,2,3), Ken-ichi AKITA(1), Hiroshi KUBO(1),
Youhei KAWAMURA(2), Hiroshi KUMAGAI (4),
Tamio TAKAMURA (5), Yuji NAKANISHI(6), and Teruyuki NAKAJIMA(7)

(1)*Graduate School of Science and Technology, Chiba University,*
Inage, Chiba 263-8522, Japan, takano@faculty.chiba-u.jp,
(2)*Faculty of Engineering, Chiba University,*
(3)*Center for Frontier Electronics and Photonics, Chiba University,*
(4)*Communications Research Laboratory,*
(5)*Center for Environmental Remote Sensing, Chiba University,*
(6) *SciTech,*
(7)*Center for Climate System Research, The University of Tokyo*

Abstract. We developed a low-power and high-sensitivity cloud profiling radar transmitting frequency modulated continuous wave (FM-CW) at 95 GHz for ground-based observations. Millimeter wave at 95 GHz is used to realize much higher sensitivity than lower frequencies to small cloud particles. An FM-CW type radar realizes similar sensitivity with much smaller output power to a pulse type radar. Two 1m-diameter parabolic antennas separated by 1.4m each other are used for transmitting and receiving the wave. The direction of the antennas is fixed at the zenith. The radar is designed to observe clouds between 0.3 and 20 km in height with a resolution of 15 m. Using the facility, test observations have been done. Results of observations show that the system can observe clouds of –30dBZ at the distance around 5km, which is sensitive enough to observe various kinds of clouds.

Using the developed millimeter-wave FM-CW radar at 95 GHz, we observed clouds in a campaign observation in Amami Island in March 2003, and on a sail on Mirai, a Japanese scientific research vessel, in September 2004 in the Arctic Ocean. The radar provided good and sensitive data in these long-term observations.

Keywords: Cloud Profiling Radar, Millimeter Wave Radar, FM-CW Radar, Cloud Properties, Active Measurements of Clouds

1. INTRODUCTION

It is getting more important to know the global environment and the global change of climate for the human beings. It is necessary to know balance of solar energy coming to the Earth and cycle of water for the comprehension and to solve severe problems such as the greenhouse warming, the drying, the ozone holes and so on. One of the most significant features to know them is cloud, which reflects and absorbs incoming solar radiation, traps the radiation from the ground, transfers the energy in it, and radiates it outside. Information on 3-dimensional structures of clouds, sizes and distribution of cloud particles, dependence on size of optical characteristics of cloud particles, motions of particles in clouds, and so on are all desirable to solve role of clouds. .

Characteristics of clouds described above, however, have not been well known yet because of lack of enough observational data to present confidential results. Observations of clouds with radars would be most powerful method to derive the information because of following advantages: a) radio waves do not suffer from heavy extinction such as visible light, and consequently can investigate interior of clouds, b) the radar technique, which is an active sensing method, has great advantage of investigating interior structures of clouds to passive methods such as total power observations of irradiance of clouds, c) Doppler measurements of clouds which have low velocities around 1 m/sec is applicable only to radio frequency waves.

Conventional radars operated at 5GHz can detect precipitation particles but are not able to detect particles in clouds because their sizes, less than a few tens microns, are much smaller that the wavelengths and, therefore, their cross sections are quite small. The cross sections of particles increase rapidly with frequency in Rayleigh scattering region. Rader observations of cloud particles at millimeter waves, which have been realized recently, have much more sensitive [1]. Several groups have reported the development and preliminary observational results that demonstrate powerful performances to investigate cloud particles [2],[3],[4].

We have designed and developed a cloud profiling radar at 94GHz. The purposes of the development of the FM-CW radar are a) evaluation and verification of an FM-CW radar at 95 GHz in Japan comparing to a pulse radar, b) obtaining millimeter wave FM-CW radar techniques and algorism of data reduction, and c) contribution to scientific research on cloud physics. In this paper, we present first observational results with the newly developed cloud profiling FM-CW radar as well as design concepts and specifications of the radar.

2. DESIGN CONCEPTS AND CONASTRUCTION

Whole view of the developed radar is shown in Fig.1 [5]. Diameter of each antenna is 1m.

2.1 FM-CW Radar

We adopt a frequency-modulated continuous wave (FM-CW) radar rather than a pulse radar because the former can achieve more sensitive system than the latter if comparing with same instantaneous output power of transmitted millimeter wave. The principle of an FM-CW radar is shown in Fig.2. The signal frequency is modulated in the range of $f_0 \pm F$. Transmitted signal from one of the antennas is reflected by cloud particles, returns, and is received by the other antenna with a delay time of t relative to the original transmitted signal. Mixing the transmitted and received frequencies, beat frequencies f_b are observed in the spectra, which are caused by ensemble of clouds particles:

$$f_b = 4 F r / (c T_m) \qquad (1),$$

where r is the height of the clouds, T_m is the modulation interval, and c is the light velocity. When the objects move in the line of sight, the frequencies of reflected signals change by f_d :

$$f_d = -2 (f_0 / c) (dr / dt) \qquad (2).$$

Fig.1. The developed cloud profiling FM-CW radar at 95 GHz.

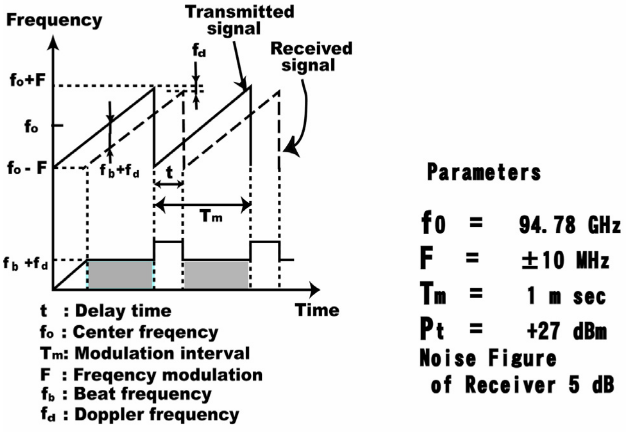

Fig.2. Principle of an FM-CW radar.

2.2 Design Concept and Requirements

Because one of the purposes of the facility is evaluation and verification of an FM-CW radar at 95 GHz, we design it to be a simple system so as to develop with commercially available components and to make maintenance and upgrade by ourselves.

We designed the facility to observe clouds between 0.3 and 15 km in height with a resolution of 15 m. The velocities measured as Doppler shift should be less than 1 m/sec. The facility should be mobile for measurement at variety of places.

2.3 Antennas and Mounting

According with the requirements described above, we decided parameters of antenna listed in Table 1 [6].

2.4 Transmitter and Receiver Section

The block diagram of the transmitter and receiver section is shown in Fig.3 and parameters are summarized in Fig. 2. All signals including the transmitted FM-CW signal at 95GHz and local frequencies are generated from and/or referred to two signal generators in 140 MHz range, which are synchronized each other.

The integrated transmitter section is shown in Fig. 4. The integrated system has been measured on its stabilities and sensitivities in laboratories [7]. Facilities for radar measurements, high stabilities of transmitted signals are necessary to obtain useful data. We measured stability of the system. In order to stabilize the output of the power of the transmitting wave, the final power amplifier for transmitting signal at 95GHz is cooled with a Peltier cooler to be around 50 ^{O}C otherwise it goes as hot as 90 ^{O}C.

The noise figure of the pre-amplifier at 95GHz was measured to be around 5.5 dB. Long term stabilities and sensitivities were measured and are good enough for our purpose.

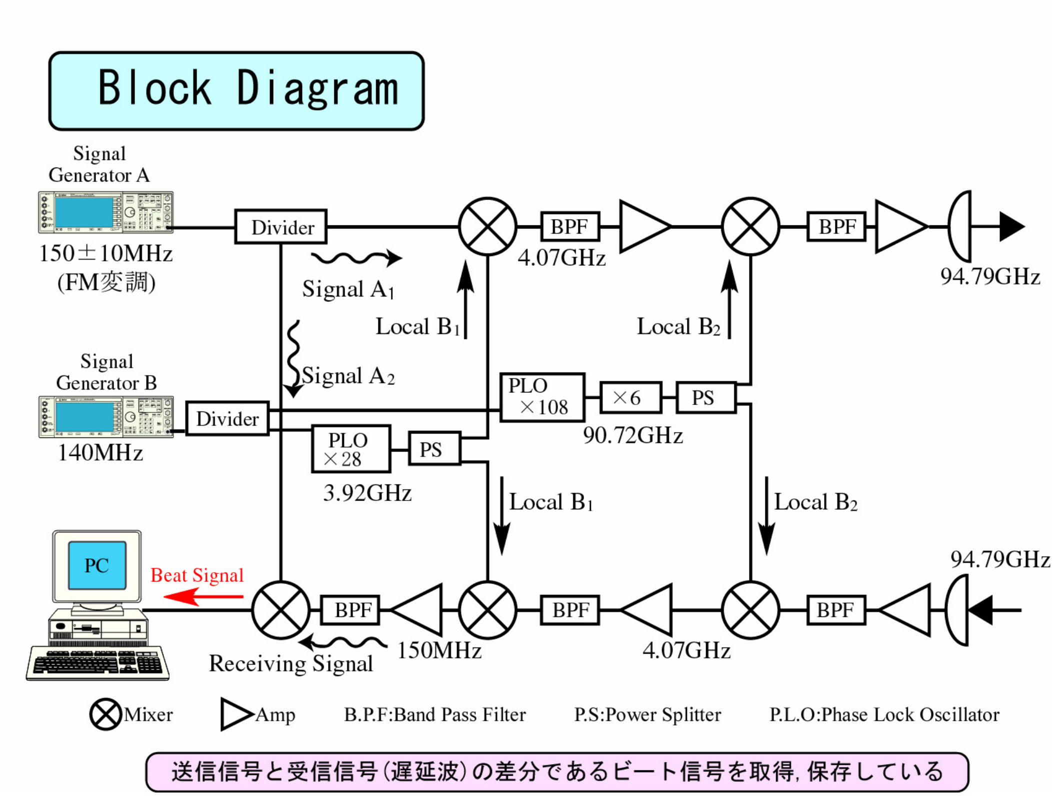

Fig.3. Block diagram of the transmitter and receiver section.

Table 1. Designed parameters of antennas.

Antenna Diameter	1 m
f/D ration of Antenna	0.35
Antenna Optics	Cassegrain
Gain of Antennas	57 dBi
Beam Width	0.18 degree
Antenna Separation	1.4 m
Direction of Antennas	Zenith
Polarization	1 Linear

Table 2. Comparison between the developed FM-CW radar and SPIDER.

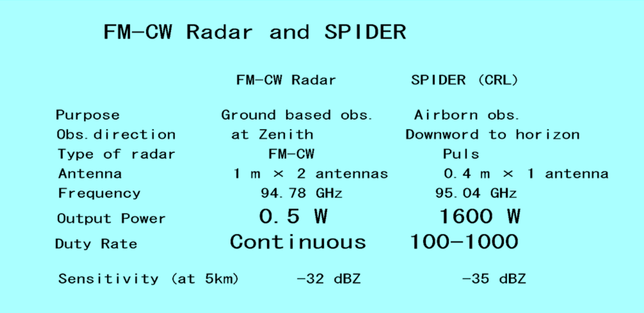

FM-CW Radar and SPIDER

	FM-CW Radar	SPIDER (CRL)
Purpose	Ground based obs.	Airborn obs.
Obs. direction	at Zenith	Downword to horizon
Type of radar	FM-CW	Puls
Antenna	1 m × 2 antennas	0. 4 m × 1 antenna
Frequency	94. 78 GHz	95. 04 GHz
Output Power	0. 5 W	1600 W
Duty Rate	Continuous	100−1000
Sensitivity (at 5km)	−32 dBZ	−35 dBZ

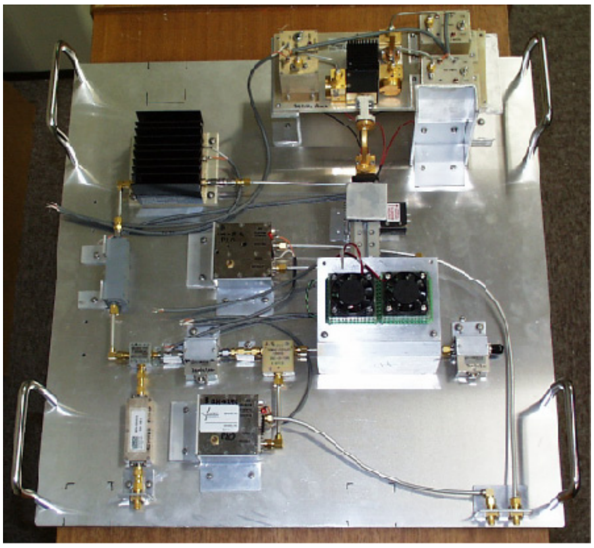

Fig.4. The transmitter section of the developed FM-CW radar.

3. Simultaneous Observations with SPIDER

After measurements of long-term stabilities, we made simultaneous observations with a pulse radar named SPIDER shown in Fig.5 of the National Institute of Information and Communications Technology (NICT), Japan. Comparison between the developed FM-CW radar and SPIDER is summarized in Table 2. We have to stress that the output power at 95 GHz of SPIDER is 3000ntimes higher than that of our FM-CW radar. An example of results is shown in Fig.6. We can recognize that same clouds were detected in both data. There results show that the radar has good performance to detect thin clouds.

Fig.5. SPIDER: a pulse radar of the National Institute of Information and Communications Technology NICT) Japan.

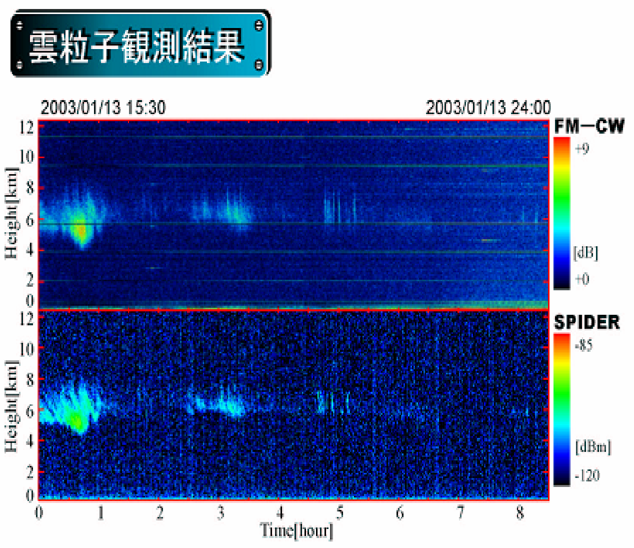

Fig.6 First results of test measurements of clouds. Measurement started 11:30 JST on 2002 June 26th and continued for 7 hours.

4. Observations of Cloud Properties

Using the developed millimeter-wave FM-CW radar at 95 GHz, we observed clouds in a campaign observation in Amami Island in March 2003, and on a sail on Mirai, a Japanese scientific research vessel, in September 2004 in the Arctic Ocean. Fig.7 shows an example of observed profiles with the lidar of the National Institute for Environmental Studies by Nobuo Sugimoto and his co-workers and our FM-CW radar at 95 GHz. FM-CW radar observed fine shower around 11:20 and structure of interior of clouds on March 20th.

The developed millimeter-wave FM-CW radar was installed on the Japanese scientific research vessel, Mirai, in August 2004 as shown in Figs.8 and 9. Mirai made observations in the Arctic Ocean in September 2004. Fig.10 shows example of observed data using the developed FM-CW cloud profiling radar during the project lead by Yasushi Fujiyoshi of Hokkaido Univ.

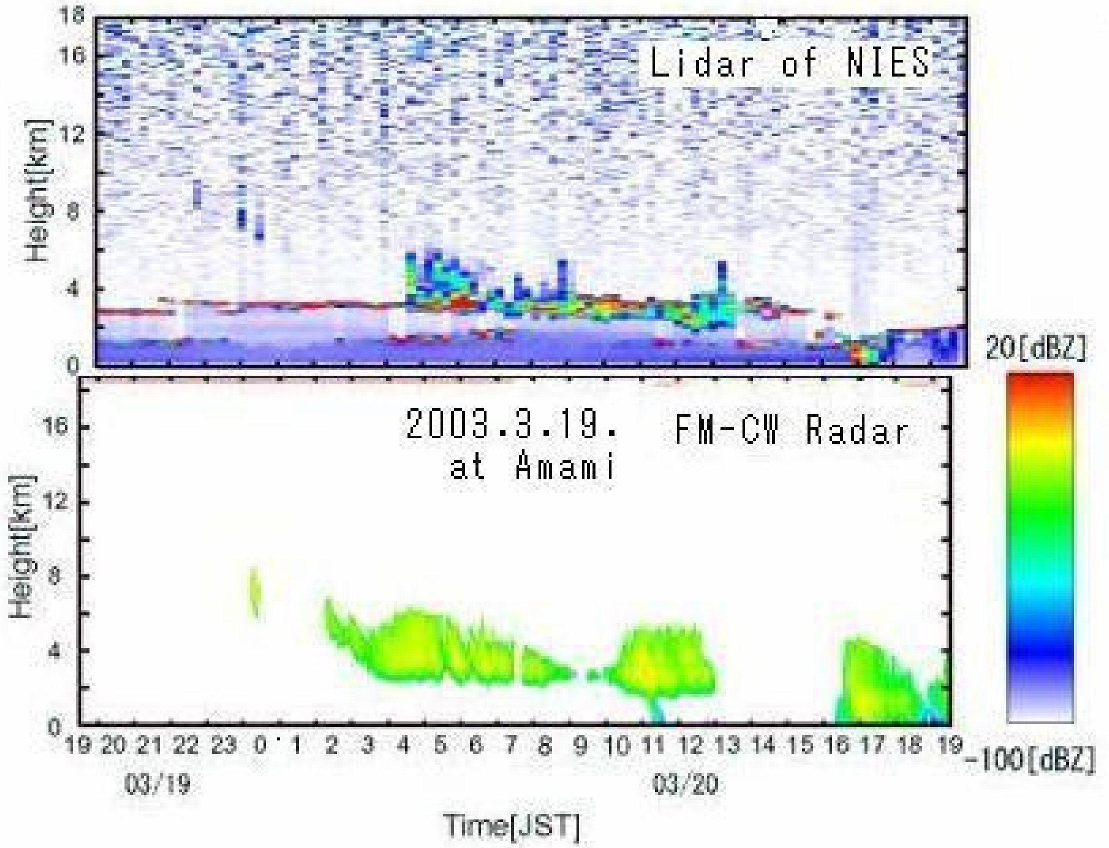

Fig.7. Observations in Amami Island in March 2003. FM-CW radar observed fine shower around 11:20 and structure of interior of clouds on March 20th.

Acknowledgments

The authors thank Nobuo Sugimoto of NICT and Yasushi Fujiyoshi of Hokkaido Univ providing their data in campaign observations. This work is supported with the project APEX (Asian Atmospheric Particle Environment Change Studies) in CREST (Core Research for Evolutional Science and Technology) of Japan Science and Technology Corporation and is in part supported with the Grant-in- Aid for Scientific Research by the Japanese Ministry of Education, Culture, Sports Science and Technology (14380241), and an open use program in the Center for Environmental Remote Sensing, Chiba University (#14-12, #15-12, #16-31).

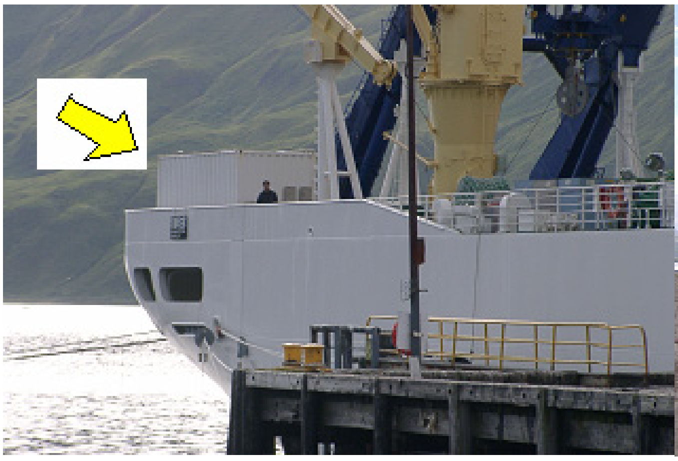

Fig.8. Container of the millimeter-wave FM-CW radar installed on Mirai.

Fig.9. Japanese scientific research vessel, Mirai.

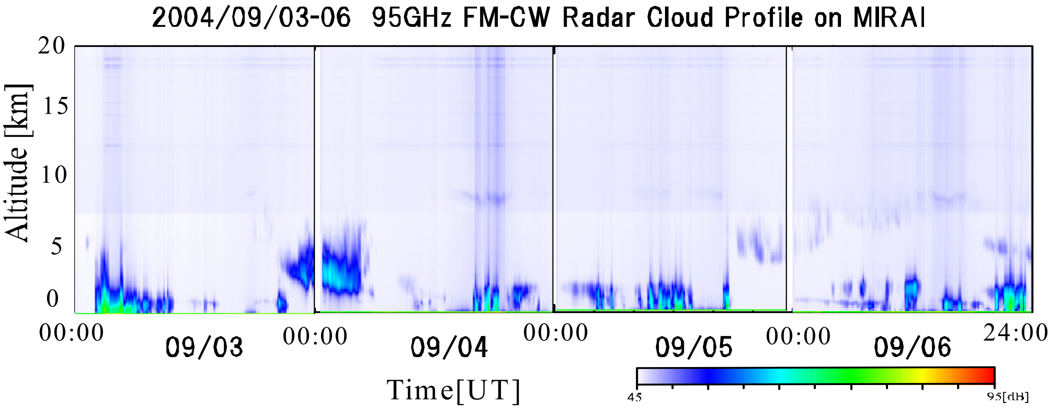

Fig.10. Example of data obtained in the Arctic Ocean using the millimeter-wave FM-CW radar.

References

[1] Clothiaux, E.E., M.A.Miller, B.A.Albrecht, T.P. Ackerman, J.Verlinde, D.M.Babb, R.M.Peters, and W.J.Syrett, “An evaluation of a 94-GHz radar for remote sensing of cloud properties”, Journal of Atmospheric and Oceanic Technology, Vol.12, No.2, p.201, 1995.

[2] Horie, H., T.Iguchi, H.Hanado, H.Kuroiwa, H.Okamoto, and H.Kumagai, “Development of a 95-GHz cloud profiling radar (SPIDER) – Technical aspects”, The Transactions of the Institute of Electronics, Information and Communication Engineers, Vol.E83-B, No.9, p.2010, 2000.

[3] Kumagai, H., H.Okamoto, H.Horie, H.Kuroiwa, and S.Iwasaki, ”Vertical profiling of liquid cloud properties retrieved from 95-GHz cloud radar and microwave radiometer”, 2001 Asia-Pacific Radio Science Conference (Tokyo), PF-27 (p.333), 2001.

[4] Matkin, N., J.Nash, T.Oakley, B.Ellison, M.Oldfield, and J.Bradford, “A trial of the Rutherford Appelleton Laboratory (RAL) 78.2GHz cloud radar”, Fifth International Symposium on Tropospheric Profiling, Adelaide, Australia, Dec.4-8, p.113, 2000.

[5] Suga, Y., S.Hoshi T.Takano, S.Shimakura, H.Kumagai, T.Takamura, and T.Nakajima, “Design and development of an FM-CW radar at 94GHz for observations of cloud particles”, 2001 Asia-Pacific Radio Science Conference (Tokyo), PF-28 (p.333), 2001.

[6] Hoshi, S., Y.Suga, Y.Kawamura, T.Takano, and S.Shimakura, “Development of an FM-CW radar at 94GHz for observations of cloud particles – Antenna section”, Proceedings of the Society of Atmospheric Electricity of Japan, No.58, p.116, 2001 (in japanese).

[7] Takano, T., Y.Suga, K.Takei, Y.Kawamura, T.Takamura, H.Kumagai, and T.Nakajima, “Development of a Cloud Profiling FM-CW Radar at 94GHz”, Proceedings of the 27nd General Assembly of the International Union of Radio Science (URSI) (Maastricht, The Netherlands), FP-11, p1789, 2002.

Retrieval of precipitable water using ADEOS-II / GLI near infrared data

Makoto Kuji*[a], Nobuyuki Kikuchi[b], and Akihiro Uchiyama[c]

[a] *Dept. of Information and Computer Sciences, Nara Women's Univ., Japan*
[b] *Earth Observation Research and application Center, Japan Aerospace Exploration Agency, Japan*
[c] *Meteorological Research Institute, Japan Meteorological Agency, Japan*

ABSTRACT

Retrieval of vertically integrated water vapor amount (precipitable water) is proposed using near infrared channels of Global Imager onboard Advanced Earth Observing Satellite-II (GLI / ADEOS-II). The principle of retrieval algorithm is based upon that adopted with Moderate Resolution Imaging Spectroradiometer (MODIS) onboard Earth Observing System (EOS) satellite series. Simulations were carried out with GLI Signal Simulator (GSS) to calculate the radiance ratio between water vapor absorbing bands and non-absorbing bands. As a result, it is found that for the case of high spectral reflectance background (a bright target) such as the land surface, the calibration curves are sensitive to the precipitable water variation. It turns out that aerosol loading has little influence on the retrieval over a bright target for the aerosol optical thickness less than about 1.0 at 500 nm wavelength. A preliminary analysis of GLI data was also carried out and the retrieved result is compared to radiosonde observations. In spite of a lag of several hours between the ADEOS-II / GLI and the radiosonde observations, the retrieved precipitable water values were coincident to those of in situ observations within 2.0 mm at a few radiosonde sites. Currently, we are trying to make fully simultaneous comparisons of the retrieved precipitable water values to those derived from continuous observations with skyradiometers or microwave radiometers. As a result, we will validate the accuracy of the retrieval algorithm for the purpose of its global application. It is also anticipated that simultaneous retrieval of the water vapor amount using GLI data along with other channels will lead to improved accuracy of the determination of surface geophysical properties, such as vegetation, ocean color, and snow and ice, through the better atmospheric correction.

Key Words: water vapor, near infrared, ADEOS-II / GLI.

1. INTRODUCTION

Water vapor is one of typical gas species governing the greenhouse effect. Investigation of water vapor distribution is a clue to understand the radiation budget of earth atmosphere system as well as the global energy and hydrological circulation. Although water vapor is mostly distributed in the lower atmosphere (planetary boundary layer from surface to a few kilometers), the water vapor amount often increases in the middle and upper troposphere accompanying horizontal advection of humid air mass. Thus, precipitable water, (i.e. the vertically integrated water vapor amount) is considered to be the most representative quantity of water vapor amount in the atmosphere.

Until now, TIROS-N Operational Vertical Sounder (TOVS) data have been often used to estimate water vapor amount at lower, middle, and upper regions of the troposphere [1)]. Although TOVS is a splendid vertical sounder with a number of channels sensitive to water vapor absorption, their footprints are about several tens kilometers, rather larger than those of environmental sensors onboard earth-observing satellites. Better spatial resolutions of several hundred meters to several kilometers are available with MODIS / EOS sensors, wavelengths and bandwidths of which are very similar to those of TOVS. Combining the near infrared data of water vapor absorbing and non-absorbing channels with the thermal infrared data, precipitable water is derived from the MODIS mission with a relatively high spatial resolution along with information of clouds and aerosols [2)].

In contrast to TOVS and MODIS, GLI onboard ADEOS-II is designed to obtain data of both the surface properties (vegetation, ocean color, and snow and ice, etc.) and atmospheric properties (cloud, aerosol, and radiation budget, etc.). In general, atmospheric correction is indispensable when surface geophysical properties are retrieved from satellite remote sensing data. Correction of atmospheric ozone, aerosol, and in particular, water vapor is important for precise retrieval of vegetation conditions and ocean color. In the GLI mission, it is currently planned that the water vapor information is incorporated from the quasi-real-time objective analysis data. Nevertheless, it is desirable to use the water vapor information concurrently obtained with the same spatial resolution as other channels. In this context, we study feasibility of using near infrared channels of GLI in the retrieval of precipitable water and make a preliminary analysis of the GLI data and its validation. The principle of the retrieval algorithm is described in Sec. 2 together with assumptions made in the present simulation. In Sec. 3, retrieved precipitable water is analyzed and validated with radiosonde observation. Section 4 presents the summary and related future works.

2. RETRIEVAL ALGORITHM AND SIMULATION

2.1 Principle

The retrieval algorithm is based upon the radiance ratio method, which utilizes the radiance ratio between water vapor absorbing and non-absorbing bands to retrieve the precipitable water. A similar method was already adopted with MODIS / EOS series [3, 4]. In the MODIS case, 940 nm and 865 nm bands were utilized as the water vapor absorbing band and non-absorbing band [3], respectively, and the retrieved results on a global scale were already reported [4].

Principle of the retrieval algorithm is explained concisely here. Figure 1 illustrates transmittance curves of water vapor in the near infrared region, calculated using the LOWTRAN 7 code [5]. As seen from Fig. 1, water vapor absorbing bands (spectral regions with smaller transmittance) are located at around 810 nm, 940 nm, 1135 nm, and 1380 nm, whereas non-absorbing bands (regions with larger transmittance; i.e., atmospheric window region) are found at 865 nm, 1050 nm, and 1240 nm. The six atmospheric models and their values for precipitable water are summarized in Table 1. The retrieval algorithm utilizes these characteristics as follows: in the water vapor absorbing bands, transmittance (i.e., radiance to be observed) varies with the water vapor amount (precipitable water) assumed in each atmospheric model, while in the non-absorbing bands, changes are much smaller.

Table 1 Atmospheric models and their precipitable water.

Model Atmosphere	Precipitable Water (mm)
Tropical	40.0
Midlatitude Summer	28.5
Subarctic Summer	20.4
US Standard 1976	13.9
Midlatitude Winter	8.38
Subarctic Winter	4.10

For the GLI application, here we propose a retrieval method in which calibration curves are determined between the radiance ratio of water vapor absorbing band (e.g., Ch. 25; 1135 nm) to non-absorbing band (e.g., Ch. 26; 1240 nm) and water vapor amount (precipitable water) in a form of nonlinear regression. The GLI channel specifications related to this feasibility study are summarized in Table 2 [6].

Table 2 Related Channel Specifications of GLI.

Channel Number	Central Wavelength (nm)	Band Width (nm)	IFOV [a] (km)	Maximum Radiance [b]	SNR [d]	Comment
19	865	10	1	228 [c]	97.5 [c]	Window Region
24	1050	20	1	203	300	Window Region
25	1135	70	1	200	350	Water Vapor
26	1240	20	1	138	70	Window Region
27	1380	40	1	94	120	Water Vapor

[a] Instantaneous Field of View.

[b] In units of W m^{-2} sr^{-1} m^{-1}.

[c] These values were attenuated by 25 % from the original ones 3).

[d] Signal to Noise Ratio.

Based upon the principle of the retrieval algorithm, the channel which is most sensitive to variation of water vapor amount is chosen as a water vapor absorption channel and, on the other hand, the one which is least sensitive to it as a non-absorbing channel. As seen from Fig. 1, there are two water vapor absorbing bands in the near infrared region, Ch. 25 (1135 nm) and Ch. 27 (1380 nm). Between two channels, Fig. 1 also indicates that Ch. 25 (with a band width of 70 nm) is more sensitive to the variation of water vapor amount than Ch. 27 (40 nm). As a result, Ch. 25 (1135 nm) is selected as a water vapor absorbing channel. For non-absorbing bands, there are three channels, Ch. 19 (865 nm), Ch. 24 (1050 nm), and Ch. 26 (1240 nm). From Fig. 1, it is expected that Ch. 26 (with a band width of 20 nm) is more sensitive to the variation than other two channels: Ch. 19 (10 nm) and Ch. 24 (20 nm). The magnitude of radiance of Ch. 19 (865 nm), however, is much larger than those of Ch. 25 (1135 nm), which leads to the smaller dynamic range of the radiance ratio (defined later). As a result, Ch. 26 (1240 nm) is selected as non-absorbing channels.

Simulations were carried out with the GLI Signal Simulator (GSS) 7) so as to calculate radiances to be observed at the GLI / ADEOS-II. The code enables us to calculate the radiance to be observed with GLI, assuming several atmospheric models including aerosol loading as well as water vapor. In the previous feasibility study, two cases of a bright target (land) and a dark target (ocean) are considered as ground surfaces with the GSS simulations 9) and we present the bright target analyses in this study.

The land model is assumed as a Lambertian surface whose spectral reflectance is 50 %, chosen as a representative case of a bright target. This assumption is based upon the grass model in the ASTER spectral library [8], which shows surface reflectance of 50.7 %, and 48.8 % for 1135 nm, and 1240 nm spectral region, respectively. For simplicity, the effect of bidirectional reflectance distribution function is not considered in this study. Simulations were carried out under clear sky conditions. Moreover, the effect of aerosol loading in the model atmosphere was also examined. For the aerosol model, a rural one incorporated in the GSS was utilized over land [7].

The upward radiances at the top of the atmosphere were simulated for the following case: over a bright target (i.e., land). Two bands, that is, one water vapor absorbing channel (1135 nm) and one non-absorbing channels (1240 nm), was used to carry out simulations, that is, the combination of 1135 nm and 1240 nm was examined to calculate the radiance ratio. In addition, the following case is assumed for scan geometry: solar zenith angle 60°, satellite zenith angle 60°, and relative azimuthal angle 90°.

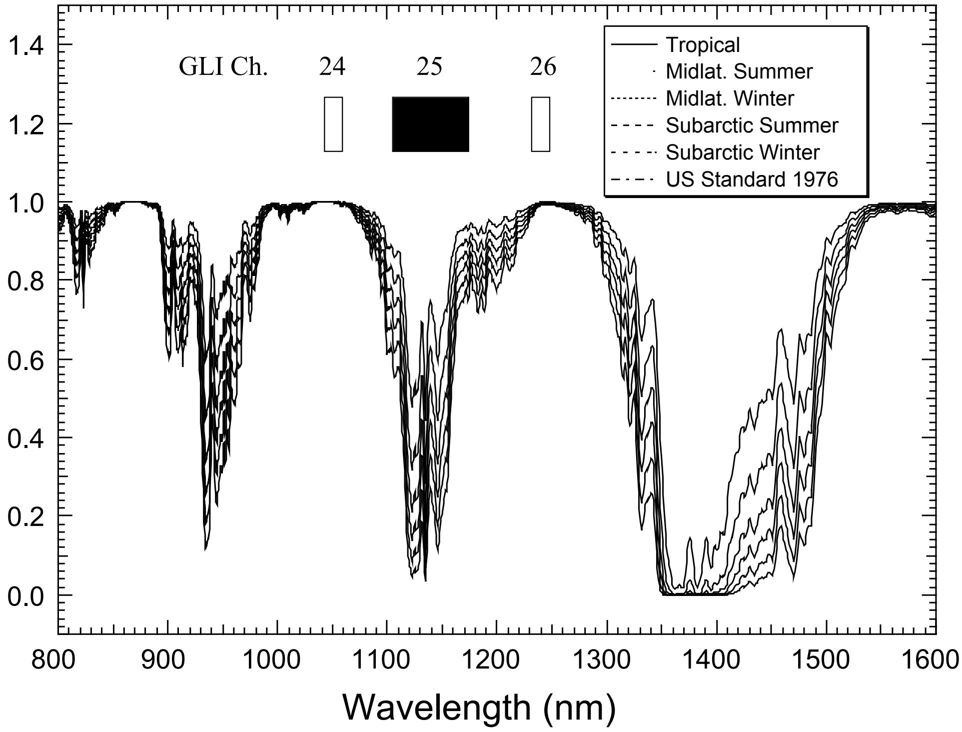

Fig. 1. Atmospheric transmittance related to water vapor in the near infrared spectral region between 800 nm to 1600 nm. Curves are calculated with the LOWTRAN 7 code for vertical one way path, as products between water vapor absorption lines and continuum absorption. The six transmittance lines correspond to the six model atmospheres listed in Table 1. Closed and open rectangles are the spectral ranges of the GLI for water vapor absorbing and window channels, respectively.

2.2 Retrieval algorithm

In this study, the radiance ratio (T_w) is defined as

$$T_w(ch1, ch2) \equiv \frac{R_{ch1}}{R_{ch2}}, \qquad (1)$$

where $ch1$ indicates a water vapor absorbing channel (i.e., 1135 nm), at which radiation undergoes strong absorption due to water vapor, $ch2$ is a non-absorbing channel (i.e., 1240 nm), and R is the radiance simulated with the GSS at the top of the atmosphere for the specified channel. This definition is essentially equivalent to that of Kaufman and Gao [3], except for a factor originating from the ratio of the extraterrestrial solar incident irradiances between the specified channels.

Based upon the above definition, a relationship (a calibration curve) is proposed between the radiance ratio (T_w) and the precipitable water (W):

$$T_w(ch1, ch2) = a + b\exp\left(-c\sqrt{W}\right), \qquad (2)$$

where a, b and c are calibration coefficients. If the coefficient a is set to zero, this relationship is equivalent to that of Kaufman and Gao [3], since the effect of the solar terrestrial incident irradiance was implicitly included in the coefficient b. Here the coefficient a is added explicitly to consider a bias that arises from the molecular scattering and aerosol loading effects [9].

In order to study the effect of scan geometry on the calibration curve, the precipitable water (W) is converted to the water vapor path (W^*). The relationship between these two parameters is given as

$$W^* = W\left(\frac{1}{\cos\theta} + \frac{1}{\cos\theta_0}\right), \qquad (3)$$

where θ and θ_0 are the satellite and solar zenith angles, respectively. Using W^* instead of W, Eq. (2) is modified as

$$T_w(ch1, ch2) = a^* + b^*\exp\left(-c^*\sqrt{W^*}\right). \qquad (4)$$

In the following analysis, radiance ratios (T_w) are calculated with Eq. (1) from the radiances simulated with the GSS, and least-squares fitting procedures are carried out with Eq. (4)

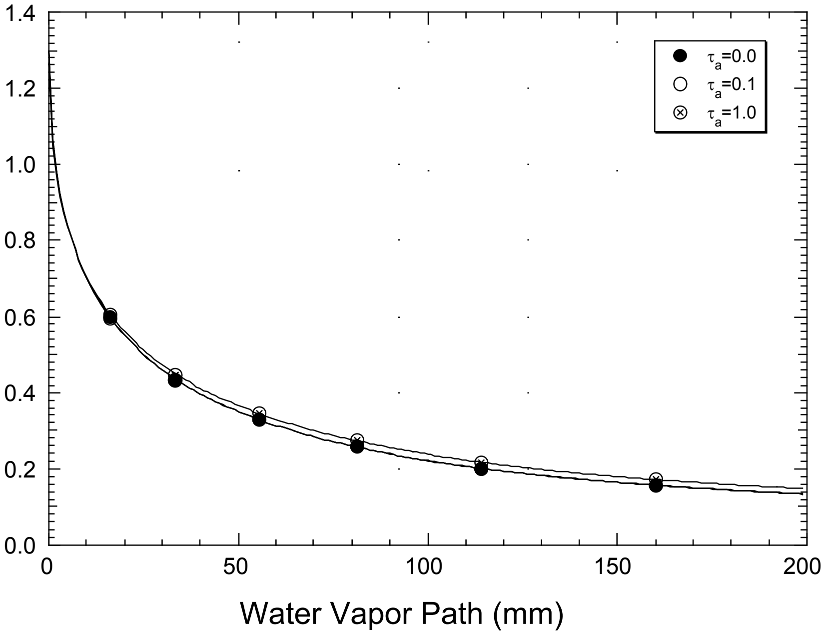

Fig. 2. Calibration curves between the radiance ratio and scaled water vapor path under rural aerosol loading (τ_a=0.0, 0.1, and 1.0) conditions over a bright target (land). All circles denote the radiance ratio between the 1135 nm and 1240 nm channels and are fitted with the calibration curves (Eq. (4)). All the cases are for a scan geometry of solar zenith angle 60°, satellite zenith angle 60°, and relative azimuthal angle 90°.

2.3 Simulations over a bright target with aerosol loading

Figure 2 shows relationships between radiance ratio and water vapor path simulated with the six atmospheric models in Table 1. This is the case with the solar zenith angle 60°, satellite zenith angle 60°, and relative azimuthal angle 90°. In order to minimize the effect of scan geometry, scaled water vapor path in Eq. (3) is used instead of the precipitable water. Here we investigated the effect of aerosol loading on the retrieval sensitivity under clear atmospheric conditions, too. Simulations with the GSS were carried out with the six model atmospheres over a bright target while changing the aerosol optical thickness at 500 nm (τ_a) as 0.0, 0.1, and 1.0 over a bright target with rural aerosol loading. Apparently, all the three cases are fitted well with the calibration curves in Eq. (4) and the curves are almost identical to each other. This indicates that the use of water vapor path enables us to retrieve the precipitable water from the observed radiance ratio over bright targets (e.g., land surfaces), even under moderate aerosol loading. In this simulation, the land surface reflectances were assumed to be 50 % for all the two channels. Consequently, the reflectance ratios of land surface are unity. But, even using the land surface reflectances in the ASTER spectral library [8)], they are actually 1.04 for R_{1135}/R_{1240}. It turns out that this assumption is not influential to the results very much in the simulations.

3. APPLICATION TO GLI DATA AND ITS VALIDATION

The algorithm was applied to the GLI data set as a preliminary analysis. The images of the relevant GLI data are illustrated in Fig. 3. There extends huge cloud system over the western part of the North American continent around California. Cloudy pixels are not retrieved, since the algorithm is applicable only over land and snow/ice surfaces, currently. Comparing these two panels, an apparent difference exists near the cloud edge over the California peninsula: there are darker pixels in the water vapor absorbing channel (Fig. 3a) compared to the non-absorbing one (Fig. 3b).

The retrieval procedure is as follows: At first, cloud screening based upon GLI processing system is carried out. Once the available pixels are determined, the radiance ratio (T_w) is calculated with the two-channel data as describe in Eq. (1). And then, the scaled water vapor path (W^*) was estimated with Eq. (4). Using the solar and satellite zenith angles of the pixels concerned, precipitable water (W) is estimated with Eq. (3) from the water vapor path. A map of precipitable water retrieved above procedure is illustrated in Fig. 4.

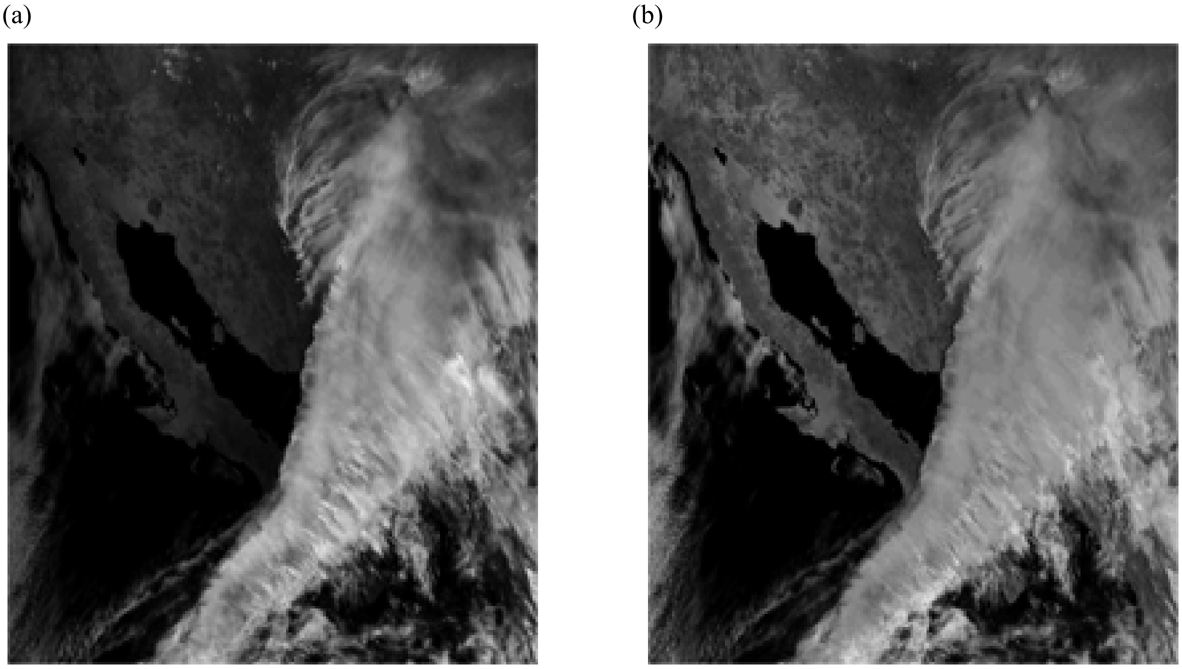

Fig. 3. An imagery of GLI near infrared data in April 10, 2003 around California, the United States of America: (a) ch25 (1135nm), (b) ch26 (1240nm). The channels 25 and 26 are a water vapor absorbing and a no-absorbing channel, respectively. There extended cloud system from the western part of a North American continent to the eastern Pacific Ocean.

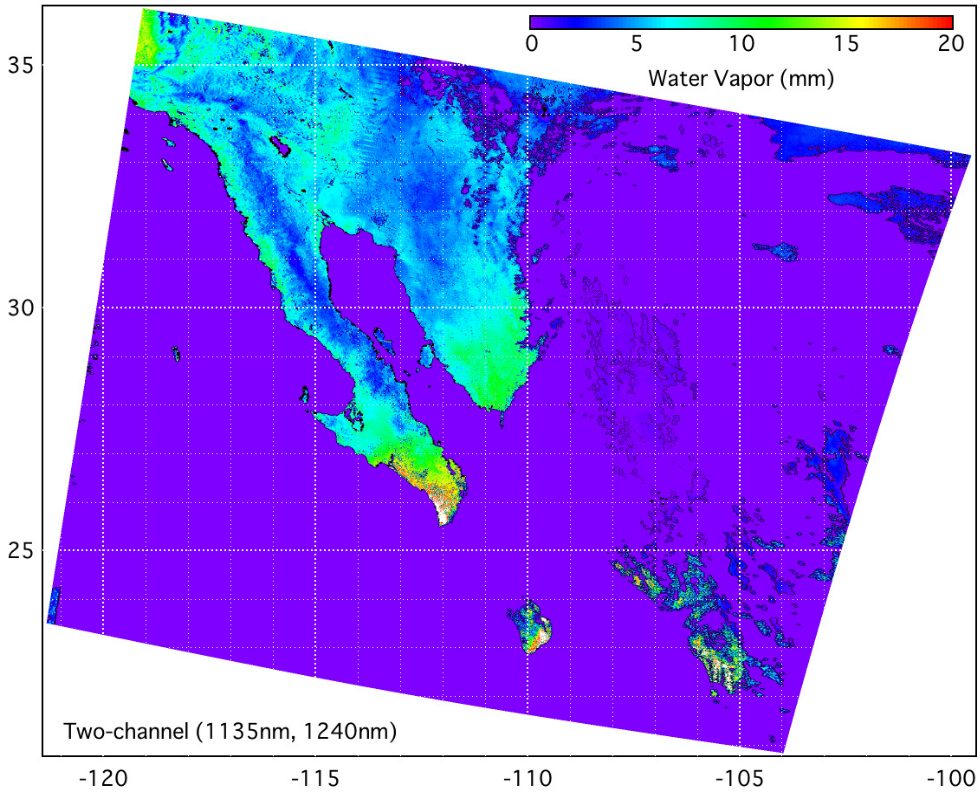

Fig. 4. A retrieved precipitable water distribution in unit of mm in April 10, 2003. The radiance ratio between two channels (1135 nm and 1240 nm) was utilized in the retrieval. The retrieval was performed only over land and snow/ice regions, that is, it was not carried out over cloud and water (ocean). The distribution is mapped on the iso-latitude and iso-longitude coordinate. The numbers around the left and bottom frames denote latitude (˚N) and loingitude (˚E), respectively. Here, a minus sign corresponds to a western longitude.

Table 3 Comparison of precipitable water. Observation time is 1200 UTC for every radiosonde event.

Site # *	Location		Precipitable water (mm)	
	Latitude (˚W)	Longitude (˚W)	GLI	Radiosonde
72293	32.83	117.12	7.3	6.9
72274	32.12	110.93	1.5	4.9
76256	27.95	110.77	11.6	10.3

* WMO site number (five digits).

As is expected with comparison of these two channels, much precipitable water was observed at the southern part of the California peninsula next to the cloudy pixels. At the northern part of the peninsula, on the other hand, there existed much smaller water vapor amount corresponding to the mountain features.

The retrieved precipitable water was compared to the radiosonde observations. Table 3 summarizes the validation. The radiosonde observation suggests that the differences between retrieved and in situ observation is about 1-2 mm for a few radiosonde sites. There was a case that had a severe discrepancy (up to factor 3) between satellite and in situ observations, however. The comparison showed the further validation study was necessary since radiosonde observation (00 and 12 UTC) is not fully coincident to the ADEOS-II / GLI operation (around 10:30 AM at local time). We have a plan to compare the retrieved values to skyradiometer and microwave radiometer observations.

4. SUMMARY AND CONCLUDING REMARKS

We have proposed the retrieval of water vapor amount (precipitable water) using GLI near infrared channels. The retrieval approach proposed in this study enables us to retrieve water vapor amount using GLI onboard ADEOS-II. The results of simulations indicate that the radiance ratio between 1135 nm and 1240 nm channels is well sensitive to the precipitable water over a bright target (higher reflectance at ground level) with Lambertian reflectivity. Over a bright target with spectral reflectance of 50 %, aerosol loading with optical thickness (at 500 nm) of less than 1.0 is not influential to the calibration curves of the retrieval.

The retrieval algorithm was applied to the GLI data around western part of the United States of America. In this preliminary analysis, the retrieval procedure worked well in the GLI data analysis system in JAXA / EORC. The retrieved results were compared to the radiosonde observation sites and the retrieved precipitable water is coincident within 2 mm at a few sites. We have a plan to compare the retrieved results with the continuous observations such as skyradiometer and microwave radiometer sites for the purpose of its global application.

ACKNOWLEDGMENTS

The authors thank GLI Algorithm Integration Team (GAIT) / EORC / JAXA for simulations with GSS and the GLI data handling. This study was supported by Japan Aerospace Exploration Agency (A2-RA-G-0030).

REFERENCES

1. B. J. Soden and F. P. Bretherton: Interpretation of TOVS water vapor radiances in terms of layer-average relative humidities: Method and climatology for the upper, middle, and lower troposphere. *J. Geophys. Res.*, **101**, pp. 9333-9343, 1996.
2. M. D. King, Y. J. Kaufman, W. P. Menzel, and D. Tanre: Remote sensing of cloud, aerosol, and water vapor properties from the moderate resolution imaging spectrometer (MODIS). *IEEE Trans. Geoscience and Remote Sensing*, **30**, pp. 2-27, 1992.
3. Y. J. Kaufman and B.-C. Gao: Remote sensing of water vapor in the near IR from EOS/MODIS. *IEEE Trans. Geoscience and Remote Sensing*, **30**, pp. 871-884, 1992.
4. B.-C. Gao and Y. J. Kaufman: Remote sensing of water vapor and thin cirrus clouds using MODIS near-IR channels. *Proc. of SPIE*, **4150**, pp. 217-224, 2000.
5. F. X. Kneizys, E. P. Shettle, L. W. Abreu, J. H. Chetwynd, G. P. Anderson, W. O. Gallery, J. E. A. Selby, and S. A. Clough: Users guide to LOWTRAN 7. AFGL-TR-88-0177, 146 pp, 1988.
6. T. Y. Nakajima, T. Nakajima, M. Nakajima, H. Fukushima, M. Kuji, A. Uchiyama, and M. Kishino: The

optimization of the Advanced Earth Observing Satellite II Global Imager channels by use of radiative transfer calculations. *Appl. Opt.*, **37**, pp. 3149-3163, 1998.

7. T. Nakajima, T. Y. Nakajima, M. Nakajima, and GLI Algorithm Integration Team (GAIT): Development of ADEOS-II/GLI operational algorithm for earth observation. *Proc. of SPIE*, **3870**, pp. 314-322, 1999.
8. http://speclib.jpl.nasa.gov/archive/jhu/becknic/vegetation/txt/grass.txt
9. M. Kuji and A. Uchiyama: Retrieval of precipitable water using near infrared channels of Global Imager / Advanced Earth Observing Satellite-II (GLI / ADEOS-II). *J. Remote Sens. Soc. Japan*, **22**, pp. 149-162, 2002.

Laboratory Test of Atmospheric Turbulence and Its Implication in the Satellite Observations

Hiroshi Okayama
Center for Environmental Remote Sensing, Chiba University
1-33 Yayoicho Inage-ku Chiba 2638522 Japan

Abstract In connection with the quantity of each parameter obtained from satellite data the atmospheric environmental information from the earth surface is measured simultaneously, and the analytical algorisms of satellite data are verified to get high precision. Major parameters to be measured are downward sun radiation, water vapor, the precipitation from clouds, the optical characteristic of aerosol, the column quantity of atmospheric molecular distribution which participates in the process of radiation, and the degrees of atmospheric turbulence.

Atmospheric turbulence is one of the important correction factors to evaluate the earth's surface using a sensor on a satellite. Aerosol and water vapor are selected as factors of turbulence. The effects of turbulence caused by aerosol and water vapor on the light reflected from the earth's surface are estimated by measuring the degradation of spatial coherence of light in a chamber in which atmospheric turbulence is generated.

Particles contained in cigarette smoke are used as an example of aerosol. Degradation of spatial coherence is measured in relation to the increase of aerosol.

Turbulence caused by water vapor is measured in the range of humidity from 49 ％ to 96 ％. The spatial coherence of light in the chamber degrades in relation to the increase of humidity and as a result the turbulence increases. The relation between the turbulence and the degree of spatial coherence is explained in formula.

I. *INTRODUCTION*

The quality of images obtained by an astronomical telescope set on the earth surface is damaged by atmospheric turbulence, although the images obtained by Hubble space telescope launched into the space are free from the effects of turbulence. These have been many papers on the study of turbulence such as those by Gamo et al [1](1978), Hill et al[2] (1978), Richard et al.[3] (1979), Okayama et al.[4,5] (1999) and Ho[6] (1970). The experiment using an atmospheric turbulence chamber was described by Gamo[1], the modified spectrum of atmospheric temperature fluctuations was discussed by Hill[2], and the optical propagation of the light in laboratory turbulence was experimented by Richard[3]. We previously made measurements of spatial coherence of the light that has passed through turbulent air at different temperatures (Okayama[4, 5]). In a remote sensing study, the effects of atmospheric turbulence on satellite data need to be corrected to make earth surface data as accurate as possible. Primary factors that are considered to cause turbulence in the atmosphere are temperature, aerosol, and carbon dioxide etc. In an attempt to quantify the turbulence, we made a chamber to simulate atmosphere and measured the spatial coherence of light with reference to the change of temperature and the quantity of aerosol. The propagation of mutual coherence in a random medium was studied by Beran[7] and Fied[8].

Correction of errors in satellite data caused by the turbulence of atmosphere is a very important subject to solve in the remote sensing field. As factors causing turbulence other than temperature, we considered water vapor and aerosol in the present experiment. Water vapor is one of the gas components of atmosphere like nitrogen and oxygen. The turbulence of atmosphere is caused by the changes of temperature, water vapor, aerosol, etc. We designed a chamber to simulate atmospheric turbulence, and measured the spatial coherence of the light passing through the chamber to estimate its turbulence (Okayama et al. 1999)[3, 4]. The results obtained by this experiment have verified theoretical ones by Ho[5] (1970) which are based on Kolmogorv's theory to describe atmospheric turbulence (Andrews et al.[6] 1994, Fante[7],1974, Lutomirski et al.[8] 1971).

II. *DEGREES OF COHERENCE*

The degree of coherence g is given by the following formula : are the intensities

$$g(x_1,x_2)=\frac{\mathrm{G}(x_1,x_2)}{\{I_1(x_1)\text{ヲ}I_2(x_2)\}^{\frac{1}{2}}},$$

where $\mathrm{G}(x_1,x_2)$ is a mutual coherence function, and $I_1(x_1)$ and $I_2(x_2)$ are the intensities of the light. Papers by Richard et al.[3] (1979), Andrews et al.[4] (1994), Fente[10] (1974), and Lutmirski et al. (1971) are related to coherence turbulence.

In our experiment, the interference fringes caused by the coherence were photographed to obtain the degree of coherence. The visibility of the interference fringes was calculated by the following formula :

$$V = \frac{I_{\max} - I_{\min}}{I_{\max} + I_{\min}} = \frac{2\left(I_1 \text{ラ} I_2\right)^{\frac{1}{2}}}{I_1 + I_2} \left|g_{12}\right| \quad ,$$

where $I_{\max}$ and $I_{\min}$ are the maximum and minimum values of effective exposures obtained when the interference fringes were exposed. I_1 and I_2 represent the laser intensities but in this experiment $I_1 = I_2 = I$. The degree of coherence g equals to the visibility V.

$$V = \frac{I_{\max} - I_{\min}}{I_{\max} + I_{\min}} = \left|g\right| \quad .$$

The theoretical analysis to obtain the degree of coherence effected by turbulence was made by Ho[5] (1970). His results show that the degree of coherence degrades with the increase of turbulence.

III. *FLUCTATIONS*

In optical turbulence in the atmosphere, the functions for the velocity field the fluctuation of temperature are given by

$$D_{RR}(R) = C_V^2 \, R^{\frac{2}{3}} \quad ,$$

$$D_T(R) = C_T^2 R^{\frac{2}{3}} \quad .$$

Where C_V^2 is the velocity (wind) structure constant and R is the spatial position. C_T^2 is the temperature structure constant. Similarly in the density of water vapor or aerosol, the structure will be given by

$$D_D(R) = C_D^2 \, R^{\frac{2}{3}} \quad ,$$

where C_D^2 is the density structure constant. For statistically homogeneous and isotropic turbulence, the related structure function exhibits the asymptotic behavior

$$D_n(R) = C_n^2 \, R^{\frac{2}{3}} \quad ,$$

where C_n^2 is the index-of refraction structure parameter.

Physically, the refractive-index structure parameter C_n^2 is a measure of the strength of the fluctuations in the refractive index.

IV. *EXPERIMENTL APPARATUS*

An atmospheric turbulence chamber as shown in Fig. 1 was made for this experiment. The beam is multiply reflected in the chamber. The optical path is about 43m long. An argon laser (Lexel Model 65) was used as an optical source. The light which has come out from the chamber after multiple reflection goes through a pinhole and next through double slits (slit width : 25 μ m, space between slits : 50 μ m)and the interference fringes are photographed by a digital camera. When the turbulence increases, the degree of coherence decreases, and the turbulence change is evaluated by measuring the degree of coherence. The double slits are shown in Fig.2.

For the experiment of the coherence degree of water vapor, the same chamber as was used for the aerosol experiment is used. The humidity in the chamber was raised by use of a humidifier. Particles contained in cigarette smoke are used as an example of aerosol.

V. *EXPERIMENTAL RESULTS*

The interference fringes obtained through the double slits were photographed by digital camera as shown in Fig. 3. Degrees of coherence obtained theoretically are shown in Fig.4. For the experiments of water vapor, one, two and no phase screens are used as illustrated Fig.5, 6, and 7, respectively. The contrast, namely coherence degree, of the interference fringes is calculated by a computer and the visibility V is obtained. The experimental results are shown in Fig. 8 and 9. When the quantities of carbon dioxide increase, the coherence degrees decrease and in the experiment of water vapor, when the humidity increases the coherence degrees decrease, and the turbulence increases. These results coincide with the theoretical analysis by Ho [5] ; namely when the degrees of turbulence increase, those of coherence decrease.

If he random medium exists along any part of the propagation path between the transmitter and the receiver, under the Ryotov approximation (Tatarski [12] 1961, Brown[13] 1967, and Yura et al.[14], 1983), the optical field at the distance z = L from the transmitter is

$$U(r,L) = U_0(r,L)\exp[\Psi_1(r,L) + \Psi_2(r,L)\cdots\cdots] \qquad ,$$

where $U_{\circ}(r,L)$ is the optical wave in the absence of the turbulence and $\Psi_1(r,L)$ and $\Psi_2(r,L)$ are first-order and second-order complex phase perturbation caused by the random medium.

VI. *CONCLUSION*

In this paper, we took up aerosol and water vapor as factors which cause turbulence of the atmosphere. If the quantity of water vapor is measured as precisely as those of other factors such as aerosol, variance of temperature, and moisture in the atmosphere, the degree of turbulence caused by aerosol will be estimated from the results of this experiment.

The results obtained by our experiments are considered to be correspondent with the theoretical results of Ho[5] . If the quantity of the objects causing turbulence in the atmosphere can be estimated in the future, these results will be applicable to the correction of satellite data.

The experimental errors are caused by those of the readings of the densities of the interference fringes. When the contrast of interference fringes is digitally obtained, the errors will become almost negligible.

REFERENCES

[1] Hideya Gamo, and Arun K. Majumdar, "Atmospheric turbulence chamber for optical transmission experiment : characterization by thermal method", Appl. Opt., Vol.17, pp3755-3762 (1978).

[2] R. J. Hill and S. F. Clifford, "Modified Spectrum of Atmospheric Temperature Fluctuations and Its Application to Optical Propagation", J. Opt. Soc. Am. Vol. 68, pp892-899 (1978).

[3] Richard A. Elliott, J. Rchard Kerr, and Philip A. Pncus, "Optical propagation in laboratory-generated turbulence", Appl. Opt., Vol. 18, pp3315-3323 (1979).

[4] H. Okayama and Li-Z. Wang, "Measurement of the spatial coherence of light influenced by turbulence", Appl., Opt., Vol. 38, pp2342-2345 1999).

[5] H. Okayama and Li-Z. Wang, Spatial Coherence Degradation of Light Influenced by Temperature and Aerosol by Use of Atmospheric Turbulence Chamber",

Remote Sen. Environ., Vol. 69, pp189-193 (1999).

[6] T. L. Ho, ”Coherence degradation of Gaussian beams in a turbulent atmosphere”, J. Opt. Soc. Am., Vol. 60, pp667-673 (1970).

[7] M. J. Beran, “Propagation of the mutual coherence function through random media”, J. Opt. Soc. Am. Vol. 56, No. 11, pp1475-1480 (1966).

[8] D. I. Fied, “Diffusion analysis for the propagation of mutual coherence”, J. Opt. Soc. Am., Vol.58, No. 7, pp961-969(1968).

[9] L. C. Andrews, W. B. Miller and J. C. Ricklin, “Spatial coherence of Gaussian-beam wave in weak and strong optical turbulence”, J. Opt. Soc. Am., Vol. 11, pp1653-1660 (1994).

[10] Ronald L. Ante, “Mutual Coherence Function and Frequency Spectrum of Laser Beam Propagation Through Atmospheric Turbulence”, J. Opt. Soc. Am., Vol. 64, pp592-598 (1974).

[11] R. F. Lutomirski and H. T. Yura, “Wave structure Function and Mutual Coherence Function of an Optical Wave in a Turbulent Atmosphere”, J. Opt. Soc. Am., Vol. 61, pp482-487 (1971).

[12] V. I. Tatarski, “Wave Propagation in a Turbulent Medium”, (*McGraw-Hill, New York* 1961).

[13] W. P.Brown, Jr, “Validity of the Rytov Approximation”, J. Opt. Soc. Am., Vol. 57, pp1539-1543 (1967).

[14] H. T. Yura, C. C. Sung, S. F. Clifford and R. J. Hill, “Second-order Rytov approximation”, J. Opt. Soc. Am., Vol. 73, pp500-502 (1983).

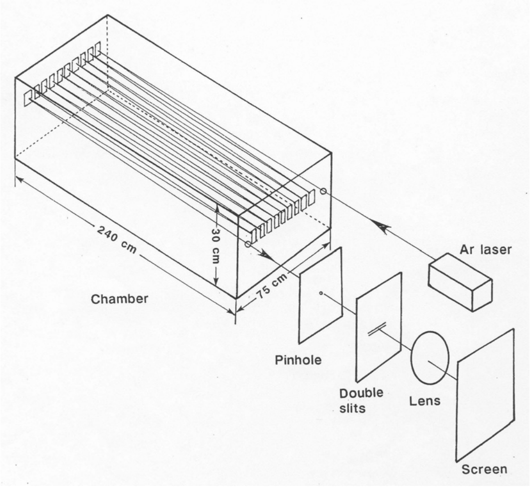

Fig.1. Optical system of the multiple reflection simulator that was used to measure atmospheric turbulence.

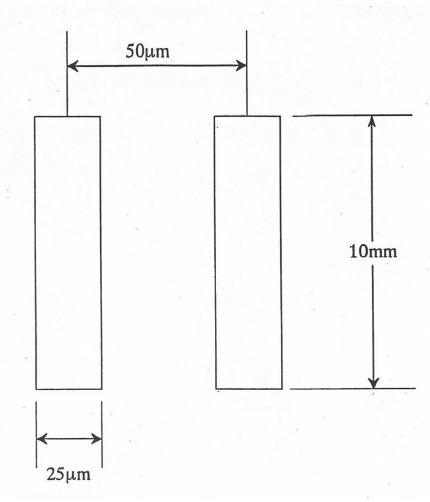

Fig.2. Double slits.

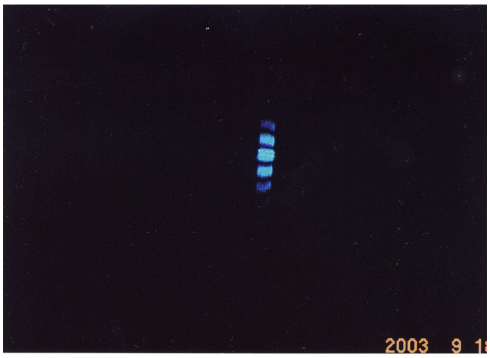

Fig.3. Interference fringe obtained through double slits.

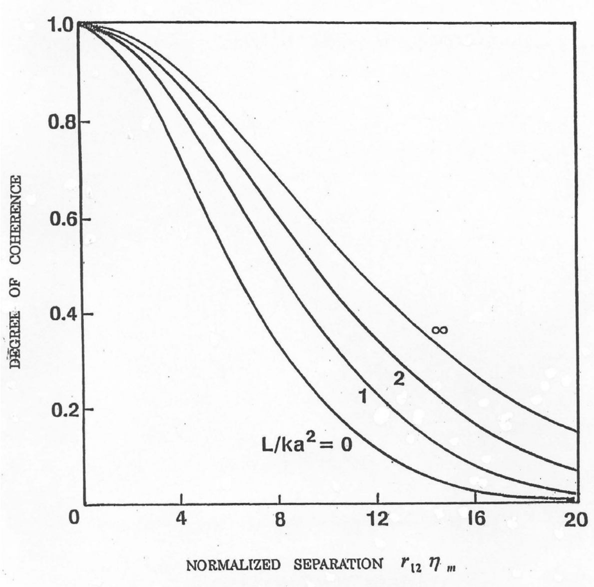

Degree of coherence of a collimated gaussian beam

For $L/kl_m^2=1$, $C_n^2k^2L\eta_m^{-5/3}=0.025$, where $\eta_m= 5.91/l_m$

The case where $L/ka^2=0$ corresponds to an infinite plane wave; the case where $L/ka^2 \to \infty$ corresponds to spherical wave

Fig.4. Degree of coherence of a collimated Gaussian beam.

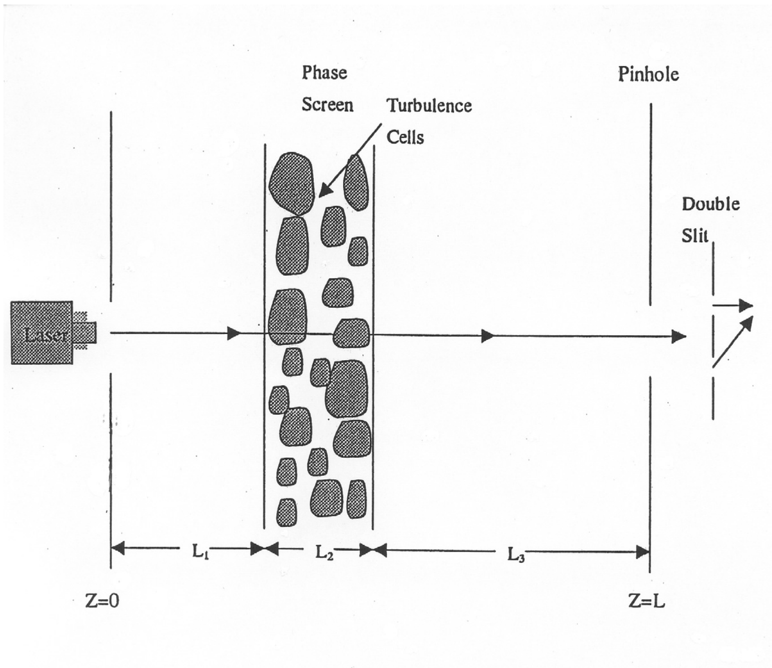

Propagation of One Phase Screen

Fig.5. Propagation geometry for a single phase screen.

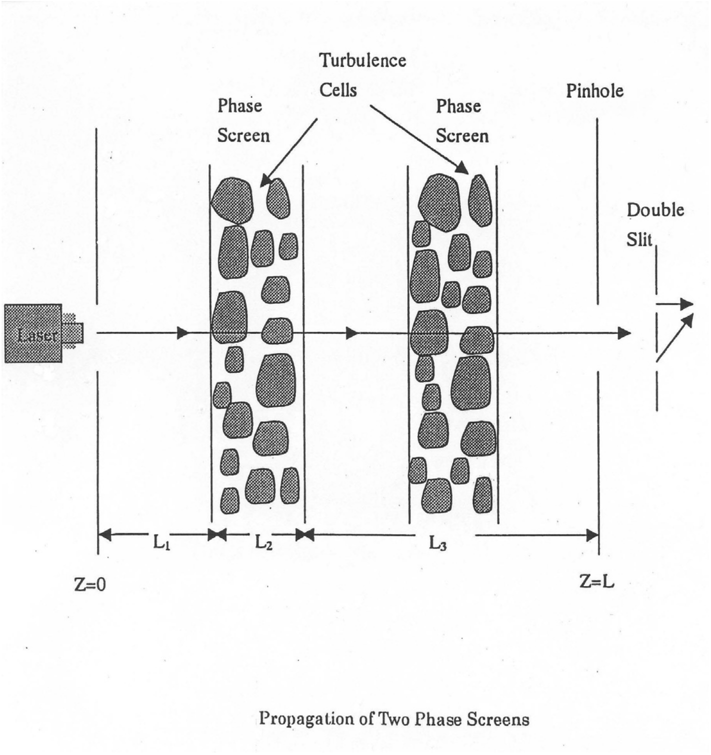

Fig.6. Propagation geometry for two phase screens.

.

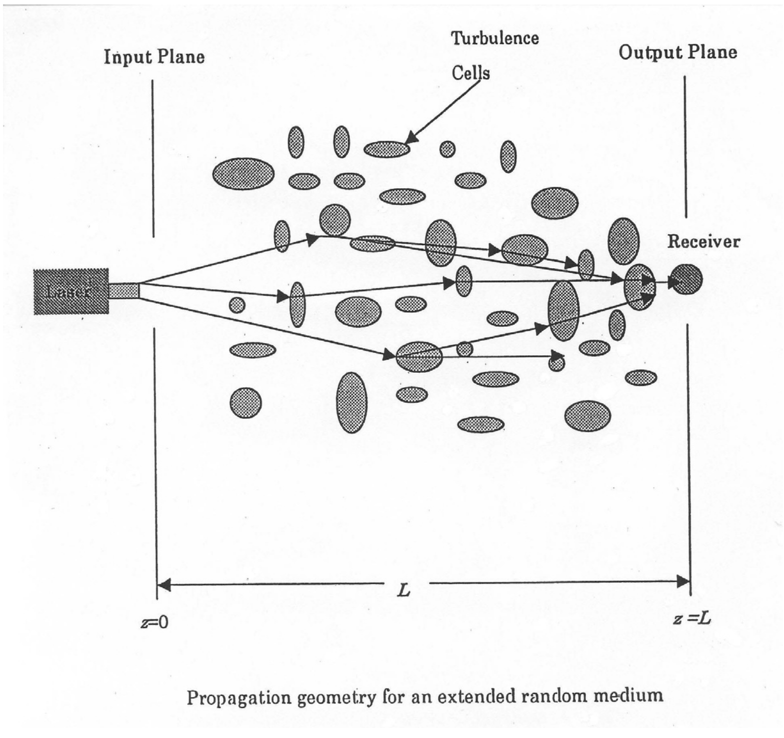

Fig.7. Propagation geometry for an extended random medium.

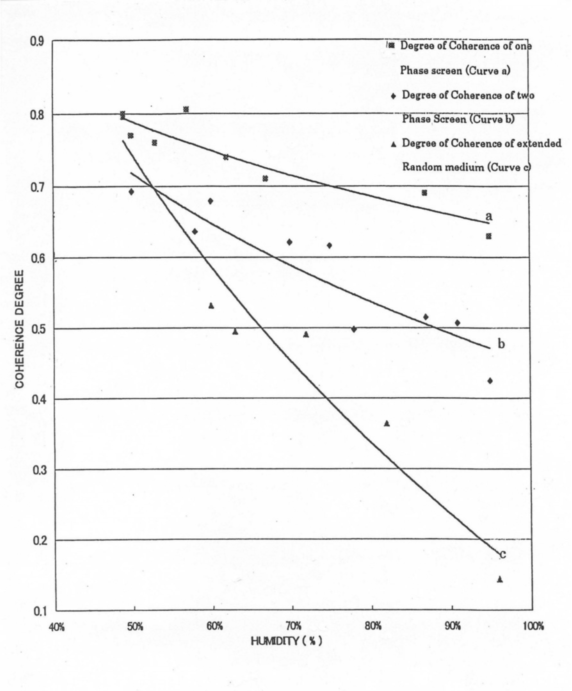

Degree of coherence of different propagation Medium

Fig.8. Experimental results of water vapor.

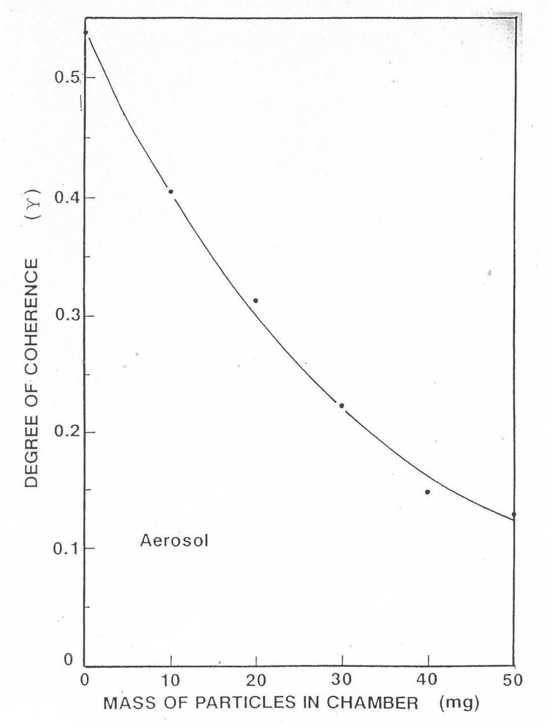

Fig.9. Experimental results of aerosol.

Comprehensive Study on Photosynthetically active radiation in Beijing

Hu Bo, Wang Yuesi, Liu Guangren,Ma Zhiqiang
Institute of atmospheric physics, Chinese academy of sciences, Beijing 100029

Abstract

The data, measured by using global photosynthetically active radiometer (LI-COR quantum sensor) and global solar radiometer in Beijing, has been analyzed, for investigating the relationship of these two radiant fluxes in Beijing. The data is used to determining timescale variability of the ratio of Photosynthetically active radiation (PAR) to global solar radiation (R_s). The seasonal variation of the ratio ranges from 1.713 to 1.990 μ mol J^{-1},monthly from 1.626 to 2.039 μ mol J^{-1},and daily from 1.42 to 2.57 μ mol J^{-1}, with annual mean value 1.841 μ mol J^{-1}.

Keywords: Solar radiation, PAR, estimate

1 Introduction

Photosynthetically active radiation (PAR) is the visible part of the electromagnetic spectrum of the solar radiation that received at the Earth's surface. Apart from its relevance to daily human activity, it contributes significantly in comprehensive studies of radiation climate, remote sensing of vegetation, radiation regimes of plant canopy and plays an important part in provides energy supports photosynthetic and primary production by green plants through the processes of chlorophyll synthesis and photosynthesis which result in the conversion of radiation energy into chemical energy and through photosensitive regulatory mechanisms such as phototropism and photoperiodic activity(Udo and Aro,1999; Jacovides et al., 2004; Dye,2004).PAR covering both photon and energy terms lies between 400nm and 700nm. PAR is a key variable in process-based models of terrestrial photosynthesis and ecosystem-atmosphere CO_2 exchange (Dye, 2004). So extensive study on PAR is necessarily and valuable. PAR is necessary input parameters in dealing with plant physiology, biomass production, natural illumination in greenhouse, and carbon cycle.

At present, there are three methods were used to measure PAR radiation:(1) indirect method, in this method PAR is often obtained as the difference between two irradiance measurements;(2) spectrally integrating method, in this method PAR is obtained by integrating spectral irradiance distribution measurements over the waveband 400-700nm;(3) direct method, in this method PAR is measured quantum sensor, the unit of PAR is μmol $m^{-2}s^{-1}$. This is base on the fact that photosynthetic efficiency of green plants is proportional to the number of photons absorbed in the spectral range 400-700nm,and not their energy. (Udo and Aro, 1999). Currently Chinese scholars often use indirect method to obtain PAR value, i.e. use different spectral solar radiometer to measure radiation, and then obtain PAR value through the difference between this two different radiometer.

Most reports on experimental results use measured values of PAR and global radiation

(R_S) to determining the PAR fraction of the global radiation, and then use this PAR fraction calculate PAR from the routinely measured global radiation. Nevertheless, the range of the PAR fraction is influenced by local climatic and geographic differences like clearness and brightness (Udo and Aro, 1999), solar elevation, dewpoint temperature and fine mode aerosols. The accurate determination of PAR is important in many applications, such as net primary productivity and carbon cycle modeling (Pinker and Laszlo, 1992 and Frouin and Pinker, 1995). Comprehensive study on PAR can provide accuracy radiation for carbon cycle study, present evidence for carbon budget.Hence, approaches to determine PAR from more widely measured variables have merit. In this paper, the measured PAR and global radiation values are used to analyzes the characteristic of PAR in Beijing and quantify the relationship between these two important solar radiation components. Based on the ratio of PAR to R_S, an empirical model was developed to estimate PAR from R_S.

2 Materials and Methods

2.1 Site descriptions:

Beijing, Capital of the People's Republic of China, and located in the northern part of the North China Plain at 39°56' north latitude and 116°20' east longitude. Mountains in the east, north and west surround it. Beijing covers an area of 16,807.8 sq. km and has a population of 11 million.

The climate in Beijing is of the continental type, with cold and dry winters, due to the Siberian air masses that move southward across the Mongolian Plateau. The summers are hot owing to warm and humid monsoon winds from the southeast bringing Beijing most of its annual precipitation.

Sampling site is situated at the crossing of the forth ring road and the third ring road. This area is part of downtown. There are inhabitant housing in the north and south， and a freeway near the eastern. Wang (2001) report measurements in this area can representation the average condition of Beijing city.

The sampling instruments are installed on a flat platform at the top of the building housing chemic laboratories, Institute of atmospheric Physics, Chinese Academy of Sciences.

2.2 Instruments used

Global radiation was measured using a Kipp&Zonen model CM-21 (Delft, The Netherlands). The PAR photon flux was measured with a Licro quantum sensor LI-190Sz (Lin-coln,Nebraska,USA).This station complete with data acquisition system(Vaisala M520 data-logger, and a storage module, Finland).The signals were conditioned with the respective instrument factors into units of W/m^2 and $\mu Em^{-2}s^{-1}$(quantum $mol^{-1}s^{-1}$ or $\mu molm^{-2}s^{-1}$).Global radiation measurements have an estimated experimental error of 2-3%,while the PAR sensor has a relative error of lees then 5%.All radiation values was measured by one minute interval, and the hourly values was driven from minute value by integrating them.

A sun tracker with a direct radiometer (TBS-2) and a global radiometer (TBQ-2)(Junzhou, China) was used to measure direct and global radiation. Direct radiation measurements have an estimated experimental error of 2-3%, while the global radiometer has a relative error of lees then 5%. A yuanhua data logger (Yuanhua,Taiwan,China) was used to collect these measured data. The measurement interval is also one minute.

Daily checks were made to ensure that the radiometers were positioned horizontally by monitoring and adjusting. The global radiometers were calibrated against a reference pyranometer,which is calibrated a standard pyrheliomter,while the LI-190SA pyranometer is calibrated against calibration lamps at factory. All this calibrated work was done at the beginning and the end of data collected. The data used is this paper from April 2004 to March, and 2005.

2.3 Methods

2.3.1 Analysis methods for PAR

The analysis is based on hourly radiometric data collected in Chinese terrestrial ecological research stations, for a period of one year (Feb. 2004-Mar.2005). The hourly data were checked for inconsistencies to eliminate problems associated with questionable measurements. Due to cosine response problems this analysis is limited to cases with solar elevation 15° < h<85° .

The well-known sky indices，sky clearness ε and brightness k_t (Perez et al., 1990) are used to classify the sky conditions. They are computed from radiation values and defined as:

$$\varepsilon = \frac{R_d + R_b}{R_d} \quad （1）$$

$$\Delta = \frac{R_d}{R_0 \sinh} \quad （2）$$

With R_d and R_b are diffuse and direct radiations on Earth's surface horizontal respectively, and R_0 is the extraterrestrial radiation. Sky condition is divided into three types. Overcast, clear and intermediate shies have been considered (Jacovides et al., 2004): (i) overcast skies ($\Delta < 0.1$, $\varepsilon < 1.2$); (ii) clear skies ($\Delta < 0.1$, $\varepsilon > 5.2$); and (iii) intermediate skies ($0.2 < \Delta < 0.3$ and $1.2 < \varepsilon < 5.2$).

2.3.2 Method for develop empirical model

A multiple linear regression equation used to develop the empirical model for estimate PAR from global radiation. The regression equation including sky conditions parameters, atmospheric water vapor, and concentration of PM10 and PM2.5. The multilinear regression is used to analyze the data; in the regression equation intercept is forced to be zero.

3 Results and discussion

3.1 Time series measurements of PAR and R_s

The hourly values of solar components radiation are grouped into daily, monthly and seasonal data sets. The daily ratio of PAR to R_s is derived from hourly values, then the monthly ratio values is from daily average values.Fig.1 shows the daily variability of both PAR and R_s for the period of the measurements. It is evident that PAR is highly correlated with R_s.So the values of PAR can be obtained directly from R_s.It has generally been the practice to express the measured hourly or daily relationship between PAR and global radiation R_s(Alados et al.,1996;Papaioannou et al.,1996;Udo and Aro,1999;Gonzalez and Callbo,2003;Jacovides et al.,2004).

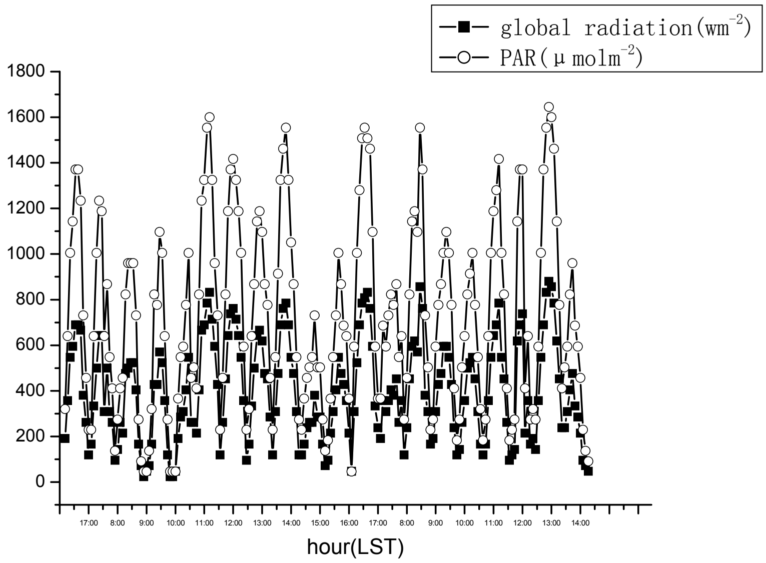

Fig. 1 Diurnal variation of PAR and R_S in Beijing

The variation characteristics of PAR and global radiation are distinct, and the variation type is presented in Fig. 1.The variation trend of Par is similarly as that of global radiation. The diurnal, seasonal variation model of PAR is the same as that of global radiation in Beijing. In the diurnal variation rule, the tine of PAR and global radiation appears at one time, the maximum value appears at noon. In the seasonal variation trend, the high values appear in summer and the low values are in winter, the values of spring and autumn are in intermediate (the variation rule is lie on the Earth rotation and the sun revolution rule). There is good correlation ship between these two solar radiation components, from this variation characteristic one of them is can be estimated from another one.

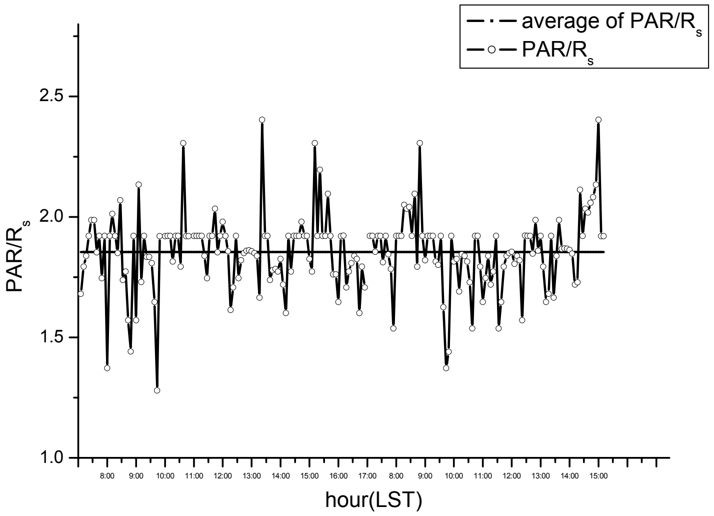

Fig. 2 Daily ratio of PAR to R_s

Daily ratio of PAR to R_s is showed in Fig.2. The minimum and maximum daily ratio value is 2.5 and 1.6 molMJ^{-1} respectively. The annual average of daily ratio was 1.954 ±0.086 molMJ^{-1},this agrees with the monthly result in Table 1.For overcast days the minimum and maximum daily ratio value are 2.6 molMJ^{-1}, 1.9 molMJ^{-1}respectively, and in clear days the minimum and maximum daily ratio value are 2.5 molMJ^{-1}, 1.8 molMJ^{-1} respectively. The cloudy days ratio was 4.3% higher than that of clear days. These results show that cloudiness and vapor have effect on the ratio.

Table 1 Ratios of PAR to global radiation on monthly, and seasonal

Period	Number of days	Ratio	R^2	Standard deviation
April	30	1.87	0.995	0.037
May	31	1.91	0.992	0.079
June	30	1.96	0.998	0.043
July	31	2.04	0.990	0.072
August	31	1.99	0.996	0.063
September	30	1.83	0.997	0.056
October	31	1.70	0.997	0.034
November	30	1.63	0.99	0.068

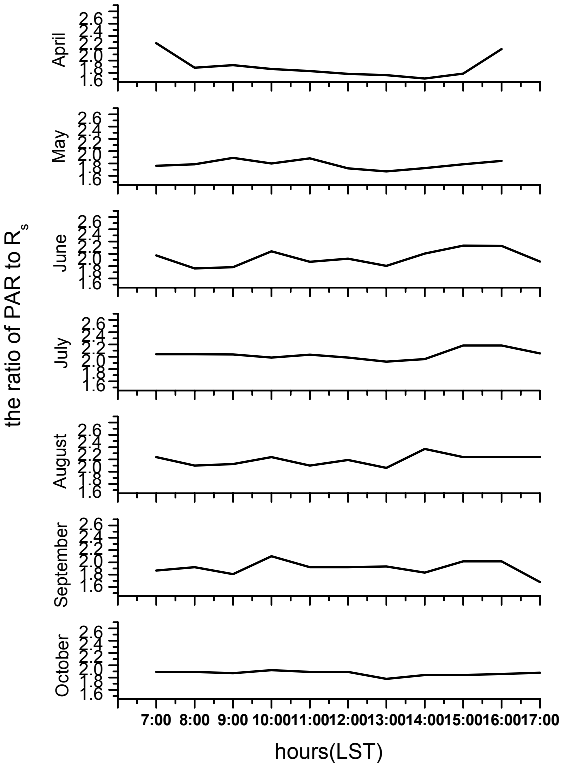

Fig. 3 Monthly mean diurnal variation of the ratio of PAR to R_S

The mean diurnal ratio on monthly was calculated from hourly ratio values. Monthly characteristic of the ratio is showed in Fig. 3. The monthly variation scope is smoother than that of daily variation range. This phenomena show that the influence of cloud on the monthly ratio is smaller than that on daily ratio. Fig.3 show that the variation of monthly ratio has a significant trend, namely, higher ratio during sunrise and sunset, and lower at noon (there is a different diurnal variation of the ratio in afternoon of October and September, this is caused by higher aerosol concentration and different variation model of humidity. In October and December dewpoint temperature is the lower in the morning, humidity is increase gradual and after noon humidity decrease.). From April the ratio is gradually increase, and the appears the maximum ratio in July, then the ratio values is decrease gradually, and the lowest ratio is appears in January. The climate variation characteristic of the control factor of the ratio variation trend, East Asia season is the mainly climate characteristic of Beijing. In this climate, there is significant rainy season, and a dry period. Monsoon is start in July (summer), and end in early September as the dry season sets in. There are many active synoptic systems (depressions) in Beijing, in July. So the surface heating causes increase moisture content. Water vapor through absorption processes markedly affects the longer wavelengths, leaving the spectral PAR portion invariability, consequently decreasing the global radiation greater than that of PAR, so the ratio increase with water vapor increasing. On the contrary, there is stabilization system control and the dry season strong, and there is almost clear day in Januarys. The concentration of aerosol is higher in this month, because of steady boundary layer and aerosol accumulative. The aerosol through scattering the PAR spectral, and have a little effects on longer wavelength radiation, so the ratio is decreasing with the concentration of aerosol (especially the fine particle in the atmospheric aerosol) increasing.

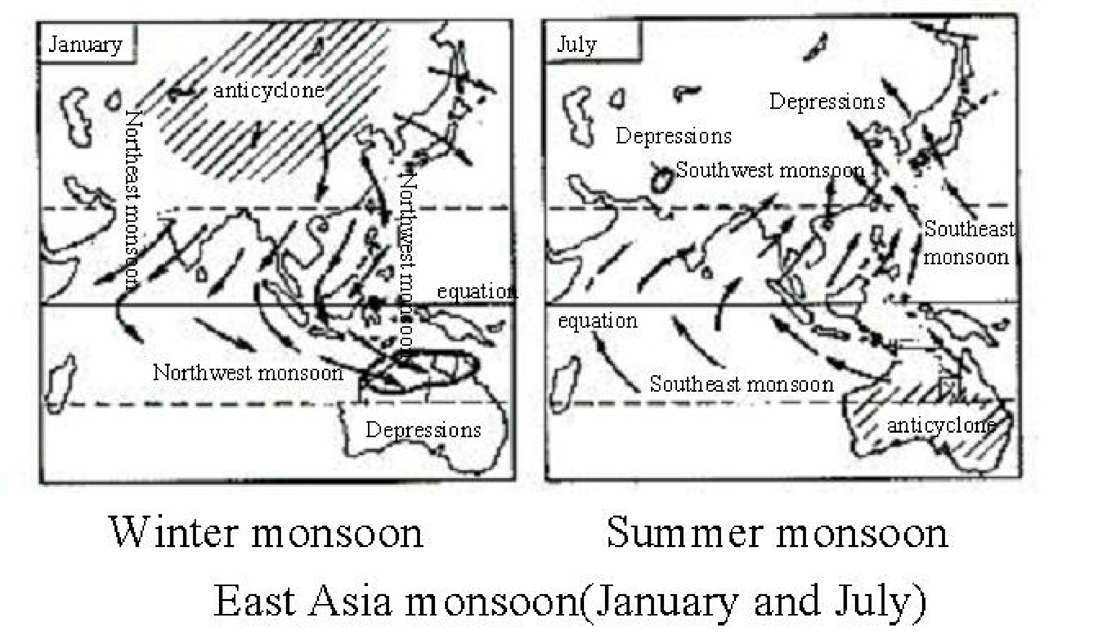

Fig. 4 Weather systems in East Asia

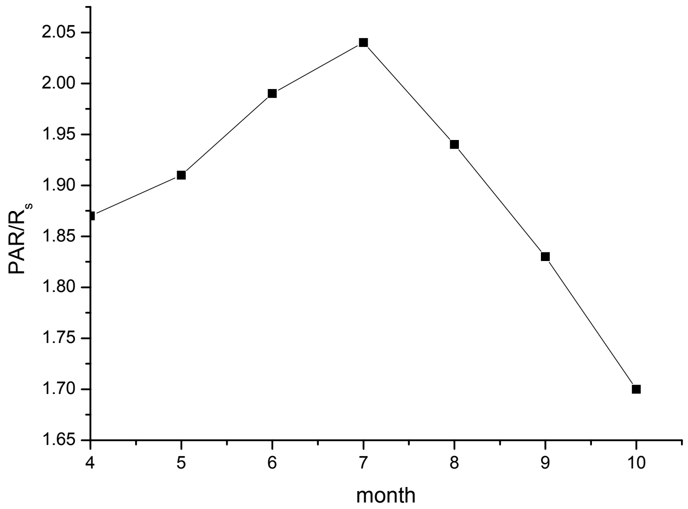

Fig. 5 Average ratio of PAR to R_S in monthly

Seasonally variation properties of the ratio is that, the highest value appeared in summer, the smallest values of ratio is appeared in winter, and the ratio values in autumn is smaller then that in spring. The mainly reason of these monthly variation properties is caused by: Beijing is situating in the East Asian monsoon area, there are a rainy season and a dry season in this region. There are many active synoptic systems (depressions) happen in this area, but concentration of the water vapor is limited and has few rain in this region, in spring (March, April, May). The rainy season is setting in June, ending in august and dry season coming. The mainly rainfall is produced in

July. In autumn season (September, October, November), Beijing is often controlled by anticyclone; the sky condition is always clearness. Subtropical anticyclone frequent happens in winter season (December, January, February), rainless and cloudless is the mainly sky condition type in this region. Spring, and winter is called dry season, because there are few rainfalls in these season. In rainy season, there are abundant water vapors in Beijing, so the ratio is highest. In the dry season, there is little water vapor and high aerosol concentration, so the smallest ratio values happened in this season.

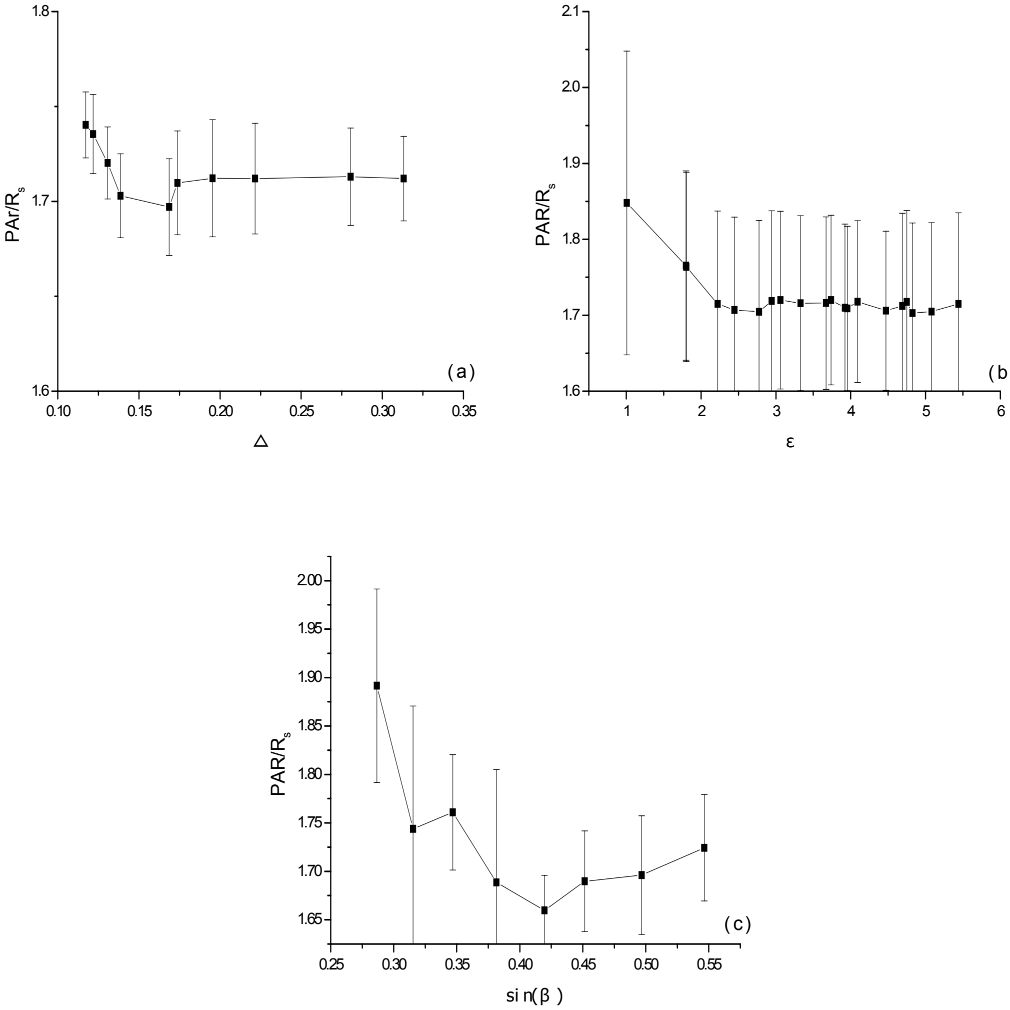

Fig.6 The Ratio of PAR to R_s vs. sky clearness ε (a), brightness Δ (b), solar elevation sin (h), and K_t. all parameters' means values are calculated for 10% intervals.

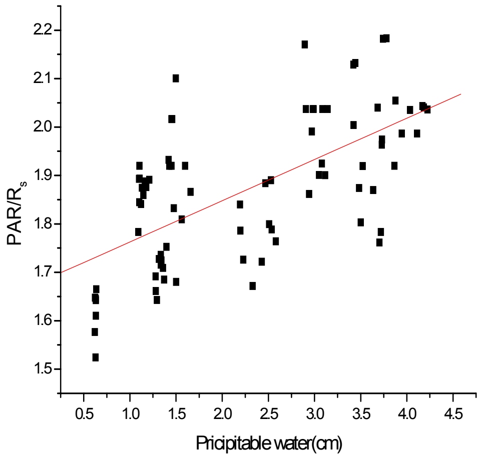

Fig. 7 The Ratio of PAR to R_s vs. percipitable water

Fig. 6-Fig. 8 show the ratio of PAR to R_s is mainly depend on the percipitable water. The ratio is gradually decreased with sky clearness ε ,and brightness increase ,then there is inflexion in the decrease trend, finally the ratio variation is steady.

3.2 Estimate model development

The sky condition index $K_s = R_s / H_0$ is used in the estimate equation rather than sky clearness ε ,because there is enslaved to diffuse radiation observe generally. R_0 is the extraterrestrial radiation is calculated by equation(Iqbal,1983):

$$H_0 = \frac{24}{\pi} S_0 L_0 \left[(\pi/180) w_s (\sin\delta \sin\phi) + (\cos\delta \cos\phi \sin w_s) \right] \quad (3)$$

Where S_0= the solar constant energy unit =1367Wm^{-2},L_0 is the correction factor of the earth's orbit,δ the solar declination,w_s is sunrise hour angle and Φ is the geographical latitude.

3.2.1 Estimating equation

Firstly, The global radiation and PAR dataset was used to developed the estimate equation. In this step the sky conditions, water vapor and the solar elevation is omitted. A linear regression equation from origin is used for estimating equation. From the analysis results, the ratio of PAR to global radiation has a significant seasonal variation characteristic, so all the data were used to developed the primary estimated equation, then the dataset is divided into dry season and rainy season to developed the primary estimating equation.

$$PAR = \begin{cases} 1.7761 * R_s, r = 0.979, clear \quad sky \\ 1.985 * R_s, r = 0.9869, intermediate \\ 2.09266 * R_s, r = 0.9889, overcast \end{cases} \quad (model \quad 1)$$

Secondly, The mainly influence factor of the ratio of PAR to global radiation is the vapor, so in the secondly step the percepitable water and sky conditions were used for the estimating equation developed. The percepitable water is calculated from ground humidity and temperature (Yang, and Qiu, 2002).

$$W = \exp(b_0' + b_1' t_d), W \quad is \quad precepitible\,water \qquad (4)$$

$$t_d = \frac{c \times b}{c \times (a/2) + b - 273.16}, a = {}^{100}\!\big/_{\ln(RH)}, b = 15.0 \times a - 2.1 \times T + 2711.5$$
$$c = T + 273.16, RH \quad is\,humidity, \quad T \quad is\,teperature$$

Because there is no scattered radiation and direct radiation in a great number of radiation observation station in china solar radiation observation station, So A estimating equation without sky conditions parameters(sky clearness ε , brightness Δ) is being developed. In this developed estimate equation progress, the means sky condition parameter K_s is used for developing the estimate equation. The sky condition index K_s is calculated by equation 3.

$$PAR / R_s = \begin{cases} 1.576 - 0.177\ln(k_s) - 0.1w + 0.31\sin(elevation), R = 0.746 \\ 1.534 - 0.121\ln(k_s) + 0.21\sin(elevation), R = 0.66 \end{cases} (\mathrm{mod}\,el \quad 2)$$

where,w is precipitable water, elevation is solar elevation,k_s is means sky conditon.

4 conclusions

The analyses of measured PAR and global radiation in Beijing are summarized as fellow: The ratio of PAR to global radiation has a significant seasonal variation trend, high values in summer (1.98 μ mol J^{-1}) and low values in autumn μ mol J^{-1}).The values of ratio in winter and spring are higher than that on autumn. The highest ratio value is presented in July(2.04 μ mol J^{-1}) and the lest ratio value presented in December (1.626 μ mol J^{-1}).

The estimating equation can be used estimate PAR from global radiation.

The diffuse PAR radiation has higher light use efficiency for plant canopy, has much less tendency to cause canopy photosynthetic saturation (Lianhong Gu et al., 2001). Farther work on PAR will setup a diffuse PAR measured systems and estimating equation for diffuse PAR will be developed.

References

Alados,I.,Foyo-Moreno,I.,Alados-Arboledas,L.,1996,Photosynthetically active radiation: measurements and modeling. Agric. For. Meteorol.**78**, 121-131.

Dennis G.Dye, 2004.Spectral composition and quanta-to-energy ratio of diffuse photosynthetically active radiation under diverse cloud conditions. J. Geophys. Res. **109**, dio: 10.1029/2003JD004251.

Frouin, R. and Pinker, R.T., 1995. Estimating photosynthetically active radiation (PAR) at the earth's surface from satellite observations. *Remote Sens. Environ.* **51**, 98–107.

Gonzalez,J. A., Callbo,J.,2002,Modelled and measured ratio of PAR to global radiation under cloudless skies, Agric. For. Meteorol.**110**, 319-325.

Jacovides,C. P.,Timvios,F. S.,Papaioannou,G.,Asimakopoulos,D. N.,Theofilou,C. M.,2004,Ratio of PAR to broadband solar radiation measured in Cyprus, Agric. For. Meteorol.**121**, 135-140.

Lianhong Gu,Dennis Baldocchi,,Shashi B. Verma,T. A. Black,Timo Vesala,Eva M. Falge,Pete R. Dowty, Advantages of diffuse radiation for terrestrial ecosystem productivity. JOURNAL OF GEOPHYSICAL RESEARCH, VOL. **107**, NO. D6, 4050, doi:10.1029/2001JD001242, 2002

Pinker, R.T. and Laszlo, I., 1992. Global distribution of photosynthetically active radiation as observed from satellites. *J. Clim.* **5**, 56–65.

Perez,R.,Ineichen,P.,Seals,R.,Michalsky,J.,Stewart,R.,1990.Modeling daylight availability and irradiance components from direct and global irradiance. Solar Energy, **44**,271-289.

Papaioannou,G.,Nikolidakis,G.,Asimakopoulos,D.,Redailis,D.,1996, Photosynthetically active radiation in Athens. Agric. For. Meteorol.**81**, 287-298.

Udo, S.O., Aro,T.O., 1999.Global PAR related to global solar radiation for central Nigeria, Agric. For. Meteorol.**97**, 21-31.

Yang Jingmei,Qiu jinghuan,A methold for estimating precipitable water and effective water vapor content from ground humidity parameters. Chinese Journal of atmospheric sciences, **26**,9-26. (in chinese)

Yue-Si Wang,Li zhou,Ming-xing Wang,Xun-Hua Zheng,2001.Trends of atmospheric methane in Beijing,Chemosphere-Global Change Science ,**3**,65-71.

Environmental application of the all-sky survey high-resolution air-shower (ASHRA) telescope — aerosol distribution measurement using a bistatic, imaging lidar

Shunsuke Fukagawa [a], Ikue Kouga [a, c], Hiroaki Kuze [a], Nobuo Takeuchi [a],
Makoto Sasaki [b], Yoichi Asaoka [b], Satoru Ogawa [c]
[a] *Center for Environmental Remote Sensing (CEReS), Chiba University*
1-33 Yayoi-chi, Inage-ku, Chiba 263-8522, Japan
[b] *Institute for Cosmic Ray Research, University of Tokyo*
5-1-5 Kashiwa-no-Ha, Kashiwa City, Chiba 277-8582, Japan
[c] *Faculty of Science, Toho University*
2-2-1 Miyama, Funabashi City, Chiba 274-8510, Japan

Abstract: All-sky Survey High Resolution Air-shower (Ashra) telescope has been developed to detect cosmic-ray neutrinos with extremely high energy, larger than 10^{16} eV. The important features of the telescope system are the wide FOV (50×50 deg) with high angular resolution (1 arcmin) and a high-speed, highly sensitive imaging system with an intelligent triggering capability. In this paper we report an imaging lidar on the basis of this novel telescope system applied to the detection of atmospheric aerosols. Because of the wide acceptance angel, the bistatic configuration enables light detection in the forward-scattering mode, greatly enhancing the signal-to-noise ratio. Eye-safe lidar operation is achieved with a laser wavelength in the operational wavelength range of the Ashra telescope (300-420 nm). Simulation studies are undertaken to establish the retrieval algorithm of aerosol distribution from the bistatic measurement.

1. Introduction

The All-sky Survey High Resolution Air-shower (Ashra) telescope project is a combined effort in the different categories of cosmic-ray physics, particle physics, and remote-sensing techniques of atmospheric sounding. In this project, the CEReS group is in charge of the application of the Ashra telescope to the monitoring of the atmosphere. The novel concept of Ashra telescope has been developed by the group of Institute for Cosmic Ray Research (ICRR), University of Tokyo. The remarkable features of the system are a wide field-of-view (FOV) (50 × 50 deg) with high angular resolution (1 arcmin = 0.29 μrad) and a high-speed, highly sensitive imaging system with an intelligent triggering capability [1-4].

The imaging lidar observation[5] is conducted in bistatic mode, in which, unlike the conventional monostatic lidar, the telescope is placed apart from the laser source. The light scattered in the atmosphere is detected in the scattering-angel range of $0<\theta<180$ deg. Although bistatic measurements of aerosols have so far been reported[6,7], the scanning of the laser beam was not attempted, leading mainly to the detection near the backscattering scheme. In contrast, forward scattering yields high signal-to-noise (S/N) ratio owing to the general property of the Mie scattering from aerosols. In the case of Ashra system, another advantage is the usage of the intelligent triggering. This greatly contributes to reduce the background light and thereby to increase the S/N ratio. These features make the three-dimensional, wide area, and real-time monitoring of atmospheric aerosols possible. Moreover, using the laser wavelength at 351nm or 355 nm, which are in the design wavelength of Ashra telescope (300-420 nm), ensures eye-safe lidar operation, since the level of maximum permissible exposure (MPE) is very high in this wavelength region.

In this paper, we describe the scheme of bistatic lidar measurement, with the results of related simulations and our preliminary experiment of the bistatic lidar measurement.

2. Bistatic measurement of aerosol

The basic configuration of the bistatic measurement is shown in Fig. 1. A laser and a telescope are located separately, with a baseline distance of *L*. The laser is illuminating a direction θ_{laser} (elevation angle), while the telescope is observing the beam path toward a direction θ_{view}. In this bistatic measurement, the lidar equation is written as

$$P = P_0 \; K \; \frac{A}{r^2} \; ds \; \beta\left(\theta_{\text{scat}}\right) T \;, \tag{1}$$

where P is the received signal intensity, P_0 the emitted laser intensity, K the efficiency of the receiving optics, A the area of telescope's mirror, r the distance between the target (aerosol particle) and the telescope, and θ_{scat} the scattering angle. The portion of the laser beam path subtended by the FOV for a single pixel of the array detector is denoted as *ds*, which is given as

$$ds \; = \frac{r \; \theta_{\text{FOV}}}{\sin\left(\theta_{\text{scat}}\right)} . \tag{2}$$

The generalized scattering coefficient, $\beta(\theta_{\text{scat}})$, is defined as

$$\beta(\theta_{\text{scat}}) = \; \alpha_1 \; f_1(\theta_{\text{scat}}) + \alpha_2 \; f_2(\theta_{\text{scat}}) \; . \tag{3}$$

Here, θ_{FOV} is the FOV for a single pixel, α the extinction coefficient, and f the phase function. Subscript 1 is for aerosol and 2 for air molecule. The transmittance along the combined laser path and viewing path is expressed as

$$T = \exp\left[-\left(\tau_{\text{t}} + \tau_{\text{r}}\right)\right]. \tag{4}$$

Here, τ_{t} is the optical thickness of the transmitter side and τ_{r} that of the receiver side. These parameter are given as

$$\tau_{\text{t}} \; = \frac{\int_0^z \{\alpha_1(z') + \alpha_2(z')\} dz'}{\sin\theta_{\text{laser}}} , \tag{5}$$

$$\tau_{\text{r}} \; = \frac{\int_0^z \{\alpha_1(z') + \alpha_2(z')\} dz'}{\sin\theta_{\text{view}}} . \tag{6}$$

3. Inversion of bistatic lidar data

In this section, we describe the inversion procedure used to derive the spatial distribution of the aerosol extinction coefficient from the bistatic lidar data. We assume that the laser beam is scanned as shown in Fig. 2. The viewing direction is numbered with an index i (= 0, 1, ...) and the laser beam direction with j (= 0, 1, ...). The aerosol extinction coefficient (i.e. the product of the aerosol number density and the total cross section) at the intersection defined by indices i and j is expressed as $\alpha_1^{(i,j)}$. From Eqs. (1) and (2), the ratio of the received signal intensities at (i, j) and $(i, j+1)$ is given as

$$\frac{P^{(i,j+1)}}{P^{(i,j)}} = \frac{\left({}_{\text{scat}}^{(i,j+1)} \right) r^{(i,j)} \sin\left({}_{\text{scat}}^{(i,j)} \right) T^{(i,j+1)}}{\left({}_{\text{scat}}^{(i,j)} \right) r^{(i,j+1)} \sin\left({}_{\text{scat}}^{(i,j+1)} \right) T^{(i,j)}} \tag{7}$$

If $\alpha_1^{(i,j)}$ is known, this equation can be used to calculate $\alpha_1^{(i,j+1)}$ from the bistatic lidar data. For this purpose, we define an error

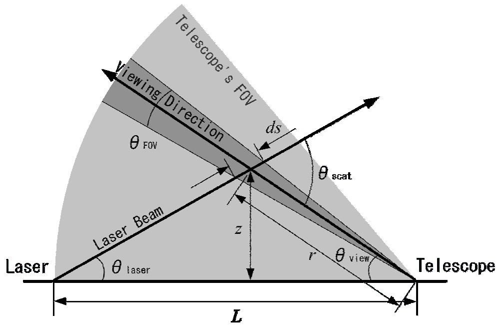

Fig.1 Schematic diagram of the bistatic measurement.

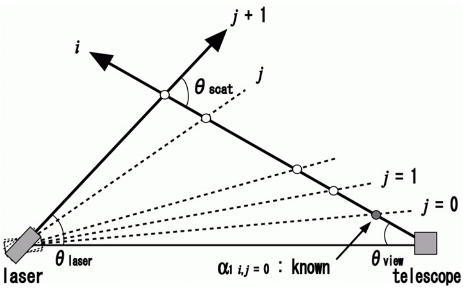

Fig.2 Schematic diagram of the inversion algorithm.

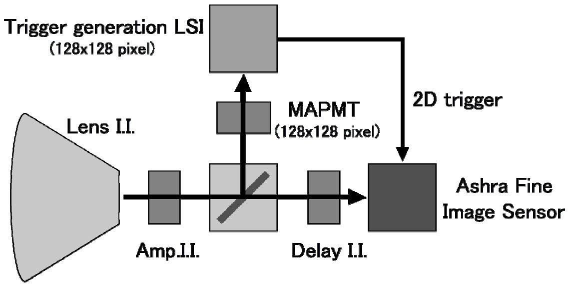

Fig.3 Schematic diagram of the imaging system of Ashra telescope with the intelligent trigger.

parameter ε as the difference between the calculated ratio and the observed ratio of the signal intensities:

$$\varepsilon = \frac{P_{\mathrm{obs}}^{(i,j+1)}}{P_{\mathrm{obs}}^{(i,j)}} - \frac{P^{(i,j+1)}}{P^{(i,j)}}. \tag{8}$$

Here, P_{obs} is the observed intensity and P is theoretically calculated using Eq.(1). The bisection method is employed to search the minimum value of $|\varepsilon|$ by changing $\alpha_1^{(i,\ j+1)}$. Since the boundary condition, $\alpha_1^{(i,\ 0)}$, can be obtained from the ground-based scattering measurement, the sequential application of the present procedure yields all the required values of $\alpha_1^{(i,\ j)}$. In practice, the application has to be iterative, since the value of the transmission T in Eq.(4) is improved successively: values of the optical thickness in Eq.(4) are re-calculated using the equations of

$$\tau_{\mathrm{t}}^{(i,j)} = \sum_{n=0}^{i-1} \frac{\alpha_1^{(n+1,j)} + \alpha_1^{(n,j)}}{2} \frac{z^{(n+1,j)} - z^{(n,j)}}{\sin(\theta_{\mathrm{laser}}^{j})}, \tag{9}$$

$$\tau_{\mathrm{r}}^{(i,j)} = \sum_{n=0}^{j-1} \frac{\alpha_1^{(i,n+1)} + \alpha_1^{(i,n)}}{2} \frac{z^{(i,n+1)} - z^{(i,n)}}{\sin(\theta_{\mathrm{view}}^{i})}, \tag{10}$$

where z is the height of the intersection point. The iterative calculation is repeated until the extinction coefficient at each intersection point converges.

3. Simulation

3.1 Signal-to-Noise Ratio

The schematic diagram of the imaging system of Ashra telescope is shown in Fig. 3. The image signal that passes through an amplification image intensifier (Amp. I.I.) is split into two paths. The first path is toward a Delay I.I. before reaching a fine image sensor, and the other path is connected to a multi-anode photo multiplier tube (MAPMT, 128 × 128 pixels). If the signal intensity detected by a certain pixel on MAPMT exceeds a trigger level, only a pixel region on the fine image sensor that corresponds to the pixel position on MAPMT is gated. The temporal width of the gate is determined by the time period in which the MAPMT pixel detects the signal (> a few ns). This operation minimizes the accumulation of sky background light on the fine image sensor, hence the S/N ratio is expected to increase significantly.

The estimation of the S/N ratio is conducted for the bistatic lidar system with and without the intelligent trigger. An example of the calculated S/N ratio is shown in Fig. 4. This simulation is based on a spectrum of daytime sky radiance reported by C.P. Jacovides et.al[8) and the aerosol extinction coefficient at the ground level of 1.0×10^{-4} m^{-1}. The vertical profile is proportional to an extinction profile model reported by Sasano[9). Figure 4 shows that the usage of the intelligent trigger enhances the S/N ratio by 2-3 orders of magnitude. A related advantage of the bistatic lidar measurement as compared with the monostatic case is the limited variation in the dynamic range of the signal intensity, which results in the ease in the detector design as a whole.

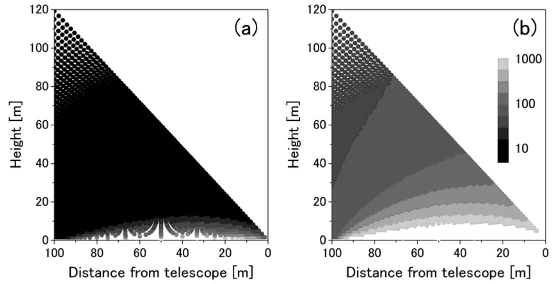

Fig.4 Two-dimensional distribution of the S/N ratio (a) without and (b) with gating (100 ns). The telescope is located at the point of 0 m viewing the FOV of 50 deg and the laser at that of 100 m. Following parameters are assumed in this calculation; laser power: 100 μJ/pulse, repetition rate: 3000 Hz, exposure time: 1 s.

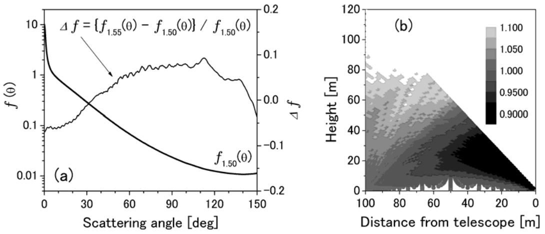

Fig.5 (a) Phase function assumed in the simulation data calculation, and difference between the one and that in the inversion. (b) Error distribution of the extinction coefficient.

3.2 Error estimation of retrieved extinction coefficient

In the inversion of lidar data, an assumption of a phase function is indispensable. The error arising from this assumption is evaluated using a simulation study. The simulation data is calculated as in the previous section. The phase function is obtained from the Mie scattering calculation with the urban model size distribution reported by Jaenicke[10] and the complex refractive index of $1.50 - 0.001i$. The inversion is conducted assuming a different phase function, i.e. the same size distribution but for different values of the complex refractive index, e.g. $1.55 - 0.001i$. These functions are shown in Fig.5(a). The distribution of the inversion error is obtained by comparing the assumed and the retrieved distributions of the extinction coefficient. Figure 5 (b) indicates that the resulting error is within a ±10% range.

4. Bistatic lidar measurement

The preliminary experiment of the bistatic lidar measurement has been conducted using a cooled CCD camera and a pulsed Nd:YAG laser (532 nm). Since the acceptance angel and the baseline distance are both insufficient, the experimental situation is rather limited as compared with the Ashra telescope case. Nevertheless, the two-dimensional measurement reveals the variation of the phase function (mostly from the Rayleigh signal) as expected from the theoretical consideration. The details will be discussed in the presentation at the conference.

Acknowledgment

The financial support from the Frontier Program of the Japan Promotion of Science and Technology Fund is gratefully acknowledged.

References

1. M. Sasaki, A. Kusaka, Y. Asaoka, Design of UHECR telescope with 1 arcmin resolution and 50° field of view, *Nucl. Instr. Meth. Phys. Res.* A492, 49-56 (2002).
2. M. Sasaki, Y. Asaoka, and M. Jobashi, "Self-triggered image intensifier tube for high-resolution UHECR imaging detector," *Nucl. Instr. Meth.* A501, 359-366 (2003).
3. Y. Arai, Y. Aita, T. Aoki, Y. Asaoka, et al. (co-authors: 33), "ASHRA Trigger and Readout Pixel Sensors," Proc. 28th International Cosmic Ray Conference (Tsukuba), 961 (2003).
4. Y. Aita, T. Aoki, Y. Arai, Y. Asaoka, et al. (co-authors: 33), "The ASHRA Detector," Proc. 28th International Cosmic Ray Conference (Tsukuba), 1061 (2003).
5. H. Kuze, S. Fukagawa, N. Takeuchi, Y. Asaoka, and M. Sasaki, "Development of a wide-area imaging lidar for atmospheric monitoring," 29th SICE Remote Sensing Symposium (Tsukuba), 61-64 (2003).
6. K. Meki, K. Yamaguchi, X. Li, Y. Saito, T.D. Kawahara, and A. Nomura, "Range- resolved bistatic imaging lidar for the measurement of the lower atmosphere," *Opt. Lett.* **21** (17), 1318-1320 (1996).
7. J.E. Barnes, S. Bronner, R. Beck, and N.C. Parikh, "Boundary layer scattering measurements with a charge-coupled device camera lidar," *Appl. Opt.* **42** (15), 2647-2652 (2003).
8. C.P. Jacovides, F. Timbios, D.N. Asimakopoulos, and M.D. Steven, "Urban aerosol and clear skies spectra for global and diffuse photosynthetically active radiation," *Agric. For. Meteorol.* **87**, 91-104 (1997).
9. Y. Sasano, "Tropospheric aerosol extinction coefficient profiles derived from scanning lidar measurement over Tsukuba, Japan, from 1990 to 1993, *Appl.Opt.*," **35** (24), 4941-4952 (1996).
10. R. Jaenicke, Tropospheric Aerosols, in "Aerosol-Cloud-Climate Interactions" (P.V. Hobbs, ed.), Academic, 1-31 (1993).

Mie-scattering simulation and measurement of mass extinction efficiency from portable automated lidar and suspended particulate matter measurements

Gerry Bagtasa [a],Nofel Lagrosas [a], Hiroaki Kuze [a], Nobuo Takeuchi [a],
Shunsuke Fukagawa [a], Yotsumi Yoshii [a], Suekazu Naito [b], Masanori Yabuki [c]

[a] *Center for Environmental Remote Sensing, Chiba University, 1-33 Yayoi-cho, Inage-ku, Chiba 263-8522, Japan*
[b] *Chiba Prefectural Environmental Research Center, 1-8-8 Iwasaki-nishi, Ichihara 290-0046, Japan*
[c] *National Institute of Polar Research, 9-10 Kaga 1-chome, Itabashi-ku, Tokyo 173-8515*

Abstract

The continuous operation of the portable automated lidar (PAL) and measurement of suspended particulate matter (SPM) results in the observation of the diurnal changes of the mass extinction efficiency (MEE). MEE is the ratio of the extinction coefficient to the SPM concentration which relates the amount of mass to the optical extinction of aerosols. Our results show that in the height region of 300 – 500 m, the daytime MEE values are smaller than the nighttime MEE values. This can be attributed to the aerosol growth (rapid growth) due to the higher relative humidity during nighttime.

Using the Mie scattering theory, a simulation study of MEE is also undertaken by computing the extinction coefficient from the 6-year averaged air sampling measurements in Chiba University. Hygroscopic effects on aerosols are considered in the simulation and results show that MEE increases with RH, in agreement with the observation stated above. When this type of direct effect of RH (rapid growth) is irrelevant, high and low MEE values can be ascribed to fine and coarse particles, respectively, for both measurement and simulation.

In addition, MEE values are computed for individual aerosol components (elemental carbon (EC), organic carbon, NH_4SO_4, NH_4NO_3, sea salt, soil, EC-NH_4SO_4 mixture), with EC having the highest computed MEE of 7.3 m^2g^{-1} and NH_4NO_3 with the lowest MEE of 1.2 m^2g^{-1}.

Keywords: Mass Extinction Efficiency, Lidar, Tropospheric aerosol, Mie scattering theory

I. INTRODUCTION

Aerosols and clouds play an important role in the radiation budget of the atmosphere. Atmospheric sensing using a compact, continuously operated lidar can lead to the real-time observation of the dynamics of the aerosols and clouds. One of the candidates of this type of remote sensing is the portable automated lidar (PAL) system, which is capable of real-time and unattended monitoring of the atmosphere.1) In this paper, we discuss the application of the PAL data to the monitoring of tropospheric aerosols.2) The inversion of the PAL data yields the vertical profile of the aerosol extinction coefficient. In the ground sampling, the aerosol quantity is often measured by the β-ray method as the suspended particulate matter (SPM) concentration. If the extinction coefficient values from the PAL data are matched with the ground-based SPM concentration measurements, the mass extinction efficiency (MEE) of the aerosols can be calculated.

II. Mass Extinction Efficiency

The MEE parameter links the mass amount to the optical extinction of the aerosols. Mathematically, the MEE is given by

$$MEE = \frac{\pi \int_{r_1}^{r_2} r^2 Q_{ext}(r,\lambda,m) n(r) dr}{\frac{4}{3}\pi\rho \int_{r_1}^{r_2} r^3 n(r) dr} \qquad (1)$$

where $Q_{\mathrm{ext}}(r,\lambda,m)$ is the extinction efficiency, r is the radius, λ is the wavelength, m is the refractive index, ρ is density, and $n(r)$ is the particle size distribution. The high and low values of the MEE are generally attributed to the presence of fine (roughly equivalent to PM2.5) and coarse particles (PM10 except the PM2.5 components). However, when the diameters of fine aerosols grow with relative humidity (RH), the efficiency of the particles to scatter light increases and this also leads to the increase in the MEE.

Figure 1 shows MEE values of different aerosol types as a function of size parameter x taken from various literatures.2)

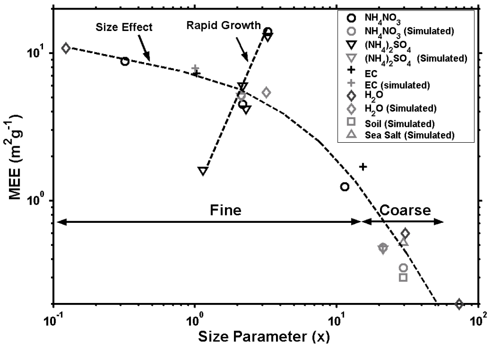

Fig. 1 MEE values as a function of size parameter from literature

It can be seen that MEE values decrease with increasing size parameter, hence the terminology of size effect. It has been pointed out that the lens effect associated with the particles of internal mixture greatly enhances the value of MEE.2) This is especially important for the soot aerosols surrounded by water (solution) droplet. On the other hand, MEE of a particular aerosol component may change due to a change in RH, and this is called the rapid growth. This latter effect is related to the rapid increase of $Q_{\mathrm{ext}}(r,\lambda,m)$ in a particular range of the size parameter (approximately $1<x<5$).

III. Setup

a) PAL System

The PAL system has been developed by CEReS, Chiba University, and operated at the Chiba Prefectural Environmental Research Center at Ichihara city (35.52N, 140.07E, about 40 km southeast of Tokyo). It is a compact Mie lidar system that can operate continuously and unattended for long periods of time. The system is equipped with an automatic re-alignment system that readjusts the laser direction every 15 minutes so that the proper system alignment is always maintained. Table 1 shows a more detailed specification of the PAL system.

Table 1: PAL Specification

Transmitter	
Laser	LD-pumped Q-switch Nd:YAG
Wavelength	532 nm
Repetition Rate	1.4 kHz
Laser Pulse Energy	15 µJ
Laser Beam Divergence	50 µrad
Receiver	
Telescope Diameter	20 cm
Telescope Type	Cassegrain
Field of View	0.2 mrad
Detector	PMT
Model	HPK-R1924P
Quantum Efficiency	10% - 25%

b) Low volume impactor

A three-stage low volume impactor (LVI) is used to characterize the local aerosol size distribution used for the present simulation. The air sampler is located at Chiba University and is able to measure mass concentration of elemental carbon (EC), organic carbon (OC), ammonium sulfate (NH_4SO_4), ammonium nitrate (NH_4NO_3), sea salt, and soil with aerodynamic sizes of less than 2.5 µm (PM2.5), 2.5 µm to 10 µm (PM10 excluding PM2.5) and greater than 10 µm. Only the measurements at PM2.5 and PM10 stages are used in the simulation.

IV. RESULTS

a) PAL - SPM counter

Each data set is composed of 12 points (one point per hour): the daytime data set is taken from 0600H to 1800H and nighttime data from 1800H to 0600H the following day. Data from January of 2003 to January of 2004 are analyzed. When there is a good correlation between the lidar-derived extinction coefficient and the ground-based SPM concentration measurements, the MEE for that data set is computed. High correlation coefficient (*R*>0.7) is usually obtained when there is a relatively clear atmosphere or high backscattered signal is detected.

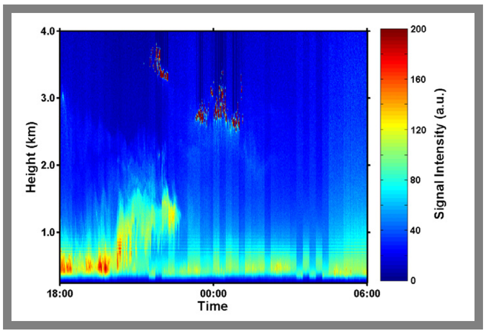

Fig. 2 Clear atmosphere range corrected Lidar data (13-14 Dec2003)

Figure 2 shows the range corrected PAL data taken on 13-14 of December 2003: this is considered clear data since no optically thick clouds are present near the ground. Fig. 3 shows the computed extinction coefficient from the same data set plotted against the SPM concentration measurement. The observed MEE value is 11.3 m^2g^{-1}.

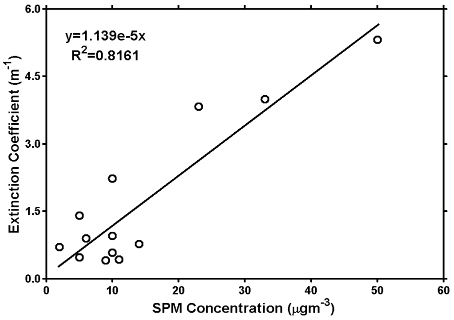

Fig. 3 Extinction coefficient vs. SPM concentration (13-14 Dec2003)

Figure. 4(a) shows lidar data of 1 April 2003. This data represents a high backscatter case due to the high signal intensity detected near the ground. Fig. 4(b) shows the extinction coefficient plotted with SPM concentration giving an MEE value of 8.1 m^2g^{-1}.

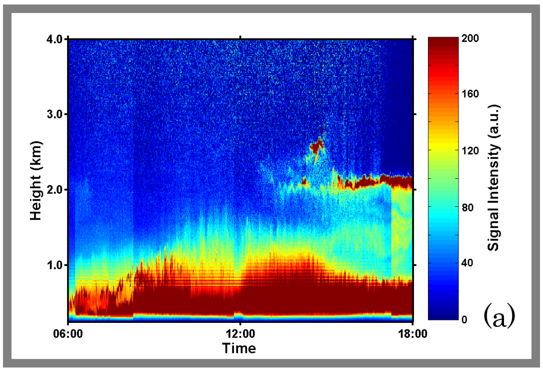

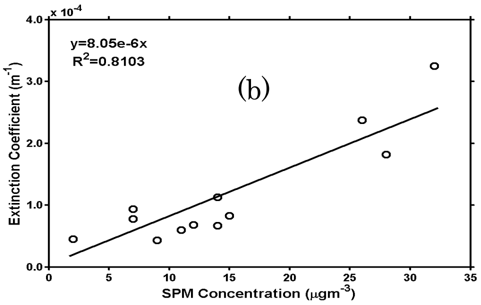

Fig. 4 (a) Range corrected PAL data, and (b) extinction coefficient vs. SPM concentration (1April 2003)

Table 2 shows the average MEE values and average relative humidity for all the analyzed data sets.

Table 2 Average (standard deviation) mass extinction efficiency (in m^2g^{-1}) and relative humidity (RH)

	Daytime	Nighttime
Relatively Clear	7.9 (5.2)	13.0 (6.2)
Average RH	56%	74%
High Backscatter	5.4 (4.0)	11.0 (7.6)
Average RH	71%	81%

Our results show that MEE values range from approximately 4-13 m^2g^{-1}. Generally, nighttime data sets yield a higher MEE values than the daytime data: this can be attributed to the Rapid Growth, due to the higher observed average relative humidity during nighttime.

Figure 5 shows the variation of the average extinction coefficient with relative humidity. Below around 70% RH, the lidar-derived extinction coefficient values appear not to change very much, whereas above 70% RH, it is seen that the extinction coefficient increases with RH. This is attributed to the aerosol growth (rapid growth).

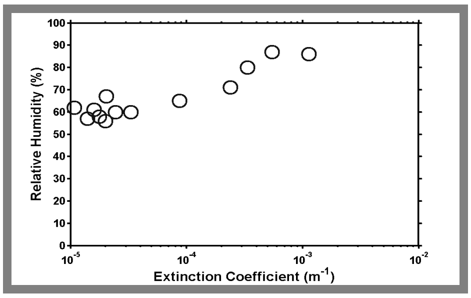

Fig. 5 Relative Humidity vs. Extinction Coefficient

Figure 6 shows the observed MEE plotted against the coarse particle concentration. The MEE value decreases with increasing amount of coarse particles, which correspond to the size effect shown in fig. 1.

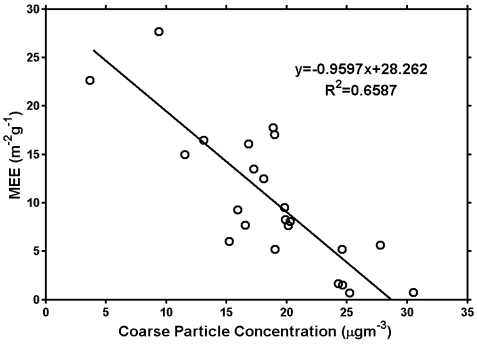

Fig. 6 MEE vs. Coarse SPM concentration

b) Simulation based on Mie scattering theory

The 6-year data of mass concentration measurements from the LVI is used to model the local aerosol size distribution in the Chiba city area for each of the following aerosol components: EC, OC, NH_4SO_4, NH_4NO_3, sea salt, soil and EC-NH_4SO_4 mixture.

From the derived size distributions, MEE value for each aerosol component can be computed using Eq. (1). Table 3 shows the result for each aerosol component. It is noted that although the MEE of a specific aerosol component remains constant regardless of the size distribution, the total MEE varies with the size distribution.

Table 3: Simulated MEE for each aerosol type

Aerosol Type	Computed MEE (m^2g^{-1})
EC	7.290
OC	2.092
NH_4SO_4	3.516
NH_4NO_3	1.194
Sea Salt	1.273
Soil	1.224
EC – NH_4SO_4 mixture	4.606

Figure 7 shows the total MEE of the 6-year average mass concentration measurement by the LVI with varying amounts of RH. There is a significant increase in the MEE value when the RH reaches 70%, which is the point where aerosols start to be coated with water. MEE value increases up to almost 300% when RH reaches 90%. This result verifies the higher MEE values observed during nighttime.

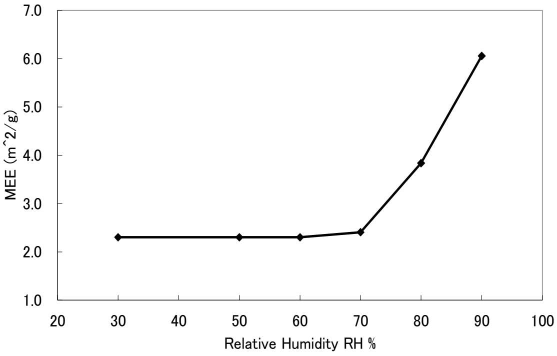

Fig. 7 MEE vs. RH Simulation

V. CONCLUSION

This study has shown that the continuous operation of the portable automated lidar (PAL) system has the capability of observing the dynamics of atmospheric aerosols. The correlation study shows that MEE observed during nighttime is generally higher than MEE observed during daytime, suggesting the influence of higher average relative humidity during nighttime. Simulations using the Mie Scattering theory support this observation: by varying the amount of relative humidity, it is shown that MEE increases with RH. Also, our simulation reveals elemental carbon (EC) as one having the highest MEE value of 7.3 m^2g^{-1}: this result is to be expected since EC has one of the highest imaginary refractive index, consequently the highest extinction.

REFERENCES

1) N. Lagrosas, Y. Yoshii, H. Kuze, N. Takeuchi, S. Naito, A. Sone, H. Kan (2004) Observation of boundary layer aerosols using a continuously operated portable lidar system, Atm. Environ. 38, 3885-3892.

2) N. Lagrosas, H. Kuze, N. Takeuchi, S. Fukagawa, G. Bagtasa, Y. Yoshii, S. Naito, M. Yabuki (2004) Correlation study between suspended particulate matter and portable automated lidar data, Aerosol Science., in press.

3) Yabuki, M. (2003) Study on algorithms for deriving optical parameters of tropospheric aerosols (in Japanese). Ph.D. thesis, Chiba University

4) Bohren, C.F., Huffman D.R. (1983) Absorption and scattering of light by small particles, New York Wiley

5) I. Tang (1996) Chemical and size effects of hygroscopic aerosols on light scattering coefficients, Journal of Geophysical Research, 101, 19245-19250.

Net Radiation Estimation Using MODIS-TERRA Data for Clear Sky Days Over Homogeneous Areas in Mongolia

J. Batbayar[1], S.Tuya[2], N. Tugjsuren[3]

[1] *Department of atmospheric physics, Mongolian University of Science and Technology*
[2] *Center for Environmental Remote Sensing (CEReS), Chiba University, JAPAN*
[3] *Mongolian University of Science and Technology, School of Materials science*

Abstract

Satellite remote sensing to estimate net radiation is essential to obtain the global energy budget. The net radiation is key role-played for the monitoring of surface energy budget. Much of heat comes from radiant energy initially provided by the absorption of solar radiation. The energy is used to warm of climate system, evaporate water and variation of the environmental processes.

The objective is to estimate instantaneous distribution of the net radiation over a large homogeneous areas in Dundgovi province of Mongolia, from the Moderate Resolution Imaging Spectroradiometer (MODIS). For this study, we used the parametrization scheme for downward short wave radiation have been developed by Nimelä et al. (2001) and for downward long wave radiation developed by Prata (1996). In this paper presented the results of estimation of the net radiation and satellite image analyses for homogeneous land surface in semi-arid and arid environment of Mongolia. Estimated incoming short wave and long wave radiations using MODIS-TERRA and ground data compared with experimental station data in Dundgovi aimag of Mongolia.

Key words: solar radiation, net radiation, longwave radiation, shortwave radiation, emissivity, albedo

INTRODUCTION

Solar radiation is primary resource of heat of the earth and atmosphere and plays an important role in air-land surface interactions; agriculture, pasture and energy from biomass, because the growth of biomass directly depends on the photosynthesis and therefore on solar radiation. The success of satellite remote sensing arises from that fact that it can provide an unparalleled spatial and temporal coverage of the globe. To benefit from this tool, research is being directed to develop better understanding of land-atmosphere interactions.

Last years several studies have attempted to estimate net radiation (or its components) by combining remote sensing observations with ancillary surface and atmospheric data (Gautier et al., 1980; Diak and Gautier, 1983; Jacobs et al., 2000; Ma et al., 2002). Recently, several parameterization schemes have been developed to estimate short wave and long wave fluxes (Niemelä et al., 2001a; Niemelä et al., 2001b; Ellingson, 1995 and Pinker et al., 1995). The climate of Mongolia has characterized by a high moisture deficit, low humidity and low levels of incident energy. Despite 260 days (mo than 3000 hours) of sunshine, total heat units above 10^0C rarely exceed 2000 and in some areas less than 1000. Snow cover is very light so soils are completely frozen in the winter. As a consequence the effective vegetation growing period is short, generally from 80 to 100, days although it can vary from 70 to 130 days depending on latitude and location (Batjargal. Z, 2001). The pastureland and agricultural areas occurs about 80 % of total territory of Mongolia and the main economic branch of our country is the agriculture and pastoral husbandry. Mongolian agriculture is strongly dominated by the geographical location and its climate. Spring and summer seasons have a long daytime and sunshine, while winter has a short day time but lmost all clear days due to high pressure systems (Tugjsuren. N et al., 2002). Many agricultural and pastoral management applications require the knowledge of surface radiation balance over a range of temporal and spatial scales in Mongolia.

The research of solar radiation species incoming into land surfice and its variability features is very important for agriculture for continental climate of Mongolia (Tugjsuren. N, 1991).

In this paper, we have attempted to estimate instantaneous distribution net radiation from remotely sensed data over homogeneous areas for clear sky days in Mongolia.

STUDY SITE

The study site is Dundgovi aimag (province) of Mongolia. The coordinates are $44^0 00'$N and $46^0 00'$N, $103^0 00'$E and $109^0 00'$E, and the area is 78 thousand km^2 an arid and semi-arid region. Annual mean precipitation is about 150-250 mm and 85-90 percent of the annual precipitation falls as rain during the summer of which 50-60% in July and August. Cloudy skies are infrequent, and 4,467 hours of sunshine per year giving a total annual solar radiation input of 7,793 MJ m^{-2}.

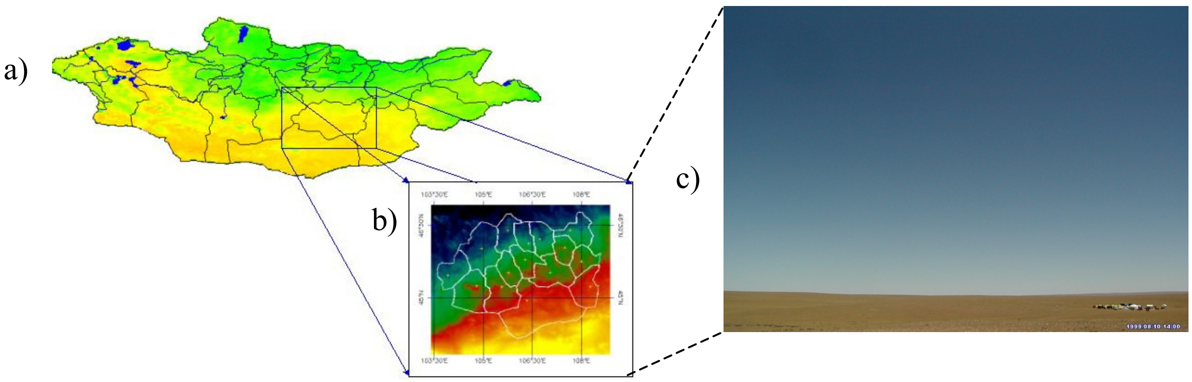

Fig.1. Study site. a) Mongolian territory, b) Study area of Dundgovi province, c) View of homogeneous area in Mandalgovi province

METHODOLOGY

Instantaneous net radiation (INR) estimates are obtained using various MODIS-Terra land products (land surface temperature, land surface emissivities and land surface albedo). Niemelä's (2001) and Prata's (1996) parameterization schemes are used to estimate downward short wave and long wave flux and air emissivity respectively.

Instantaneous net radiation

Net radiation (Rn) is given by the surface radiation balance can be expressed in terms of its components as:

$$R_n = R^{\downarrow}_s - R^{\uparrow}_s + R^{\downarrow}_L - R^{\uparrow}_L \qquad (1)$$

where $R^{\downarrow}_s$ and $R^{\uparrow}_s$ are short wave radiation fluxes downward (Wm^{-2}) and upward (Wm-2) respectively and $R^{\downarrow}_L$ and $R^{\uparrow}_L$ are the long wave radiation fluxes downward (Wm^{-2}) and upward (Wm^{-2}) respectively.

Short wave downward radiation

The short wave radiation can be expressed as:

$$R^{\downarrow}_s - R^{\uparrow}_s = (1-\alpha) R^{\downarrow}_s \qquad (2)$$

where α is land surface albedo

In the calculation of downward short wave radiation ($R^{\downarrow}_s$) we used the parameterization scheme developed by *Niemel et al.,* 2001. The downward short wave radiation can be expressed as:

$$R^{\downarrow}_s = S_o \tau_{sw} \cos\theta \qquad (3)$$

where τ_{sw} is the atmospheric clear sky short wave transmission factor, S_o is the solar constant at the atmospheric top, which is about 1367 Wm^{-2} and θ is the solar zenith angle.

The long wave radiation can be expressed using the Steffan-Boltzmann equation as:

$$R^{\downarrow}_L - R^{\uparrow}_L = \sigma\varepsilon_a T^4_a - \sigma\varepsilon_s T^4_s \qquad (4)$$

where ε_a is air emissivity, ε_s is surface emissivity, Ta is air temperature (Kelvin), Ts is land surface temperature (Kelvin) and $\sigma = 5.67 \times 10^{-8}\ W\ m^{-2}\ K^{-4}$ is the Steffan-Boltzmann constant.

Long wave upward radiation

Hence, long wave upward radiation can be expressed as.

$$R^{\uparrow}_L = \sigma\varepsilon_s T^4_s$$

In this case, surface emissivity (ε_s) is estimated using NDVI and an empirically-derived method in SEBAL (Van de Griend and Owe, 1993), as following.

$$\varepsilon_s = 1.009 + 0.047\ \mathrm{In}(NDVI) \qquad (5)$$

where NDVI > 0

And, surface temperature (T_s) was computed based on formulation proposed by Price (Price, 1984). The formula is expressed as follows:

$$T_s = BT_{31} + 3.33(BT_{31} - BT_{32}) \qquad (6)$$

where BT_{31} and BT_{32} brightness temperatures from MODIS channels 31 and 32, respectively.

Long wave downward radiation

Further, we used which *Prata* (1996) developed a parameterization scheme for long wave downward radiation using vapor pressure and air temperature.

Prata's downward long wave radiation ($R^{\downarrow}_L$) is defined as

$$R^{\downarrow}_L = \sigma\varepsilon_a T^4_a \qquad (7)$$

where $\varepsilon_a = [1-(1+\xi)\ exp\{-(1.2+3\xi)^{1/2}\},$ and $\xi=46.5e_o/T_a$

IMAGE ANALYSES AND RESULTS

MODIS TERRA data (22 July, 5 and 25 August, 4. 14, 21, 28 September) were used in this study. We used 1 km resolution data and broad bands albedo for ch. 1-5, 7; brightness temperature for ch. 31, 32 of MODIS TERRA for the image processing. The images were processed 7 times during the period of end of July to September in 2002. Also we have determined and processed that images as follows:

a) Land surface albedo α, for estimation shortwave downward radiation

b) NDVI, surface emissivity $\varepsilon_{s,}$ surface temperature T_s for estimation longwave upward radiation

In the table 1. illustrated estimated values NDVI, surface albedo α, surface emissivity $\varepsilon_{s,}$ surface temperature T_s on the selected points of the Dundgovi province from processed images on dated 22 July, 25 August and 21 September, 2002

Figure 2 shows a distribution of shortwave downward radiation in 22 July, 25 August and 21 September, 2002 by MODIS TERRA. Around in this dated, the shortwave downward radiation value was around 704.1 – 969.8 Wm^{-2}. The shortwave downward radiation higher value shows in July and low value in September.

Figure 3 shows a distribution of longwave upward radiation in 22 July, 25 August and 21 September, 2002 by MODIS TERRA. In the images shortwave downward radiation value was around 325.8 – 549.9 Wm^{-2}. The longwave upward radiation higher value shows in August and low value in July.

The instantaneous distribution of net radiation in the above mentioned dated by MODIS TERRA showing in Fig. 4. As seen this figure the net radiation value was around 432.6 – 817.6 Wm^{-2}. The net radiation value in July seems larger than in September for homogeneous area of Dundgovi province.

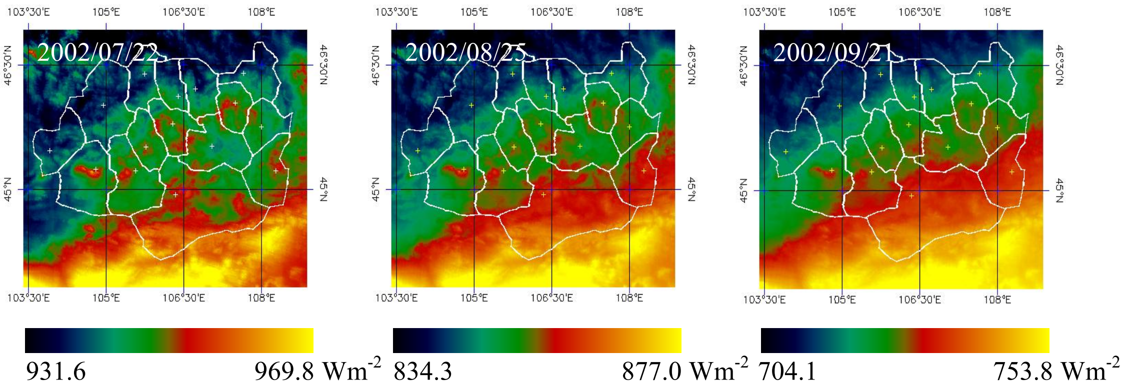

Fig. 2. Instantaneous shortwave downward radiation from MODIS-TERRA data

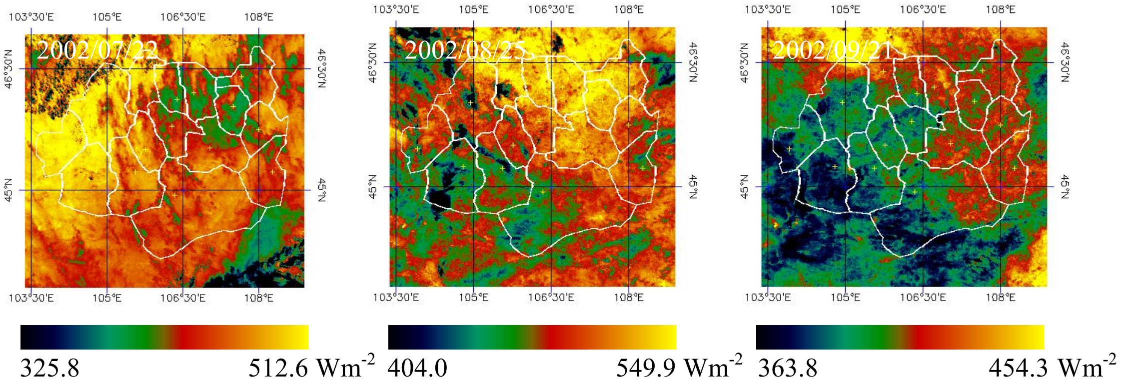

Fig. 3. Instantaneous longwave upward radiation from MODIS-TERRA data

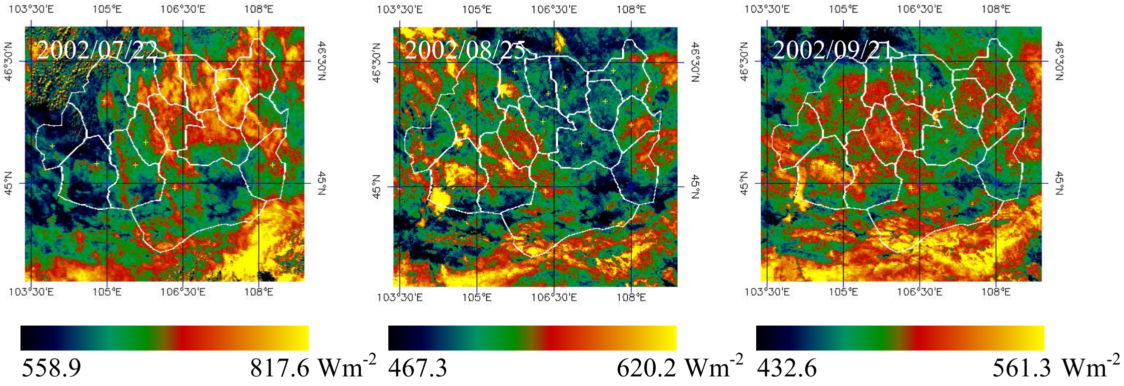

Fig. 4. Instantaneous net radiation from MODIS-TERRA data

Tab.1. Estimated land surface parameters using MODIS TERRA data on the selected points.

Points	**Lat/ Long**	**Albedo, α**			**NDVI**			**Emissivity, ε_{σ}**			**Temperature, T_s, C^0**		
		7/22	8/25	9/21	7/22	8/25	9/21	7/22	8/25	9/21	7/22	8/25	9/21
Mandalgovi	45.46 106.17	0.18	0.17	0.16	0.17	0.17	0.14	0.93	0.92	0.91	27	41	23
Saikhan-Ovoo	45.44 103.89	0.16	0.16	0.15	0.10	0.07	0.08	0.90	0.89	0.89	49	29	22
Adaatsag	46.22 105.46	0.15	0.16	0.14	0.24	0.26	0.16	0.94	0.94	0.92	28	43	26
Bayanjargalan	45.45 108.00	0.14	0.16	0.13	0.12	0.15	0.13	0.91	0.92	0.91	33	40	25
Olziit	44.56 106.20	0.16	0.16	0.15	0.08	0.11	0.10	0.89	0.90	0.90	41	40	23

Fig. 5. and Fig. 6 shows trend of estimated and observed downward radiation fluxes from 22 July to 21 September, 2002. According to the scatter graphs for comparison of estimation and observed downward short and long wave radiation shown in Fig.7 and Fig 8. A better relationship is seen in the between estimated and observed short and long wave downward radiation in study area. But should be noted that relationship is only for value at experimental station in Mandalgovi. The regression line in the above mentioned dated is E = 1.1308x + 50.357 and R^2 = 0.8341 for shortwave downward radiation and E = 0.9182x + 29.02, and R^2 = 0.7246 for longwave downward radiation.

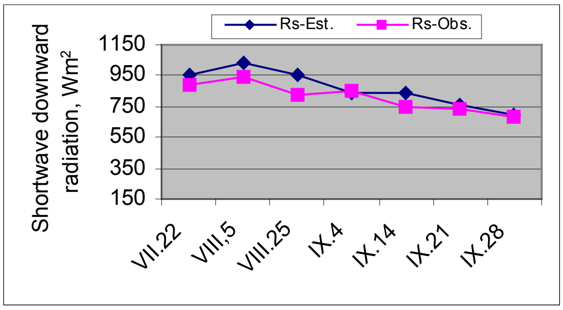

Fig.5. Estimated and observed shortwave downward radiation from July to September in 2002 at the experimental station in Mandalgovi.

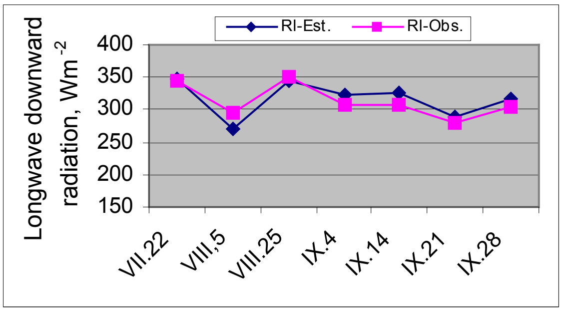

Fig.6. Estimated and observed longwave downward radiation from July to September in 2002 at the experimental station in Mandalgovi.

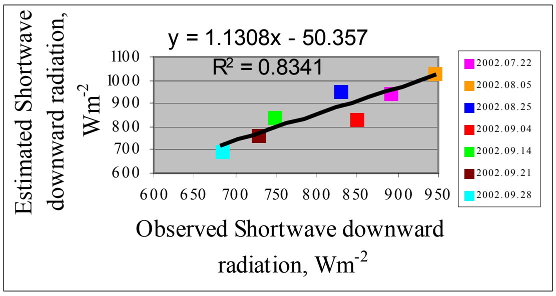

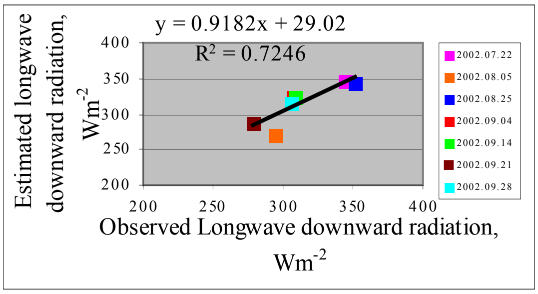

Fig.7. Comparison of estimated and observed shortwave downward radiation from July to September in 2002 at the experimental station in Mandalgovi.

Fig.8. Comparison of estimated and observed longwave downward radiation from July to September in 2002 at the experimental station in Mandalgovi.

CONCLUSION

In the present study, MODIS TERRA satellite and ground data were used in estimating the instantaneous distribution of the net radiation in homogeneous area of Mongolia using the parameterization schemes for short wave radiation fluxes downward and long wave radiation fluxes downward.

We obtained better results between estimated short wave downward radiation (R^2=0.8341) and longwave wave downward radiation (R^2=0.7246) with the observed data. However, we did not compared the estimated net radiation, due to insufficient of real measured net radiation data on the ground. To overcome this problem, measured value of net radiation on the ground are required to validate the results of estimation instantaneous net radiation using satellite data.

The study was one of first attempth to estimate instantaneous distribution net radiation using satellite and ground data. However, the study results are gave better understanding of the instantaneous distribution of net radiation in homogeneous area of Mongolia. We should improve the research for net radiation using satellite data in further.

Acknowledgements

We would like to thank to Prof. Takamura Tamio and Mr. Itari Okada of Atmospheric Radiation Division of CEReS of Chiba University, for providing with the observed data at the Experiment Station in Mandalgovi province of Mongolia.

References

1. Batjargal, Z. (2001). Desertification in Mongolia. *RALA Report No.200*
2. Diak, G. R., & Gautier, C. (1983). Improvements to a simple physical model for estimating insolation from GOES data. *Journal of Climate and Applied Meteorology,22*, 505-508.
3. Gautier, C., Diak, G., & Masse, S. (1980). A Simple Physical Model to Estimate incident Solar Radiation at the Surface from GOES Satellite Data. *Journal of Applied Meteorology, 19*, 1005-1012.
4. Ellingson, R. G. (1995). Surface Longwave Fluxes from Satellite Observations: A critical review. *Remote Sensing of Environment, 51*, 89-97.
5. Gautier, C., Diak, G., & Masse, S. (1980). A Simple Physical Model to Estimate Incident Solar Radiation at the Surface from GOES Satellite Data. *Journal of Applied Meteorology, 19*, 1005-1012.
6. Jacobs, J. M., Myers, D. A., Anderson, M. C., & Diak, G. R. (2000). GOES surface insolation to estimate wetlands evapotranspiration. *Journal of Hydrology*, *266*, 53-65.
7. Ma, Y., Su, Z., Li, Z., Koike, T., & Menenti, M. (2002). Determination of regional net radiation and soil heat flux over a heterogeneous landscape of the Tibetan Plateau. *Hydrological Processes, 16*, 2963 - 2971.

8. Niemelä, S., Räisänen, P., & Savijärvi, H. (2001a) Comparison of surface radiative flux parameterizations Part I: Longwave radiation. *Atmospheric Research, 58*, 1-18.
9. Niemelä, S., Räisänen, P., & Savijärvi, H. (2001b). Comparison of Surface radiative flux parameterizations Part II: Shortwave radiation. *Atmospheric Research, 58*, 141- 54.
10. Pinker, R. T., Frouin, R., & Li, Z. (1995). A Review of Satellite Methods to Derive Surface Shortwave Irradiance. *Remote Sensing of Environment, 51*, 108-124.
11. Prata, A. J. (1996). A new long-wave formula for estimating downward clear-sky radiation at the surface. *Quarterly Journal of the Royal Meteorological Society, 122,* 1127-1151.
12. Price, J. C., (1984) Land surface temperature measurements from the split window channels of the NOAA 7 Advanced Very High Resolution Radiometer. *Journal of Geophysical Research, 89,* 7231-7237.
13. Tugjsuren, N. (1991). Solar radiation distribution feature in Mongolia. *Bulletin of Science and Information Center, Mongolia, 150/1.*
14. Tugjsuren, N., Takamura, T. (2001). Investigation for photosynthetically active radiation rejime in the Mongolian grain farm region, *Journal of Agric. Meteorol., 57(4)*, 201-207.
15. Van de Griend, A. A., and Ome, M. (1993). On the relationship between thermal emissivity and the normalized difference vegetation index for natural surfaces. *Int. Jour. of Remote Sensing, vol 14(6),* 1119-1131.

Measurement of NO_2, SO_2, O_3, H_2O and aerosol in the troposphere using differential optical absorption spectroscopy (DOAS)

Toru Kimura, Toyofumi Umekawa
Kyoto Electronics Manufacturing Co.,Ltd.
68 Ninodan-cho, Kisshoin Minami-ku, Kyoto 601-8317, Japan
Si Fuqi, Hiroaki Kuze, Nobuo Takeuchi
Center for Environmental Remote Sensing, Chiba University
1-33 Yoyoi-cho, Inage-ku, Chiba 263-8522, Japan

Abstract

We report on air-pollution monitoring campaign in the Kyoto and Chiba area during 2004. With differential optical absorption spectroscopy (DOAS) method, average concentrations of NO_2, SO_2, O_3, H_2O and aerosol particles can be measured. For NO_2, SO_2, O_3 and H_2O, the DOAS results are found to be consistent with the results of the ground sampling measurements. For aerosol, the optical thickness at 550 nm is correlated with the concentration of ground-measured suspended particulate matter (SPM), leading to a good correlation between the DOAS and SPM data. Also, the mass extinction efficiency (MEE) is analyzed for aerosol particles in the lower troposphere. From Chiba measurements, it is found that the average MEE is about 7.6 m^2g^{-1}, and the value exhibits a good inverse correlation with the particle size.

Kyewords: air pollution, mass extinction efficiency, Aerosol, Extinction coefficient

1. Introduction

The technique of differential optical absorption spectroscopy (DOAS) is widely used to monitor atmospheric pollutant species such as NO_2, NO, SO_2, and O_3.[1-3] These molecular species exhibit characteristic absorption patterns in the visible and UV parts of the spectrum. By using the path length of a few kilometers, and by extracting the absorption features that vary rapidly with the wavelength, the DOAS method enables the retrieval of molecular concentrations of the order of ppb.

In the present paper, we describe our recent DOAS results measured in Chiba and Kyoto urban regions. The Chiba data are based on the novel method of pulsed DOAS, in which an aviation obstruction light is utilized as the light source.[3] Figure 1 shows a schematic of the experimental setup. The path length is about 5.5 km, and the wavelength range covered in this experiment is about 300-800 nm. From Chiba data, the absorption of NO_2, H_2O, and the extinction due to aerosol particles are investigated. The measurement of aerosols is feasible by monitoring the change in the received intensity, since if the alignment of the system is sufficiently stable, the intensity change is brought about solely from the variation of aerosol quantity along the light path. The monitoring of H_2O along the path is important from the viewpoint of the increase in the aerosol extinction efficiency due to high relative humidity.[4] The

Kyoto system, on the other hand, is operated with a cw light source dedicated to the DOAS measurement, with a distance of 2.4 km. The operational wavelength range is extended to 280 nm, thus making it possible to observe the absorption of SO_2, O_3, and NO_2 simultaneously.

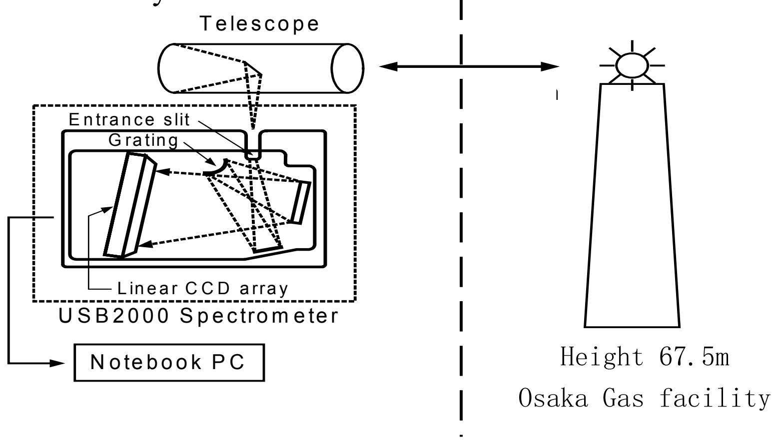

Fig. 1 Experimental setup for measuring NO_2, H_2O, and aerosol extinction.

2. DOAS spectrum

2.1 Retrieval of NO_2, SO_2, O_3 and H_2O retrieval

In the Chiba measurement (resolution = 0.3 nm/channel), the wavelength range of 400-450 nm is used for NO_2, 500-550 nm for aerosol, and 710-740 nm for H_2O. In the Kyoto measurement (resolution = 0.11 nm/channel), NO_2 is measured in a wavelength range of 350-360 nm, O_3 in 280-290 nm, and SO_2 in 295-305 nm.

The analysis of the DOAS spectra is based on the Beer-Lambert's law expressed as

$$I(\lambda) = kI_0(\lambda)e^{-L\sigma(\lambda)n}, \tag{1}$$

where k is the system constant, $I(\lambda)$ is the measured intensity, $I_0(\lambda)$ the unattenuated reference intensity, L the path length, $\sigma(\lambda)$ the wavelength-dependent absorption cross section, and n the number density of the species. The dimensionless quantity $\tau = L\,\sigma\,n$ is referred to as the optical thickness.

In the real atmosphere both molecules (Rayleigh scattering) and aerosols (Mie scattering) contribute to the radiation extinction. Adding these contributions to eq. (1) gives

$$\tau(\lambda) = \ln\frac{I_0(\lambda)}{I(\lambda)} = L\big(\sigma(\lambda)n + \varepsilon^{\mathrm{M}}(\lambda) + \varepsilon^{\mathrm{A}}(\lambda)\big) - \ln k\,. \tag{2}$$

Here $\varepsilon^{M}(\lambda)$ is the molecular extinction coefficient which is the product of the molecular cross section, $\sigma^{M}(\lambda)$, and the number density of air molecules, n_m. Similarly, the aerosol extinction coefficient, $\varepsilon^{A}(\lambda)$, is defined as $\sigma^{A}(\lambda)n_a$, where $\sigma^{A}(\lambda)$ is the aerosol cross section, and n_a the number density of the aerosol particles.

Cross sections in eq.(2) can be separated into two components, slowly varying one, $\sigma_i^s(\lambda)$, and rapidly varying one, $\sigma_i'(\lambda)$, with wavelength. Both the molecular and aerosol cross sections are slowly varying components of the optical thickness. Hence we obtain

$$\tau(\lambda) = L\sum_i \sigma_i'(\lambda) n_i + L\left(\sum_i \sigma_i^{\mathrm{s}}(\lambda) a_i + \sigma^{\mathrm{M}}(\lambda) n^{\mathrm{M}} + \sigma^{\mathrm{A}}(\lambda) n^{\mathrm{A}}\right) - \ln k, \qquad (3)$$

where subscript *i* denotes trace gas species such as NO_2, O_3 or SO_2. On the right-hand side of eq. (3), the first term describes the rapidly varying part, and the second the slowly varying part.

2.2 Aerosol retrieval and MEE

The aerosol optical thickness α_a can be defined as

$$\tau_a = \alpha_a L = \ln kI_0(\lambda) - \ln I(\lambda) - \tau_{\mathrm{Rayleigh}}(\lambda) - \tau_{\mathrm{gas}}(\lambda), \qquad (4)$$

where *I*, τ_{Rayleigh} and τ_{gas} can be obtained from the analysis of DOAS signals. After removing contributions of the gas absorption and Rayleigh scattering, we can determine the aerosol optical thickness if the correlation factor *k* is known. The visibility at 550 nm, *V*, can be calculated from Mie extinction coefficient using the well known Koschmieder relationship:

$$V = 3.912/\alpha_a. \qquad (5)$$

Here we assume that the visibility of $V = 50$ km represents a typical condition for a relatively clear atmosphere. Since in the Chiba case, the distance of the DOAS measurement is 5.5 km, V=50 km leads to the aerosol optical thickness of $\tau_a = 0.43$. This value is used to empirically determine the system constant *k*. It is noted that when the value of *V* is changed by ±10%, for instance, the resulting value of *k* changes only slightly (k=9.0±0.2).

The basic principle of the aerosol retrieval was described in our previous paper (Yoshii et al., 2003). The following dependence on the wavelength λ is assumed for the aerosol optical thickness $\tau_a(\lambda)$:

$$\tau_a(\lambda) = B\left(\frac{\lambda}{550}\right)^{-A} \qquad (6)$$

Here, constants *A* (Angstrom exponent) and *B* (turbidity constant, i.e. the aerosol extinction coefficient corresponding to the wavelength of 550 nm) are to be determined by fitting this expression to the optical thickness derived from the DOAS spectra. The aerosol extinction coefficient at 550 nm is calculated by the relationship of $\alpha_a(550) = B/L$, and the mass extinction efficiency (MEE) is obtained by

$$\mathrm{MEE} = \alpha_a(550)/\rho, \qquad (7)$$

where ρ is the SPM concentration measured by the ground sampling (with a β-ray detector).

3. Results and discussion

3.1 Concentration of NO_2 from DOAS and ground point measurements

In the Kyoto measurement, we measured O_3, SO_2, NO_2, and aerosols. The Chiba measurement, on the other hand, is used for the retrieval of NO_2, H_2O, and aerosols. Figure 2(a) shows the NO_2, SO_2, O_3 data observed for one day in Kyoto, and Fig. 2 (b) shows H_2O and absolute humidity observed for one month in Chiba. From these figures, reasonable correlations are found between the result of the long-path DOAS measurement and the data from ground stations below the optical paths.

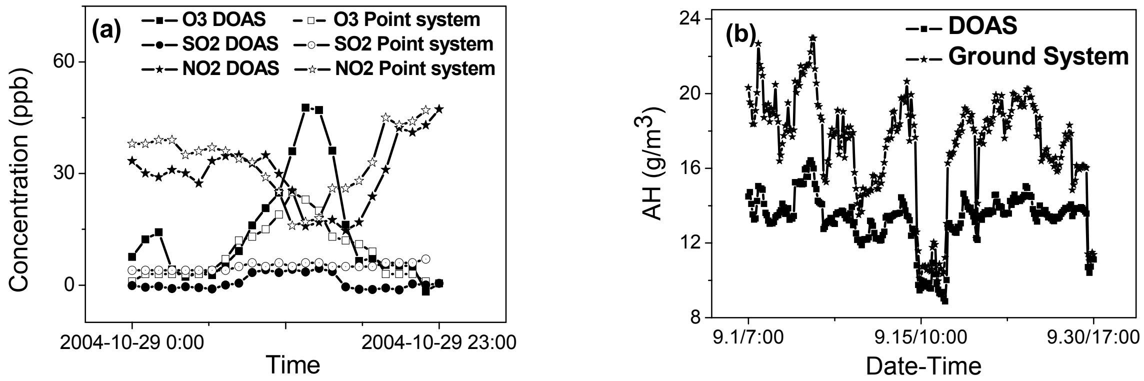

Fig. 2. (a) One day change of NO_2, SO_2 and O_3 concentration observed in the Kyoto measurement on 29 October 2004. (b) One month change of absolute humidity measured by the DOAS and ground systems in Chiba.

3.2 Aerosol retrieval

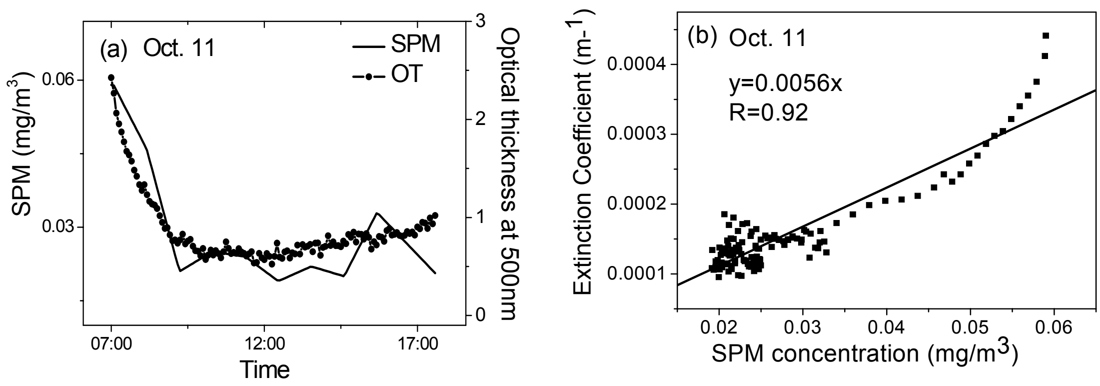

Fig. 3. (a) Optical thickness at 550 nm data and SPM data on 15 December 2004, and (b) the correlation plot to derive the MEE value (5.6 m^2g^{-1}).

Here we describe the aerosol retrieval from the Chiba data. Figure 3(a) shows the correlation between the SPM concentration and aerosol optical thickness at 550 nm and Fig. 3(b) the correlation between the SPM concentration and aerosol extinction coefficient in a day (daytime). For both cases, good correlations are evident, and the MEE value is calculated to be about 5.6 m^2g^{-1}. The variations of MEE and the

Angstrom exponent during one month are shown in Fig. 4, in which a data point represents an average of the diurnal data. Also a good correlation can be found between these two parameters. The Angstrom exponent is a good measure of the particle size, high and low values suggesting the dominance of fine and coarse particles, respectively. This result indicates well that the particle size is influential to the value of MEE, as recently proposed as the size effect on the MEE value.4)

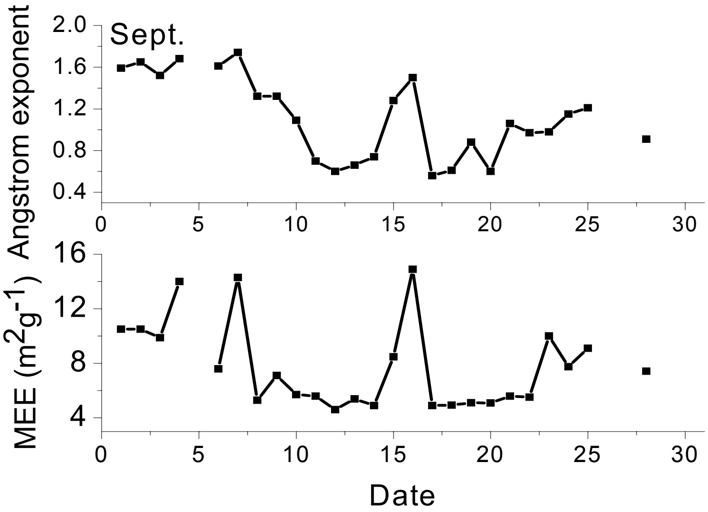

Fig. 4 One month variation of the MEE and Angstrom exponent, leading to a correlation coefficient of about 0.83. The average value for the MEE data is about 7.6 m^2g^{-1} and that for the Angstrom exponent is 1.1.

4. Conclusion

We have applied the pulsed DOAS technique to the measurement of NO_2, SO_2, O_3, H_2O and aerosol particles. Through the Kyoto and Chiba campaigns, reasonable correlations have been found between the long-path and ground-based observations of the NO_2, SO_2, O_3 and H_2O concentrations. For aerosol retrieval, the optical thickness at 550 nm is correlated with the concentration of ground-measured suspended particulate matter (SPM), also leading to a good correlation between the DOAS and SPM data. This correlation makes it possible to analyze the mass extinction efficiency (MEE) of aerosol particles in the lower troposphere. It is found that the monthly average value of MEE in Chiba (September 2004) is about 7.6 m^2g^{-1}. This relatively high value of MEE suggests the dominance of fine aerosols, though additional effect of the humidity should also be considered.

Acknowledgements

The authors are grateful to Mr. T. Tsutsui and Mr. K. Yamakawa of Kyoto Prefectural Institute of Hygienic and Environmental Sciences for the cooperation in the Kyoto campaign during the winter in 2004. This work is supported by the

Organization for Small & Medium Enterprises and Regional Innovation, Japan.

References

1) J. Stutz, U. Platt, Numerical analysis and estimation of the statistical error of differential optical absorption spectroscopy measurements with least-squares method. Appl. Opt. 35, 6041–6053 (1996).

2) H. Edner, P. Ragnarson, S. Spannare, S. Svanberg, Differential optical absorption spectroscopy (DOAS) system for urban atmospheric pollution monitoring. Appl. Opt. 32, 327–333 (1993).

3) Y. Yoshii, H. Kuze, N. Takeuchi, Long-path measurement of atmospheric NO_2 with an obstruction flashlight and a charge-coupled-device spectrometer, Appl.Opt.42, 4362-4368 (2003).

4) N. Lagrosas, H. Kuze, N. Takeuchi, S. Fukagawa, G. Bagtasa, Y. Yoshii, S. Naito, M. Yabuki, Correlation study between suspended particulate matter and portable automated lidar data, Aerosol Science, in press (2005).

Analysis of the Asian Dust Aerosol Optical Properties over the Ocean

Dodi Sudiana[1], Mitsuo Minomura[2], Hiroaki Kuze[2], Nobuo Takeuchi[2]

[1]Graduate School of Science and Technology, Chiba University,
1-33 Yayoi-cho, Inage-ku, Chiba 263-8522, Japan
e-mail: dodi@ceres.cr.chiba-u.ac.jp
[2]Center for Environmental Remote Sensing, Chiba University,
1-33 Yayoi-cho, Inage-ku, Chiba 263-8522, Japan

Abstract

An algorithm using the Second Simulation of the Satellite Signal in the Solar Spectrum (6S) radiative transfer code has been developed to analyze the optical properties of aerosols over the ocean using NOAA/AVHRR data. Visible and NIR channel data was utilized to retrieve aerosol optical thickness at 632 nm and 843 nm over the ocean around Japan during clear (non-dust) and Asian dust events in March 18-19, 2002. The sea surface albedo measured during the non-dust events is used as reference, and the relation between the albedo and the optical thickness is derived. Using Mie calculations and bi-lognormal size distribution parameters inferred from measurements, the correlation between the optical thickness of the Asian dust and the digital number of visible and NIR channels is analyzed. Good agreements are found between the simulated results and the optical thickness retrieved from ground-based, Sunphotometer measurements.

Keywords: aerosol optical properties, NOAA/AVHRR, 6S, Asian dust

1. INTRODUCTION

A number of studies have pointed out the significance of aerosols in the climate system [Charlson et al., 1992; Kaufman et al., 2002]. Aerosols can have a profound impact on the global and regional climate, both by directly interacting with solar radiation and by indirectly modifying cloud microphysics. One of the key parameters that must be accurately quantified in measuring the aerosols in the atmospheres is aerosol optical thickness (AOT), which is a measure of the aerosol extinction on radiative transfer [Charlson et al., 1992; Chylek and Wong, 1995; Russel et al., 1997]. Various methods have been developed to measure the distribution and quantity of AOT using ground-based Sunphotometers (SP) [Holben et al., 1998], lidar [Welton et al., 2002] and aircraft [Russel et al., 1999]. Although these measurements are accurate, their space and time coverage are limited. Satellite measurements, due to their large coverage and high temporal resolution, are the most effective way to infer the quantity of AOT. However, in order to enhance the accuracy of aerosol properties from satellite measurements, the ground-based and/or aircraft measurements are still needed.

During the spring, a large amount of Asian dust (Kosa, in Japanese) is flown from dust storms in Gobi and Taklamakan deserts in Mongolia and China. The dust particles have the potential of affecting global climate by influencing the radiative balance of the atmosphere. They are initiated by strong winds, caused by cold fronts or low-pressure systems. These dusts significantly increase the atmospheric turbidity over East Asia and Pacific regions. In situ and satellite remote sensing studies have indicated that the dusts from the Asian continent could be transported over the Pacific Ocean to the western coast of United States [Takemura et al., 2002; Tratt et al., 2001; Husar et al., 2001], showing that the dust is not limited to the Asian regional climate. Due to such a great impact of the dust on not only regional but global climate, there is a stringent need to analyze the optical characteristics of Asian dust particles.

In this research, we analyze the distribution and magnitude of AOT during clear (non-dust) and Asian dust events in spring 2002 using visible and near-infrared channels of

Advanced Very High Resolution Radiometer (AVHRR) data from the NOAA polar orbiting satellites. This study demonstrates a simple method to infer the AOT by utilizing the Second Simulation of the Satellite Signal in the Solar Spectrum (6S) radiative transfer code [Vermote et al., 1997] over the ocean. The AOT data concurrently measured by a ground-based sun-photometer are also used to confirm the modeling results.

2. METHODOLOGY

In this research, we use the visible and near-infrared channels (channel 1 and 2) of NOAA/AVHRR data obtained in March-April 2002. Selected areas over the Sea of Japan with size 200×200 pixels area are analyzed for clear and dusty/Kosa cases. For the clear case (non-dust, non-cloudy), here we assume the maritime aerosol model in the 6S library to infer the relationship between the satellite albedo and the AOT at 632 nm and 843 nm. For the turbid (dusty) case, we derive this relationship on the basis of the aerosol model of the bi-lognormal size distribution. Finally, the relationship between the NOAA/AVHRR albedo and the AOT of channel 1 and 2 are retrieved using the clear sea surface reflectance achieved from the ship measurement as reference [Kozai et al., 2000]. The algorithm of the AOT retrieval is schematically described in Fig. 1.

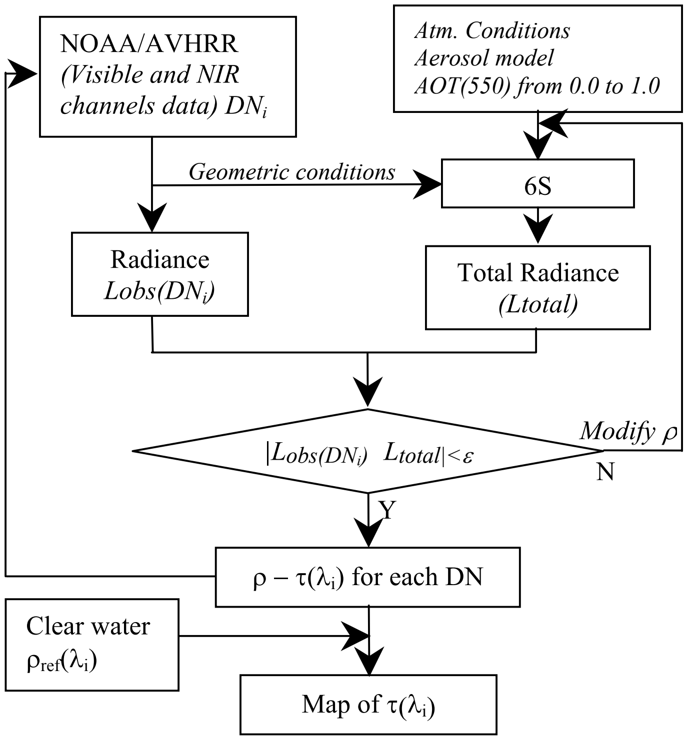

Fig. 1. Schematic diagram of AOT retrieval

2.1. 6S

The 6S code is a radiative transfer code originally developed to analyze the satellite signal between 0.25 and 4.0 μm assuming cloudless atmosphere. It is used for the atmospheric radiative calculations, as well as for the relevant sensitivity analysis [Vermote et al., 1997]. Atmospheric vertical profiles of pressure, temperature, concentration of water vapor and ozone are considered, in addition to a Lambertian ocean surface. The input parameters needed in the calculations are: geometrical conditions, atmospheric model for gaseous components, aerosol model, spectral condition and ground reflectance.

As illustrated in Fig. 2, the total radiance that irradiates the satellite sensor can be formulated as

$$L_{\mathrm{total}} = L_{\mathrm{atm}}\,(\tau, M_{\mathrm{atm}}) + L_{\mathrm{tar}}\,(\rho, \bar{\rho}, \tau, M_{\mathrm{atm}}) + L_{\mathrm{env}}\,(\bar{\rho}, \tau, M_{\mathrm{atm}}) \tag{1}$$

where M_{atm} stands for the atmospheric model of molecules and aerosols, ρ the target albedo, $\bar{\rho}$ environment albedo, and τ the aerosol optical thickness through the entire atmosphere.

2.2. NOAA/AVHRR

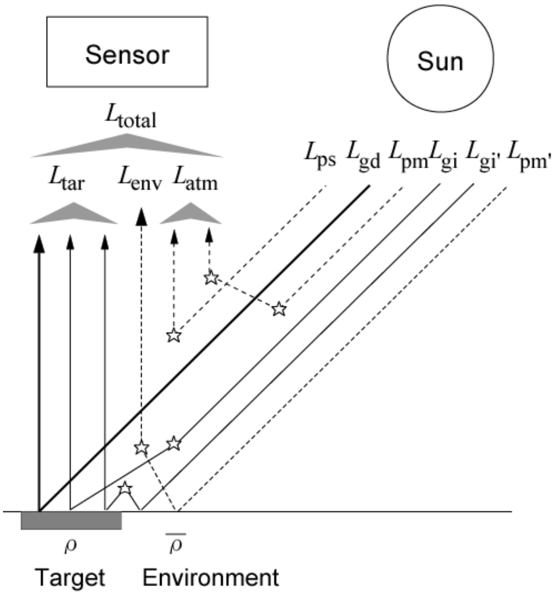

Fig. 2. The 6S radiative model

The NOAA-16, which was launched on September 21, 2000, has 5 channels of AVHRR: visible, near-infrared, short-wave infrared, and two thermal-infrared channels. It has continuously been operated since February 27, 2001. The satellite radiance can be calculated by the following equation:

$$L_{obs} = (S \times DN + I)\, E_S / 100\,\pi \,, \qquad (2)$$

where S and I are calibration factors of AVHRR visible and near-infrared channels, DN is the digital number, E_S is the solar spectral irradiance expressed in units of $Wm^{-2}sr^{-1}\mu m^{-1}$

For NOAA-16, we employ the albedo A_i of each channel using the following equations (http://noaasis.noaa.gov/NOAASIS/ml/n16calup.html):

$$A_i = S_i \times DN + I_i \qquad (3)$$

Channel 1:

$$A_1 = \begin{cases} 0.0523 \times DN - 2.016 & \text{for } DN < 497.5 \\ 0.1528 \times DN - 51.91 & \text{for } DN > 497.5 \end{cases} \qquad (4)$$

Channel 2:

$$A_2 = \begin{cases} 0.0513 \times DN - 1.943 & \text{for } DN < 500.3 \\ 0.1510 \times DN - 51.77 & \text{for } DN > 500.3 \end{cases} \qquad (5)$$

2.3. Algorithm

First, we select an area of interest which has 200×200 pixels in size (nearly 200 km × 200 km). The geometrical conditions are derived from the center point of the area and we employ atmospheric models of mid-latitude winter and maritime aerosol model as the input parameters for 6S simulation. AVHRR data on April 10, 2002 is selected as sample data for clear case and the data on March 18, 2001 for dusty/Kosa case. The simulation is performed by entering AOT(550) from 0.0 to 1.0 with the atmospheric and geometrical conditions. The radiance observed by the satellite sensor is then compared with the radiance calculated by 6S. For each AOT(550) value, the calculation is repeated by modifying the sea-surface albedo value if the difference between the two radiances is larger than 10^{-5} $Wm^{-2}sr^{-1}\mu m^{-1}$, arbitrarilty set as a threshold value. For the range of digital number values that actually occur in the area, the relationship between the value of AOT and the albedo value is calculated and stored for each channel of AVHRR. If we can appropriately assume the surface albedo value (see the following), the lookup table calculated in this manner enables the determination of AOT for each channel (AOT(λ_i)).

Since the albedo of the sea surface (reference albedo) is the key parameter in the present retrieval, its accuracy directly affects the accuracy of the AOT retrieved from the satellite images. We used the measurement of clear sea surface albedo as the reference, as performed by Kozai et al. (2000). The values measured at the effective wavelengths of channel 1 (632nm) and channel 2 (843nm) are 0.28% and 0.15%, respectively.

3. RESULTS AND DISCUSSIONS

3.1 Clear case

The algorithm is applied to analyze clear area over the Sea of Japan on April 10, 2002. The area of interest is shown in Fig. 3(a). The aerosol model is maritime and applied to the center point of the area (140.27^{o}E, 46.78^{o}N). For each digital count in the area, we calculate

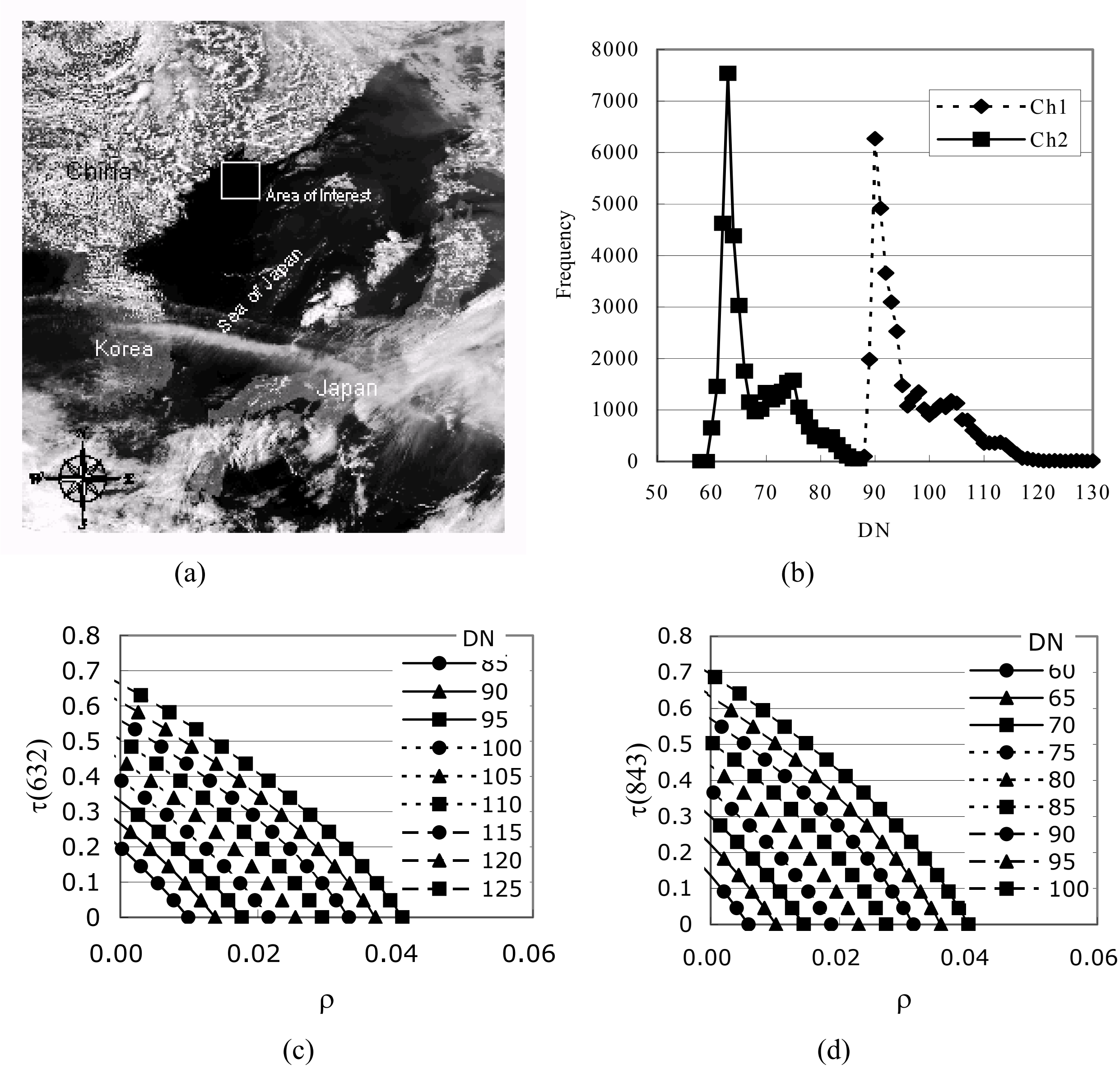

(a) (b)

(c) (d)

Fig. 3. Simulation results of clear case: (a) area of interest; (b) histogram; simulation results of: (c) channel 1; (d) channel 2, respectively

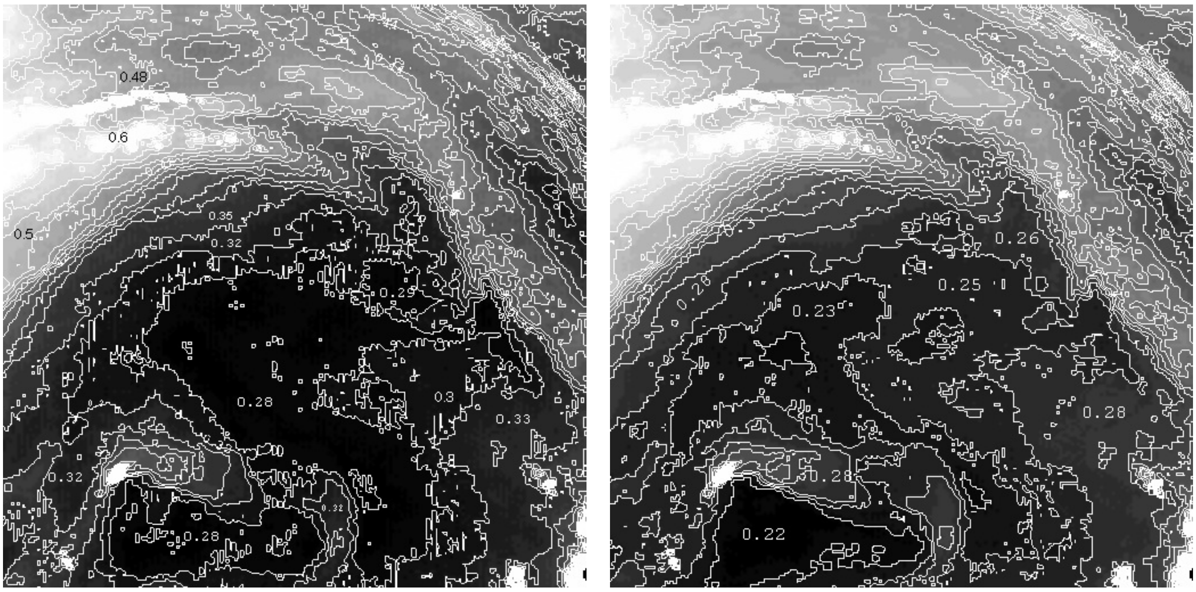

(a) (b)

Fig. 4. AOT map of: (a) channel 1 (λ=632nm) and (b) channel 2 (λ=843nm), respectively.

the relationship between the albedo and the AOT at 550nm wavelength. For each channel, the histogram of digital count and the simulation results are shown in Fig. 3(b) and (c)-(d). The aerosol model used in the simulation is maritime and the atmospheric model is midlatitude winter. Using the sea surface albedo as reference (ρ_{ref}), the AOT(λ_i) maps are retrieved for channel 1 and channel 2, as shown in Fig. 4(a) and 4(b), respectively.

The simulation results of AOT showed that AOT values of channel 2 (AOT(843)) are relatively smaller than the AOT values channel 1 (AOT(632)).

3.2 Turbid case

According to the observations, Asian dust/kosa events occurred in March-April 2002. For this case, we apply the algorithm using the bi-lognormal size distribution as reported by Wang [Wang et al., 2003]. The particle volume distribution can be computed as:

$$\frac{dV}{d\log_{10} r} = \sum_{n=1}^{2} C_n \exp\left[-\frac{1}{2}\left(\frac{\log_{10} r - \log_{10} r_{vn}}{\log_{10}\sigma_n}\right)^2\right], \tag{6}$$

where n is the mode number, r_{vn} is the volume mean radius, σ_n is the standard deviation, and C_n is the peak of n-th mode. In this study, we used r_{vn} value of 0.18 μm and 1.74 μm, and σ_n of 2.16 and 1.78, which are derived by Wang et al. (2003), to represent the first and second mode, respectively. The refractive index is highly variable depending on the chemical compositions of aerosols [d'Almeida et al., 1991]. While the same value of the real part of the effective refractive index (i.e. 1.50-1.55) is adopted in several literatures, the imaginary part varies from non-absorbing [Rao et al., 1989] to values considerably absorbing values of 0.003-0.005i [Higurashi and Nakajima, 2002]. A survey of aerosol network AERONET has reveled that the imaginary part of the refractive index of desert dust and oceanic aerosols range from 0.0015 to 0.0007 [Dubovik et al., 2002]. In this study we use the refractive index of 1.53 – 0.002i at 632 nm and 843 nm. Figure 5(a)-(f) shows the area of interest of NOAA/AVHRR data on March 18, 2002; the histogram; simulation results and AOT(λ) map of channel 1 and 2, respectively.

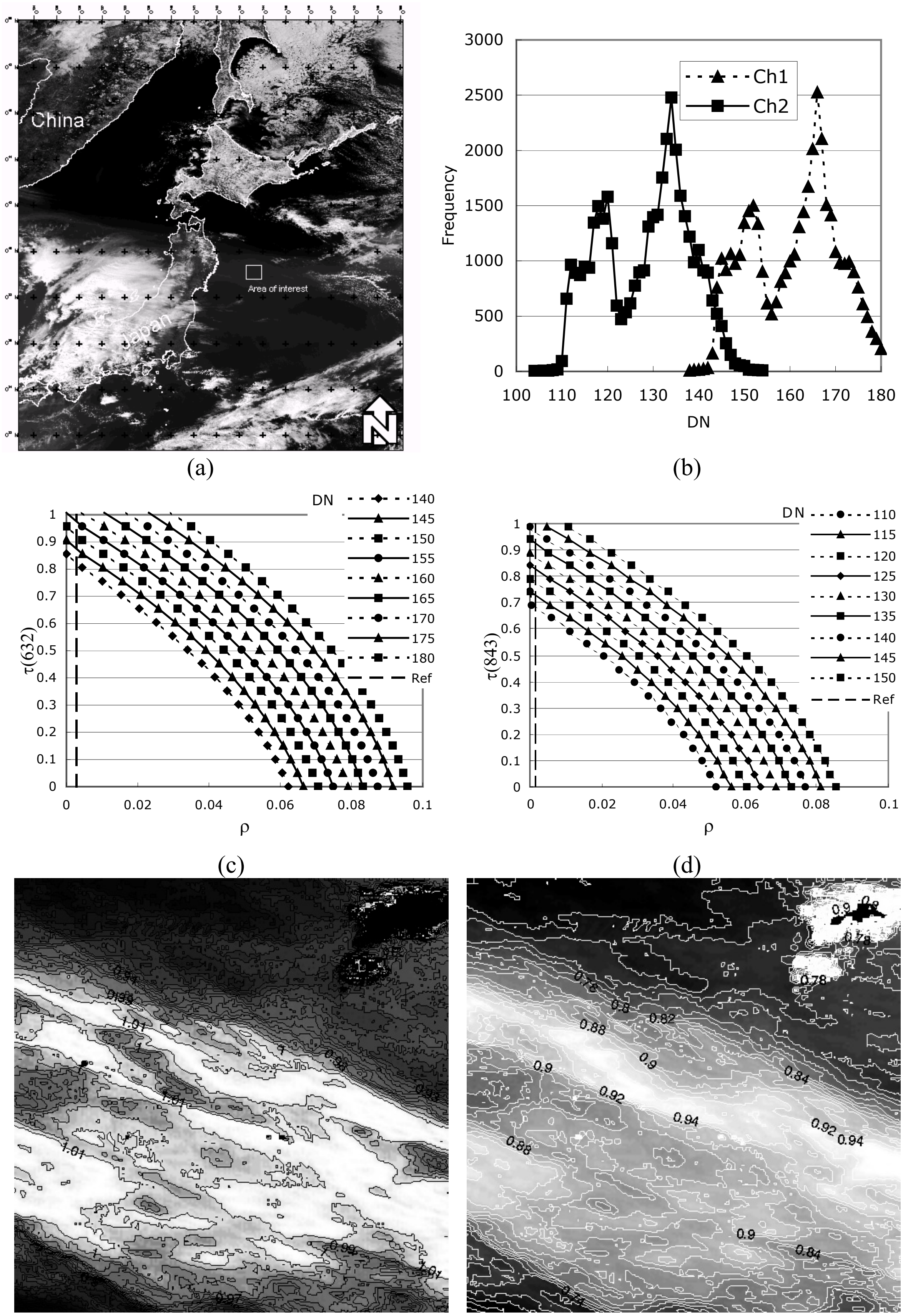

(a) (b)

(c) (d)

(e) (f)

Fig. 5. The simulation results of dusty case: (a) area of interest; (b) histogram; simulation result of: (c) channel 1; (d) channel 2, respectively; the AOT(λ) of: (e) channel 1 and (f) channel 2.

3.3. Validation

In order to check the validity of the simulation, we compare the AOT(λ_i) with the measurement of sun-photometers operated at Chiba University (35.62°N, 140.12°E). The NOAA/AVHRR on March 17, 2002 is used as a sample data. The site of the validation site is shown as a star in Fig. 6 which according to the NOAA header data, was scanned at 12:52:09 JST. The aerosol model used in the simulation is bi-lognormal and ρ_{ref} is assumed to be 0.28% and 0.15% as mentioned above. Since the sun-photometer bands are centered at 368 nm, 500 nm, 675 nm, 778 nm (each having a width of 5 nm), the AOT at 632 nm and 843 nm is calculated by interpolation. From the AVHRR channel 1, the resulting value of AOT(632) is 0.66. In comparison, the concurrent sun-photometer measurement leads to a value (AOT_{SP632}) of 0.66 (relative error ξ = 0.43%). On the other hand, from channel 2, the AOT(843) is 0.57, comparing to AOT_{SP843} = 0.58 gives the relative error ξ = 3.11%. Using maritime model, for another validation result on March 19, we obtain AOT(550) of 0.3306, whereas AOT_{sp550} is 0.3235 (relative error ξ = 2.2%).

These results show that a $\rho_{ref}(\lambda_1)$ value of 0.28% and $\rho_{ref}(\lambda_2)$ value of 0.15% and aerosol model (maritime, bi-lognormal) utilizing in the 6S code are indeed appropriate for accurately estimating the AOT.

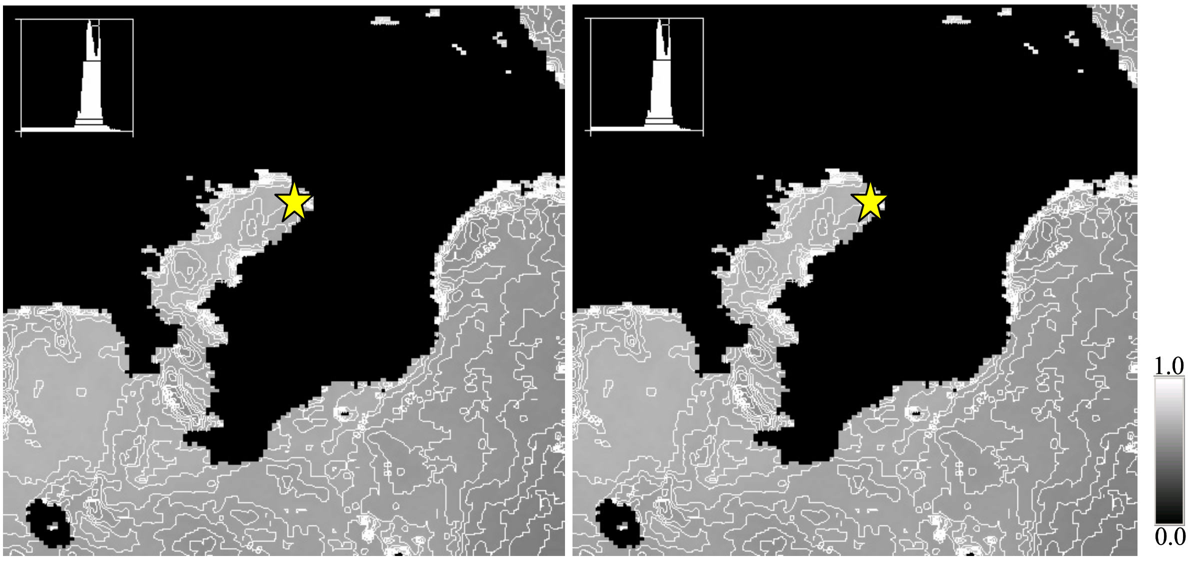

(a) (b)

Fig. 6. The AOT retrieved from the simulation: (a) AOT(632); (b) AOT(843)

4. SUMMARY

The radiance from the NOAA/AVHRR is simulated using 6S radiative transfer code to retrieve the aerosol optical thickness over the ocean during clear/non-dust and Asian dust events. The model based on maritime and bi-lognormal size distribution for clear and turbid cases, respectively. The simulation results indicate that by using the sea-surface albedo measured from the ship as the reference, the AOT values derived from the satellite images satisfactorily agree with the values from ground-based measurements.

5. REFERENCES

Charlson, R.J., S.E. Schwartz, J.M. Hales, R. D., Cess, J.A. Coakley, J.E. Hansen, and D.J. Hoffman, Climate forcing by anthropogenesis aerosols, *Science*, *255*, 423-430, 1992.

Chylek, P., and J. Wong, Effect of absorbing aerosols on global radiation budget, *Geophys. Res. Lett.*, *22*, 929-931, 1995.

d'Almeida, G.A., P. Koepke, and E.P. Shettle, *Atmospheric Climatology and Radiative Characteristics*, 561 pp., A. Deepak, Hampton, Va., 1991.

Dubovik, O., B. Holben, T.R. Ech, A. Smirnov., Y.J. Kaufman, M.D. King, D. Tanre, and I. Slutsker, Variability of absorption and optical properties of key aerosol types observed in worldwide locations, *J. Atmos. Sci*., *59*, 590-608, 2002.

Higurashi, A., and T. Nakajima, Development of two-channel aerosol retrieval algorithm on a global scale using NOAA AVHRR, *J. Atmos. Sci., 56*, 924-941, 1999.

Holben, B. N., T. F. Eck, I. Slutsker, D. Tanré, J. P. Buis, A. W. Setzer, E. F. Vermote, J. A. Reagan, Y. J. Kaufman, T. Nakajima, F. Lavenu, I. Jankowiak, and A. Smirnov, AERONET-A federated instrument network and data archive for aerosol characterization. *Remote Sens. of Env.* , *66*, 1-16, 1998.

Husar, R.B. et al., Asian dust events of April 1998, *J. Geophys. Res., 106*, 18,317-18,330, 2001.

Kaufman, Y.J., D. Tanré, and O. Boucher, A satellite view of aerosols in climate systems, *Nature*, *419*, 215-223, 2002.

Kozai, K., K. Ishida, M. Kuskari, M. Sasaki, Evaluation of aerosol effect on the satellite-derived ocean color in the western equatorial Pacific ocean using 6S code, Umi to Sora, 76(2), 41-44, 2000.

Rao, C.R. L.L. Stowe, and P. McClain, Remote sensing of aerosols over oceans using AVHRR data, theory, practice and application, *Int. J. Remote Sens.*, *10*, 743-749, 1989.

Russel, P.B., S.A. Kinne, and R. W. Bergstrom, Aerosol climate effects: Local radiative forcing and column closure experiments, *J. Geophys. Res.*, *102*, 9397-9408, 1997.

Russel, P.B., J.M. Livingstone, P. Hignett, S. Kinne, J. Wong, A. Chien, R. Bergstrom, P. Durkee, and P.V. Hobbs, Aerosol-induced radiative flux changes off the US mid-Atlantic coast: Comparison of values calculated from Sun photometer and in situ data with those measured by airborne pyranometer, *J. Geophys. Res., 104*, 2289-2307, 1999.

Takemura T., I. Uno. T. Nakajima, A. Higurashi, and I. Sano, Modeling study of long-range transport of Asian dust and anthropogenic aerosols from east Asia, *Geophys. Res. Lett.*, *29*(24), 2158, doi:10.1029/2002GL016251, 2002.

Tratt, D.M., R.J. Frouin, an D.L. Wesphal, April Asian dust event: A southern California perspective, *J. Geophys. Res., 106*, 18, 18,371-18,379, 2001.

Vermote, E.F., D. Tanré, J.L. Deuzé, M. Herman, and J.-J. Morcrette, Second simulation of the satellite signal in the solar spectrum, 6S: An overview. *IEEE Trans. on Geosci. and Remote Sens.*, *35*, 675-686, 1997.

Wang J., S.A. Christopher, F. Brechtel, J. Kim, B. Schmid, J. Redeman, P.B. Russel, P. Quinn, and B. Holben, Geostationary satellite retrieval of aerosol optical thickness during ACE-Asia, *J. Geophys. Res*., *108*(D23), 8657, doi:10.1029/2003JD003580, 2003.

Welton E.J., K.J. Voss, P.K. Quinn, P. Flatau, K. Markowics, J. Campbell, J.D. Spinhirne, H.R. Gordon, and J. Johnson, Measurements of aerosol vertical profiles and optical properties during INDOEX 1999 using micropulse lidars, *J. Geophys. Res.*, *107*(D19), 8019, doi:10.1029/2000JD000038, 2002.

Retrieval of aerosol optical properties over Chiba land area from Landsat/TM imagery

- Part II: Determination of aerosol size distribution -

Koji Asakuma[*], Mitsuo Minomura[**], Hiroaki Kuze[**] and Nobuo Takeuchi[**]

*Faculty of Bio-industry, Tokyo University of Agriculture
196 Yasaka, Abashiri 099-2493, Japan
** Center for Environmental Remote Sensing (CEReS), Chiba University,
1-33 Yayoi-cho, Inage-ku, Chiba 263-8522, Japan

Key Words: Atmospheric correction, Aerosol optical properties, Aerosol optical thickness, Landsat/TM

Abstract:

We present a case study in which aerosol optical properties over Chiba land area are derived from Landsat/TM visible channel data. First, the surface albedo value is obtained for each pixel from the atmospherically corrected TM image (January 14, 1999) with relatively small aerosol optical thickness (AOT). After the correction using the 6S code, this ‘clean’ image provides the “ρ map” that can be used as a reference. Second, a test image (December 13, 1998) with relatively large AOT is compared with the clean image to study the aerosol optical properties. By changing the aerosol particle radius, this test image is also subjected to the atmospheric correction, and the resulting surface albedo is compared with the ρ map. The parameter optimization is carried out on the basis of the standard WMO-WCP55 continental aerosol model, with the contribution from WMO-WCP112 water-soluble particles. The aerosol particle radius over Chiba area on December 13, 1998 is found to be 4.0×10^{-3} μm, slightly smaller than the radius of the standard water-soluble particles.

1. INTRODUCTION

Atmospheric correction is indispensable to retrieve accurate surface albedo from satellite images in the visible and near infrared bands. The essential parameter for the correction is the accurate value of aerosol optical thickness (AOT) [1-3]. The wavelength dependence of AOT is also important, and in general, this is automatically given by the aerosol model (such as the continental, maritime or urban aerosol model) [2,3]. The actual aerosol property at the time of the satellite overpass, however, is unknown for most cases. On the other hand, simulation studies indicate that the relationship between the ground albedo and the AOT can vary significantly in accordance with the aerosol properties such as the size distribution and the refractive index. Thus, even if the value of AOT is given from the ground observation (e.g. by means of a sun photometer), different assumption about the aerosol model can lead to a different value of the surface albedo as a result of the atmospheric correction [3].

In this paper we present an algorithm of deriving the aerosol size distribution from Landsat/TM images. The algorithm is demonstrated on the image observed over the Chiba land area. By means of the radiative transfer calculation, the aerosol size distribution is determined from the condition that the apparent albedo at the top of the atmosphere agrees with the “reference” surface albedo. This reference albedo is obtained from the atmospheric correction of the ‘clear’ image (see Part I: Determination of spatial distribution of aerosol optical thickness). On the other hand, the apparent albedo is obtained from the TM image with ‘turbid’ atmospheric condition. As for the AOT values, we make use of the values measured by a sun photometer operated on the campus of Chiba University.

2. METHODOLOGY

We employ the 6S radiative transfer code [4] for determination of the aerosol size distribution. The code gives the apparent albedo once the surface albedo, AOT and the aerosol model are specified. In addition to the seven standard models such as the continental, maritime, and urban models, the 6S code allows the user to specify detailed aerosol parameters in a form of the multi-modal log normal distribution, the modified gamma distribution, or the Junge power-law distribution. In the standard aerosol model equipped in the 6S code, the user can also modify the volumetric percentage of four basic components (dust-like, water-soluble, oceanic and soot aerosols). Table 1 shows the default percentage of these components [5], given as the WMO-WPC55 standard aerosol models. While the continental and maritime models have large influence of the water-soluble component, the urban aerosol model is remarkably contributed by soot aerosols with large absorption.

As explained in Part I, the analysis of TM data over Chiba land area indicates that reasonable values of the AOT can be retrieved when continental or maritime aerosol models are employed, but not with the urban model. In view of this effect, here we rely on the continental model, and the surface albedo is simulated for various values of the particle radius R_M of the water-soluble component. Table 2 shows the specification of four basic components given in WMO-WCP112, where the mean particle radius of the water-soluble component is 0.005 μm. Here we change the value of this parameter in a range of 0.001 to 1.0 μm. In order to focus on the effect of this size distribution, other parameters including the reflective index are fixed in the present simulation.

Table 1. Volumetric percentage for WMO-WPC55 standard aerosol models.

	Dust Like	Water Soluble	Oceanic	Soot
Continental	2.265×10^{-6}	0.9383	---	0.0617
Maritime	---	0.9996	4.208×10^{-4}	---
Urban	1.651×10^{-7}	0.5925	---	0.4075

Table 2. Specifications of the four basic components in WMO-WCP112: R_M is the mean radius, the standard deviation, V the volume concentration, N the particle number concentration, and n_r-in_i the refractive index.

	Dust Like	Water Soluble	Oceanic	Soot
R_M [m]	0.500	0.005	0.300	1.180×10^{-2}
σ	2.99	2.99	2.51	2.00
V [m^3/cm^3]	1.140×10^{2}	1.140×10^{-4}	5.114	5.978×10^{-5}
N [cm^{-3}]	5.473	1.869×10^{6}	2.761×10^{2}	1.806×10^{6}
n_r at 488 nm	1.530	1.530	1.377	1.750
n_i at 488 nm	8.00×10^{-3}	5.00×10^{-3}	1.38×10^{-8}	4.50×10^{-1}

The best value of the particle radius R_M is sought under the condition that ground albedo values in the clear-day image agree with the values from the turbid-day image after the atmospheric correction. The target pixel is the one that corresponds to the location of the Chiba University. From the data on January 14, 1999 (clear day), we obtain $\rho^{(C)}_{485} = 0.14$ and $\rho^{(C)}_{560} = 0.16$ for TM channel 1 and 2, respectively. The turbid image is observed on December 13, 1998 with AOT values (observed at Chiba University) of $\tau_{485} = 0.294$ at 485 nm and $\tau_{560} = 0.241$ at 560 nm.

3. RESULTS AND CONCLUSION

Figure 1 shows the relationship between the aerosol particle radius R_M and the ground albedo $\rho^{(T)}_{485}$ at 485 nm (TM channel 1) obtained from the turbid image. This value has been obtained through the radiative transfer calculation by assuming that the calculated AOT at 485 nm (τ'_{485}) is equal to the value from the sun photometer (τ_{485}). In the calculation, the AOT value at 550 nm (τ_{550}) was changed from 0.0 to 0.4. The digital number (DN) of the target pixel is 75 for channel 1. The ground albedo $\rho^{(T)}_{560}$ at 560 nm (TM channel 2) is also obtained from the same calculation with the corresponding pixel DN value of 31. In Fig. 1, the calculated albedo $\rho^{(T)}_{485}$ for channel 1 agrees with the reference albedo $\rho^{(C)}_{485} = 0.14$ at $R_M = 4.0\times10^{-3}$ and $R_M = 4.7\times10^{-2}$ μm. Similarly, we obtain $\rho^{(T)}_{560} = \rho^{(C)}_{560} = 0.16$ for channel 2 for the particle radius of $R_M = 4.0\times10^{-3}$ and $R_M = 6.5\times10^{-2}$ μm. Consequently it is likely that the aerosol model over Chiba area

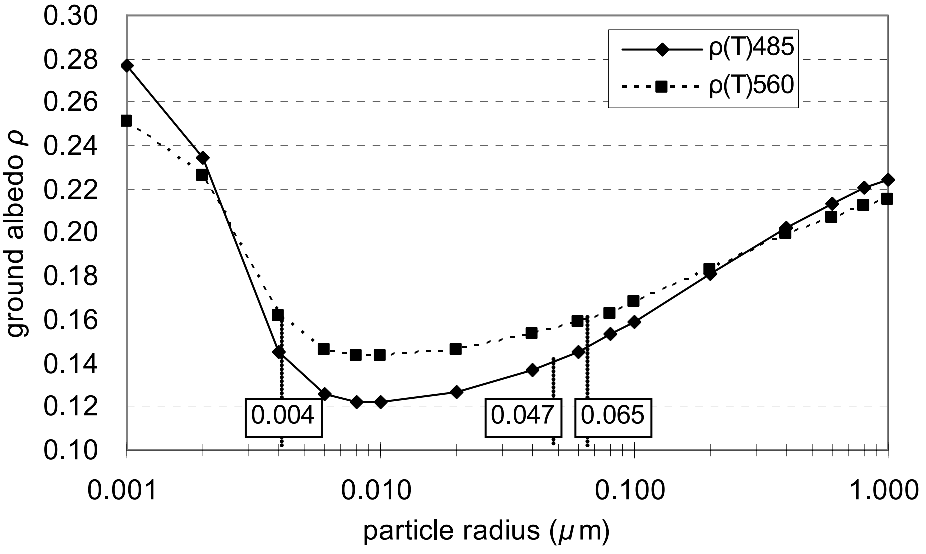

Figure 1: Relationship between the aerosol particle radius λ_m and atmospherically corrected ground albedo. The solid line shows the result at 485 nm (TM channel 1) and dotted line is at 560 nm (channel 2).

on December 13, 1998 can be described as the continental aerosol model with the particle radius of 4.0×10^{-3} μm. This value is only slightly smaller than the standard water-soluble particle which is the main component of the continental model.

RREFERECES

1. H. Oudirari and E. F. Vermote, Operational atmospheric correction of Landsat TM data, Remote Sensing Env. 29, pp. 4 – 15, 1999.
2. D. Tanre, Y. J. Kaufman, M. Herman and S. Mattoo, Remote sensing of aerosol properties over oceans using MODIS/EOS spectral radiances, J. Geophys. Res. 102 (D14), pp. 16971 – 16988, 1997.
3. H. Kuze, M. Minomura, Y. Furusawa, Y. Todate and N. Takeuchi, Atmospheric correction of satellite data over Chiba area, Proceedings of the CEReS international symposium on remote sensing 'Monitoring of environmenta change in ASIA', pp. 139 – 144, 2003.
4. E. F. Vermote, D. Tanre, J. L. Deuze, M. Herman and J. J. Mocrette, Second simulation of the satellite signal in the solar spectrum, 6S: An overview, IEEE Trans. Geosci. Remote Sensing 35 (3), pp. 657 – 686, 1997.
5. E. F. Vermote, D. Tanre, J. L. Deuze, M. Herman and J. J. Mocrette, 6S User Guide Version 2 'Subroutine Mie and Exscphase', pp. 109 – 127, 1997.

Micro Pulse Lidar Observation of Low Relative Humidity Layer

Jin-jia Guo Zhi-shen Liu Zhao-ai Yan

Ocean Remote Sensing Laboratory of the Ministry of Education of China
Ocean Remote Sensing Institute, Ocean University of China, Qingdao, 266003, China
Email: guojj@orsi.ouc.edu.cn Tel: 86-532-2032901-809 FAX:86-532-2032992

Abstract: A very clear layer from 3km to 5km was observed by Micro pulse lidar (MPL) on April 14th, 2004 in Qingdao. This was in agreement with the measurement results of High Spectral Resolution Lidar (HSRL). From the raw data of radiosondes, we found from 3km to 5km the relative humidity (RH) was very low and kept as a constant. This low RH layer was also found in a large area mainly in Shandong peninsula and west coast of Korea.

Key Words: lidar, radiosond, relative humidity

Introduction: Lidar is a unique remote-sensing technique to obtain the vertical profiles of various optical properties of atmospheric aerosol and meteorological information. A eye-safe micro pulse lidar(MPL) and a High Spectral Resolution Lidar (HSRL) were used to make regular measurements every night in Ocean Remote Sensing Laboratory of the Ministry of Education of China, Ocean University of China, Qingdao, China. On April 14th when we observed with the MPL at 21:00 (local time), we found the backscattering signal from 3Km to 5Km was very weak (Fig 1). At first we thought it was caused by pulse pile up because the micro pulse lidar worked at photon counting mode and the backscattering signal between 3Km to 5Km was too strong to count. We checked the High Spectral Resolution Lidar signal which worked at analog mode. And also found the backscattering signal from 3Km to 5Km was very weak. From the radiosond data at 20:00 (local time) on April 14th, we found the relative humidity was very low from 3Km to 5Km and kept as a constant (2%). And from the radiosond data (Fig 2) we found this low relative humidity layer not only existed in Qingdao(120:19E,36:04N) but also in Jinan (117:02E, 36:40N). So we assumed this low RH layer was in a large scale area. From the radiosond network (Fig. 3) data, we found our assumption was correct. And the low RH layer was mainly in Shandong peninsula and west coast of Korea (Fig. 4).

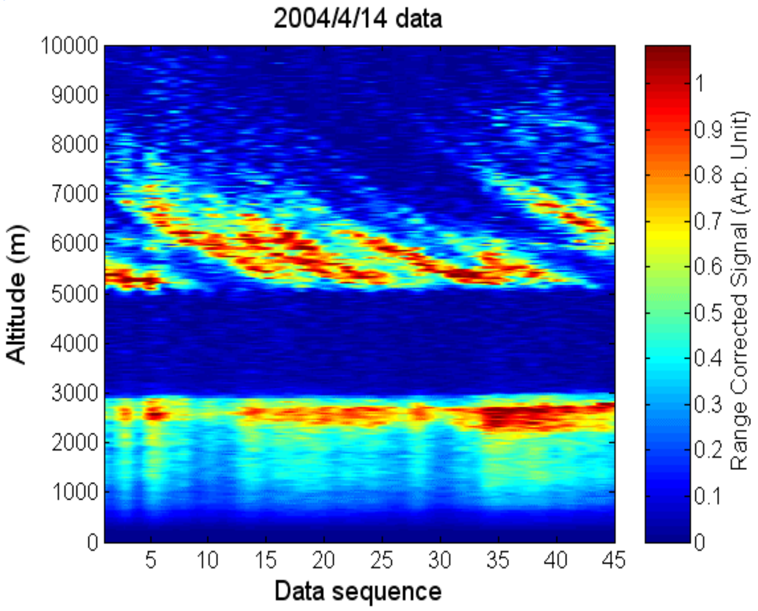

Fig 1 A very clear layer was found by MPL at 21:00 in Qingdao on April 14th from 3Km to 5Km.

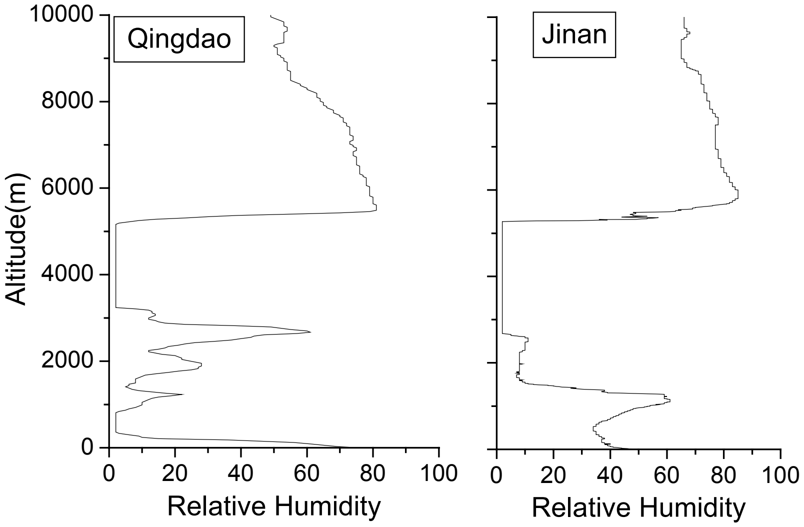

Fig. 2 Radiosond data showed that Qingdao and Jinan both had the low RH layer from 3 Km to 5Km, which was in agreement with the results of lidar observation.

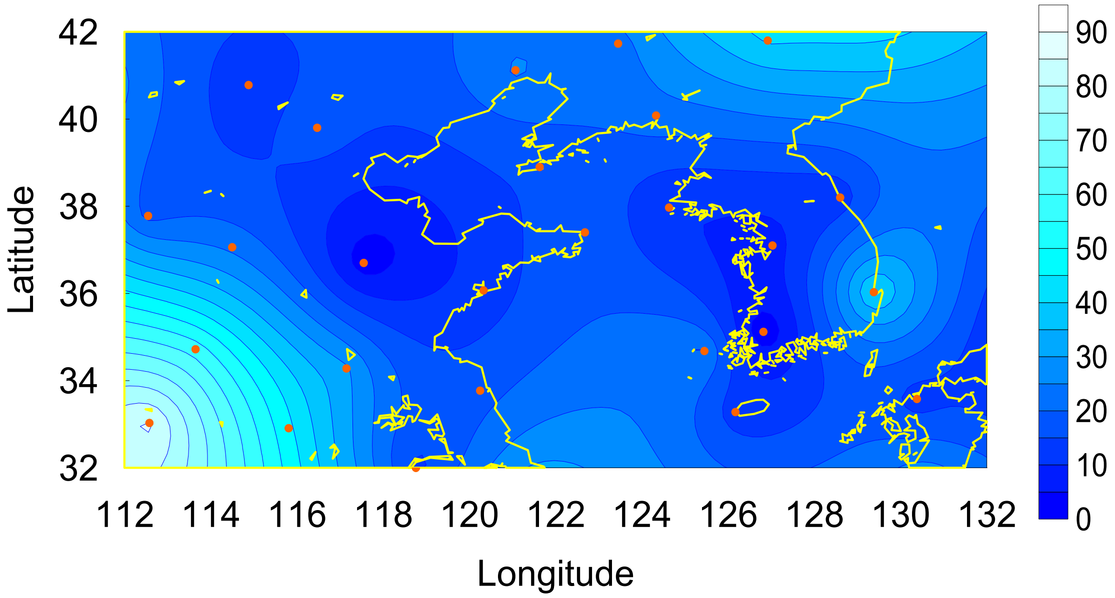

Fig. 4 Relative Humidity field distribution in 700hpa pressure. It showed that the low RH layer exist in a in a large area, mainly in Shandong peninsula and west coast of Korea. The red points show the location of radiosond station.

Cloud optical thickness and effective particle radius derived from transmitted solar radiation measurements: Comparison with cloud radar observations

Nobuhiro Kikuchi, Hiroshi Kumagai and Hiroshi Kuroiwa
National Institute of Information and Communications Technology
Teruyuki Nakajima
Center for Climate System Research, University of Tokyo
Akihide Kamei
National Institute for Environmental Studies
Ryosuke Nakamura
Japan Aerospace Exploration Agency

A method is presented for determining the optical thickness and effective particle radius of stratiform clouds from transmitted solar radiation measurements. The procedure compares measurements of the transmission function at water-absorbing and non-absorbing wavelengths with lookup tables of the transmission function precomputed for plane-parallel, vertically homogeneous clouds. Cloud thermodynamic phase may also be inferred from transmission function measurements at 1.02, 1.6, and 2.2 μm. The cloud optical thickness determined from transmission function measurements may be used to derive vertical profiles of cloud microphysics in combination with radar reflectivity factor. We have also developed an algorithm for solving the radar equation with a constraint of cloud optical thickness at visible wavelength. Observations of clouds were conducted during August and September in 2003 at Koganei, Tokyo, Japan, using a PREDE i-skyradimeter and a 95-GHz cloud radar SPIDER. Optical thickness and effective particle radius of water clouds were derived from i-skyradiometer observations. Then, utilizing the optical thickness obtained from i-skyradiometer observations, vertical profiles of the effective particle radius and liquid water content were derived from SPIDER observations. We found that the effective particle radius derived by using these two instruments were in good agreement.

Key Words: cloud remote sensing

1. INTRODUCTION

It is commonly accepted that the cloud radiative effect is one of the most uncertain factors in predicting future global warming. Cloud radiative properties depend largely on the optical thickness and particle size. So far, several methods to remotely sense these parameters have been proposed, in which solar radiation reflected by clouds is measured at visible and near-infrared wavelengths from aircrafts or satellites (e.g., Nakajima and King 1990;

Nakajima and Nakajima 1995).

This paper deals with ground-based measurements of transmitted solar radiation by a multi-spectral radiometer. As in the solar reflectance method, the principle of a method presented in this paper to infer cloud optical thickness and particle size is the fact that the transmission function of clouds at non-absorbing wavelengths is primarily a function of the optical thickness, whereas the transmission function at water-absorbing wavelengths is primarily a function of the particle size.

In deriving the cloud optical thickness and particle size from reflected/transmitted solar radiation measurements, clouds are usually assumed to be vertically homogeneous. In reality, water clouds contain significant vertically inhomogeneity, which may influence the retrieval results. To address this issue, 95-GHz cloud radar observations were also made. We also present an algorithm for solving the radar equation with a constraint of cloud optical thickness at visible wavelength, by which we can derive vertical profiles of cloud microphysics.

2. CLOUD OPTICAL THICKNESS AND EFFECTIVE RADIUS DERIVED FROM TRANSMISSION FUNCTION MEASUREMENTS

Let us consider the solar radiation incident on a plane-parallel atmosphere. We express the diffusely transmitted radiation at the bottom of the atmosphere as $I(\tau_c,\mu,\phi)$. The transmission function $T(\tau_c;\mu,\mu_0,\phi)$ is then defined by

$$T(\tau_c;\mu,\mu_0,\phi)=\frac{\pi I(\tau_c,\mu,\phi)}{\mu_0 F_0}. \qquad (1)$$

In this expression, τ_c is the optical thickness of the atmosphere (or cloud), μ is the absolute value of the cosine of the observation angle measured with respect to the positive τ_c direction, ϕ is the relative azimuth angle between the direction of propagation of the emergent radiation and incident solar radiation, μ_0 is the cosine of the solar zenith angle, and F_0 is the incident solar flux density. Since observations presented in this paper were made at zenith, we will not consider the dependence of the transmission function on μ and ϕ.

For a cloud particle size distribution, we adopt a log-normal distribution of the form

$$n(r)=\frac{N}{\sqrt{2\pi}\sigma r}\exp\left[-\frac{(\ln r-\ln r_0)^2}{2\sigma^2}\right], \qquad (2)$$

where N is the total number concentration, r_0 is the mode radius, and σ is the standard deviation. In terms of these parameters, the effective particle radius may be expressed as

$$r_e=r_0\exp(5\sigma^2/2). \qquad (3)$$

In this paper, we assume $\sigma = 0.35$.

We computed the transmission function for various values of τ_c, r_e, and the solar zenith angle θ_0 using rstar-4b, which is an accurate and efficient atmospheric radiation transfer code (Nakajima and Tanaka 1986, 1988). Figure 1 demonstrates the principles of the simultaneous determination of τ_c and r_e. The left panel shows computed relationships between the transmission function at 1.02 and 1.6 μm for water clouds when $\theta_0 = 30°$. The dashed lines represent the transmission function that results for specified values of τ_c, whereas the solid lines represent the transmission function that results for specified values of r_e. If cloud thermodynamic phase is known a priori, τ_c and r_e may be determined from transmission function measurements at these two wavelengths.

In general, cloud thermodynamic phase is not known. Therefore, transmission function measurements at 1.02 and 1.6 μm alone will not suffice to unambiguously determine τ_c and r_e. This ambiguity may be reduced by the additional 2.2 μm channel. The right panel of Fig. 1 is similar to the left panel, but for computed relationships between the transmission function at 1.02 and 2.2 μm. If the cloud we now observe is actually a water cloud, and if we use lookup tables computed for water clouds, then almost same values of τ_c and r_e should be derived from analysis using either 1.6 μm or 2.2 μm. On the other hand, if the cloud is composed of ice particles, we should get better agreement between 1.6 μm and 2.2 μm from lookup tables computed for ice particles. This is the principle for inferring cloud thermodynamic phase.

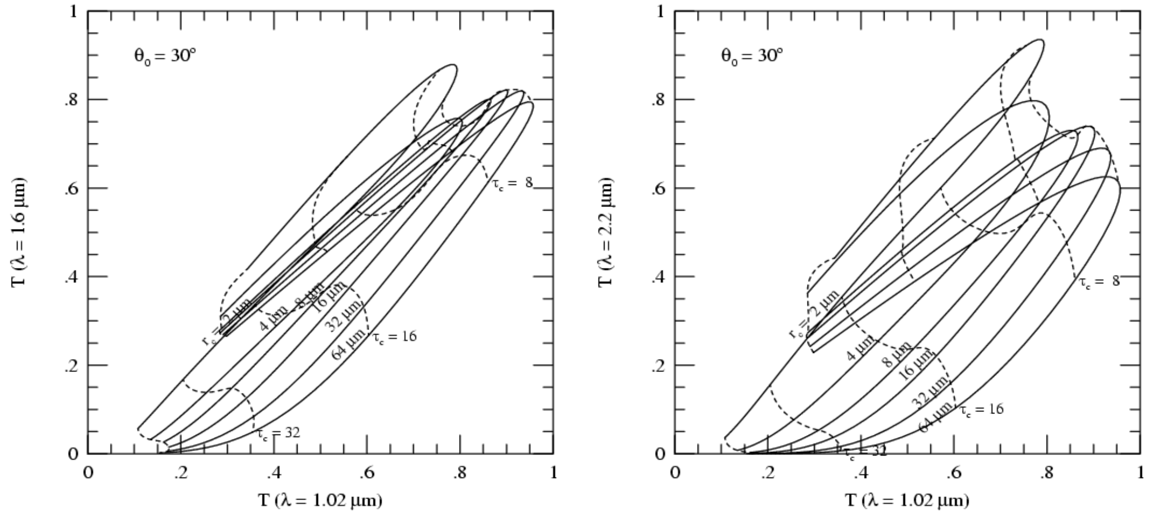

Figure 1. Computed relationships between the transmission function at 1.02 and 1.6 μm (*left*) and 1.02 and 2.2 μm (*right*) for various values of the cloud optical thickness and effective particle radius.

3. CLOUD VERTICAL PROFILES DERIVED FROM RADAR OBSERVATIONS

The radar signal $P(R)$ from the range R can be written in units of power as

$$P(R) = \frac{C}{R^2} Z_e(R) \exp\left[-2\int_0^R \sigma_{\text{ext}}(R')dR'\right], \qquad (4)$$

where Z_e is the effective reflectivity factor and σ_{ext} is the extinction coefficient. For a cloud with particle size distribution $n(r)$, Z_e and σ_{ext} are expressed as

$$Z_e = \frac{\lambda^4}{\pi^5 |K|^2} \int_0^\infty C_{\mathrm{back}}(r) n(r) dr , \tag{5}$$

and

$$\sigma_{\mathrm{ext}} = \int_0^\infty C_{\mathrm{ext}}(r) n(r) dr , \tag{6}$$

where λ is the radar wavelength, K is defined using complex refractive index of water as $K = (m^2-1)/(m^2+1)$, and $C_{\mathrm{back}}(r)$ and $C_{\mathrm{ext}}(r)$ are the backscattering and extinction cross section of a particle with radius r, respectively.

We denote liquid/ice water content by ρ. Then Z_e and σ_{ext} may be written as

$$Z_e = \rho \varsigma(r_e) , \tag{7}$$

$$\sigma_{\mathrm{ext}} = \rho \kappa(r_e) , \tag{8}$$

where $\zeta(r_e)$ is the effective reflectivity factor per unit liquid/ice water content, and $\kappa(r_e)$ is the mass extinction coefficient. For a particle size distribution given by equation (2), ζ and κ may be computed as a function of the effective radius r_e.

Kumagai et al. (2000) presented a method for solving equation (4) to obtain vertical profiles of cloud microphysics ρ and r_e, with a constraint of total liquid water path obtained from a microwave radiometer. We have developed another method for solving equation (4) with a constraint of the cloud optical thickness at visible wavelength, which may be obtained from transmission function measurements as described in Section 2. Details of our method will be described elsewhere.

4. RESULTS

Ground-based observations of clouds were conducted during August and September in 2003 at Koganei (35.71°N, 139.49°E), Tokyo, Japan. The instruments used were a PREDE i-skyradiometer and a 95-GHz cloud radar SPIDER.

Figure 2 shows cloud optical thickness (top panel) and effective particle radius (bottom panel) derived from the transmission function observed by the i-skyradiometer. For the time period shown in Fig. 2, our algorithm suggests that cloud particles were in liquid water phase. At the same time, SPIDER detected a cloud layer at about 1 km height, indicating that the cloud thermodynamic phase was properly determined by our algorithm.

The cloud optical thickness shown in Fig. 2 was used, in combination with radar reflectivity factor taken by SPIDER, to derive vertical profiles of cloud microphysics using the algorithm presented in Section 3. Figure 3 shows the time-height profile of the effective particle radius for the same time period as Fig. 2.

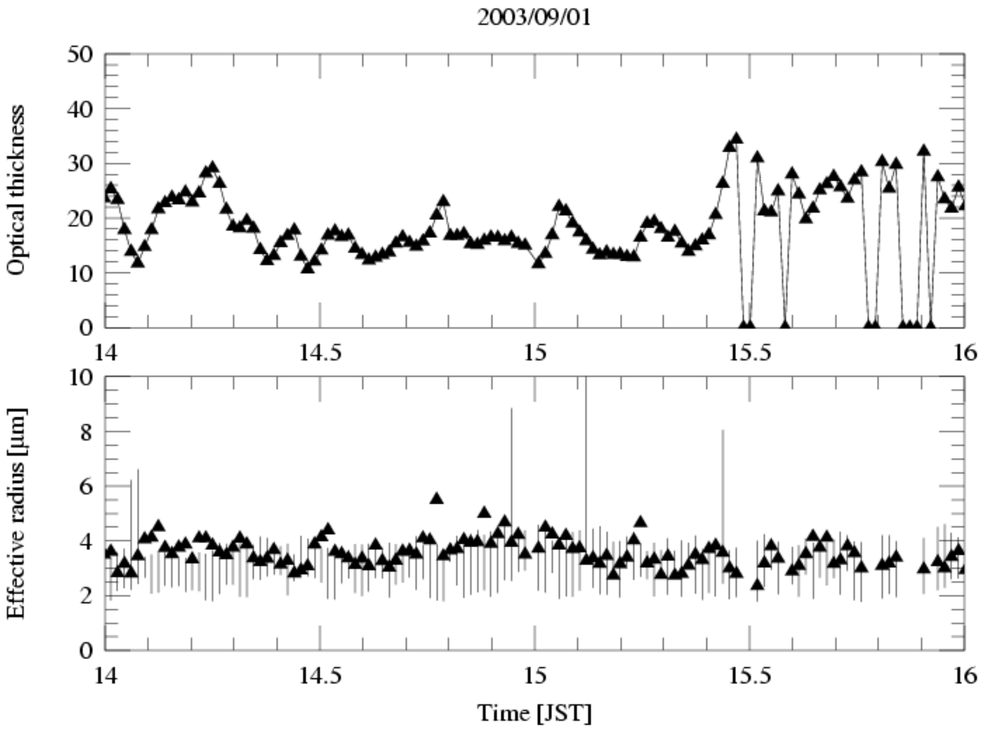

Figure 2. Cloud optical thickness (top) and effective particle radius (bottom) derived from transmission function measurement.

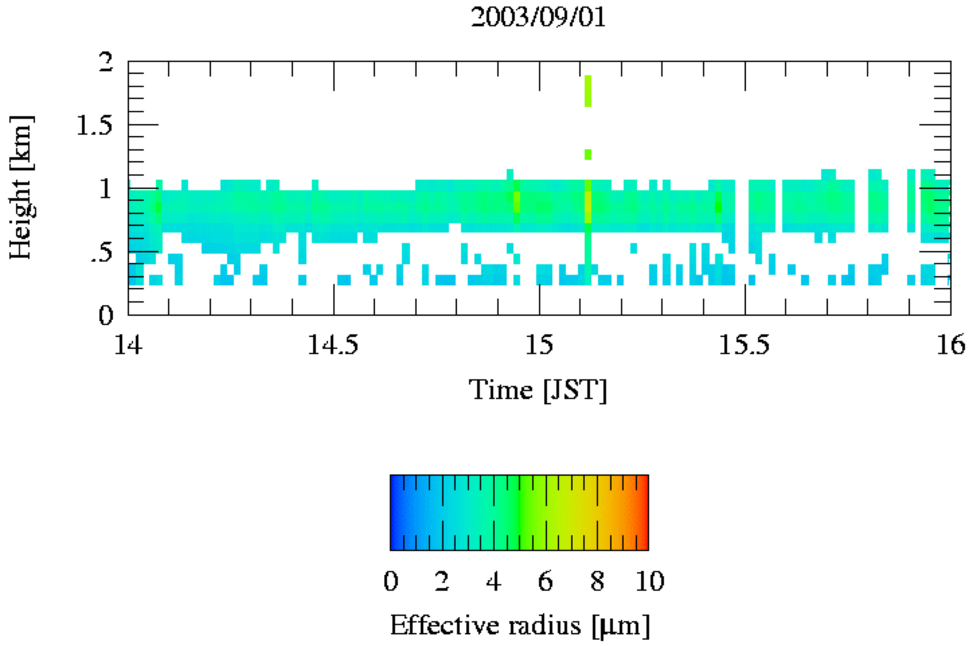

Figure 3. Effective particle radius derived from SPIDER with a constraint of cloud optical thickness obtained from i-skyradiometer.

From this analysis, minimum and maximum values of the effective radius are determined along the vertical direction, which are denoted by vertical bars in bottom panel of Fig. 2. Comparing the effective radius derived by the two different algorithms, we find good agreement between them.

5. CONCLUSIONS

We have developed an algorithm to derive the optical thickness and effective particle radius of stratiform clouds from measurements of the transmission function at near-infrared wavelengths. A method for deriving cloud vertical profiles from cloud radar observations has also been introduced, in which cloud optical thickness at visible wavelength is used as a constraint in solving the radar equation. Good agreement was obtained between these two methods for the effective particle radius, suggesting that the method to solve the radar equation with a constraint of visible optical thickness is also promising.

REFERENCES

Kumagai, H., H. Horie, H. Kuroiwa, H. Okamoto and S. Iwasaki, 2000: Retrieval of cloud microphysics using 95-GHz cloud radar and microwave radiometer, *Proc. SPIE*, **4152**, 364−371.

Nakajima, T., and M. D. King, 1990: Determination of the optical thickness and effective radius of clouds from reflected solar radiation measurements. Part I: Theory. *J. Atmos. Sci*., **47**, 1878−1893

Nakajima, T., and M. Tanaka, 1986: Matrix formulation for the transfer of solar radiation in a plane-parallel scattering atmosphere, *J. Quant. Spectrosc. Radiat. Transfer*, **35**, 13−21.

Nakajima, T., and M. Tanaka, 1988: Algorithms for radiative intensity calculations in moderately thick atmospheres using a truncation approximation, *J. Quant. Spectrosc. Radiat. Transfer*, **40**, 51−69.

Nakajima, T. Y., and T. Nakajima, 1995: Wide-area determination of cloud microphysical properties from NOAA AVHRR measurements for FIRE and ASTEX Regions, *J. Atmos. Sci*., **52**, 4043−4059

AUTHOR INDEX

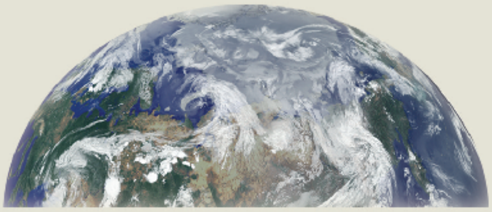

CEReS

Center for Environmental Remote Sensing,
Chiba University